DEPARTMENT OF CIVIL AND ENVIRONMENTAL ENGINEERING

EXPERIMENTAL AND COMPUTATIONAL INVESTIGATION OF THE STRUCTURAL RESPONSE OF ADOBE STRUCTURES

DOCTOR OF PHILOSOPHY DISSERTATION

ILLAMPAS ROGIROS

2013

DEPARTMENT OF CIVIL AND ENVIRONMENTAL ENGINEERING

EXPERIMENTAL AND COMPUTATIONAL INVESTIGATION OF THE STRUCTURAL RESPONSE OF ADOBE STRUCTURES

ILLAMPAS ROGIROS

A Dissertation Submitted to the University of Cyprus in Partial Fulfillment of the Requirements for the Degree of Doctor of Philosophy

2013

VALIDATION PAGE

Doctoral Candidate: Rogiros Illampas

Doctoral Thesis Title: Experimental and computational investigation of the structural response of adobe structures

The present Doctorate Dissertation was submitted in partial fulfillment of the requirements for the Degree of Doctor of Philosophy at the Department of Civil and Environmental Engineering, and was approved on the 3rd of September 2013 by the members of the Examination Committee.

Examination Committee:

Thesis Advisor: Ioannis Ioannou …….
Assistant Professor, Department of Civil and Environmental Engineering, University of Cyprus

Thesis Co-Advisor: Dimos Charmpis ……
Assistant Professor, Department of Civil and Environmental Engineering, University of Cyprus

Committee Chair: Stavroula J. Pantazopoulou ……
Professor, Department of Civil and Environmental Engineering, University of Cyprus

Committee Member: Paulo B. Lourenço …….
Professor, Department of Civil Engineering, University of Minho, Portugal

Committee Member: Ioannis Psycharis …….
Associate Professor, Department of Civil Engineering, National Technical University of Athens, Greece

DECLARATION OF DOCTORAL CANDIDATE

The present doctoral dissertation was submitted in partial fulfillment of the requirements for the degree of Doctor of Philosophy of the University of Cyprus. It is a product of original work of my own, unless otherwise mentioned through references, notes, or any other statements.

Rogiros Illampas

……..

ΠΕΡΙΛΗΨΗ

Η παρούσα διατριβή εξετάζει τη συμπεριφορά υλικών και κατασκευών από ωμό πηλό μέσω ενδελεχούς πειραματικής και υπολογιστής έρευνας. Για τους σκοπούς της μελέτης, έγινε δειγματοληψία σημαντικού αριθμού ωμόπλινθων από διάφορους σύγχρονους Κύπριους παραγωγούς. Οι ωμόπλινθοι αυτοί υποβλήθηκαν σε δοκιμές θλίψης και κάμψης με στόχο τον προσδιορισμό των μηχανικών τους ιδιοτήτων. Τα πειραματικά αποτελέσματα που προέκυψαν χρησιμοποιήθηκαν, για πρώτη φορά, στη διατύπωση αναλυτικών σχέσεων τάσεων-παραμορφώσεων που περιγράφουν τη μη-γραμμική απόκριση του υλικού σε καμπτικά φορτία. Διεξήχθηκαν πειράματα μονοτονικής θλίψης, θλιπτικής φόρτισης-αποφόρτισης και διαγώνιου εφελκυσμού σε δοκίμια ορθοδομικής και δρομικής τοιχοποιίας. Από τις δοκιμές αυτές προέκυψαν χρήσιμα στοιχεία σχετικά με τις μορφές αστοχίας, τη φέρουσα ικανότητα και την παραμορφωσιμότητα των ωμοπλινθοδομών. Έγιναν επίσης μετρήσεις του μέτρου ελαστικότητας, του μέτρου διάτμησης και του λόγου Poisson.

Για τη διερεύνηση της στατικής απόκρισης κτηρίων από ωμόπλινθους σε οριζόντια φορτία, διεξήχθησαν εργαστηριακές δοκιμές σε ένα υπό κλίμακα (1:2) μοντέλο παραδοσιακού οικήματος. Κατά τη διάρκεια των πειραματικών ελέγχων, καταγράφηκαν οι τυπικοί μηχανισμοί σεισμικής βλάβης που απαντώνται σε κατασκευές από άοπλη ωμοπλινθοδομή. Εξετάστηκαν παράγοντες, όπως η αλληλεπίδραση των φερόντων στοιχείων και η διαφραγματική λειτουργία της στέγης, οι οποίοι επηρεάζουν τη γενική στατική συμπεριφορά τέτοιων δομημάτων. Ακόμα, προσδιορίστηκαν στάθμες επιτελεστικότητας με βάση την καμπύλη αντίστασης του εξετασθέντος κτηρίου και τα επίπεδα βλάβης που παρατηρήθηκαν στις διάφορες επιβληθείσες μετατοπίσεις. Η συμπεριφορά κατασκευών από ωμόπλινθους διερευνήθηκε περεταίρω μέσω μη-γραμμικών αναλύσεων πεπερασμένων στοιχείων. Η τοιχοποιία από ωμόπλινθους προσομοιώθηκε ως ένα ιδεατό ομοιογενές μέσο χρησιμοποιώντας καταστατικό μοντέλο πλαστικότητας σκυροδέματος με βλάβες (damaged plasticity). Η υπολογιστική διερεύνηση επικεντρώθηκε στην προσομοίωση των δοκιμών θλιπτικής φόρτισης-αποφόρτισης και διαγώνιου εφελκυσμού σε τοιχάρια, καθώς και στις δοκιμές οριζόντιας φόρτισης του υπό κλίμακα κτηρίου. Σε όλες τις περιπτώσεις, επιτεύχθηκε ικανοποιητική σύγκλιση μεταξύ αριθμητικών και πειραματικών αποτελεσμάτων, τόσον όσο αφορά την μορφή αστοχίας όσο και την αναλογία φορτίου-μετατόπισης.

Η πειραματική και υπολογιστή διερεύνηση που διεξήχθη στα πλαίσια αυτής της διατριβής, διευρύνει την υφιστάμενη γνώση και συνεισφέρει δυναμικά στην ανάπτυξη κατάλληλων μεθόδων αποτίμησης και ανάλυσης. Επιπροσθέτως, η βάση δεδομένων που σχηματίστηκε από τον εκτενή πειραματικό έλεγχο τοπικών ωμόπλινθων αποτελεί χρήσιμο εργαλείο για πρακτικές εφαρμογές και διευκολύνει τη μελλοντική ακαδημαϊκή έρευνα σε παρεμφερή πεδία.

ABSTRACT

This thesis examines the behaviour of adobe materials and structures through rigorous experimental and computational research. Within this framework, a considerable number of adobe bricks were sampled from contemporary Cypriot producers and were subjected to compressive and flexural strength tests, in order to assess their mechanical properties. The experimental results were used, for the first time, in the development of an analytical model describing the full non-linear stress-strain response under bending. Furthermore, uniaxial monotonic and loading-unloading compression tests, as well as diagonal tension tests, were undertaken on stack-bonded prisms and running bond wallettes. These tests produced valuable information regarding the modes of failure, the bearing capacity and the deformability of adobe elements. Estimates for the modulus of elasticity, the shear modulus and Poisson's ratio of local adobes were also derived.

The structural behaviour of complete adobe buildings under horizontal loading was investigated through static laboratory tests on a 1:2 scaled replica of a single-storey traditional dwelling. During experiments, commonly encountered seismic failure mechanisms were reproduced. Factors which critically affect the global response of earthen buildings, such as the interaction among their load-bearing members and the diaphragmatic function of their roof configuration, were examined. Moreover, damage limit states at different deformation levels were identified. Adopting a continuum macro-modeling strategy and using a damaged plasticity constitutive law, non-linear finite element analyses of adobe structures were carried out. The numerical work focused on the simulation of the loading-unloading compression test, the diagonal tension test and the lateral loading test on the scaled model building. In all cases, comparisons made between numerical and experimental data revealed good agreement, both in terms of damage distribution and force-displacement response.

The experimental and numerical investigation of the structural response of adobe masonry elements and buildings, carried out in the framework of this thesis, extends existing research knowledge and vigorously contributes to the development of appropriate assessment procedures and computational analysis methods. Furthermore, the database of results formulated through the rigorous testing of local adobes may be utilized by practitioners and can facilitate future research in the field.

ACKNOWLEDGMENTS

The present study was developed at the Department of Civil and Environmental Engineering of the University of Cyprus. Research was carried out under the supervision of Assistant Professor Ioannis Ioannou and Assistant Professor Dimos Charmpis. I would like to express my gratitude to both supervisors for their guidance, careful advice, support and incitement throughout the duration of my tuition.

Experimental work was carried out at the Building Materials Laboratory of the University of Cyprus and its implementation would not have been successful without the valuable assistance of the laboratory staff. In particular, I would like to thank Dr. Loukas Petrou, head of the laboratory, for his interest and advice. I am also grateful to the laboratory technician, Mr. Micahlis Micahel, for his help in the preparation of the specimens and the test set-ups.

The funding granted by the University of Cyprus, as well as the financial support provided by the European Regional Development Fund and the Republic of Cyprus through the Cyprus Research Promotion Foundation in the framework of research programs ΕΠΙΧΕΙΡΗΣΕΙΣ/ΠΡΟΙΟΝ/0609/41 and ΝΕΑΥΠΟΔΟΜΗ/ΝΕΚΥΠ/0308/17 are gratefully acknowledged.

Last but not least, I would like to thank my family for their encouragement and unconditional support and my beloved Kyriaki for her enduring love and patience.

TABLE OF CONTENTS

LIST OF GRAPHS / ILLUSTRATIONS

LIST OF TABLES

1 INTRODUCTION

1.1 General

The term "adobe" is of Spanish/Arabic origin and is used to describe construction materials that are fabricated from moistened earth and allowed to dry naturally (Brown and Clifton, 1978). In most cases, the term refers to unfired clay masonry blocks, although earth-based mortars and plasters are also quite common. Adobe bricks, in particular, are composed of sand, silt and clay, which, when mixed with water to plastic consistency, can be cast into the desired form. Quite often, fibers such as chuff, flax straw, seaweed or hair are added to increase the material's resistance to cracking (Yetgin et al., 2008). In addition, adobe tends to contain varying amounts of small stones or gravel, while residual grass and twigs may also be present.

Adobe bricks have been used for thousands of years and are probably one of the first man-made building materials. According to archaeological evidence, mud bricks were invented 10,000-12,000 years ago; the moulded production of adobe developed in Mesopotamia 7,000 years ago (Morton, 2008). In our days, adobe masonry is no longer a prevailing form of construction in Western countries. However, it is still used in many developing countries, while a great number of earthen buildings still survives in most regions of the world and constitutes an essential part of the international architectural and cultural heritage. It is estimated that, even today, 30% of the earth's population is housed in earthen structures and these are mostly built of adobe (Houben and Guillard, 1994). Furthermore, the simplicity, low cost and almost negligible embodied energy associated with the production of adobes render them an attractive option for use in contemporary sustainable construction. Therefore, significant efforts are currently being made to reintroduce adobes as environmentally-friendly building materials and to optimize their properties.

Despite the fact that research related to earth-based materials has been intensified over the past decade, the production of mud bricks, the repair of existing adobe structures and the construction of new ones are still largely based on traditional techniques and empirical wisdom, instead of detailed engineering methods. The efficient use of adobe in conservation/restoration projects and in contemporary architecture is hindered by the lack of internationally accepted building standards, codes and regulations referring specifically to unfired earth. Considerable problems arise from the absence of extensive experimental data adequate to describe the full range of the material's and masonry's mechanical

characteristics. Moreover, available computational tools that have been developed for the analysis of conventional masonry structures (i.e. analytical relations and numerical models intended for masonry composed of stone, fired clay bricks, concrete blocks, etc.) have not yet been thoroughly examined and validated in the context of adobe construction.

Cyprus has a strong tradition of earthen architecture, since adobe was continuously and extensively used from the Neolithic era until the mid 20th century. Local adobe bricks have a characteristic slab-like form. Their dimensions are (height x width x length) 50 x 300 x 450 mm^3. Adobes in Cyprus were, almost exclusively, used for the construction of load bearing masonry walls. These walls were always built upon a stone foundation (Figure 1.1) and were 300 (internal walls) to 500 mm (external walls) thick. The bricks were laid with the application of a straw-based earth mortar, the composition of which was very similar to that of adobes. Additional architectural and structural elements made of wood and/or stone were always installed in local traditional earthen buildings. These included roof rafters, lintels, binding beams, posts, stone arches, wooden balconies and buttresses.

Figure 1.1: Photos of traditional Cypriot earthen dwellings showing adobe masonry walls constructed upon a rubble stone foundation. Note the variation in grain texture due to the use of different locally available materials.

Earthen buildings were mostly erected on the island's lowland regions, urban centers and coastal areas. In the semi-mountainous and mountainous regions, where natural building stones were available in abundance, the use of adobe was predominantly limited to the

upper floors. Surviving adobe structures in Cyprus date mainly from the first half of the 20th century and range from simple low-rise dwellings to two-storey buildings (Figure 1.2a) and large workshops. Currently, the use of adobe is confined to the rehabilitation of such historic and traditional buildings (Figure 1.2b). Unfortunately, even though adobe construction is considered to be an ancestral technique and the use of adobes in the restoration of listed earthen buildings is mandatory, available technical information regarding the material and local structures has been, until recently, rather limited.

(a) **(b)**

Figure 1.2: (a) Vernacular two-storey adobe masonry building in the village of Kakopetria, Cyprus. (b) Use of adobe bricks for the restoration of a traditional earthen dwelling in Cyprus.

In light of the above, it is evident that there is a need for further experimental and computational research in the field of adobe construction. Bearing in mind the natural randomness and inhomogeneity of earth-based materials, the properties of local adobes should be examined. Of critical importance is the investigation of the response of adobe masonry to various loading scenarios. The high seismic vulnerability of unreinforced earth masonry construction (Razani, 1978; Tolles et al., 1996) and the strong seismisity of areas where a significant number of earthen structures exists (i.e. wider Eastern Meditteranean region, South Asia, South America), indicate that the behaviour of adobe structures under horizontal loads should be studied in detail. In addition, they imply that appropriate assessment methodologies, accounting for the specific characteristics of local adobe masonry, should be developed. Such research outcomes shall not only facilitate the appraisal and rehabilitation of local existing earthen structures, but will also act as a basis

for improving the behaviour of traditional adobes and for adopting them in contemporary earthen architecture, without precluding rational engineering design.

1.2 Thesis objectives

The present thesis aims to address previously noted fields of research, where further work is required. It examines adobe materials and masonry structures, focusing on structural aspects of their behaviour. It adopts an integrated approach that includes both laboratory testing and computational analysis. The specific objectives of the thesis are to:

- record the current state-of-the-art;
- experimentally assess the mechanical properties of local adobe bricks;
- investigate the structural response of adobe masonry structural members and buildings through laboratory tests;
- evaluate the applicability of analytical and numerical methods for the analysis of unreinforced adobe masonry structures.

It is anticipated that, the outcomes of these objectives will be exploited in the context of future academic research and will provide technical guidance to engineers and practitioners.

1.3 Thesis outline

Chapter 2 reviews the current state of the art in the general field of adobe construction. References to research work conducted at international and local levels are cited, while the gaps that occur in the literature are highlighted.

Chapter 3 examines the behaviour of adobe bricks form Cyprus through the implementation of compressive and flexural strength tests. Extensive experimental data are reported and useful information regarding the bearing capacity and deformability of local adobes is provided. The effect of material composition and specimen form and size on the experimental results is discussed. Possible correlations among material properties are also considered. In addition, the experimental data is used for deriving analytical relations that describe adobe's stress-strain response under compression and bending.

The structural behaviour of adobe masonry is investigated in Chapter 4. Its compressive and diagonal tensile strengths are determined through laboratory tests on assemblages composed of local adobe bricks and compatible earth mortar joints. Again, focus is given not only on the ultimate strength of the specimens, but on their deformation characteristics as well. Values for the elastic modulus, shear modulus and Poisson ratio are also obtained experimentally. Using these data, the ability of various equations to predict the compressive strength of adobe masonry is evaluated.

Chapter 5 deals with the finite element simulation of adobe masonry structural members. An introductory overview of the different strategies used for modeling masonry is made. For carrying out numerical analyses, a continuum macro-modeling approach and a damaged plasticity constitutive law are used. The selection of appropriate parameters is discussed, based on the experimental results reported in this thesis and on data quoted in the literature. A uniaxial compression and a diagonal tension test are simulated and the numerical outcomes yielded are compared against corresponding experimental data.

The response of complete adobe structures to lateral loads is investigated in Chapter 6. This includes monotonic loading laboratory tests on a 1:2 scaled replica of an adobe building and finite element simulations of the experiments. The structural behaviour of earth masonry buildings is described in terms of displacement capacity and damage initiation and propagation. Through the numerical analyses conducted, a finite element continua model is calibrated to reproduce the recorded force-displacement response and the observed modes of failure. Moreover, the validity of the modeling parameters used in the simulation of individual structural elements is verified.

Finally, Chapter 7 presents an extended summary and reports the major conclusions derived from this study. Recommendations for future research are also made.

2 INTERNATIONAL AND LOCAL STATE OF THE ART

2.1 Introduction

A brief overview of the international and local state of the art in the general field of adobe-related research is hereby given. References are made to studies: (a) focusing on architectural aspects, (b) investigating pathology mechanisms, (c) involving experimental research on adobe materials and structures, (d) aiming to evaluate repair and strengthening techniques and (e) dealing with the analysis of earthen buildings. The various technical guides (i.e. national building codes and directive documents) that are presently available are also noted. By examining the existing literature, the gaps that occur in the scientific area of adobe construction are identified.

2.2 International state of the art

Despite the fact that earth masonry in not a prevailing construction technique in our days, international academic research related to adobe materials and structures has been intensified during the past few decades. This can be mainly attributed to two factors: (a) the necessity of protecting existing earthen structures and (b) the growing need for introducing environmentally friendly materials to the building industry.

Several research studies have been conducted in order to record the numerous typologies of earthen structures encountered in various regions of the world (e.g. Correia et al., 2011; Fratini et al., 2011; Zurakowska et al., 2009; Atzeni and Sanna, 2008; Delgado and Guerrero, 2006; Quagliarini, 2006; Jerome et al., 1999). Through these studies the architectural composition of adobe buildings is examined. In addition, the components forming the buildings' structural system are identified, while data regarding the properties of local materials is given. Different traditional construction and repair practices are recorded and their evolution through history is investigated (Keefe, 2005).

Certain researchers explore both the heritage of earthen construction and the significance of adobe in the modern building industry (Minke, 2009; Morton, 2008; Little and Morton, 2001; Norton, 1997; Doat et al., 1991; McHenry, 1989). In this framework, the potential applications of the material and the opportunities for development are assessed. Furthermore, recommendations regarding the production, quality control and use of adobe

bricks, based both on empirical practices and scientific research, are given. A number of case studies referring to the use of adobe for the construction of new buildings can also be found in the literature (Dowling, 2004; Ngowi, 1997).

Many researchers deal with the pathologies of adobe buildings. Tavares et al. (2012), for instance, have recorded and analyzed the factors that cause deterioration of adobe masonry. Due to the fact that earth masonry construction is susceptible to water-induced damage, some studies have focused primarily on evaluating the long-term durability of earthen materials exposed to wet climatic conditions in the field (Bui et al., 2009b; Guettala et al., 2006) or subjected to accelerated durability tests in the laboratory (Walker, 2004). Furthermore, efforts have been made to investigate the complicated mechanism of moisture ingress in unfired clay bricks (Pineda-Piñón et al., 2008; Hall and Djerbib, 2004, 2006a, 2006b; Packard, 1967). The use of technologically advanced methods for mapping and monitoring the progressive erosion of earthen archeological sites has also been considered (Fujii et al., 2009). Other studies aiming to examine commonly encountered forms of deterioration include investigations on the chemical degradation of adobes (Calabria et al., 2009), as well as on the processes of freeze-thaw damage and wind erosion (Qu et al., 2006).

Particular attention has been given to the effects of seismic action. For this purpose, both in-situ inspections of damaged buildings and large-scale laboratory tests have been implemented. Noticeable work has been undertaken by Tolles et al. (1996) who investigated the effects of the 1994 Northridge earthquake on historic adobe buildings. Field studies concerning the global structural response of adobe construction, the evolution of seismic damage and the occurrence of collapse mechanisms have also been conducted by Sayin et al. (2012), Rojas et al. (2008), Maheri et al. (2005), Kiyono and Kalantari (2004), Yucheng and Liu (1987) etc. On the other hand, Hardwick and Little (2010), Bartolomé et al. (2009) and Samali et al. (2004) carried out vibration laboratory tests on U-shaped models to examine the dynamic response of unconfined and confined adobe masonry construction. Yamin et al. (2004) performed cyclic loading tests on full-scale wall configurations and shake table tests on scaled-down complete adobe buildings. Systematic seismic studies on scaled models of complete adobe buildings have also been undertaken by Ottazzi et al. (1988) and Tolles and Krawinkler (1990). Samali et al. (2011) compared the seismic capacity of structures with square and circular configuration of load-bearing walls through static-tilt table tests on scaled masonry specimens.

Considerable work has been carried out on the characterization of adobe bricks and other earth-based construction materials. Experimental investigations have been undertaken to evaluate the physico-mechanical and thermal properties of adobes (Silveira et al., 2012; Piattoni et al., 2011; Vega et al., 2011; Kouakou and Morel, 2009; Okunade, 2009; Oti et al., 2009; Binici et al., 2007) and to determine their mineralogical and chemical composition (Adorni et al., 2013; Pagliolico et al., 2010; Millogo et al., 2008). Relative laboratory testing projects have also been implemented on clay-based composites (Galán-Marín et al., 2010; Ghavami et al., 1999), compressed earth bricks (Muntohar, 2011), rammed earth (Reddy and Kumar, 2010; Bui et al., 2009a) and mud-mortars (Azeredo et al., 2007). The fracture characteristics of unfired earth blocks and the evolution of cracking/damage under compression and bending have been investigated by Lenci et al. (2011) and Clementi et al. (2008). Studies aiming to examine the effects of the raw materials on the behaviour of mud-bricks have also been performed. Through experimental investigation, the suitability of different types of soils has been evaluated (Delgado and Guerrero, 2007) and the effect of fibers on the material's properties has been assessed (Hejazi et al., 2012; Aymerich et al., 2012; Quagliarini and Lenci, 2010; Yetgin et al., 2008). Reviews and comments regarding the various destructive testing methods currently used for the mechanical characterization of unfired clay building materials can be found in Morel et al. (2007) and Morel and Pkla (2002). Based on experimental data, Silveira et al. (2013) have determined correlations between the results obtained from the adoption of different testing procedures and have formulated stress-strain relations describing the compressive behaviour of adobes from Portugal.

Apart from assessing the properties of traditional adobes, efforts have been made to improve their mechanical characteristics and to promote their re-introduction in contemporary structures. For this purpose, researchers have emphasized the use of various types of natural and synthetic fibers (Islam and Iwashita, 2010; Binici et al., 2005). The addition of polymers, water repellants and stabilizers (concrete, gypsum, lime, etc.) in order to enhance the material's resistance to moisture penetration has also been considered (Burroughs, 2008; Pineda-Piñón et al., 2007; Degirmenci, 2008; Ren and Kagi, 1995).

Concerning the mechanical properties of adobe masonry, research is currently focused on investigating the response of wallettes to various loading scenarios. Within this context, laboratory tests have been performed on adobe assemblages, as well as on full- and reduced-scale walls, to assess their compressive, bending and shear capacity (Quagliarini et al., 2010; Heath et al., 2009; Torrealva et al., 2008; Walker, 2004; Yamin et al., 2004;

Gavrilovic et al., 1998). Using the outcomes of laboratory tests, the stress-strain behaviour of adobe construction has been examined, while estimates for the elastic modulus and Poisson's ratio have been derived (Wu et al., 2012). Acknowledging the influence that earth mortar joints pose on the behaviour of mud-brick masonry, Reddy et al. (2009), Dowling et al. (2004) and Azeredo and Morel (2009) have conducted bonding and direct shear laboratory tests. Similar field experiments have been implemented on adobe walls that had sustained seismic damage by Kiyono and Kalantari (2004). Larger scale, in-situ destructive and non-destructive testing has also been carried out on existing adobe buildings. The assessment methods adopted in this case include sonic transmission monitoring, penetration tests, ambient vibration measurements, as well as in-plane horizontal and diagonal loading tests (Varum et al., 2008; Liberatore et al., 2006).

Moreover, research projects on the repair, strengthening and retrofitting of adobe structures have been carried out. Grau et al. (2006) and Tolles et al. (2000) investigated, among other retrofitting measures, passive protection methods based on the installation of horizontal straps and perimeter cables. In addition, Tolles et al. (2000) and Ginell and Tolles (2000) examined the introduction of center-core steel rods in adobe masonry for improving its flexural strength. Integrated retrofitting systems composed of bamboo or cane vertical reinforcements and horizontally placed ropes or fencing wires have been studied by Torrealva et al. (2006) and Dowling et al. (2005). Furthermore, Garcia et al. (2004) performed laboratory tests to evaluate whether the application of vertical and horizontal Glass Fiber Reinforced Polymer (GFRP) bars can reduce the risk of seismic collapse. For increasing the global deformation capacity of earthen buildings, Yamin et al. (2004) examined the addition of boundary timber elements. Other strengthening methods considered include the use of polymer and steel welded wire meshes, fiberglass-reinforced plasters and geo-grids (Turanli and Saritas, 2011; Tipler et al., 2010; Blondet et al., 2008a; Torrealva et al., 2006; Yamin et al., 2004). The use of grout mixtures for the repair of cracked adobe masonry has been examined by Silva et al. (2009, 2010), Toumbakari (2010) and Roselund (1990). Tolles et al. (2003) have made recommendations regarding the execution of repair works and suggestions on how to improve the overall response of adobe buildings. Case studies describing the application of both innovative and empirical restoration techniques can also be found in the literature (e.g. Jager and Fuchs, 2010; Hurd, 2006; Jerome et al., 1999; Green and Watson, 1988; Hammond, 1973).

Although the structural analysis of conventional masonry construction has been studied in depth through academic research (e.g. Lourenço, 2002; Psycharis et al. 2001) and a broad

variety of computational tools does exist (Lourenço, 1994, 2000; Galasco et al. 2006; Tastani et al. 2009; Vamvatsikos and Pantazopoulou, 2010), the applicability of detailed engineering assessment methodologies for the appraisal and/or design of adobe structures has not yet been adequately evaluated. This is highlighted by the lack of extensive research on analytical methods and the rather limited number of studies dedicated to the numerical simulation of earthen structures. Static and dynamic finite element simulations, based on continuum models, have been undertaken by Tarque et al. (2010a, 2012a, 2012b), who calibrated numerical models based on experimental data obtained from tests on full-scale wall configurations and buildings. Emphasis was given on macroscopically capturing the general behaviour (mode of failure, displacements, etc.) of the modules tested in the laboratory. Tarque et al. (2012c, 2010b) have also presented computational assessments of the seismic capacity and fragility of adobe buildings. More detailed micro-modeling strategies have been adopted by Islam and Watanabe (2004) and Cao and Watanabe (2004). These researchers developed and analyzed 3D models to reproduce experimental results and to make predictions on the response of mud-brick buildings to earthquakes. Using the discrete element method, Morales and Delgado (1992) performed 2D numerical analyses to implement a feasibility study regarding the construction of two-storey adobe buildings in Peru. Furukawa and Ohta (2009) and Furukawa et al. (2009) also adopted the discrete element method to undertake dynamic simulations on 3D models of mud-brick structures, aiming to investigate the application of vulnerability functions for casualty estimation in the case of earthquake-induced collapse. The use of computational tools for the design of retrofitting/strengthening methods has not yet been examined in depth.

Recently, due to the fact that several urban war operations have taken place in Asian and Arab regions, where there is still an abundance of earthen buildings, another aspect related to adobe has grasped the attention of researchers. This is the response of adobe masonry to high-velocity impact. For this purpose, the U.S. Army Corps of Engineers has conducted laboratory tests to assess the mechanical and dynamic characteristics of adobe materials and masonry components (Beatty et al., 2012). The results of this work have been used for performing physics-based penetration simulations of high-fidelity adobe wall models (Meyer, 2013).

As seen above, research related to earthen materials and structures is quite common nowadays. Unfortunately, the accumulated knowledge has not yet been incorporated into the scopes of internationally accepted technical documents. In particular, internationally accepted building standards, codes and regulations that refer to masonry construction (e.g.

Eurocode 6) preclude adobe from their clauses, or simply assume masonry units to be comprised of stone, fired-clay bricks, concrete blocks, etc. The lack of standardized testing procedures is clearly mirrored in the literature, where a variety of testing methodologies, specimen types, failure criteria and sample curing techniques is encountered. Consequently, many of the data reported in different studies are not directly comparable, while the validity of research results cannot be indiscriminately broadened. Furthermore, the lack of applicable computational tools forces engineers who deal with the appraisal of earthen buildings to depend mostly on experiential judgment, rather than scientific-based assessment. It is worth noting that certain individual countries and states have developed national building codes and directive documents, which mainly prescribe methods for the quality control of earthen materials and structural components. Such countries and states are: Australia (Walker, 2002), New Zealand (NZ4297; NZ4298; NZ4299), Germany (Lehmbau Regeln), Peru (NTE E0.80) and New Mexico State (14.7.4NMAC). It must be stressed out however, that the applicability of these documents is confined only to national level, due to the inhomogeneity of earthen materials, the unique mechanical properties of local adobes and the different production techniques encountered in each country.

2.3 Local state of the art

Contrary to the broad field of research encountered at an international level, in Cyprus data regarding adobe construction is currently scarce. Information about the pre-historic use of adobe materials in the island can be found in Philokyprou (1998). This study includes a substantial amount of archeometrical data concerning ancient construction techniques, as well as the composition, size and grain texture of adobes found in local Neolithic settlements.

References on the traditional building techniques with unfired earth and the typology of adobe structures can be found in Papacharalambous (1968) and Sinos (1976). The aforementioned studies, however, mainly record local traditions and describe features of vernacular architecture, without addressing technical aspects. A summary of the state-of-the-art of earthen architecture in Cyprus has been compiled by Illampas et al. (2011a). Demetriou et al. (2006) have fairly recently published some indicative data on the physico-mechanical characteristics of local adobes. They have also made recommendations for the conservation and restoration of the island's earthen buildings, based mostly on empirical practices and on research conducted in other countries.

In the last few years the University of Cyprus has undertaken and is carrying out considerable research initiatives regarding adobe construction. Currently two research projects examining adobe materials and structures are in progress. The first project, in the framework of which this thesis has been conducted, focuses on the experimental and computational investigation of the structural response of adobe buildings. Up-to-date, the research activities completed include a study on the pathology and repair of earthen buildings (Illampas et al. 2010a, 2013) and a broad experimental investigation of the behaviour of adobe bricks, masonry assemblages and complete structures (Illampas et al. 2011b, 2010b-c). The application of novel micro-destructive techniques, such as scratch testing, in the evaluation of the mechanical properties of adobes has also been studied (Illampas et al., 2010b). In addition, the application of analytical and numerical methods for the appraisal of adobe construction has been examined (Illampas et al. 2011c-d, 2010c).

The second research project deals with the production of adobe bricks with improved properties and aims to promote the use of adobe in contemporary architecture as an alternative environmentally friendly form of construction. Within this context, modifications for optimizing the material's production techniques have been considered. Furthermore, several methods (i.e. mix design variations, use of different types of fibers, chemical stabilization and addition of water-repellants) for enhancing the material's physico-mechanical characteristics have been evaluated through laboratory testing (Eftychiou, 2013).

2.4 Summary

To sum up, one can argue that, although significant progress has been achieved recently in the field of earthen-materials research, considerable work is still required in order to ensure the effective preservation of mud-brick structures and the efficient application of adobe materials in contemporary architecture. At local level, systematic research should be undertaken to evaluate the current state of earthen structures and to assess the properties of adobe bricks. In addition, appropriate testing methodologies that would account for the specific characteristics of unfired earth should be studied and their applicability on local materials should be examined. The lack of technical guidance concerning the design/appraisal of adobe construction internationally further indicates that there is an imminent need for conducting investigation on both analytical and numerical structural analysis methods. This implies that computational studies based on experimental material

data must be conducted and modeling parameters appropriate for the simulation of adobe construction should be calibrated.

The present thesis aims to address areas of research in the wider adobe masonry field, where gaps, such as those noted above, occur. For this purpose, it emphasizes on structural aspects and incorporates both experimental and numerical work. Adobe bricks from Cyprus are characterized in terms of their mechanical strengths, while the structural response of adobe masonry assemblages and buildings is examined through laboratory tests. Experimental research outcomes are utilized for the derivation of analytical relations describing the material's response to loading. They are also used for the formulation and analysis of finite element numerical models.

3 EXPERIMENTAL INVESTIGATION OF THE MECHANICAL PROPERTIES OF ADOBE BRICKS

3.1 Introduction

This chapter refers to the methodologies used for the mechanical characterization of adobe bricks. It also includes experimental results from compressive and flexural strength tests on samples from Cyprus and it discusses the use of appropriate failure criteria for the evaluation of adobe compressive strength in the context of engineering design.

The experimental results are compared with corresponding data from the literature and are used for the definition of mathematical models describing the stress-strain behaviour of adobe bricks under compression and three-point bending. Possible correlations between the material's mechanical properties are also examined.

3.2 Overview of the mechanical characterization of adobe materials

Up to date, there is a distinct lack of formal technical guidance concerning the laboratory testing of adobes and an absence of globally accepted standardized procedures accounting for the material's specific characteristics. Internationally used building codes and regulations that refer to the mechanical strength testing of masonry units (e.g. EN 772-1, EN 772-6, ASTM C67 - 12, ASTM C1006 - 07) exclude materials composed of unfired earth from their scopes. Standardized testing methods for evaluating the unconfined compressive strength of cohesive soils do exist (ASTM D2166 - 06) and have been used for investigating the response of fiber-reinforced clay-based composites (e.g. Bera et al., 2009; Gullu and Hazirbaba, 2010). These procedures, however, examine earthen materials from the point of view of geomechanics, rather than in the context of common building applications.

Some useful guidelines for assessing the mechanical properties of earthen materials can be found in national directive documents that have been developed by certain individual countries and states such as Australia (Walker, 2002), New Zealand (NZ4298), Germany (Lehmbau Regeln), Peru (NTE E0.80) and New Mexico (14.7.4NMAC). These documents include specific references to testing methodologies and prescribe permissible strength values. Unfortunately, there is little consensus among the procedures described and the

limits set (Morel et al., 2007; Walker and Morris, 1997). Moreover, their broader applicability is arguable due to the heterogeneity of earthen materials, the variations in shape and form that occur between different areas and the different production techniques encountered in each region.

3.2.1 Assessment of compressive strength

Masonry materials are primarily incorporated into load-bearing walls carrying vertical loads and are hence subjected to compressive stresses. Consequently, the assessment of the uniaxial compressive strength of individual bricks is essential for the design/appraisal of masonry construction and is considered to be a universally accepted measure for specifying its quality. In addition, the determination of the materials' complete stress-strain compressive behaviour is required for the implementation of non-linear structural analyses.

In the absence of globally accepted standards referring to earthen materials, the compressive strength testing of adobe bricks has largely relied on procedures developed for other types of masonry units, the majority of which have significantly different properties and microstructure. The most widely adopted methodology is the direct load testing of specimens. Samples are generally tested in the direction in which they will be laid during construction. Load is applied following either a load- (Quagliarini and Lenci, 2010; Vega et al., 2011) or, more often, a displacement-controlled (Silveira et al., 2012, 2013; Lenci et al., 2011; Fratini et al., 2011) process. The uniaxial compressive strength (f_b) is estimated using the equation:

$$f_b = \frac{P}{A} \tag{3.1}$$

where P is the maximum load exerted and A the original cross-sectional area of the specimen. To achieve a uniform distribution of the compressive load when the specimens' surfaces have significant irregularities, it is usually proposed to use capping. This can be plywood, softwood (Norton, 1997), mortar (McHenry, 1989; Silveira et al., 2013) or a layer of sand (Lenci et al., 2011; Piattoni et al., 2011). Alternatively, the surfaces of test specimens may be smoothened by abrasion (Adorni et al., 2013).

Adobe samples obtained from existing earthen walls (Fratini et al., 2011; Silva et al., 2010; Silveira et al., 2013), cut from full size bricks (Quagliarini and Lenci, 2010; Piattoni et al., 2011; Lenci et al., 2011) or formed through mould casting (Binici et al., 2005; Yetgin et al., 2008) have been examined by a number of researchers. Several sizes and forms of test

units are quoted in the literature and have been used for assessing adobe's compressive strength. These include full scale bricks (Piattoni et al., 2011; Vega et al., 2011), prisms with length-to-width ratio of at least 2 (14.7.4NMAC; Lenci et al., 2011; Adorni et al., 2013) or with an approximate height-to-width ratio of 0.5 (Quagliarini and Lenci, 2010; Piattoni et al., 2011; Okunade, 2009) and cubes with edges of 40 mm (Galán-Marín et al., 2010), 50 mm (Lenci et al., 2011; Norton, 1997), 100 mm (Silveira et al., 2013; Yetgin et al., 2008) and 150 mm (Binici et al., 2005). The use of cylinders with 1:1 and 2:1 aspect ratios and diameters ranging from 50 to 150 mm is also encountered in the literature (Silveira et al., 2012, 2013; Martins and Varum, 2006; Keefe, 2005; Norton, 1997). The broad variety of test specimens' shapes and sizes mentioned above leads to questions regarding the effects of geometry on the results obtained. However, in practice, platen restrain effects are usually neglected and the average compressive strength is simply expressed following statistical analysis of individual test results. Hence, direct comparison of tests results is almost impossible.

Considerable differences occur in the treatment of samples prior to testing. Many researchers prefer to store adobe specimens under stable thermo-hygrometric conditions for a certain period of time (Quagliarini and Lenci, 2010; Lenci et al., 2011; Fratini et al., 2011), whereas others apply drying at a certain temperature up to constant weight (Yetgin et al., 2008). In some cases, samples are allowed to dry outdoors under direct sunlight, so as to replicate traditional production methods (Vega et al., 2011; Okunade, 2009). The curing of specimens in wet gunny bags and the implementation of tests after 28, 72 and 96 days of casting is also noted (Binici et al., 2005).

The majority of researchers investigating the compressive behaviour of adobes focus on assessing the ultimate bearing capacity of specimens. The results of compression tests reported in the literature vary from 0.6 to 8.3 MPa. The most commonly encountered values range between 0.8 and 3.5 MPa. The lowest acceptable values set in national directive documents for the compressive strength of individual adobe units range from 1.2 (NZ4298; NTE E0.80) to 2.1 MPa (14.7.4NMAC).

It is worth noting that, apart from the mere determination of the failure stress, loading-unloading experiments have been carried out in order to quantify the reduction in the material's Young's modulus in terms of scalar damage parameters (Lenci et al., 2009, 2011). Moreover, Silveira et al. (2013) and Adorni et al. (2013) have utilized stress-strain data obtained from tests on cylindrical and cubic specimens to define corresponding analytical equations capable of describing the non-linear compressive response of adobes.

3.2.2 Assessment of flexural and tensile strengths

Occasionally, masonry units alone or within assemblages may fail in a tensile mode due to lateral stresses generated by the imposition of significantly high concentrated compressive loads (e.g. setting of slender beams into masonry). Therefore, the results of bending and/or splitting tensile strength tests are also used as indicators of the units' loading ability. Furthermore, these tests are commonly used in practice for examining the presence of defects (i.e. voids, fissures, impurities) in masonry materials.

For assessing the flexural and tensile strength of adobes, two methodologies are primarily used: three-point bending tests and splitting tests. Although some researchers comment that the results yielded by these tests have relatively little direct bearing on suitability for most earth block applications, they acknowledge that they can be a useful indicator of the material's quality (Minke, 2009; Walker, 2004). This, along with the ease of application, has often led to the adoption of, mainly, three-point bending tests for the in-situ quality control of adobe bricks.

As in the case of compression tests, the implementation of bending and splitting tests is mostly based on standards developed for other types of materials (e.g. EN 12372; EN 772-6, 2001; ASTM C1006 - 07), on the guidelines of national directive documents (e.g. 14.7.4NMAC) and on the recommendations of academic researchers (e.g. Keefe, 2005; Norton, 1997; Doat et al., 1991). In three-point bending tests, specimens are placed on two parallel tube supports spaced 200-350 mm apart. A concentrated force is applied at a constant rate to a horizontal tube placed in the middle of the unit to be tested until this fails. For examining adobe materials, the force imposition usually follows a displacement-controlled procedure (Silveira et al., 2013; Aymerich et al., 2012; Lenci et al., 2009). The flexural strength ($f_{t,flex}$) is computed using the following formula:

$$f_{t,flex} = \frac{3Pl}{2bt^2} \tag{3.2}$$

where P is the rupture load, l the span between supports, b the width of the sample and t the sample height.

Three-point bending tests have been performed on full size blocks (Silveira et al., 2013; Vega et al., 2011; Liberatore et al., 2006), half bricks (Clementi et al., 2008) and prisms (Adorni et al., 2013; Aymerich et al., 2012; Lenci et al., 2009). The samples examined were either obtained from existing structures (Silveira et al., 2013; Adorni et al., 2013) or prepared in the laboratory (Aymerich et al., 2012; Vega et al., 2011). Both specimens with

and without initial notches have been examined in order to assess the material's flexural strength and to investigate its fracture characteristics (Aymerich et al., 2012; Clementi et al., 2008). Furthermore, cyclic tests have been carried out to study post-yield damage propagation and stiffness degradation (Lenci et al., 2009).

A wide range of flexural strength values (i.e. 0.2 to 1.0 MPa) are quoted in the literature. According to the New Mexico Building Code (14.7.4NMAC) and to the data reported by McHenry (1989), adobe bricks should have a minimum average flexural strength of 0.35 MPa. Similarly, the Peruvian Standard (NTE E0.80) proposes a minimum flexural strength of 0.4 MPa. On the other hand, the New Zealand Standard (NZ4298) states that the flexural tensile strength of adobe, measured by the three-point bending test, is quite variable, with most results lying between 10% and 20% of the material's compressive strength. The ratio depends on the quality of the material and whether it is stabilized or unstabilized. Although such correlations between the flexural and compressive strength have been experimentally verified for compressed earth blocks (Morel et al., 2007; Morel and Pkla, 2002), they have not yet been established for handmade adobe bricks.

In splitting tensile strength tests, the load is applied along the length of a cylindrical specimen, on two diametrically opposite lines, until failure occurs. Theoretically, opposite compressive forces generate a nearly uniform state of tension across the plane subjected to loading, causing a tension mode failure (Carmona and Aguado, 2012). The tensile strength ($f_{t,split}$) is evaluated as:

$$f_{t,split} = \frac{2P}{\pi dl} \tag{3.3}$$

where P is the maximum load imposed, d the specimen height or diameter and l the length of the specimen over which the load is imposed.

Split testing of adobes has been undertaken by Adorni, et al. (2013), Silveira et al. (2012, 2013) and Martins and Varum (2006) on cylindrical specimens extracted from historic buildings. The experimental data derived by these researchers range between 0.05 and 0.40 MPa and present significant deviations. Comparisons made by Silveira et al. (2013) indicate that the outcomes of three-point bending tests are systematically higher than those of splitting tests.

3.3 Material sampling

In order to examine the behaviour of adobes from Cyprus, sample bricks were obtained from three different local producers (Ly, Ath and Ge) (Figure 3.1). It should be pointed out that, in the absence of a local or European standard for the quality control of earthen materials, the production of adobes in Cyprus is currently carried out by small-scale family-owned enterprises and it is almost exclusively based on experience and empirical methods, rather than proper industrialized procedures.

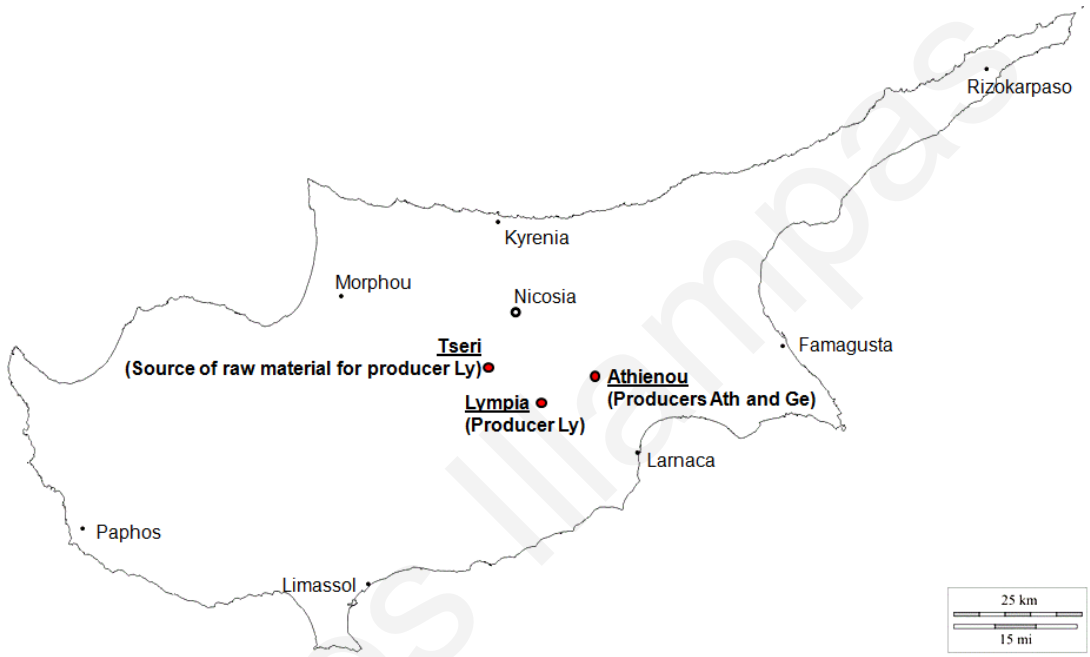

Figure 3.1: Map of Cyprus showing the sampling locations and the source of raw material (i.e. soil) used by a certain local producer.

Table 3.1: List of samples provided by three local producers. The number of samples is reported as *y*(*Xb*), where *y* = number of bricks, *X* = manufacturer code, *b* = batch code.

Manufacturer	Production area	Number of samples obtained from each batch
Ly	Lympia, Nicosia District	5(LyA) + 6(LyB) + 110(LyC)
Ath	Athienou, Larnaca District	4(AthA) + 5(AthB) + 8(AthC) + 5(AthE) + 5(AthF)
Ge	Athienou, Larnaca District	3(GeA)

Full-size local adobes measure approximately (height x width x length) 50 x 300 x 450 mm^3. The samples collected belonged to various production batches. Table 3.1 lists the samples supplied by each manufacturer and records the number of bricks belonging to each batch. Descriptions regarding the composition of the adobes examined and the procedures used in their production are given in the following subsections.

3.3.1 Samples obtained from the Lympia area

Adobes supplied by producer Ly belonged to three separate batches (i.e. LyA, LyB and LyC). The soil used in the production of all bricks came originally from an area near the village of Tseri (Figure 3.1), which has also been used as a source of raw material for the local ceramic industry. A relatively small amount of finely chopped straw fibers (3-25 mm in length) were also used as binder in the mix. The soil, fibers and water were mixed in a planetary mixer (Figure 3.2a). The mixture was left to ferment and was then cast into aluminium moulds. The bricks that were formed were laid on a flat concrete surface and were left to dry for 3 days (Figure 3.2b). Following drying, they were stack in palettes and were stored in a roofed area.

(a) **(b)**

Figure 3.2: (a) Planetary mixers used by producer Ly for kneading the mixture used in the production of adobes. (b) Drying of adobe bricks produced by manufacturer Ly.

The finished product had quite smooth surfaces and relatively parallel edges. Stereomicroscopic images (Figure 3.3) of random specimens from various production batches confirmed that all adobes had similar grain texture and consistency. Straw fibers

were evenly distributed within the material's matrix, while a limited number of small (≤ 4 mm in size) stones and/or gravel were occasionally present.

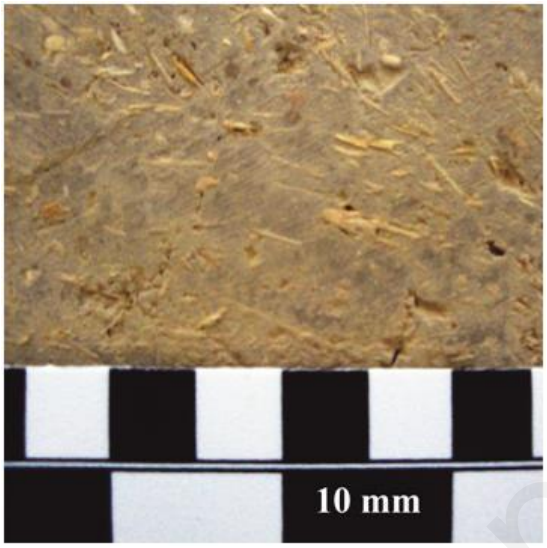

Figure 3.3: Stereomicroscopic image of representative adobe brick from producer Ly.

Despite the fact that all adobes produced in the Lympia area were uniformly sized and appeared to be homogeneous and compact, their homogeneity was very often disturbed by surface cracks measuring up to 1 mm in width. In a limited number of samples, cracks >1 mm wide were also detected. In many cases, cracks appearing on the surface of the samples extended into the core of the material. Discontinuities were accumulated at the bottom surface of the bricks and were probably the result of non-uniform drying shrinkage, following the placement of adobes on the relatively impermeable concrete drying surface, which prevented the efficient ventilation and smooth curing of the wet mixture.

3.3.2 Samples obtained from the Athienou area

Adobe bricks from five different production batches (AthA, AthB, AthC, AthE and AthF) were supplied by producer Ath. The raw material (i.e. soil) used for the production of these adobes mostly originated from random excavations at various different locations on the island. This was mixed with the binder (variably sized straw of length 2-65 mm) and water in a large earth crater (Figure 3.4a). The mixture was kneaded with the use of an excavator and shovels. It is worth noting that producer Ath opted to randomly modify the mix design among the various production batches. Both aluminium and timber moulds were used for casting the adobes. The end-products were laid on earth covered with straw (Figure 3.4b)

to dry for a period of 1-3 days. Following drying, they were stack in piles, which were then covered with nylon sheets. The piles were stored in an open field.

(a) **(b)**

Figure 3.4: (a) Earth crater in which manufacturer Ath mixes the raw materials for the production of adobes. (b) Adobe bricks cast by manufacturer Ath laid on field ground covered with straw to dry under the sun.

The upper exposed surfaces of all samples provided by producer Ath were quite rough, possibly due to inadequate leveling during casting. Furthermore, due to the uneven spreading of the earth mixture in the moulds, the edges of the material were not always parallel and in some cases the height of the bricks exceeded the locally established usual height of 50 mm.

The composition of the adobes provided by producer Ath varied considerably among batches. Bricks belonging to batch AthA had a solid matrix that did not incorporate any stones/gravel or indeed discontinuities (Figure 3.5a). In addition, they contained significant amounts of straw fibers, the length of which was between 2 and 30 mm. On the other hand, the mixture used in batches AthB and AthC included medium-sized straw fibers (4-40 mm length) and noticeable amounts of stones (mostly chalks and marls), the size of which, in some cases, exceeded 35 mm (Figure 3.5b-c). In certain bricks, traces of organic material (roots, wood, coal etc.) were detected. Adobes belonging to the other two batches (AthE and AthF) were also quite inhomogeneous (Figure 3.5d). They contained a significant amount of stones and gravel (2-20 mm in size), as well as fragments of ceramics and wood. In addition, both the distribution and the size of the straw fibers were rather random in these two batches.

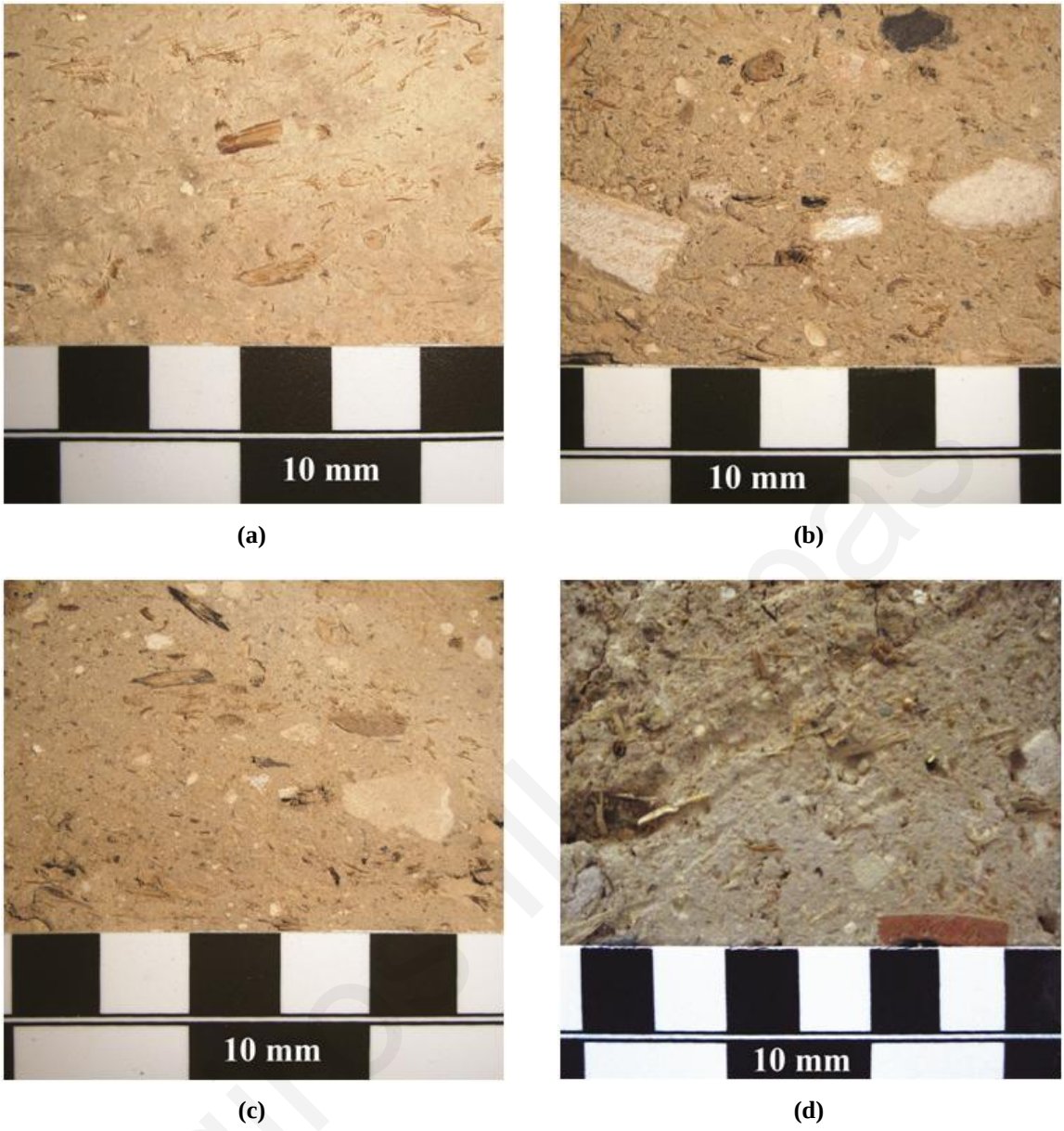

(a) **(b)**

(c) **(d)**

Figure 3.5: Stereomicroscope images of adobes provided by producer Ath. (a) Batch AthA, (b) Batch AthB, (c) Batch AthC and (d) Batch AthF. Note the distinct differences in the composition of the material as a result of the random mix design modification and the application of non-standardized production techniques.

Adobes provided by producer Ge belonged to a single batch (GeA). For the production of these bricks, soil excavated from selected agricultural fields around the village of Athienou was used. This soil was first roughly processed and then mixed with straw fibers (5-30 mm length) and water in a small crater formed in-situ. The raw materials were thoroughly kneaded with a shovel throughout the mixing procedure. When the mixture reached plastic consistency, it was cast into timber moulds and was left to dry on earth covered with straw.

Following drying, the bricks were stack in piles, which were partially covered with nylon sheets and stored in an open field space (Figure 3.6a).

(a) **(b)**

Figure 3.6: (a) Pile of adobe bricks produced by manufacturer GeA. (b) Stereomicroscope image of adobe brick belonging to production batch GeA.

The upper exposed surface of the adobes provided by producer Ge was also rough, while their height sometimes exceeded 50 mm. The other surfaces of the samples were quite smooth and their edges were relatively parallel. The material appeared to be homogeneous and did not incorporate shrinkage cracks. It contained a high percentage of fibers and considerable amount of fine gravel (diameter < 5 mm) (Figure 3.6b). In some samples, small fragments of wood were also observed.

3.4 Compressive strength testing of adobe bricks

3.4.1 Specimen preparation

It was decided to test specimens in the direction in which the brick they originated from would have been laid for construction purposes. This implied that the maximum allowable specimen height would be 50 mm. To evaluate the effects that the specimens' shape and form pose on the results, three types of test units were examined: (a) cylinders with height = diameter = 50 mm, (b) prisms with dimensions height x width x length = 50 x 100 x 100 mm^3 and (c) cubes with 50 mm edges.

Cylindrical specimens were extracted from adobe bricks using a fixed-base rotary core drilling system. Prismatic and cubic test units were obtained by dry cutting the sample bricks with a masonry saw. To accommodate for surface unevenness and to allow a uniform distribution of the load during the tests, the upper and lower faces of all specimens were smoothened by abrasion. For this purpose an electric sander was used. Prior to testing, specimens were oven dried at 70 ^{o}C to constant mass, so as to preclude the possible effects of moisture on the material's mechanical properties.

3.4.2 Testing methodology

The experimental procedure adopted was decided after thorough literature review. Both load- and displacement-controlled uniaxial compression tests were performed. The aim of the latter was to provide information regarding the post-yield behaviour of the material.

Displacement-controlled tests were conducted on a Lloyd LR300K mechanical press with two parallel steel loading plates (Figure 3.7). Specimens with aspect ratios of 1 (cylinders and cubes) and 0.5 (prisms) were tested using 10 and 300 kN load-cells, respectively. Loading was applied without shock and increased continuously until the deformation of each specimen exceeded 30% of its original height. The speed of the machine's travelling head was set at 4.5 mm/min, based on the recommendations of the Australian earth building handbook (Walker, 2002) that prescribes rates 1-5 mm/min.

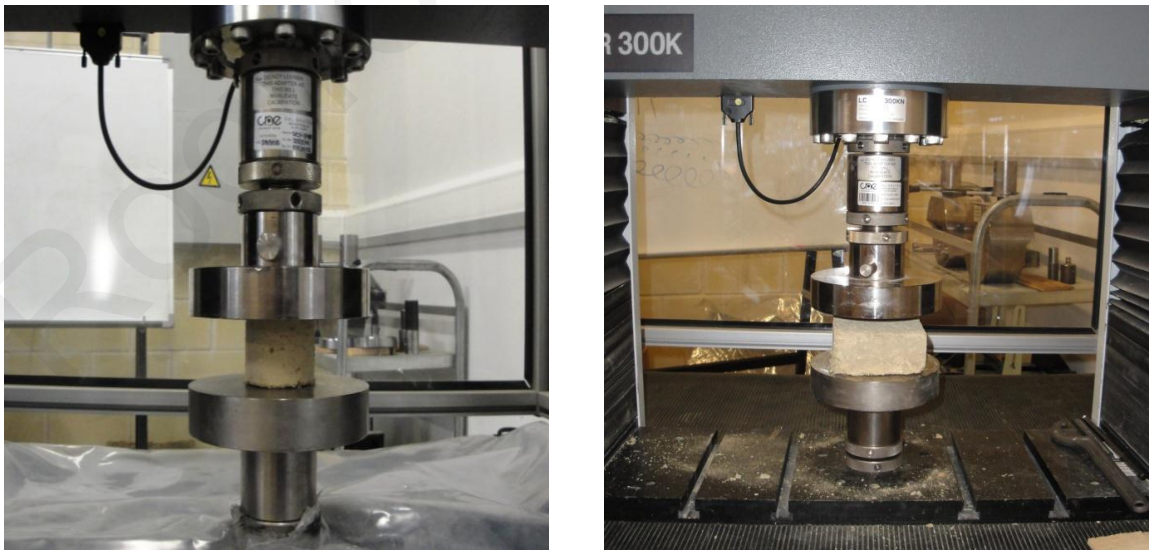

(a) **(b)**

Figure 3.7: Set-ups used for the implementation of uniaxial compressive strength tests on (a) cylindrical and (b) prismatic adobe specimens.

A Control's Advantest 9 hydraulic machine with two loading frames and swivel head platens was used for the implementation of load-controlled tests. Cylindrical specimens were tested using a 30 kN cell, whereas prisms were loaded with a 250 kN cell. Compressive stresses were exerted at a rate of 0.1 MPa/s (EN 772-1) until a 10% load-drop occurred.

During all tests, deformations were measured from the relative displacement of the machines' platens. This tends to overestimate true strains; however, the texture and size of the specimens did not allow the application of strain gauges or other strain measuring devices. Experiments were conducted at ambient conditions (22 °C and 55% RH). A total of 338 specimens cut from 52 brick samples were examined. In particular, 86 cylindrical, 196 prismatic and 56 cubic specimens were subjected to uniaxial compressive strength tests.

3.4.3 Results and discussion

3.4.3.1 Modes of failure in compression

The failure mechanism of specimens with aspect ratios equal to 1 (cylinders, cubes) was characterized by bulging and the formation of several near-vertical cracks on their surfaces (Figure 3.8a, b). At maximum compressive stress, the specimen did not instantly fail, but was subjected to significant deformation before its structure finally collapsed. Such a response to compressive loading has also been observed by other researchers while testing fiber-reinforced soils (e.g. Lenci et al., 2011; Ghavami et al., 1999). Certain scientists have related this behaviour to a redistribution of the internal forces within the soil matrix through the straw fibers (Lenci et al., 2011; Galán-Marín et al., 2010; Ghavami et al., 1999). This can be justified, to some extent, by the fact that, following the completion of the compression tests, the material had not fully disintegrated. Instead, the natural fibers held together significant parts of the soil matrix, thus delaying failure. In addition, no rupture of the straw fibers occurred, although a loss of bond between the fibers and the soil matrix was recorded at the vicinity of the cracks.

(a)

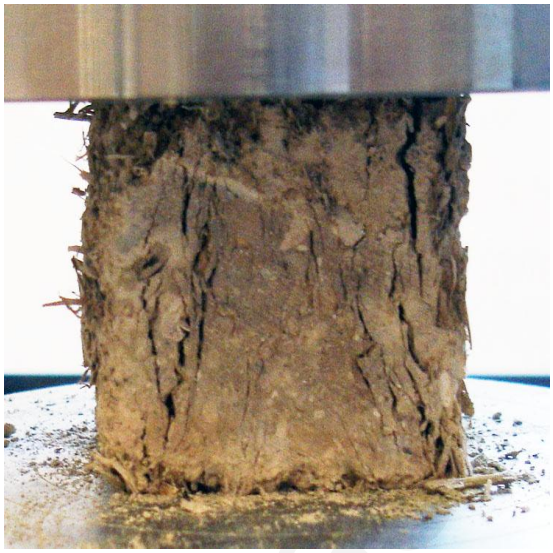

(b)

(c)

Figure 3.8: Typical modes of failure in uniaxial compression recorded for (a) cylindrical, (b) cubic and (c) prismatic adobe specimens.

The mode of failure experienced by prismatic specimens was characterized by compressive crushing and "exfoliation" of the lateral sides (Figure 3.8c). The gradual application of the load induced large inelastic longitudinal and transversal deformations to the specimens and caused their lateral sides to crack and fall off. Immediate failure after a critical load was not recorded. All specimens undertook considerable cracking and deformation, but sustained their ability to withstand compressive loading. Despite the fact that the lateral sides of the bricks suffered significant damage, their central core remained sufficiently integer and did not lose coherence. Similar behaviour for adobes under compression has

been reported by Quagliarini and Lenci (2010) and by Piattoni et al. (2011) who examined full scale bricks and prismatic specimens with height-to-width ratios < 1.

The observed failure patterns indicate that the specimens' response to uniaxial compression is largely dependent upon their size and form, while the results of tests can be significantly affected by platen restrain effects. These are generated by the differential tendencies of lateral expansion between the testing machine's steel platens and the less stiff adobe specimens. Platen restrain effects introduce friction at the interface between the test unit and the loading plate and lead to the generation of tangential forces at either end of the specimen. The magnitude of restraining forces decreases with distance from the platen, i.e. towards the center of the specimen. As the height-to-width ratio of the specimen reduces, the forces opposing lateral expansion increase (Azeredo et al., 2007). Specimens with considerably low height-to-width ratio, as in the case of the prisms hereby examined (height-to-width ratio = 0.5), have most of their volume experiencing high restrain. Hence, only the outer layers of their lateral sides are subjected to potential cracking and failure, whereas their central cores remain relatively undamaged. Continued loading to higher stresses simply causes such specimens to further deform into a flatter disc. Consequently, greater plastic deformations are induced but no structure breakdown and subsequent loss of bearing capacity occur. Ultimate failure takes place only after complete crushing.

On the other hand, specimens with width or diameter approximately equal to their height are not subjected to such severe platen restrain effects. Cylindrical and cubic test units tend to plastically deform into a barrel-like shape. As the specimens become shorter and wider, lateral strains are induced on their circumference, and this in turn generates the development of tensile stresses. Cracking develops perpendicular to these strains, i.e. parallel to the load direction. A network of cracks that gradually grow and intersect is formed, and eventually the material's matrix disintegrates. As opposed to cylindrical units, the concentration of stresses at the edges of cubes leads to fragmentation and section detachment in the final stages of loading.

3.4.3.2 Stress-strain behaviour and ultimate compressive strength

Stress-strain diagrams derived from the implementation of unconfined compression tests are given in Figure 3.9. As shown in Figure 3.10, the recorded behaviour can generally be divided into three phases. Initially, a contact adjustment phase occurs, during which the rigid loading plates crush any pre-existing asperities on the specimens' surface (Kouakou

and Morel, 2009). During the early stages of loading, the material also undergoes consolidation: the soil grains are redistributed, gradually filling the voids that exist in the material's structure, until a "steady" state is reached. It was noted that, in prismatic specimens consolidation took place at a larger strain range. In the second phase, compressive hardening occurs until the maximum stress is reached. From this point onwards, the material is subjected to compression softening up to the ultimate strain sustained (Lenci et al., 2009). It should be stressed out that softening behaviour was observed only in the case of cylindrical and cubic test units. At the levels of deformation examined, prisms were capable of deforming while undertaking greater loads. Similar continuous compressive hardening of adobe specimens has been reported by Piattoni et al. (2011) who tested full-scale bricks with dimensions (height x width x length) 130 x 310 x 460 mm^3. It is pointed out that the behaviour hereby described is based on average engineering strain recordings that correspond to relative displacement of the testing machines' platens. A more detailed examination of the material's deformation characteristics requires further experimental investigation involving close monitoring of displacements with appropriate laboratory equipment.

(a)

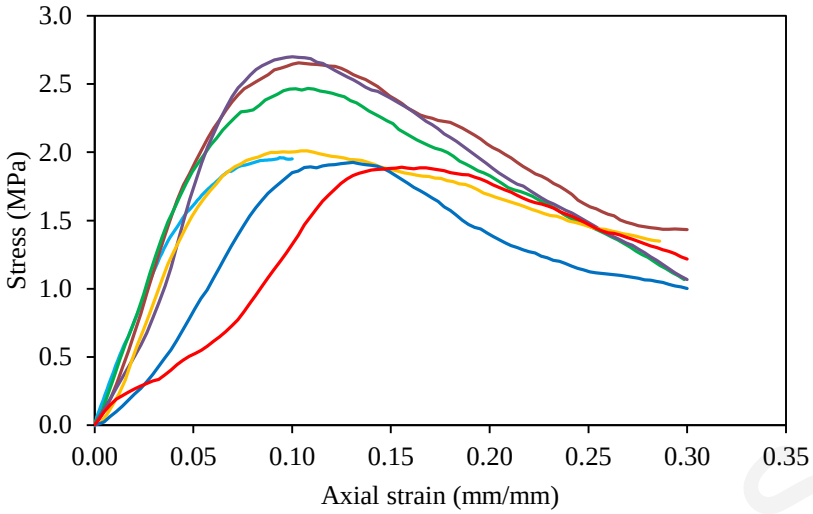

(b)

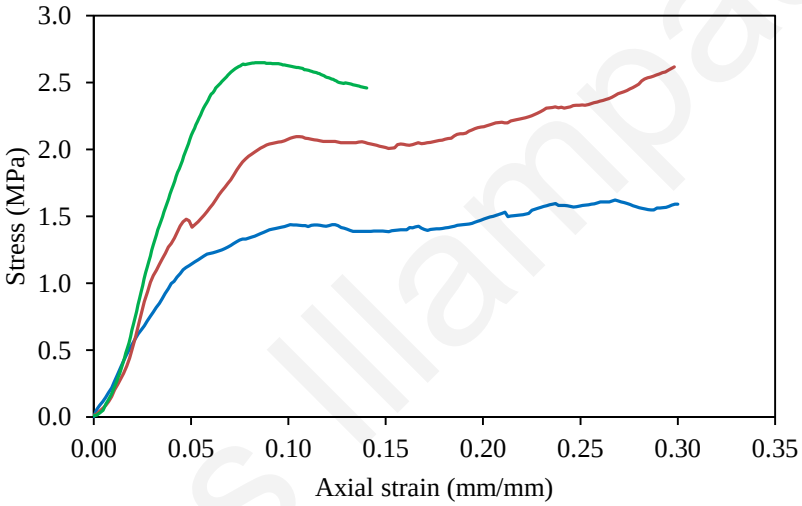

(c)

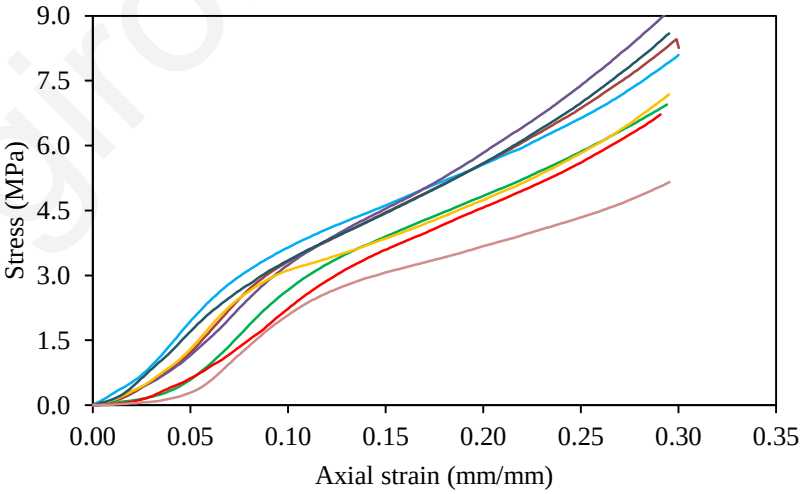

Figure 3.9: Stress-strain diagrams obtained from the implementation of displacement-controlled unconfined compression tests on (a) cylindrical specimens (height = diameter= 50 mm) cored from sample brick LyC7, (b) cubic specimens (height = width = 50 mm) cut from sample brick LyB1 and (c) prismatic specimens (height x width x length = 50 x 100 x 100 mm^3) cut from sample brick LyB1.

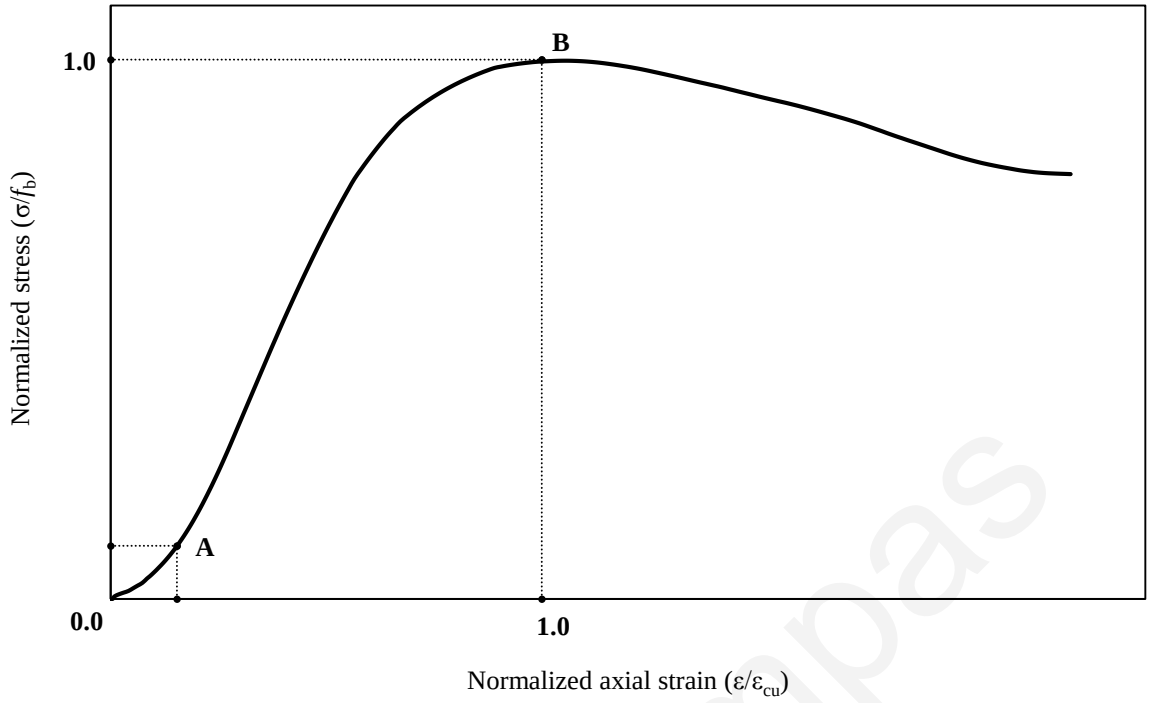

Figure 3.10: Normalized stress-strain diagram showing the response of adobe bricks to compression. Normalization has been conducted by dividing compressive stresses (σ) with the peak stress (f_b) and axial strains (ε) with the strain at the peak stress (ε_{cu}). Initially, a contact adjustment phase occurs during which the material undergoes consolidation (0-A). Up to the maximum allowable stress, compressive hardening takes place (A-B). This is followed by a softening regime.

The outcomes of all compressive strength tests are given in Annex 1. Comparable results regarding the ultimate bearing capacity of cylindrical, prismatic and cubic specimens are summarized in Table 3.2. The table reports size-independent mean compressive strength values and coefficients of variation (= standard deviation/mean value). Compressive strength was estimated by dividing the maximum recorded load with the loaded area as per equation 3.1. For prisms and cubes, the loaded area was assumed to be equal to the original cross-sectional area.

Table 3.2: Size-independent mean compressive strength values and corresponding coefficients of variation for cylindrical, prismatic and cubic adobe specimens. Samples are referenced as "X a b", where "X" refers to the manufacturer (Ly, Ath or Ge), "a" denotes the production batch and "b" indicates the sample (adobe brick) number.

Sample brick (cylinders + prisms + cubes)	Size-independent mean compressive strength [MPa] (coefficient of variation)		
	Cylinders	Prisms	Cubes
Ly A 1 (0 + 5 + 5)	- -	2.27 (21.2%)	2.26 (11.8%)
Ly A 2 (0 + 6 + 5)	- -	2.02 (27.4%)	2.05 (11.6%)
Ly B 1 (0 + 8 + 3)	- -	5.66 (17.4%)	1.90 (22.1%)
Ly B 2 (0 + 8 + 4)	- -	5.23 (12.5%)	1.80 (11.3%)
Ly C 7 (7 + 2 + 0)	1.80 (24.3%)	5.12 (17.2%)	- -
Ly C 8 (8 + 2 + 0)	1.97 (27.5%)	5.99 (21.3%)	- -
Ly C 9 (7 + 1 + 0)	1.65 (19.7%)	6.85 (-)	- -
Ly C 10 (8 + 3 + 0)	2.06 (20.9%)	2.68 (42.5%)	- -
Ath A 1 (0 + 5 + 4)	- -	1.24 (4.3%)	0.87 (31.6%)
Ath A 2 (0 + 6 + 6)	- -	2.69 (15.3%)	1.16 (15.7%)
Ath B 3 (0 + 8 + 4)	- -	5.67 (17.4%)	1.90 (22.1%)
Ath B 4 (0 + 8 + 4)	- -	5.12 (11.4%)	1.80 (11.3%)
Ath C 1 (0 + 5 + 3)	- -	2.02 (18.5%)	1.00 (24.9%)
Ath C 2 (0 + 7 + 3)	- -	2.13 (15.9%)	0.82 (27.3%)
Ath C 3 (0 + 8 + 4)	- -	1.44 (23.7%)	0.78 (76.8%)
Ath E 1 (4 + 1 + 0)	1.11 (17.7%)	1.85 (-)	- -
Ath E 2 (6 + 1 + 0)	1.24 (2.6%)	2.79 (-)	- -
Ath E 3 (6 + 1 + 0)	1.20 (15.4%)	4.96 (-)	- -
Ath E 4 (6 + 1 + 0)	1.24 (10.3%)	4.28 (-)	- -
Ath E 5 (6 + 1 + 0)	1.13 (10.8%)	3.38 (-)	- -
Ath F 1 (6 + 1 + 0)	1.56 (11.9%)	9.19 (-)	- -
Ath F 2 (6 + 1 + 0)	1.20 (11.4%)	6.65 (-)	- -
Ath F 3 (6 + 1 + 0)	1.37 (12.7%)	4.76 (-)	- -
Ath F 4 (5 + 1 + 0)	1.33 (14.1%)	6.38 (-)	- -
Ath F 5 (5 + 1 + 0)	1.50 (16.0%)	6.31 (-)	- -
Ge A 1 (0 + 8 + 3)	- -	2.12 (14.7%)	0.94 (32.9%)

Data obtained from tests on cylinders were processed in accordance with ASTM D2166 - 06, which indicates that the cross-sectional area (A_c) used for estimating the compressive stress induced at a deformation step should be corrected as:

$$A_c = \frac{A_o}{(1-\varepsilon_c)} \tag{3.4}$$

where A_o is the original cross-sectional area of the specimen and ε_c is the axial strain at the deformation step. The correction applied accounts for the significant lateral deformations that are generated at high levels of loading.

In order to calculate size-independent mean compressive strength values for the different types of units tested, the shape factors δ suggested in EN 772-1 were adopted. For specimens with width or diameter = height = 50 mm, the EN 772-1 specifies a correction factor of 0.85. The prescribed value of δ for specimens with 50 mm height and 100 mm width is 0.75.

The size-independent mean compressive strength values yielded by cylinders range from 1.1 MPa (AthE1) to 2.1 MPa (LyC10). Results obtained from cubes lie between 0.8 (AthC3) and 2.3 MPa (LyA1). These outcomes are similar with the data reported by Silveira et al. (2012, 2013), Wu et al. (2012), Fratini et al. (2011), Yetgin e al. (2008) and by Demetriou et al. (2006). The results of most individual tests exceed the 1.3 MPa boundary value set by NZ4298. However, the vast majority of mean values does not conform to the 2.1 MPa strength requirement prescribed in 14.7.4NMAC.

Prisms produced compressive strength values that are systematically higher than those of specimens with an aspect ratio of 1 (i.e. 1.2 MPa (AthA1) to 9.2 MPa (AthF1)). Such values correspond to the compressive strength of the adobe bricks tested by Piattoni et al. (2011). Despite the application of shape factors, a correlation among the outcomes obtained by specimens with different aspect ratios could not be achieved. It is anticipated that, in future tests, reducing friction at the specimen-platen interfaces through the application of lubricants or the introduction of friction-reducing pads (e.g. Teflon) will cater for the inconsistencies recorded when examining prisms (Azeredo et al., 2007; Van Mier, 2012).

Regardless of the type of specimen examined, it was noted that considerable deviations occur in the evaluated compressive strength. Variations occur in the properties of: (a) adobes produced by different manufacturers (e.g. see results for samples AthE1 and LyC10); (b) adobes made by the same manufacturer, but originating from different

production batches (e.g. see results for samples AthE1 and AthF1) and (c) specimens originating from the same adobe brick (e.g. see coefficients of variation for samples LyC7, AthA1, GeA1). Many researchers (Silveira et al., 2013; Varum et al., 2008, Velosa et al., 2010; González, 1999) agree that such discrepancies are common. They are primarily attributed to the inherent inhomogeneity and randomness of adobes arising from the adoption of non-industrialized production methods, the modification of the mix design and the lack of standard criteria for the selection of raw materials.

Examining the experimental outcomes within the context of engineering design, it may be argued that, not only the assessment of ultimate bearing capacity is important, but also the derivation of the material's deformation capacity is substantial. For the adobes tested it was noted that maximum compressive stress was generated after a specimen had suffered at least 10% reduction in its height. Strains at peak stress are considerably higher than most corresponding values quoted in the literature. The latter generally range from 0.5% to 4% (Islam and Iwashita, 2010; Fratini et al., 2011; Silveira et al., 2013). The intense deformability of local adobes is related to the production procedure followed in Cyprus. In particular, due to the fact that the mixture is poorly compacted during casting, a significant volume of voids is formed within the material's matrix. When pressure is exerted, soil grains slide and shift, thus occupying available void space. As loading increases progressively, the soil grains are compacted and the material's density increases. Consequently, it gradually becomes stiffer, retaining its ability to resist loading, and ultimate failure is shifted towards higher levels of deformation.

A deformation capacity exceeding 10% is excessive for most common structural applications. In practice this will probably result in the failure of an adobe load-bearing member and/or the detachment of adjacent elements (e.g. roof beams). Therefore, the assessment methodologies recommended by most testing standards, which associate compressive strength with the maximum stress recorded, cannot be injudiciously adopted in the case of local adobes. Since the material is susceptible to compaction upon loading, applying a combination of load- and displacement-based failure criteria appears to be more appropriate. According to this approach, compressive strength can be assumed to be equal, either to the peak stress induced, or the stress generated at a certain strain value, whichever occurs first (Islam and Iwashita, 2010). The permissible strain limit can be selected based on the intended use of the material and the expected magnitude of loading. Hence, different boundary values of axial strain can be set, depending on whether the material will be

incorporated in load-bearing walls, infill or partition walls, elements requiring specific ductility, etc.

3.4.4 Determination of stress-strain relation for adobe under compression

Using stress-strain curves derived from uniaxial compression tests on cylindrical adobe specimens, analytical relations describing the material's response to compressive loading were developed. The experimental data used correspond to 30 specimens originating from 4 different adobe bricks (LyC7-10). In order to propose equations applicable to adobes with varying load-bearing and deformation capacities, stress and strain values were normalized. Hence, for each specimen considered, normal stresses (σ_c) were divided by the peak stress (f_b) and axial strains (ε_c) were divided by the strain at the peak stress (ε_{f_b}) as follows:

$$\bar{\sigma}_c = \frac{\sigma_c}{f_b}$$
$$\bar{\varepsilon}_c = \frac{\varepsilon_c}{\varepsilon_{f_b}} \quad (3.5)$$

The normalized stress-strain data used are shown in Figure 3.11.

Third order polynomial equations of the following form were adopted for capturing adobe's non-linear compressive behaviour:

$$\bar{\sigma}_c = \alpha_0 + \alpha_1 \bar{\varepsilon}_c + \alpha_2 \bar{\varepsilon}_c^{\,2} + \alpha_3 \bar{\varepsilon}_c^{\,3} \quad (3.6)$$

The fitting of such curves (equation 3.6) to the stress-strain experimental data was treated as a constraint optimization problem. The objective of the optimization process was to maximize the coefficient of determination R^2 or, equivalently, to minimize $-R^2$ (typically, optimization problems are formulated and handled as minimization problems). Thus, the optimum fit which represents the variability of the data the best way possible was sought.

To ensure that valid normalized stress-strain equations were identified, the following constraints were incorporated in the formulation of the optimization problem: (a) the fit passes through the origin ($\bar{\sigma}_c = \bar{\varepsilon}_c = 0$), (b) the fit passes through the point with $\sigma_c = f_b$ and $\varepsilon_c = \varepsilon_{f_b}$ ($\bar{\sigma}_c = \bar{\varepsilon}_c = 1$), which is in fact the point of maximum stress, and (c) as we consider two separate strain intervals with a different polynomial fitted at each interval, we enforce continuity of the polynomials and of their first derivatives at their common point.

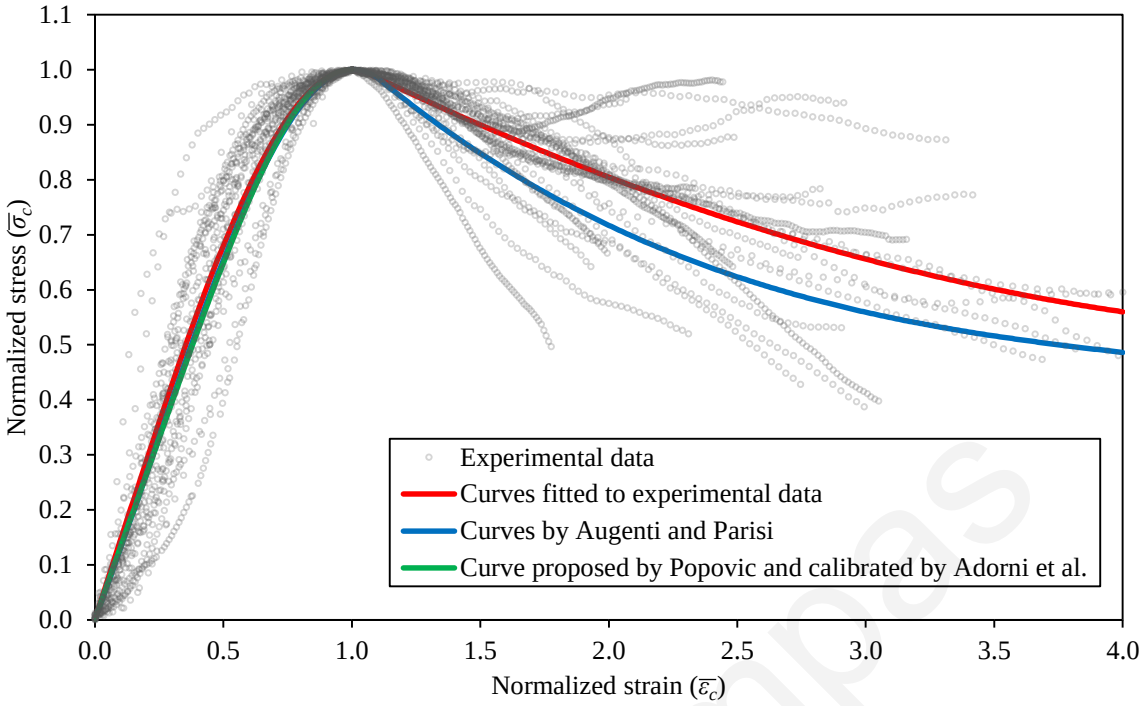

Figure 3.11: Graphical illustration of normalized stress-strain experimental data obtained from compression tests on 30 cylindrical adobe specimens. The red line depicts the curves fitted to these data. The blue line shows the curves fitted by Augenti and Parisi (2010) to corresponding tuff masonry data. The green line depicts the curve proposed by Popovic (1973) for concrete and calibrated by Adorni et al. (2013) based on adobe compression test data. Note the agreement of all three models in the ascending hardening branch.

The optimization problem described above was efficiently solved using standard MATLAB minimization routines, which yielded the following fitted curves:

$$\bar{\sigma}_c = \begin{cases} 1.44065\bar{\varepsilon}_c + 0.11869\bar{\varepsilon}_c^{\,2} - 0.55935\bar{\varepsilon}_c^{\,3} & \text{for } 0 \le \bar{\varepsilon}_c \le 1.07 \\ 1.26585 - 0.28512\bar{\varepsilon}_c + 0.02752\bar{\varepsilon}_c^{\,2} - 0.00009\bar{\varepsilon}_c^{\,3} & \text{for } 1.07 \le \bar{\varepsilon}_c \le 4 \end{cases} \tag{3.7}$$

The positioning of the common point of the two curves at $\bar{\varepsilon}_c = 1.07$ was automatically attained by the optimizer (a corresponding decision parameter was defined in the implemented optimization procedure). A rather satisfactory overall R^2 = 0.89 was achieved, which indicates that stresses are well predicted by the polynomials of equation 3.7. Adequate correspondence between analytical and experimental data is graphically verified in Figure 3.11.

Stress-strain relations for adobe materials subjected to compressive loading have also been proposed by Silveira et al. (2013):

$$\sigma_c = \begin{cases} -0.744 f_b (5.99 * 10^{-11})^{\frac{\varepsilon_c}{f_b}} + 0.744 f_b & \text{for } \varepsilon_c \le 0.096 f_b \text{ ‰} \\ -0.576 f_b (5.17 * 10^{-3})^{\frac{\varepsilon_c}{f_b}} + 1.01 f_b & \text{for } \varepsilon_c > 0.096 f_b \text{ ‰} \end{cases} \quad (3.8)$$

The above relations, however, do not follow a dimensionless format and depend on the specific experimental peak stress magnitudes and strains at peak stress measured by the authors themselves. Consequently, a direct comparison between equation 3.8 and the equation proposed in this thesis cannot be made.

Using experimental data from compression tests on adobe specimens with height-to-width ratios >1, Adorni et al. (2013) implemented a non-linear least squares method with an optimization algorithm to calibrate the stress-strain equation proposed by Popovic (1973) for concrete:

$$\bar{\sigma}_c = \frac{4.11\bar{\varepsilon}_c}{4.11 - 1 + (\bar{\varepsilon}_c)^{4.11}} \qquad \text{for } 0 \le \bar{\varepsilon}_c \le 1 \quad (3.9)$$

Comparing equation 3.9 with the proposed model (equation 3.7) over the ascending hardening branch ($0 \le \bar{\varepsilon}_c \le 1$) where the former is applicable, an excellent correspondence is observed (Figure 3.11).

A very similar approach to the one described in this thesis has been adopted by Augenti and Parisi (2010) who examined the compressive behaviour of masonry prisms made of tuff stones (consisting of consolidated volcanic ash) and sand-based mortar. These researchers used third order polynomials and considered two separate strain intervals in the framework of an iterative procedure to fit the following curves to stress-strain laboratory test measurements:

$$\bar{\sigma}_c = \begin{cases} 1.2595\bar{\varepsilon}_c + 0.4549\bar{\varepsilon}_c^{\,2} - 0.7144\bar{\varepsilon}_c^{\,3} & \text{for } 0 \le \bar{\varepsilon}_c \le 1.12 \\ 1.545 - 0.6487\bar{\varepsilon}_c + 0.1388\bar{\varepsilon}_c^{\,2} - 0.0107\bar{\varepsilon}_c^{\,3} & \text{for } 1.12 \le \bar{\varepsilon}_c \le 5 \end{cases} \quad (3.10)$$

Despite the obvious physical differences between tuff masonry prisms and adobe brick specimens, the curves of equation 3.10 seem to describe relatively well the experimental data hereby quoted (Figure 3.11). This is particularly true for the pre-peak compressive hardening regime.

Another interesting observation is the very large variability of material behaviour for $\bar{\varepsilon}_c$>1 (i.e. after the point of maximum stress). Thus, the fitting achieved in equation 3.7 for $\bar{\varepsilon}_c$<1

(where the experimental measurements for the 30 adobe specimens are less variable) is certainly of better quality than for $\bar{\varepsilon}_c$>1. Most probably, the large variability that arises when $\bar{\varepsilon}_c$>1 is the main reason explaining the difference observed between the curves of equation 3.7 and those of Augenti and Parisi (2010). However, additional investigation is required in the post-peak softening range ($\bar{\varepsilon}_c$>1), in order to identify the sources of high uncertainty in material behaviour and more reliably estimate the stress-strain relation.

3.5 Flexural strength testing of adobe bricks

3.5.1 Specimen preparation

The specimens subjected to three-point bending tests were half bricks (dimensions: height x width x length = 50 x 150 x 450 mm^3) cut from full-size adobes in dry conditions using a masonry saw (Figure 3.12a). Their surfaces were smoothened by abrasion using an electrical sander. Prior to testing, the specimens were oven dried to constant weight at 70 ^{o}C.

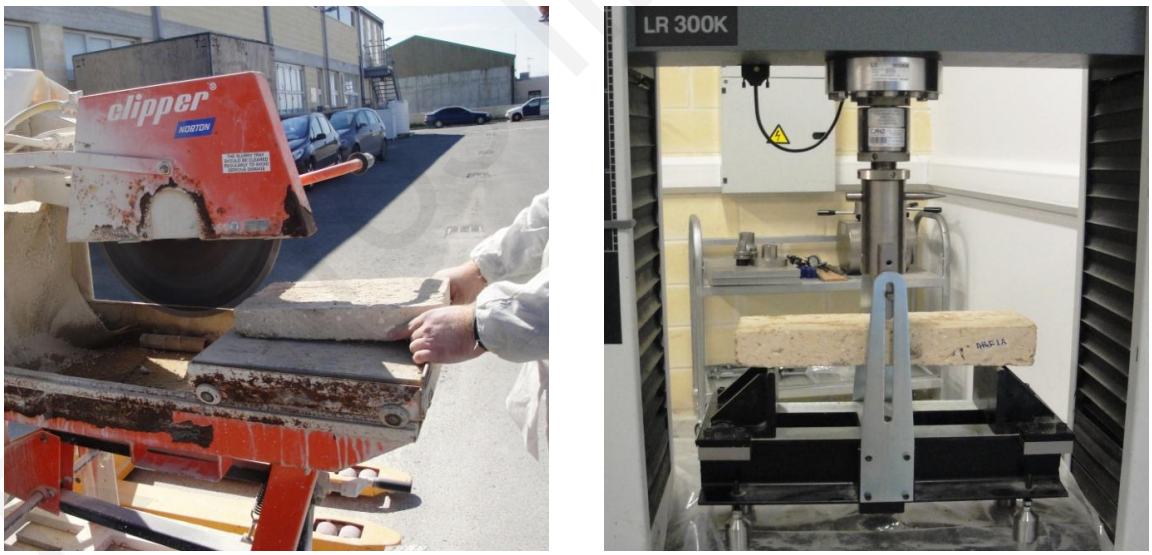

(a) **(b)**

Figure 3.12: (a) Half-brick specimen cut from an adobe brick using a masonry saw. (b) Experimental setup used for the implementation of three-point bending tests on half-brick adobe specimens.

3.5.2 Testing methodology

The experimental methodology adopted was mainly based on the one described in the New Mexico Building Code (14.7.4NMAC). The test units were placed on two parallel

cylindrical supports spaced 350 mm apart. A concentrated force was applied by imposing displacement at a constant rate of 0.9 mm/min on a horizontal tube positioned at the middle of the specimen. Loading was exerted until specimen failure. The tests were conducted at ambient conditions (22 °C and 55% RH) using a Lloyd LR300K universal testing machine. The setup used is shown in Figure 3.12b.

During the tests, displacements were monitored based on the relative movement of the machine's load-head. The maximum bending strain (ε_f) at each step was computed as:

$$\varepsilon_f = 6dt/l^2 \quad (3.11)$$

where d is the load-head displacement, t the sample height and l the span between supports. Bending stresses were evaluated according to equation 3.2.

Tests were performed on a total of 55 specimens originating from 29 different adobe bricks. After the implementation of the bending tests, the parts of the sample that had remained intact from flexural failure were cut into at least four prismatic (height x width x length = 50 x 100 x 100 mm^3) or cylindrical (diameter = height = 50 mm) specimens. These were subjected to further compressive strength tests in order to investigate possible correlations between the mechanical properties of local adobes.

3.5.3 Results and discussion

The mode of failure under flexure was greatly influenced by the presence of discontinuities within the mass of the material (Figure 3.13). As noted in section 3.2, the bricks' homogeneity was often disrupted by shrinkage cracks and/or the presence of large-sized particles (stones, gravel, fragments of wood, etc.). When loading was applied, these discontinuities formed local planes of weakness, decreasing the bearing capacity of the specimens and forcing failure to develop at their vicinity. Failure at the central axis, where loading was exerted, occurred only in homogenous specimens. The effect of pre-existing discontinuities on the flexural strength of materials composed of unfired clay has been verified by Clementi et al. (2008), Lenci et al. (2009, 2012) and Aymerich et al. (2012).

Figure 3.13: Flexural failure of half brick adobe specimens. Note that in certain cases failure did not occur in the middle of the sample, as expected; instead it propagated through pre-existing planes of weakness, such as shrinkage cracks and areas where stones or gravel disrupted the homogeneity of the soil matrix.

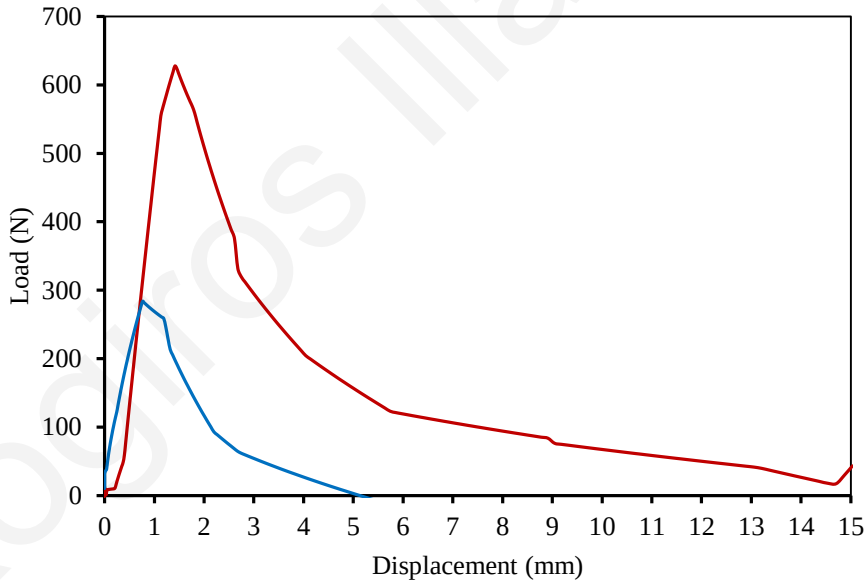

Figure 3.14: Load-deflection diagrams obtained from the implementation of three-point bending tests on half-brick specimens cut from the same adobe sample (AthF5).

Characteristic load-deflection diagrams showing the flexural behaviour of the material are given in Figure 3.14. These indicate that, when bending loads are imposed on adobes, the material responds almost linearly until cracking is generated. After the initiation of cracking, an abrupt load drop with a drastic loss of residual strength occurs. As the crack

opening progressively increases, the flexural strength of the specimen reduces in an exponential mode. At the final stages of loading the specimen tends to separate into two pieces. Subsequently, its load carrying capability is practically lost.

In all specimens examined the linearly ascending loading branch was limited to deflection levels not exceeding 3 mm. The corresponding strain range over which flexural yielding occurred was 0.45%-1.85%. Ultimate failure was recorded at deflections between 5 mm and 18 mm. This accounts for maximum bending strains approximately 7 times greater than the initial yielding strain. The response hereby described is in agreement with the observations made by other researchers as well (Clementi et al., 2008; Lenci et al., 2009, 2012).

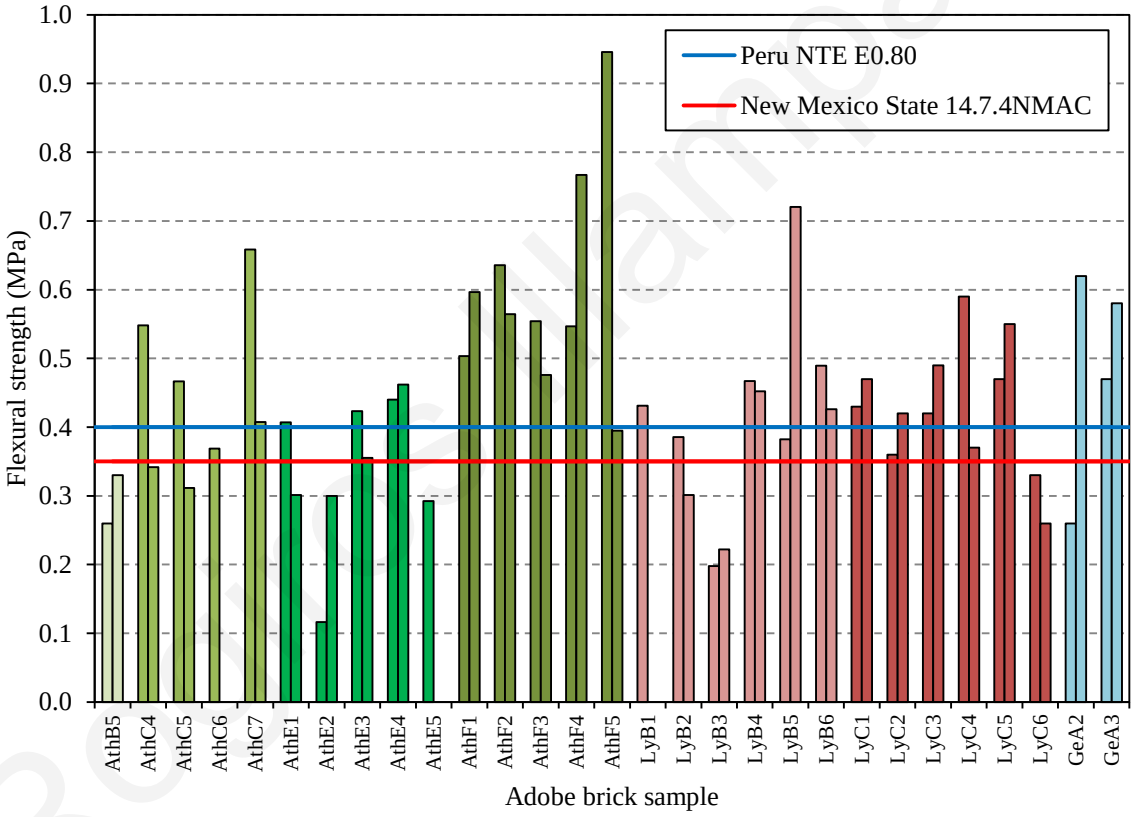

Figure 3.15: Results of three point bending tests on half-brick adobe specimens. The minimum acceptable flexural strength values prescribed in the Peruvian standard and the New Mexico State code are also shown on the diagram.

The results of all bending tests carried out in the framework of this research are presented in Figure 3.15. Flexural strength values derived vary from 0.1 MPa to 0.95 MPa (mean flexural strength = 0.4 MPa, coefficient of variation = 30%). Similar experimental results have been reported by Silveira et al. (2013), Adorni et al. (2013), Vega et al. (2011),

Liberatore et al. (2006) and Norton (1997). The data obtained indicate that the flexural strength of adobe bricks is quite random, as it relies greatly on the homogeneity of the specimen examined. Considering that strength variability was also evident in the results of compression tests (see section 3.4.3.2), it may be argued that uncertain mechanical behaviour can be typically expected from non-industrialized earthen materials of random composition. Due to the inherent inhomogeneity and randomness of the material, several of the specimens examined do not fulfill the requirements of the Peruvian standard (NTE E0.80) and the New Mexico State code (14.7.4NMAC). The lower flexural strength limits prescribed in these documents are 0.40 and 0.35 MPa, respectively.

Comparisons among the mean flexural strength of half-brick specimens and the corresponding size-independent mean compressive strength values derived from testing prismatic and cylindrical units originating from the same adobe are shown in Figure 3.16. For each sample brick, the mean flexural strength was calculated from the results of the two half-brick specimens examined. The corresponding size-independent mean compressive strength was computed by applying the EN 772-1 shape factors on the results yielded by the specimens cut from those sections of the same brick that had remained intact after flexural failure.

Regarding the correlation between adobe's mechanical properties, this appears to be very low and the values of flexural strength are not necessarily between 10%-20% of the compressive strength as noted in the international literature (Norton, 1997; NZ4298). Although the correlation between the flexural and the compressive strength of prismatic specimens appears to be more consistent, this is rather misleading since the results obtained from the compression tests of the latter are significantly affected by platen constrain effects. The considerable discrepancy in the outcomes of three-point bending tests is also confirmed by Silveira et al. (2013) who examined traditional adobe bricks sampled from existing earthen buildings. It is worth noting that recent experimental studies (Eftychiou, 2013) on laboratory produced adobes report less variable strength data and a better correlation between mechanical properties ($f_{t,flex} = 0.6 f_b$; $R^2 = 0.7$). This indicates that the application of carefully controlled production processes and mix designs can detrimentally affect the behaviour of the material.

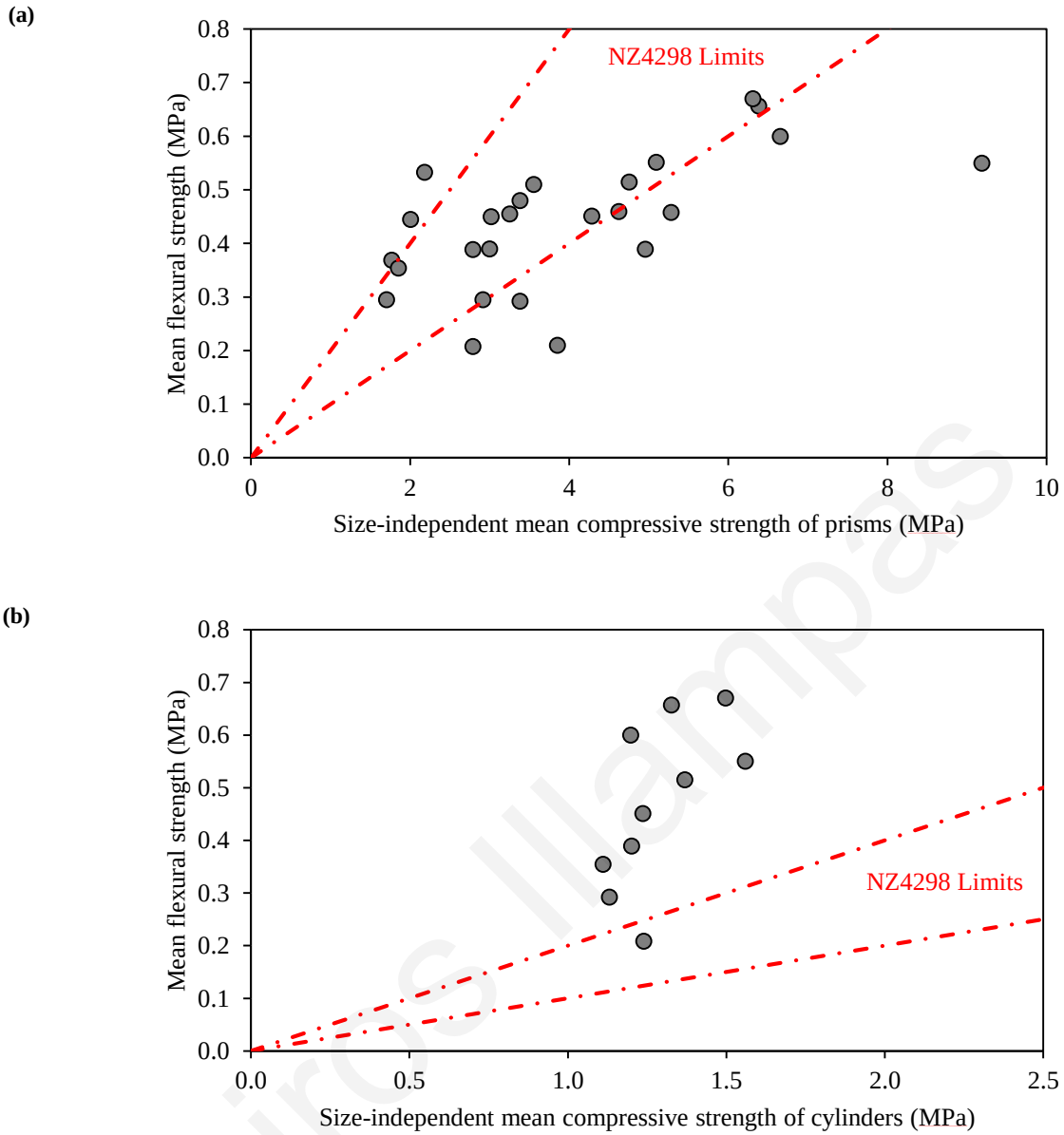

Figure 3.16: Comparison between the mean flexural strength and the size-independent mean compressive strength derived from testing prismatic (a) and cylindrical (b) specimens originating from the same sample brick. The red lines denote the limits suggested by the New Zealand NZ4298 standard.

3.5.4 Determination of stress-strain relation for adobe under three-point bending

Following a similar curve fitting procedure as the one described in section 3.4.4, a model for predicting the response of adobe to three-point bending was developed. In this case, the experimental data used corresponded to all 23 half-brick specimens tested from producer Ly (LyB1-6, LyC1-6). Data normalization was applied by dividing stress (σ_t) and strain

(ε_t) values with the maximum bending stress sustained by each specimen ($f_{t,flex}$) and the bending strain at the peak stress ($\varepsilon_{f_{t,flex}}$) respectively:

$$\bar{\sigma}_t = \frac{\sigma_t}{f_{t,flex}}$$
$$\bar{\varepsilon}_t = \frac{\varepsilon_t}{\varepsilon_{f_{t,flex}}} \quad (3.12)$$

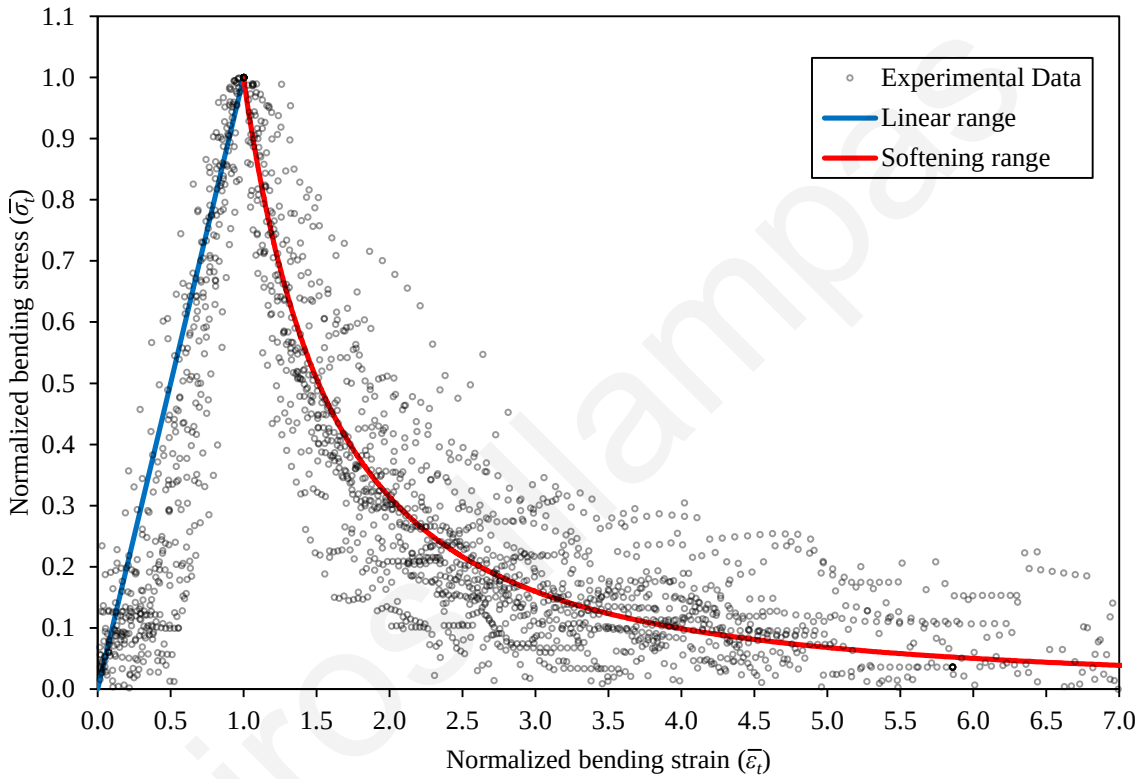

Figure 3.17: Graphical illustration of normalized stress-strain experimental data obtained from three-point bending tests on 23 half-brick adobe specimens. The blue line depicts the linear approximation assumed up to the maximum stress point, while the red line depicts the power reduction factor relation adopted over the softening range.

The full range of experimental data values is shown in Figure 3.17. Adobe's stress-strain flexural behaviour was idealized in two separate sections. Initially, the material was assumed to respond linearly to bending loads until the maximum allowable stress was attained, as suggested by Aymerich et al. (2012) and Clementi et al. (2008). This assumption defines a priori the relation among normalized stresses and strains, since the linear fit should: (a) pass through the origin ($\bar{\sigma}_t = \bar{\varepsilon}_t = 0$) and (b) pass through the peak-

stress point where $\sigma_t = f_{t,flex}$ and $\varepsilon_t = \varepsilon_{f_{t,flex}}$ ($\bar{\sigma}_t = \bar{\varepsilon}_t = 1$). For the post-peak softening regime, equations with power reduction factors of the following form were considered:

$$\bar{\sigma}_t = \bar{\varepsilon}_t^{\alpha},\ a < 0 \tag{3.13}$$

This equation format enforces the second brunch to pass though the maximum stress point ($\bar{\sigma}_t = \bar{\varepsilon}_t = 1$) ensuring continuity over the two strain intervals. The power reduction factor *a* was derived through an optimization process where the aim was to maximize the coefficient of determination R^2 for the $\bar{\varepsilon}_t > 1$ data range. Based on the above, the model formulated is as follows:

$$\bar{\sigma}_t = \begin{cases} \bar{\varepsilon}_t & \text{for } 0 \le \bar{\varepsilon}_t \le 1 \\ (\bar{\varepsilon}_t)^{-1.67} & \text{for } 1 \le \bar{\varepsilon}_t \le 7 \end{cases} \tag{3.14}$$

According to the results obtained, the power reduction relation is more adequately fitted to the experimental data than the initial linear relation. This is indicted by the $R^2 = 0.83$ obtained for the non-linear range, compared to the $R^2 = 0.74$ value computed for the elastic section. This can be attributed to the fact that experimental data in the first strain interval may have been influenced by pre-loading imposed by the machine at the beginning of the testing procedure. In addition, the presence of pre-existing discontinuities in certain specimens (i.e. shrinkage cracks) affected the distribution of stresses, practically precluding material linearity. Nevertheless, considering the inhomogeneous and random nature of local adobes, the overall fitting of equation 3.14 can be deemed as sufficient.

3.6 Summary

Extensive laboratory testing revealed that the response of adobes to compression depends on the form (cube, cylinder, prism) and size of the specimen examined. Compressive failure of cubes and cylinders with height-to-width ratios of 1 usually occurs in the form of cracking parallel to the direction of loading. Compressive strength values derived from these specimens range from 0.8 to 2.3 MPa. On the other hand, the behaviour of prisms with height-to-width ratios < 1 is greatly influenced by platen restrain effects. Prismatic specimens suffer axial shortening and circumferential spalling during compression tests. The maximum compressive stresses sustained by these specimens deviate considerably and lie between 1.2-9.2 MPa. Such values are extraordinarily high and indicate that the use of

specimens with significantly low aspect ratios can lead to overestimation of the material's actual bearing capacity.

In general, the compressive behaviour of traditional adobes is characterized by intense deformability due to compaction of the material's granular soil matrix. For the cubic and cylindrical specimens hereby examined, strains at peak stress were in the region of 10%, whereas for prismatic specimens corresponding values were often as high as 30%. This implies that existing compressive strength assessment criteria should be revised so that they do not solely rely on stress recordings, but account for the material's deformation capacity as well.

When subjected to three-point bending, the behaviour of adobes is affected by the presence of discontinuities within their mass. Hence, the maximum bearing capacity of the material can be rather variable. This is verified by the wide range of flexural strength values (0.1-0.95 MPa) derived and by the weak correlation observed among the flexural and compressive strengths.

The uncertain mechanical behaviour of adobes is attributed to the inherent inhomogeneity and natural randomness of earthen materials. Discrepancy is further affected by the adoption of empirical non-industrialized production methods. Moreover, inconsistencies arise by the lack of internationally accepted standardized testing procedures referring to unfired clay masonry materials.

The constitutive model developed for describing adobe's stress-strain behaviour under compression is well fitted to the experimental data obtained from cylindrical specimens. The proposed equation is based on third order polynomials and includes relations for the pre-peak hardening range and the post-failure softening range. The three-point bending model is also in good agreement with the outcomes of laboratory tests on half-brick specimens. The equation proposed in this case assumes a linear response up to the initiation of cracking and uses a power reduction factor to approximate strength degradation in the post-yield regime. All equations follow a dimensionless format, since for their formulation stresses and strains were normalized following division by peak strengths and peak-stress deformations, respectively. Therefore, their use can be potentially extended to other adobes with different strengths and deformation capacities.

4 EXPERIMENTAL INVESTIGATION OF THE MECHANICAL PROPERTIES OF ADOBE MASONRY

4.1 Introduction

In this section, a review of up-to-date experimental research on adobe masonry is presented. Particular references are made to compressive and shear strength testing. In addition, the response of adobe masonry assemblages tested in the laboratory in compression and diagonal tension (shear) is examined.

The investigation of the response of adobe masonry to compression includes monotonic and loading-unloading tests on stack-bonded prisms and running bond wallettes. The modes of failure induced are reported and the compressive strength values obtained are compared against corresponding data from the literature. Furthermore, the use of existing analytical equations for the prediction of compressive strength is considered.

The behaviour of adobe masonry under shear loading is studied through diagonal tension tests on a wall panel. The experimental data are used to deduce conclusions concerning damage initiation and propagation. Moreover, estimates of the masonry's diagonal tensile strength and shear modulus are derived.

4.2 Review of experimental research on adobe masonry

The laboratory and in situ testing of masonry components focuses on examining the combined response of masonry units and mortar joints to loading actions that are commonly encountered in practice. Emphasis is thus given on studying the behaviour of these assemblages under compression and shear loading. Mechanical properties are generally assessed through tests on full or reduced-scale wallettes, following the methodologies prescribed in globally accepted building codes and standards (e.g. EN 1052-1, EN 1052-3, ASTM C1314 - 12, ASTM E519 / E519M - 10). The experimental data obtained are used to verify compliance with a specified minimum strength value and/or to define the masonry's stress-strain behaviour. Unfortunately, the scopes of existing international norms refer to industrialized materials and conventional forms of masonry, practically excluding earthen construction.

Specific references to the laboratory testing of adobe masonry can be found in the Peruvian earth building standard (NTE E0.80). The technical guidance provided by this document includes recommendations for the implementation of uniaxial compression and diagonal tension tests. Permissible strength limits are also provided in the aforementioned standard.

4.2.1 Assessment of compressive strength

Since load-bearing walls are subjected to vertical loads, assessing the masonry's capacity to sustain compressive forces is considered critical. Response to compression is usually investigated through direct loading tests on assemblages. The load is normally applied uniformly to failure through two stiff and flat hardened steel platens. The compressive strength (f_w) is assumed to be equal to the maximum stress exerted on the specimen. Tests are either conducted in full agreement to the EN 1052-1 and ASTM C1314 – 12 standards or, more often, simply confront to certain clauses of formal technical documents.

For investigating the compressive strength of adobe masonry, two forms of specimens are mainly used: (a) stack-bonded prisms and (b) running bond wallettes. In stack-bonded prisms, masonry units are set directly above each other, whereas in running bond wallettes units are laid in consecutive courses offset by a half brick. The scale and size of the specimens tested by different researchers vary considerably. The materials used in the tests include adobe bricks manufactured in the laboratory (Gavrilovic et al., 1998) or extracted from existing buildings (Binda et al., 2008), jointed with earth- (Wu et al., 2012), gypsum- (Mahini et al., 2007) and lime-based (Varum et al., 2011) mortars. To assure the uniform distribution of stresses on the specimens, mortar capping is occasionally applied (Mahini et al., 2012).

A large number of load-controlled compression tests has been carried out by Blondet and Vargas (1978) and Vargas and Ottazzi (1981). These researchers studied the behaviour of column-like specimens with width-to-height (slenderness) ratios ranging from 1:1 to 1:5. Compression tests on adobe piers with 1:2 width-to-height ratios have been undertaken by Tolles and Krawinkler (1990). Gavrilovic et al. (1998) also constructed and tested stack-bonded prisms, the height of which was twice their width. In addition, Gavrilovic et al. (1998) performed compression tests on running bond wallettes with height approximately equal to their width (≈ 600 mm). Binda et al. (2008) collected adobes from traditional buildings in Portugal; these were used along with lime-based mortar in the preparation and testing of three-layered prisms with dimensions (height x width x length) 400 x 200 x 200

mm^3. Similar test units composed of three bricks placed one above the other with the application of earth jointing mortar have been examined by Dowling (2006). Quagliarini et al. (2010) tested assemblages comprising of three masonry courses, built with full- and half-bricks placed in a running bond pattern. Mahini et al. (2012, 2007) investigated the response of adobe masonry to compression perpendicular and parallel to the bed joints. These researchers carried out experiments on both unconfined and partially confined stack-bonded cubic and prismatic specimens, aiming to replicate the boundary conditions that exist in adobe masonry vaults. Bartolomé et al. (2009) assessed the compressive strength of both seven-layered stack-bonded prisms and walls with height = width = 800 mm. Wu et al. (2012) derived experimental data regarding the full stress-strain response of adobe masonry, following the implementation of load-controlled tests on assemblages consisting of nine layers of bricks, eight bed joints and three axial head joints. On the other hand, Varum et al. (2006, 2011) tested small-scale assemblages. In this case, the upper and lower layers of the specimens were formed by a single block, while the middle row consisted of two half-blocks separated by a vertical mortar joint.

Compression test results quoted in experimental studies lie between 0.6 and 1.6 MPa, with most researchers obtaining mean compressive strength values in the region of 1 MPa. These outcomes are significantly higher than the 0.2 MPa limit suggested by the NTE E0.80 code. It is interesting to note that, despite the variety of specimens and materials examined, compressive strength values for adobe masonry do not present the same high levels of variance as those for individual bricks (see section 3.4).

4.2.2 Assessment of shear strength

Shear strength is a mechanical property directly related to the resistance of masonry walls to lateral in-plane loads. Therefore, its determination is essential not only for the static analysis of a masonry structure, but for the evaluation of its seismic capacity as well.

In Eurocode 6, the response of unreinforced masonry to horizontal loads is conventionally defined by a Mohr-Coulomb failure envelope that relates the shear strength f_{vk} to the shear bond strength f_{vko}, an apparent friction coefficient μ and the compressive stress f_v perpendicular to shear at the level under consideration:

$$f_{vk} = f_{vko} + \mu f_v \tag{4.1}$$

The characteristic initial shear strength at zero compression (f_{vko}) and the friction coefficient μ are determined by testing specimens made of three masonry units, according

to EN 1052-3. The procedure involves the coinstantaneous imposition of load on the triplet's central unit and the application of pre-compression (f_v). For each specimen tested, the shear strength (f_{vki}) is calculated using the following equation:

$$f_{vki} = \frac{P_{i,max}}{2A_i} \tag{4.2}$$

where $P_{i,max}$ = maximum load exerted and A_i = cross-sectional area of the specimens parallel to the shear force. In order to obtain adequate data for the validation of the Mohr-Coulomb failure criterion, tests are conducted at different levels of pre-compression.

The approach adopted by Eurocode 6 presumes that in-plane horizontal loading will cause the shear sliding failure of masonry. However, experience has shown that masonry walls under shear tend to develop diagonally oriented cracks that may propagate through the bed- and head-joints, pass through the units or partly follow the joints and partly intercept the units (Tomaževič, 2009). Turnšek and Čačovič (1970) comment that it is not possible to explain the formation of diagonal cracks using the friction theory. They indicate that, by assuming homogeneous and isotropic behaviour of masonry walls, shear failure can be caused by the principal tensile stresses generated under the combination of vertical and lateral loads. On this basis, diagonal cracks are expected to occur when the principal tensile stresses exceed a value called the ''tensile'' or ''diagonal tensile" strength of masonry (f_{tk}). For the evaluation of f_{tk}, the ASTM E519 / E519M – 10 and the NTE E0.80 code suggest loading masonry assemblages in compression along one diagonal (forces imposed at an angle of 45^o in relation to the bed-joints). This produces diagonal tension failure, with the specimen splitting apart parallel to the direction of load. The tensile strength of masonry f_{tk} is estimated as:

$$f_{tk} = a\frac{P_{max}}{A_n} \tag{4.3}$$

where P_{max} = maximum load exerted, A_n = net area of the specimen subjected to loading and a = 0.707 assuming a uniform stress state in the masonry (ASTM E519 / E519M - 10) or 0.5 if the theoretical elastic isotropic solution of Frocht (1931) is adopted (Calderini et al., 2010; Tomaževič, 2009; Brignola et al., 2008).

Both the aforementioned testing methodologies have been used for investigating the shear response of adobe masonry. Dowling et al. (2004) carried out a series of horizontal loading tests on stack bond and running bond triplets. Direct shear testing of three-layered prisms has also been conducted by Quagliarini et al. (2010). Furthermore, Almeida (2012)

performed tests on specimens composed of two adobe blocks and a lime-mortar joint to evaluate the increase in shear strength as a function of the imposed normal stress. In this study, cohesion among the adobes was found to be f_{vko} = 0.096 MPa, while a friction coefficient of approximately 1.35 was derived. The resistance of adobe masonry to horizontal loading, evaluated by direct shear tests, varied from 0.03 to 0.55 MPa, depending on the type of mortar used and the magnitude of pre-compression applied.

Noticeable experimental work has been undertaken in order to examine the response of adobe masonry to diagonal tension. Adobe wallettes with dimensions ranging from 500 x 500 mm^2 to 800 x 800 mm^2 have been tested by Gavrilovic et al. (1998), Vargas and Ottazzi (1981) and Turanli and Saritas (2011). Yamin et al. (2004) performed laboratory tests on full-scaled and 1:5-scaled wall specimens. Reduced-scale test units have also been used by Tolles and Krawinkler (1990). Varum et al. (2006, 2011) examined small specimens composed of three rows of blocks, two bed-joints and a single central head-joint. Moreover, Liberatore et al. (2006) implemented in-situ tests on sections of partially demolished adobe structures. The values of shear strength deduced by the researchers mentioned above range between 0.015 and 0.2 MPa. Shear moduli (G) computed from shear resistance curves vary from 10 to 70 MPa.

Apart from direct shear and diagonal tension tests, horizontal in-plane loading experiments have been conducted on full scale adobe walls. Both panels constructed in the laboratory (Vera and Miranda, 2004) and walls of existing adobe structures (Varum et al., 2008) have been examined. Shear loading of the specimens is achieved by imposing either monotonously increasing (Vargas et al., 1986) or reversing forces (Varum et al., 2008; Vera and Miranda, 2004; Yamin et al., 2004). In-plane loading tests have been used for investigating aspects such as rigidity, displacement capacity, ductility and residual shear strength after damage initiation. In some cases, the same tests have been used for estimating energy dissipation and damping capacities (Yamin et al., 2004). According to Vera and Miranda (2004), in-plane loading tests reproduce the cracking pattern observed in diagonal tension tests and confirm that shear cracking in adobe walls can develop at stress levels between 0.01 and 0.1 MPa.

4.3 Compressive strength testing of adobe masonry assemblages

4.3.1 Specimen preparation

4.3.1.1 Construction of stack-bonded prisms

All bricks used for the construction of stack-bonded prisms were obtained from manufacturer Ly and belonged to the same production batch (LyC). The earth mortar applied in the joints was prepared in the laboratory using crushed adobe bricks of the same batch and water (1.155 kg per 1.85 kg of solid constituents). These were mixed to plastic consistency using a mechanical mixer. Stones and gravel with diameter exceeding 4 mm were sieved away from the dry solid constituents.

The mortar was tested in accordance with EN 1015-11. A total of 6 prismatic specimens with dimensions (height x width x length) 40 x 40 x 160 mm^3 were cast into steel moulds and subjected to three-point bending tests after 28 days (Figure 4.1a). The mean flexural strength of the specimens was 0.48 MPa. The two half-specimens that resulted from each flexural strength test were subjected to compression tests (Figure 4.1b). The average compressive strength recorded was 3.32 MPa.

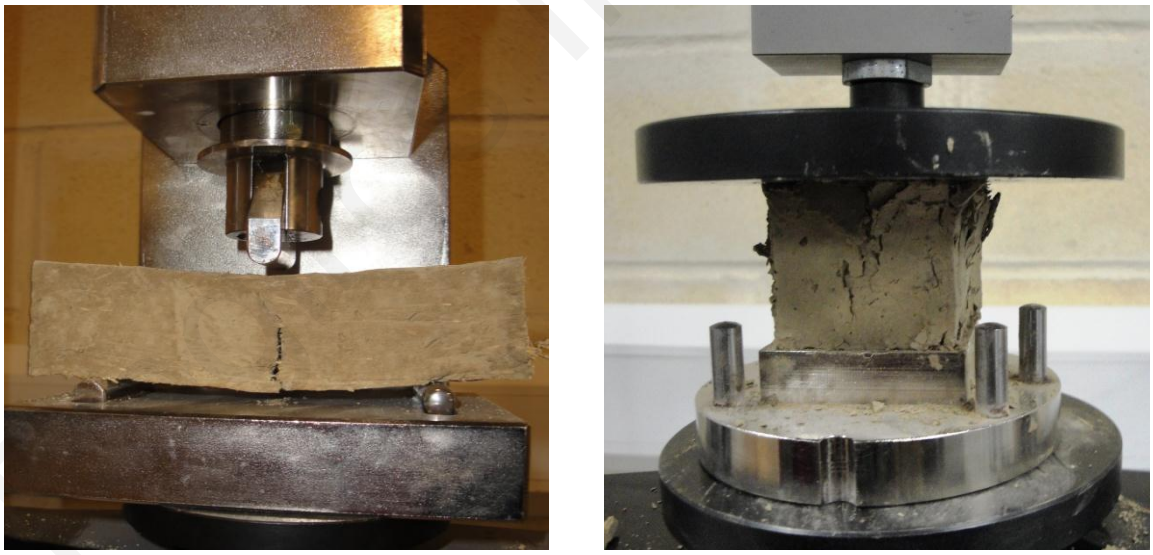

(a) **(b)**

Figure 4.1: Experimental set-ups implemented for conducting three-point bending (a) and compressive strength (b) tests on earth mortar specimens sampled from the mixture used in the joints of masonry specimens. The characteristic modes of failure sustained by mortar specimens under bending and compression are also shown.

The results derived indicate that the mechanical properties of earth mortar are superior to those of adobe bricks with analogous composition (see results for bricks originating from batch LyC in section 3). This can be attributed to the higher density (1500 kg/m^3) of the mortar specimens (as opposed to 1300 kg/m^3 for the bricks), which resulted from the mechanical compaction of the fresh mixture during the standardized sampling process (EN 1015-11).

Prisms were formed by placing five full-size adobe bricks, one above the other (Figure 4.2). Mortar was applied at relatively thin layers (≤ 10 mm) between the adobes. The composition of the mortar and the formation of thin joints were intentionally selected in order to replicate the joint pattern encountered in local traditional earthen structures. The average dimensions of the resulting masonry assemblages were (height x width x length) 280 x 300 x 450 mm^3. Prior to testing, specimens were allowed to cure for at least 3 weeks in the laboratory (29 ± 2 ºC and 45 ± 6% R.H.) in order to ensure sufficient bonding between the bricks and the mortar.

Figure 4.2: Preparation of stack-bonded adobe masonry prisms.

4.3.1.2 Construction of running bond wallettes

Running bond wallettes were constructed with adobes produced in the laboratory using raw materials (soil and straw) supplied by manufacturer Ly. The raw materials were identical to those used in production batches LyA, LyB and LyC. The mixture composing the bricks consisted of 48% soil, 20% straw and 32% water (vol/vol). It was first kneaded in a planetary mechanical mixer and was then cast into aluminum moulds with dimensions (height x width x length) 55 x 200 x 275 mm^3. The bricks were laid on a large timber pot

filled with soil and covered with geotextile fabric and were allowed to cure indoors (20 ± 3 ^{o}C and 45 ± 8% R.H.) for 4 weeks before being used in the construction of wallettes.

The jointing mortar was prepared by manually mixing 11.1 kg of soil, 0.15 kg of straw and 530 ml of water with shovels. Sampling and testing of the mortar followed the same procedure described in section 4.3.1.1. The mean flexural strength in this case was found to be 0.14 MPa, while the average compressive strength was 3.77 MPa. The lower flexural strength, compared to the one recorded for the mortar used in the construction of stack-bonded prisms, is likely due to the lesser amount of straw added to the mixture. It is worth noting that traditional mud bricks in Cyprus contain approximately 25-35% straw (vol/vol) (Eftychiou, 2013; Demetriou et al., 2006).

For the construction of the wallettes, two full size adobes were used at the base of the specimens. Above these, four masonry courses were laid in such a way that no continuous vertical joints were formed. Head-joints in each course were centered on the bricks in the row below. Where required, half-bricks were used to fill the masonry courses (Figure 4.3). Leveling of the specimens' upper and lower surfaces was achieved by abrasion and application of a thin layer (< 5 mm) of gypsum plaster (Figure 4.3b).

(a) **(b)**

Figure 4.3: (a) Construction of an adobe masonry assemblage used in compression tests. (b) Completed running bond wallette after the application of gypsum plaster capping.

Two wallettes were constructed. Their final dimensions were (height x width x length) 323 x 279 x 374 mm^3 and 315 x 271 x 428 mm^3. The curing period for these specimens was 8 weeks.

4.3.2 Testing methodology

Adobe masonry specimens were subjected to both monotonic and loading-unloading compression tests. For the imposition of monotonic compressive loads, a CONTROLS Advantest 9 servohydraulic compression test frame with 5000 kN capacity and a Lloyd LR300K universal testing machine with 300 kN capacity were used (Figure 4.4). The latter was used for displacement-controlled tests, while the former for load-controlled experiments. The platens mounted on both testing frames incorporated swivel heads to accommodate non-parallel bearing surfaces. It is noted that the patens installed on the Lloyd LR300K machine were custom-made and were composed of 25 mm-thick solid steel.

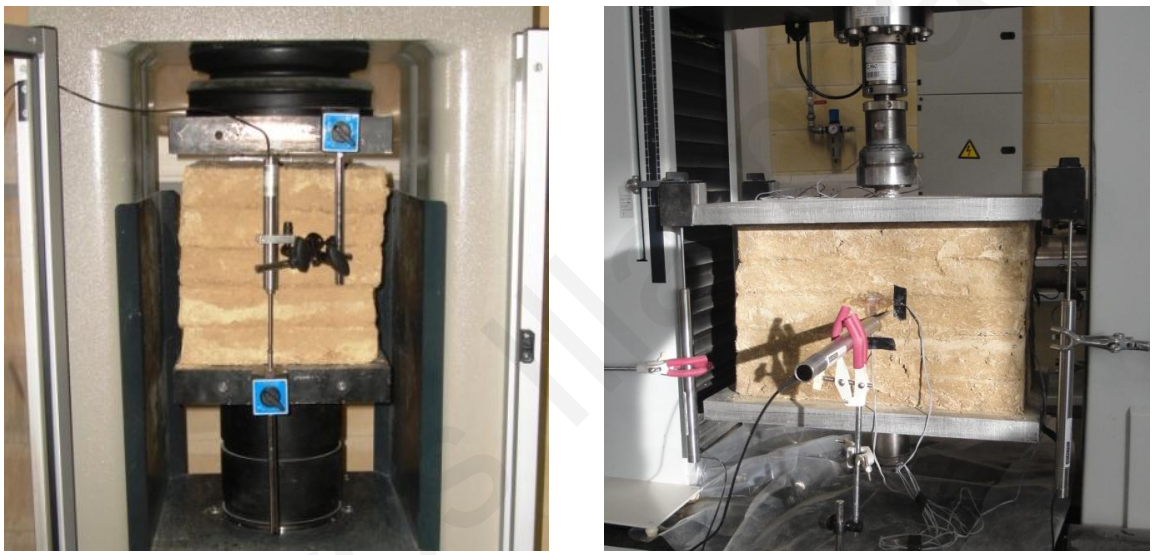

(a) **(b)**

Figure 4.4: Experimental set-ups used for the implementation of (a) load-controlled and (b) displacement-controlled compressive strength tests on stack-bonded adobe masonry prisms.

During testing, longitudinal displacements were recorded using vertical Linear Variable Differential Transformer transducers (LVDTs) (range ±50.8 mm, accuracy ±0.25%) attached to the corners of the loading plates. In the case of a selected specimen, transversal deformations were also monitored using two horizontal LVDTs placed at each side of the assemblage. Compressive loading was applied to the specimens either by exerting a constant force at a rate of 10 kN/min, or by imposing a constant displacement at a rate of 4.5 mm/min. Load-controlled tests were conducted 3 weeks after specimen preparation, whereas displacement-controlled tests after 43 weeks. One of the purposes of the displacement-controlled tests was to examine the post-peak softening response of adobe

masonry. However, due to intense deformability of the specimens (see section 4.3.3.2) this could not be achieved. A total of 12 stack-bonded prisms (SB1 to SB12) were examined through monotonic compression tests.

To further investigate the elastic and post-yield structural response of adobe masonry, loading-unloading tests were performed on a single stack-bonded prism and on two running bond wallettes. Forces on these specimens were imposed through the application of displacement at a constant rate of 6 mm/min, using a 300 kN load frame (Figure 4.5). In the case of the stack-bonded prism (SB13), unloading cycles were programmed to take place successively when the applied load reached a value of 10, 30, 50, 100, 150 and 200 kN. For the first running bond wallette (RB14), unloading steps were set at 10, 20, 30, 40, 70, 200 and 230 kN, whereas for the second (RB15) they were set at 10, 20, 30, 40, 70, 140 and 230 kN.

Figure 4.5: Experimental set-up used for the implementation of displacement-controlled loading-unloading compression tests on running bond adobe wallettes.

4.3.3 Results and discussion

4.3.3.1 Modes of failure in compression

In stack-bonded prisms, failure was characterized by considerable reduction of height accompanied by severe circumferential spalling (Figure 4.6). Compressive loading caused specimens to deform in both transversal directions. This generated the development of several tensile cracks on all lateral sides. Cracks were approximately parallel to the direction of loading, with some of them forming at an angle to the applied load. Gradually,

crack opening increased, leading to detachment of the lateral sides of the specimens. At the final stages of loading, prisms presented a distinctive conical fracture shape.

(a) **(b)**

Figure 4.6: Mode of failure in compression experienced by stack-bonded adobe masonry prisms. Note the conical fracture shape (a) and the "absence" of joints due to compaction during loading (b).

During the tests, stack-bonded prisms responded monolithically to vertical loading. Despite sustaining significant damage at their surface, their core remained coherent. Compression resulted in the compaction of adobe and mortar in the central axis of the assemblages. This led to the formation of a central zone within the body of the masonry, where the visual distinction between the individual adobe bricks and the mortar joints was no longer feasible. Moreover, no significant cracks or slips occurred at the joints during the loading procedure. A similar mode of failure has been noted by Mahini et al. (2012, 2007), Quagliarini et al. (2010), Binda et al. (2008) and Dowling (2006) when testing specimens of the same form.

On the other hand, damage in running bond wallettes was mainly characterized by vertical cracking passing through the head-joints (Figure 4.7a). The tendency of the specimens to laterally expand under uniaxial compression, created tensile stresses in the mortar. As soon as the principal tensile stress reached the tensile strength of the mortar and/or exceeded the cohesion at the brick-mortar interface, cracking was formed. Initially, principal tensile stresses were localized at the specimens' mid-height, thus causing failure of the central head-joint. The first cracks were recorded at loads around 10-15 kN. When loading increased to 25-30 kN, damage developed at the other four vertical joints as well. Up to the imposition of 200 kN compressive force, further opening of the cracks at the joints and

axial deformation took place. However, no failure of the masonry units was noted. Eventually, when the load reached 230 kN, damage at the central head-joint propagated to the adjacent masonry courses. This resulted to tensile splitting of the adobes that were directly above and below the mortar joint. Recorded crack widths ranged from 1 to 4 mm (Figure 4.7b). The mode of failure hereby described has also been observed by Wu et al. (2012), who tested adobe wallettes, and by Walker (2004) who examined compressed earth block masonry.

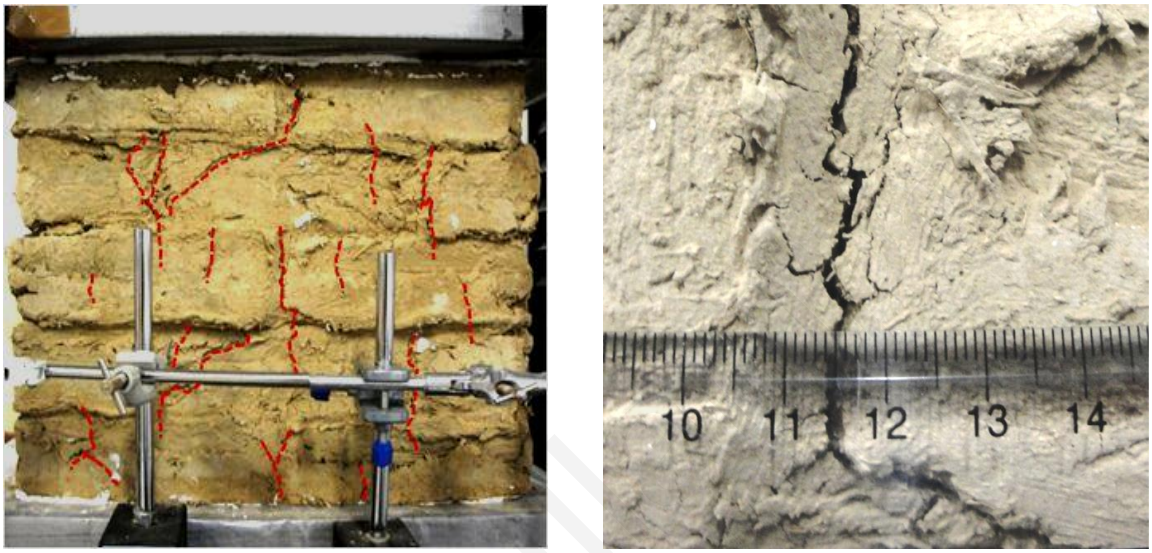

(a) **(b)**

Figure 4.7: Mode of failure in compression experienced by running bond adobe masonry wallette (a) and characteristic crack opening recorded at the central head-joint (b).

4.3.3.2 Stress-strain behaviour

Characteristic stress-strain diagrams obtained from monotonic compression tests on stack-bonded prisms are shown in Figure 4.8. Data concerning the variation of the compressive stress generated on a masonry prism, in relation to both the axial and transversal strains induced, are reported in Figure 4.9. The stress-strain diagrams obtained from all specimens (SB1 to SB12) examined under monotonic compression are given in Annex 2. The outcomes of the three loading-unloading tests are presented in Figure 4.10. It is worth noting that, compressive stress values quoted in the diagrams have been computed by dividing the exerted load with the initial cross-sectional area of each specimen. Axial strains have been estimated based on the average recordings of the transducers monitoring displacements.

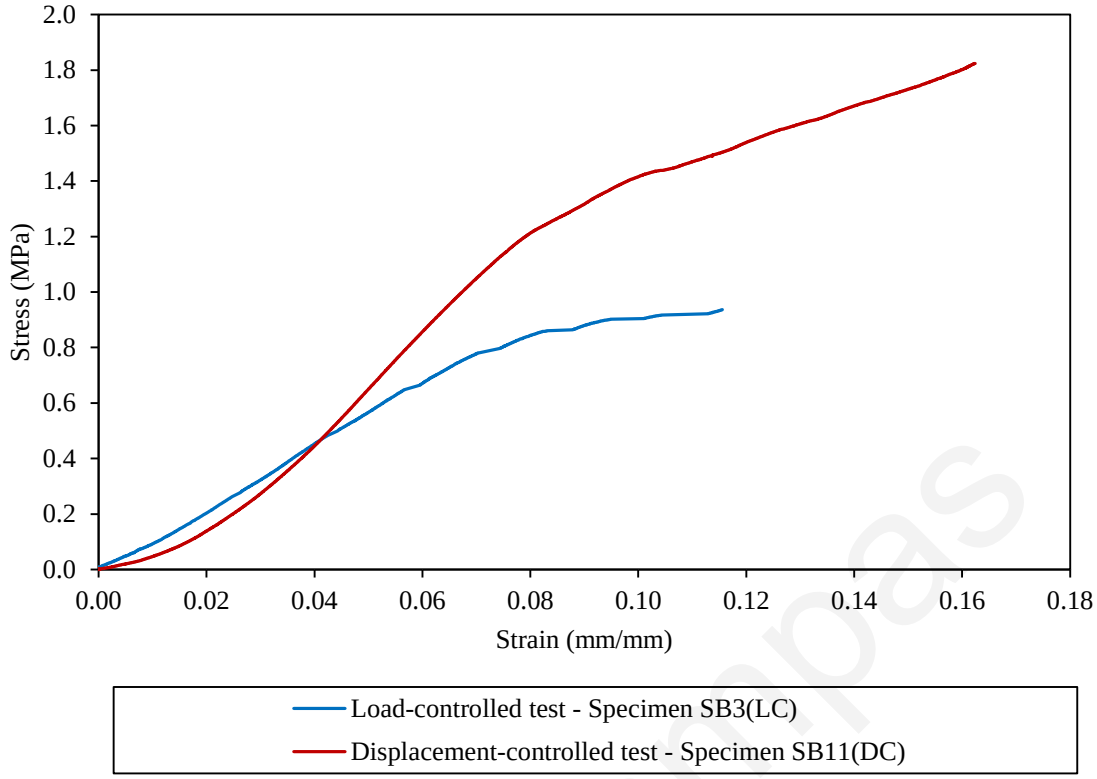

Figure 4.8: Characteristic stress-strain curves obtained from the implementation of load- and displacement-controlled monotonic compression tests on stack-bonded prisms.

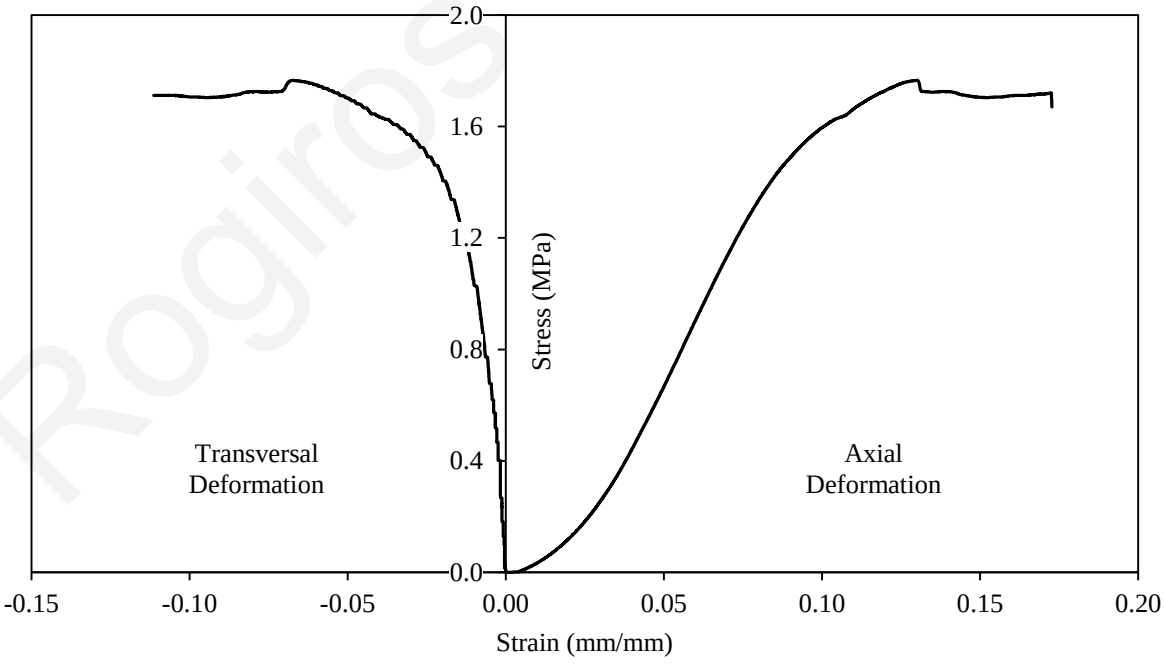

Figure 4.9: Stress versus compressive axial and transversal strain diagram obtained from the compressive strength testing of a stack-bonded adobe masonry prism (specimen SB12(DC)).

(a)

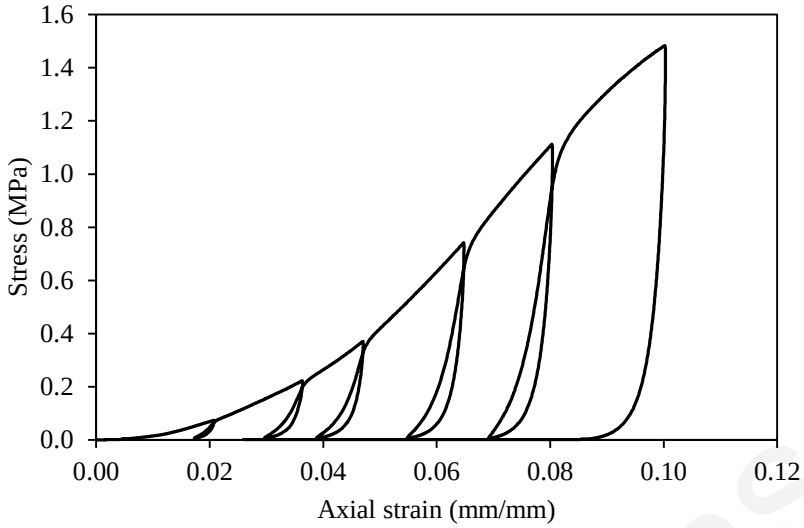

(b)

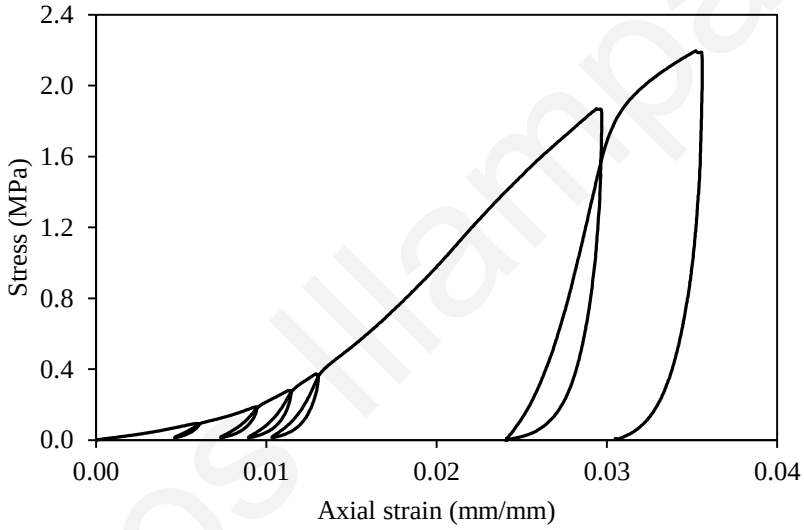

(c)

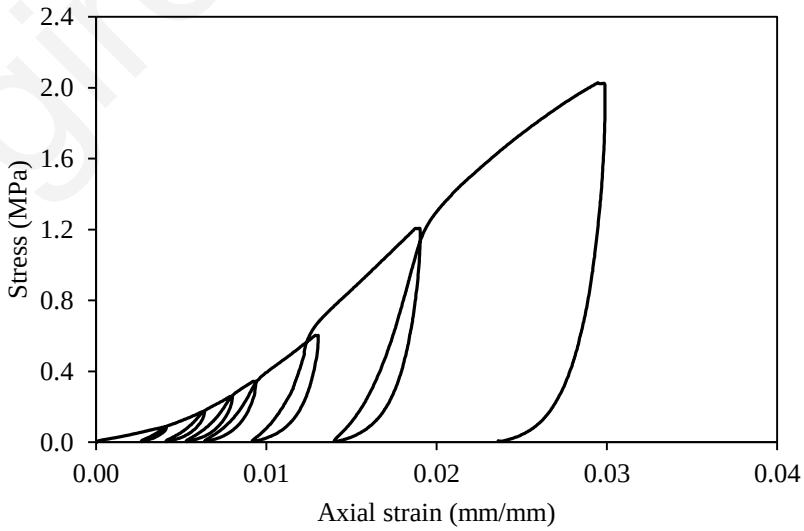

Figure 4.10: Stress-strain diagrams obtained from the implementation of loading-unloading compression tests on (a) stack-bonded prism SB13(DC) and running bond wallettes (b) RB14(DC) and (c) RB15(DC).

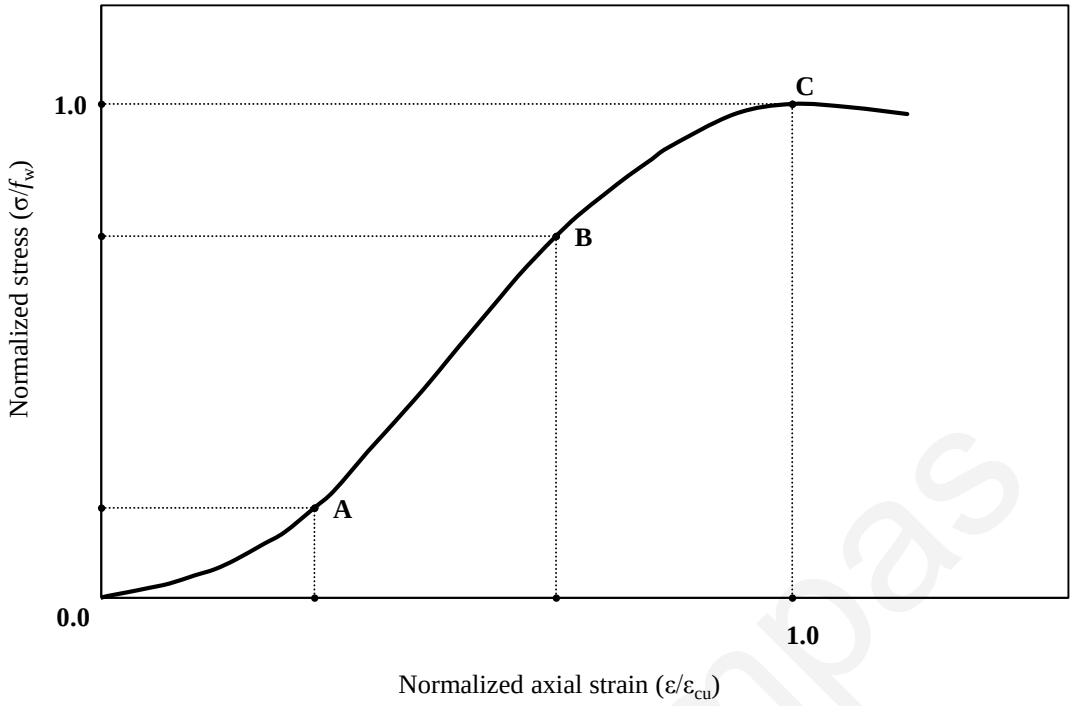

Figure 4.11: Normalized stress-strain diagram showing the response of adobe masonry to compression. Normalization has been conducted by dividing compressive stresses (σ) with the peak stress (f_w) and axial strains (ε) with the strain at the peak stress ($ε_{cu}$). Initially, a consolidation phase occurs (0-A). This is followed by compressive hardening until the maximum stress is reached (A-C). The hardening phase includes a stress range over which deformations tend to increase linearly (A-B).

Experimental data indicate that the response of adobe masonry to compressive loading is analogous to that of the individual adobe bricks (see section 3.4). Initially, a consolidation phase occurs, which accounts for 5-30% of the total axial strain recorded (Figure 4.11). At this stage, the poorly compacted soil particles within the brick and mortar matrices are redistributed, while tiny pores and air-voids are crushed. Consolidation is followed by a compression hardening phase, up to the point where the ultimate compressive strength f_w is reached. As loading progressively increases, all voids within the materials collapse and the specimen is densified. This process is followed by tensile cracking, of either the unconfined perimeter or the loosely coherent vertical joints. When the ability of the adobe masonry to sustain higher loads is diminished, the imposition of forces simply causes greater inelastic deformations and leads to fracturing. In the ranges of axial strains examined, masonry assemblages were capable of deforming while undertaking compressive loading. Hence, a post-yield softening branch could not be defined.

According to the results of the loading-unloading tests, the behaviour of adobe masonry under compression is highly non-linear and is characterized by intense plasticity and deformability. The recorded unloading branches reveal that, when the exerted load is released, the deformation induced is only partially recovered, while considerable inelastic strains remain present. Plastic deformations start to develop even when the specimens are subjected to low compressive stresses (< 0.1 MPa). This behaviour is typical for granular cohesive frictional geomaterials (Meyer, 2013); it is attributed to the fact that the sliding and displacement mechanisms, which take place between the soil grains due to the application of pressure, are non-reversible.

4.3.3.3 Ultimate compressive strength and deformation capacity

Compressive strength was assumed to be equal to the maximum stress exerted on each specimen. The values derived are reported in Table 4.1 along with each specimen's curing period, strain at peak stress and secant modulus (see section 4.3.3.4). The bearing capacity of the 9 assemblages tested after 3 weeks of curing lies between 0.82 and 1.13 MPa. The mean compressive strength of these specimens is 0.94 MPa. The results' coefficient of variation is 10.8%. Stack-bonded prisms tested 43 weeks after construction were capable of sustaining compressive loads from 1.48 to 1.85 MPa. In this case, the mean strength is 1.73 MPa, while the corresponding coefficient of variation is 9.8%. The compressive strengths of the two running bond wallets exceed 2.0 MPa.

Table 4.1: Compressive strengths, strains at peak stress and secant moduli for adobe masonry assemblages. Specimens are reported as *Xa(Y)*, where *X* = specimen form (SB for stack-bonded prisms and RB for running bond wallettes), *a* = specimen number and *Y* = load imposition procedure (LC for load-controlled and DC for displacement-controlled compressive loading).

Specimen	Curing period (weeks)	Compressive strength (MPa)	Strain at peak stress (mm/mm)	Secant modulus (MPa)
SB1(LC)	3	0.95	0.090	17.4
SB2(LC)	3	1.08	0.114	15.4
SB3(LC)	3	0.94	0.116	11.6
SB4(LC)	3	0.82	0.076	14.0
SB5(LC)	3	1.13	0.092	23.1
SB6(LC)	3	0.94	0.079	15.0
SB7(LC)	3	0.85	0.090	11.7
SB8(LC)	3	0.89	0.080	14.7
SB9(LC)	3	0.89	0.077	15.9
SB10(DC)	43	1.85	0.144	22.6
SB11(DC)	43	1.82	0.162	20.0
SB12(DC)	43	1.77	0.130	23.1
SB13(DC)	43	1.48	0.100	21.5
RB14(DC)	8	2.20	0.035	97.3
RB15(DC)	8	2.03	0.029	90.7

The experimental results indicate that higher strength values can be obtained by prolonging the specimens' curing period. This is reasonable, considering that the presence of moisture in earth-based materials can drastically reduce their mechanical properties (Minke, 2009; Keefe, 2005; Walker, 2004; Norton, 1997). The effect of specimen age on the results of compression tests is also encountered in the data reported by Vargas and Ottazzi (1981).

The marginally higher compressive strength of running bond wallettes may be attributed to the construction technique itself or indeed the better mechanical properties of the mud bricks used. Mud bricks produced in the laboratory generally show improved mechanical properties (Eftychiou, 2013) due to the adoption of more careful casting techniques, which lead to better compaction. This, in turn, leads to higher densities and increased bearing capacities.

The compressive strengths of stack-bonded prisms are in line with the outcomes of Mahini et al. (2012), Quagliarini et al. (2010), Bartolomé et al. (2009), Binda et al. (2008), Silveira et al., (2007) and Gavrilovic et al. (1998). On the other hand, the results yielded by running bond wallettes exceed the strength values reported in most of these studies. According to the stress-strain data obtained, the deformability of all tested assemblages is substantially higher than that of similar specimens examined elsewhere (Wu et al., 2012; Binda et al., 2008; Mahini et al., 2007; Dowling, 2006); this is attributed to the low density of adobes used (1300 kg/m^3 compared to densities between 1500 and 2000 kg/m^3 reported elsewhere (Yetgin et al., 2008; Quagliarini et al., 2010; Adorni et al., 2013). For stack-bonded prisms, the range of axial deformation over which maximum stresses were generated was 7.6% to 16.2%. Axial strains induced by the imposition of a 250 kN load on running bond assemblages were in the region of 3%. Values of strain at peak stress quoted in the literature generally vary from 0.05% to 2%. The lesser deformation of wallettes implies that these were stiffer than prisms and verifies the influence of the material density on the overall structural response. Deformations above 6% have been observed only by Quagliarini et al. (2010).

4.3.3.4 Elastic modulus and Poisson ratio

Considering the granular structure of earthen materials, it may be argued that elasticity in the case of adobes has limited physical significance. In practice, the onset of non linear response will occur at extremely low levels of loading (Meyer, 2013). Therefore, the elastic modulus can be considered as a stiffness parameter rather than an indicator of actual material linearity. Furthermore, from the outcomes of loading-unloading experiments, it is evident that adobe masonry behaves differently under monotonic compression and loading-unloading conditions.

During the imposition of continuously ascending loads, masonry response is governed by a primary deformation modulus. This was approximated by a secant modulus (E_{sec}) associated with a certain stress range over which strains increase linearly (see range A-B in Figure 4.11). Examining the experimental data, linear stress-strain response in all assemblages was noted between about 25% and 60% of the compressive strength. Secant moduli were thus estimated as:

$$E_{\text{sec}} = \frac{(\sigma_{c,60\%} - \sigma_{c,25\%})}{(\varepsilon_{c,60\%} - \varepsilon_{c,25\%})} \tag{4.4}$$

where $\sigma_{c,25\%}$ and $\sigma_{c,60\%}$ are the compressive stresses at 25% and 60% of the maximum load exerted on each specimen and $\varepsilon_{c,25\%}$ and $\varepsilon_{c,60\%}$ are the corresponding axial strains. The results of these calculations are presented in Table 4.1.

Stack-bonded prisms gave E_{sec} values from approximately 11 to 23 MPa. Running bond wallettes had moduli around 90 and 97 MPa. Comparable results have been reported by Wu et al. (2012). These researchers derived tangent and secant moduli between 30 and 115 MPa. However, most values encountered in the literature are significantly higher than those hereby reported. The tests conducted by Mahini et al. (2012) produced secant moduli in the region of 214 MPa, while values as high as 630 MPa and 1400 MPa have been obtained by Binda et al. (2008) and Gavrilovic et al. (1998). These values are attributed to the specific characteristics of the masonry units and mortars under test and in particular their deformability. As it was previously mentioned (see sections 3.4 and 4.3.3.3), recorded strains at peak stress for local adobe bricks and masonry assemblages are much higher than equivalent values quoted in the literature.

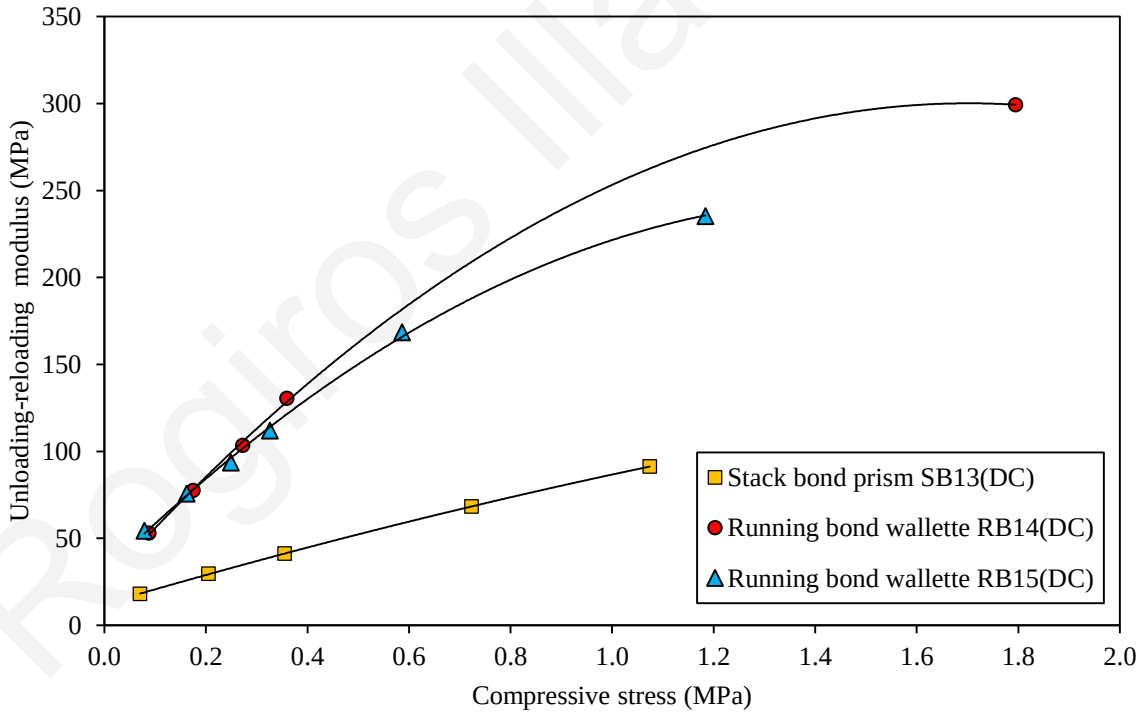

Figure 4.12: Variation of computed unloading-reloading modulus, in relation to compressive stress. Reported stress values correspond to stresses at which unloading was initiated.

Upon unloading, the response of the specimens follows the path set by the unloading-reloading modulus (E_{ur}). Based on the recommendations of Briaud (2001) and Briaud et al. (2006), E_{ur} was defined as the slope of the line passing through the origin of the reloading

curve and the point where the unloading and reloading branches coincide. Values of E_{ur} were computed for every unload-reload loop. The variation of the evaluated moduli in relation to the magnitude of the exerted stress is shown in Figure 4.12. The outcomes indicate that E_{ur} is strongly stress-dependent.

For running bond wallettes, E_{ur} raises non-linearly from 50 to 300 MPa as compressive loads increase from 0.005 to 1.8 MPa. In the case of the stack-bonded prism, the initial value of E_{ur} is approximately equal to that of the secant modulus (≈ 20 MPa). With the progressive application of compressive loads, E_{ur} increased almost linearly, finally reaching the value of 91 MPa. This verifies that compression leads to compaction of adobe masonry which, in turn, causes stiffness augmentation.

By monitoring the transverse and axial deformations of a stack-bonded prism under compression (Figure 4.9), an estimate for adobe masonry's Poisson ratio could also be derived. Poisson ratio was evaluated as the ratio of transverse to axial strain and was found to be about 0.3. Recordings within the stress range over which both axial and transversal strains increased linearly (25-60% of maximum compressive stress) were used in the above calculation. It should be pointed out that, although Poisson ratio is by principle an elastic parameter, the strain range adopted corresponds to non-linear deformations. The use of such data was dictated by the distinct inelastic response exhibited by adobe masonry under compression. Nevertheless, the result yielded is within the 0.1-0.4 range of values reported by Wu et al. (2012).

4.3.4 Evaluation of existing analytical equations for estimating the compressive strength of adobe masonry

Various analytical equations have been proposed for evaluating the characteristic compressive strength (f_w) of conventional masonry construction. The formulation and validation of the available models is usually based on the statistical analysis of experimental results. Most equations relate the compressive strength of masonry assemblages to the individual compressive strengths of the masonry units (f_b) and the mortar (f_m) used for their construction. In some cases, the geometrical properties of the materials composing the masonry, as well as specific construction details, have also been taken into consideration. The various analytical relations encountered in the international bibliography are quoted in the following paragraphs.

To examine whether these relations can be used in the appraisal of adobe construction, the values obtained by their application are compared with the results of compressive strength tests carried out in the framework of this thesis. Since all assemblages tested were composed of bricks that either originated from or had the same composition as production batch LyC, relevant experimental data were used in the calculations. The compressive strength of masonry units was set to be equal to the size-independent mean normalized compressive strength of the cylindrical specimens tested from production batch LyC (see section 3.4): f_b = 1.87 MPa. The respective strength of the mortar was assumed to be equal to the average strength of all samples examined in accordance to EN 1015-11 (see section 4.3.1): f_m = 3.55 MPa.

Eurocode 6, which refers to the design of masonry structures, indicates that, when results of laboratory tests are not available, the characteristic compressive strength of masonry may be deduced from the following equation:

$$f_{wc} = K\, f_{bc}^{0.7}\, f_{mc}^{0.3} \tag{4.5}$$

Equation 4.5 refers to unreinforced masonry constructed with the application of general purpose mortar, the compressive strength of which is $f_{mc} \leq \min\{20\text{ MPa}, 2f_{bc}\}$. The characteristic compressive strengths of the units (f_{bc}) and mortar (f_{mc}) were assumed to be equal to 80% of the corresponding average values (Eurocode 6). The constant multiplication factor K depends on specific features of the masonry units and certain construction details and is in the range $0.25 \leq K \leq 0.55$. The proposed model is deemed valid when the masonry structure under study has been built in accordance with Eurocode 6 and the coefficient of variation of f_{bc} does not exceed 25%. It should be noted that, adobe bricks are not within the list of masonry units included in Eurocode 6 and their mechanical properties do not fulfill the permissible limits stated. In addition, it is pointed out that the prerequisite set in Eurocde 6 for the jointing mortar to be weaker than the masonry units does not apply for the materials hereby examined. Nevertheless, in order to adopt equation 4.5, it was assumed that adobe bricks fall within Group 1 of the units classified in Eurocode 6 and were thus categorized as "manufactured stones". Using K = 0.45 and adopting the limitation $f_{mc} = 2f_{bc}$, equation 4.5 produces a value of characteristic compressive strength f_{wc} = 0.820 MPa.

Of similar format with the model included in Eurocode 6 is the expression derived by Mann (1982):

$$f_w = 0.83\, f_b^{\,0.67}\, f_m^{\,0.33} \tag{4.6}$$

This relationship has been deduced through the analysis of 925 laboratory tests on masonry walls. By substituting the compressive strengths of adobe and earth mortar in equation 4.6, the estimated compressive strength is f_w = 1.918 MPa.

By undertaking a statistical analysis on an extensive database of experimental results, Dymiotis and Gutlederer (2002) have suggested the equation quoted below:

$$f_w = 0.3266\, f_b (1 - 0.0027\, f_b + 0.0147\, f_m) \tag{4.7}$$

When adopting this model, the computed value for the compressive strength of adobe masonry is f_w = 0.640 MPa.

An empirical equation has been proposed by Tassios (1987):

$$f_w = \frac{f_b}{6} + \frac{\sqrt{f_b\ f_m}}{4} - \frac{f_m}{20} + 1.4 \tag{4.8}$$

In line with equations 4.5, 4.6 and 4.7 the value of compressive strength derived from equation 4.8 depends solely on the mechanical properties of the masonry units and mortar. For the mechanical properties of the earth mortar and adobes used in this study, the value of compressive strength obtained by this equation is f_w = 2.178 MPa.

Apart from equation 4.8, Tassios (1987) has also proposed empirical equations which take into account the geometrical characteristics of the elements composing the masonry assemblage. These are:

for $f_b < f_m$ $\qquad f_w = (1 - 0.8\sqrt[3]{\alpha})\, f_b$ (4.9a)

for $f_b > f_m$ $\qquad f_w = \left(1 - 0.8\sqrt[3]{\alpha}\right)[\, f_m + 0.4(\, f_b - f_m)]$ (4.9b)

where $\alpha = h_m/h_b$ is a factor that depends on the thickness of the mortar joints (h_m) and the height of the masonry units (h_b). For h_m = 8 mm and h_b = 50 mm, the result obtained using equation 4.9a is f_w = 1.058 MPa.

By undertaking compressive strength tests on masonry assemblages composed of fired clay bricks and lime-pozzolana mortar joints, Karaveziroglou and Papayianni (1993) have developed the following model:

$$f_w = \frac{1}{100}\left(62 - 0.8 t_m\right)(0.557\, f_m^{\,2} + 0.0695\, f_m + 10.061) \tag{4.10}$$

where t_m is the thickness of the mortar joints in mm. It is worth noting that the model proposed by Karaveziroglou and Papayani has been developed in order to provide estimates for the compressive strength of masonry with thick mortar joints. When used for computing the compressive strength of adobe masonry constructed with thin mortar joints (t_m = 8 mm), f_w = 9.634 MPa.

Although models 4.5 and 4.9 do not refer to masonry composed of unfired earth, and despite the fact that the requirements set in Eurocode 6 for the application of equation 4.5 are not satisfied, the estimates provided by adopting the aforementioned relationships fall within the range of experimental data hereby presented (0.82-2.20 MPa). Comparing the values derived with the mean compressive strength of specimens at 43 weeks of age (1.73 MPa), it may be argued that these models can be adopted for conservative calculations.

The equation proposed by Dimiotis and Gutlederer tends to underestimate the compressive strength of adobe masonry hereby examined, since it produces outcomes which are 20% lower than the minimum derived value (0.82 MPa). On the other hand, models 4.6 and 4.8 give considerably higher predictions which generally overestimate the compressive strength of stack-bonded prisms. However, the outcomes of the aforementioned equations approach the results obtained from running bond wallettes. The relation suggested by Karaveziroglou and Papayani appears to be non-applicable in the case of adobe masonry, since it yields estimates which greatly exceed the experimental data range. Nevertheless, in order to deduce more valid conclusions regarding the suitability and accuracy of the various existing empirical equations, a very broad and thorough experimental investigation is required. This should include the formation of an extensive database of results that will enable the re-consideration and calibration of all equation parameters.

4.4 Diagonal tension testing of adobe masonry wallette

4.4.1 Specimen preparation

In order to examine the response of adobe masonry to diagonal tension, a wall panel composed of scaled-down (approximately 1:1.5) adobes and compatible earth mortar joints was prepared and tested (Figure 4.13). The size of the blocks used in the construction of the specimen was (height x length x width) 50 x 300 x 150 mm^3. These were obtained by cutting full-scale bricks originating from production batch LyC. Earth mortar was prepared in the laboratory by mixing soil, straw and water. Raw materials were supplied by

manufacturer Ly and were identical to those used in the production of the adobes. The approximate composition of the mortar mixture was 3:1:3 (soil:straw:water) by volume. Mortar constituents were manually kneaded using a shovel. When the mixture reached adequate workability, it was stored in a tray covered with nylon and was allowed to ferment for 3 days. During this time, moisture was homogeneously distributed among the soil's clay particles. Following fermentation, the mixture was kneaded again and the mortar was applied in thin layers. The thickness of the joints was intentionally kept below 10 mm, since this is the common case in existing earthen structures.

The wallette was built following the running bond construction pattern. A total of 11 consecutive masonry courses were laid. The final dimensions of the wallette were (height x length x width) 600 x 600 x 300 mm^3. A specially designed steel frame accommodated the specimen during construction and testing (Figure 4.13). The frame consisted of 350 mm wide 'C'-section steel plates. It incorporated hinges at the corners, thus enabling free rotation of its members. Tests were conducted 28 days after the wallette was constructed. During this period, the specimen was stored in the laboratory at 25 ± 3 ºC and 42 ± 5% R.H..

(a) **(b)**

Figure 4.13: The adobe masonry wall specimen used in the diagonal tension tests (a) during and (b) after its construction.

4.4.2 Testing methodology

For the implementation of the experimental procedure, ASTM E519 / E519M – 10 and NTE E0.80 were consulted. The test set-up used (Figure 4.14) was formulated based on the

recommendations of Monk (1962). The masonry specimen was placed between the test machine's loading platens at an angle of 45 degrees relative to the vertical axis. Diagonal compression was exerted on the specimen through the application of displacement on its upper part at a constant rate of 4.5 mm/min. For this purpose, a Lloyd LR300K universal testing machine with 300 kN loading capacity was used.

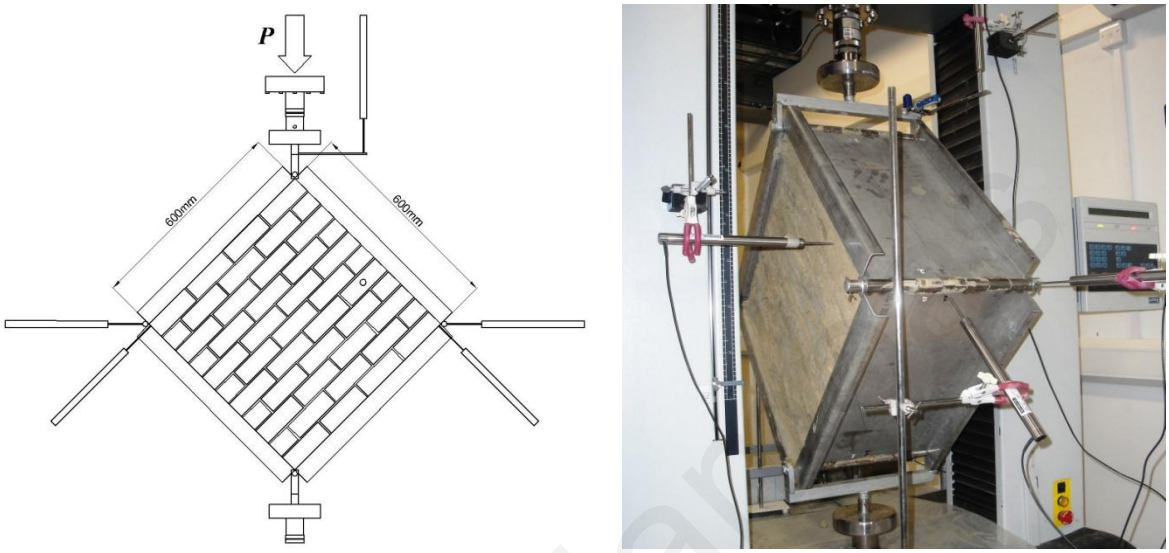

(a) **(b)**

Figure 4.14: Schematic representation (a) and photograph (b) of the experimental set-up used for the implementation of the diagonal tensile strength tests on the running bond adobe wallette.

Since the bed-joints of the masonry assemblage were at an angle to the loading direction, the imposition of compression forces caused the generation of shear stresses. The decomposition of compression forces into shear components was achieved by means of the enclosing frame's hinges. It was assumed that the boundary conditions imposed to the experimental set-up were capable of simulating those encountered in shear wall elements in adobe buildings. In addition, the monotonic diagonal load imposed on the specimen resulted in a state deemed similar to that of the stresses produced by the in-plane lateral loading of walls.

Three successive loading cycles were imposed on the same test unit. During each test, the force was applied until visible damage (i.e. cracking) occurred. It should be pointed out that, in none of the tests the ultimate limit state (i.e. total or partial collapse of the specimen's structure) was reached. Throughout the tests, LVDTs (range ±50.8 mm, accuracy ±0.25%) in contact with the steel frame were used to measure displacements

along the vertical and horizontal diagonals. The out-of-plane deformation of the wallette was also monitored.

4.4.3 Results and discussion

4.4.3.1 Mode of failure in diagonal tension

In all tests conducted, failure of the specimen occurred in the form of cracking along the direction of the applied forces (Figure 4.15a). Cracking had a stepped pattern and propagated through the masonry joints. Despite the fact that damage was concentrated at the joints, no tensile splitting of the mortar was recorded. Instead, loss of cohesion at the brick-mortar interface and subsequent debonding of masonry units were observed.

Damage was initiated at the central head-joint; this was followed by the almost simultaneous cracking of the two head-joints closest to the load imposition platens (upper and lower). Thereupon, cracking developed at the adjacent bed joints. Gradually, a network of cracks passing through all vertical and horizontal joints intercepting the line of loading was formed. The imposition of higher loads caused a progressive increase in crack width, practically splitting the specimen in two halves. At the final stages of each test, crack opening reached 6 mm (Figure 4.15b). In addition, some damage (i.e. sliding of mortar joints and tensile splitting of adobe bricks) at the specimen's two lateral corners also developed; this was the result of localized stress development from the stiff shear steel frame. Apart from the two lateral corners, no other fracturing of adobe bricks was noted. More importantly, premature failure of the specimen's upper and lower corners due to excessive stress concentration at the points where loading was imposed did not occur. Furthermore, no out-of-plane movement of the masonry units or bulging of the specimen were reported. However, in the last test cycle partial detachment of the wallette's lateral corners from the enclosing steel frame was observed (Figure 4.15c). Upon unloading, the fissures formed in the joints closed and only hair-like cracks manifested the existence of shear damage. The mode of failure hereby described is in agreement with the observations of Turanli and Saritas (2011), Liberatore et al. (2006) and Vargas and Ottazzi (1981), who also conducted diagonal tensile strength tests. The cracking mechanism noted verifies the comments of Turanli and Saritas (2011), who indicate that shear strength depletion in unreinforced adobe masonry is primarily the product of the weak bonding among the bricks.

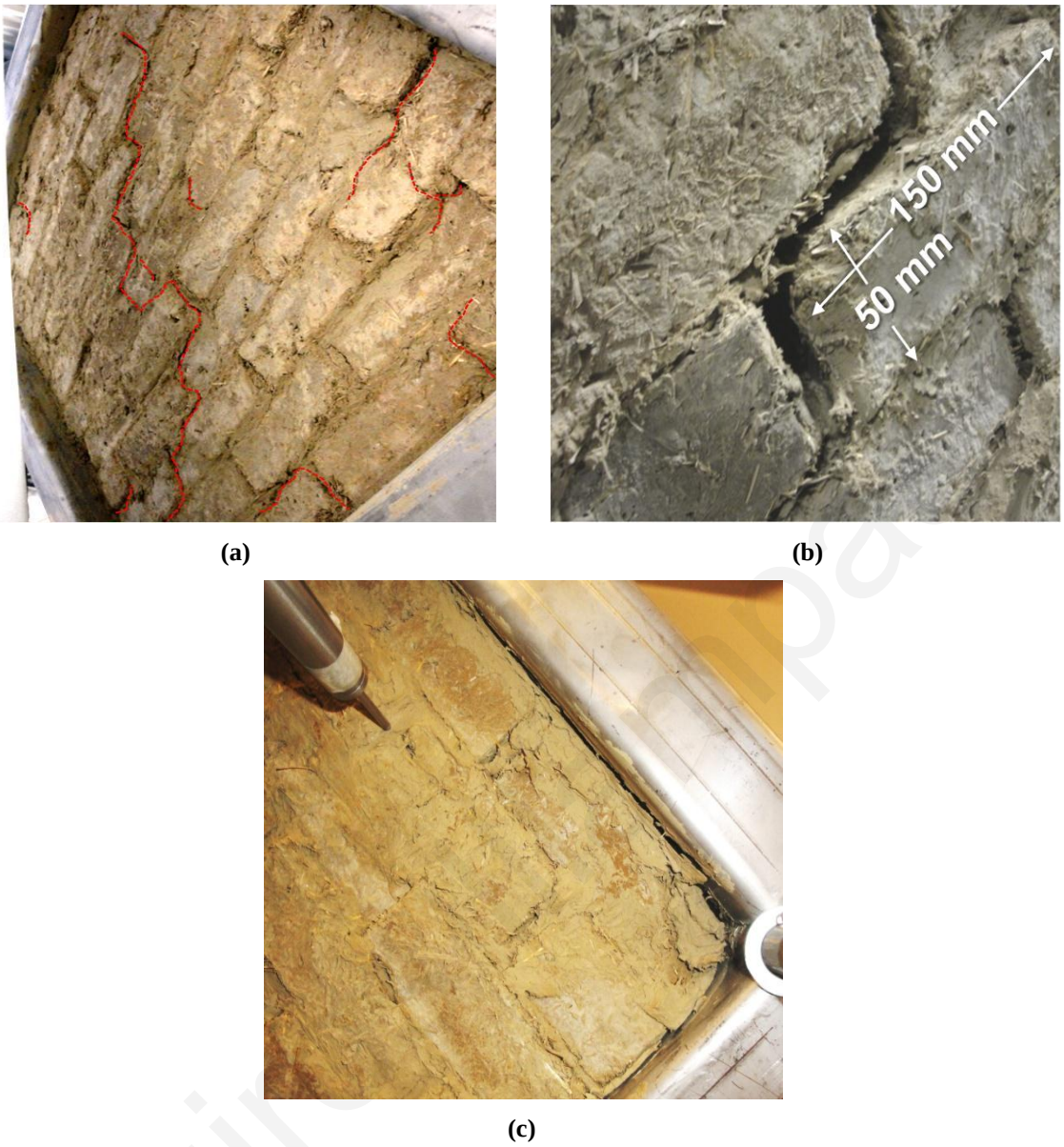

Figure 4.15: (a) Mode of failure sustained by running bond adobe masonry panel in diagonal tension. (b) Close view of the crack formed at the vicinity of the central head-joint. (c) Partial detachment of the wallette's lateral corner from the enclosing steel frame.

4.4.3.2 Stress-strain response under shear

For the analysis of the experimental data, the theoretical solution developed by Frocht (1931) was adopted. According to this approach, masonry is idealized into an isotropic linearly elastic medium. Failure of the specimen is associated with the maximum principal tensile stress σ_I attained at its center. If a compressive force P is applied on one of the specimen's diagonals, the elastic solution provides the following stress state at the mid-height of the masonry (Figure 4.16):

$$\sigma_x = \sigma_y \approx -0.56\frac{P}{A} \tag{4.11a}$$

$$\sigma_{xy} \approx 1.05\frac{P}{A} \tag{4.11b}$$

$$\sigma_I \approx 0.5\frac{P}{A} \tag{4.11c}$$

$$\sigma_{II} \approx -1.62\frac{P}{A} \tag{4.11d}$$

In equations 4.11a-d, A is the net area of the panel in the direction of loading (along the vertical diagonal). It must be noted that, this interpretation differs from the clauses of ASTM E519 / E519M -10. The latter assumes that, during the test, a uniform stress field develops ($\sigma_I / \sigma_{II} = -1$, loading direction angle 45^o) and hence suggests that shear stresses can be calculated as:

$$\sigma_{xy} = 0.707\frac{P}{A} \tag{4.12}$$

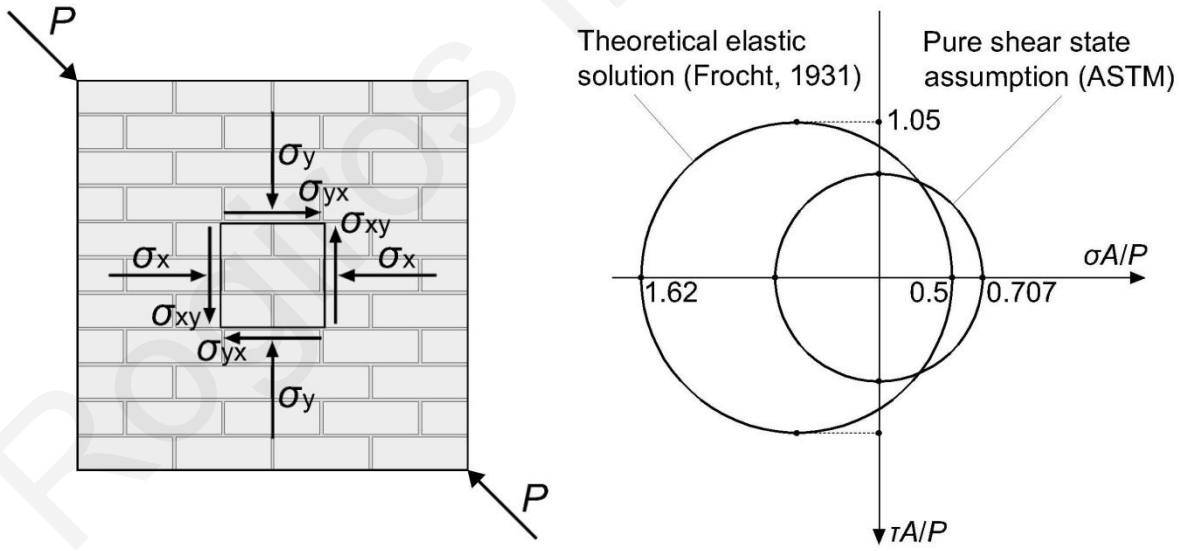

(a) **(b)**

Figure 4.16: (a) Stress state at the center of the masonry panel during the application of diagonal compression. (b) Mohr's circle representation of the stress state at the center of the specimen assuming a uniform stress field (ASTM E519 / E519M – 10) and according to the isotropic linearly elastic model of Frocht (1931).

Figure 4.16b compares these two different interpretations of the diagonal tension test in terms of the Mohr's circle. Despite the fact that formal technical guides accept the pure shear stress state hypothesis, experimental and numerical studies undertaken by Calderini et al., (2010), Brignola et al. (2008) and Yokel (1976) have shown that the elastic solution can provide more reliable results. In addition, Brignola et al. (2008) indicate that Frocht's model can be extended to the non-linear range, since the post-yield load redistribution within the masonry does not significantly affect the computed stress magnitudes.

Based on the above, shear stresses (σ_{xy}) were evaluated using equation 4.11b. Shear strains (γ_s) were calculated using the length of the specimen's diagonals ($d = b\sqrt{2}$, b = height and length of the specimen = 600 mm) and the recorded magnitudes of vertical shortening (δV) and horizontal extension (δH) as:

$$\gamma_s = \frac{(\delta V + \delta H)}{d} \tag{4.13}$$

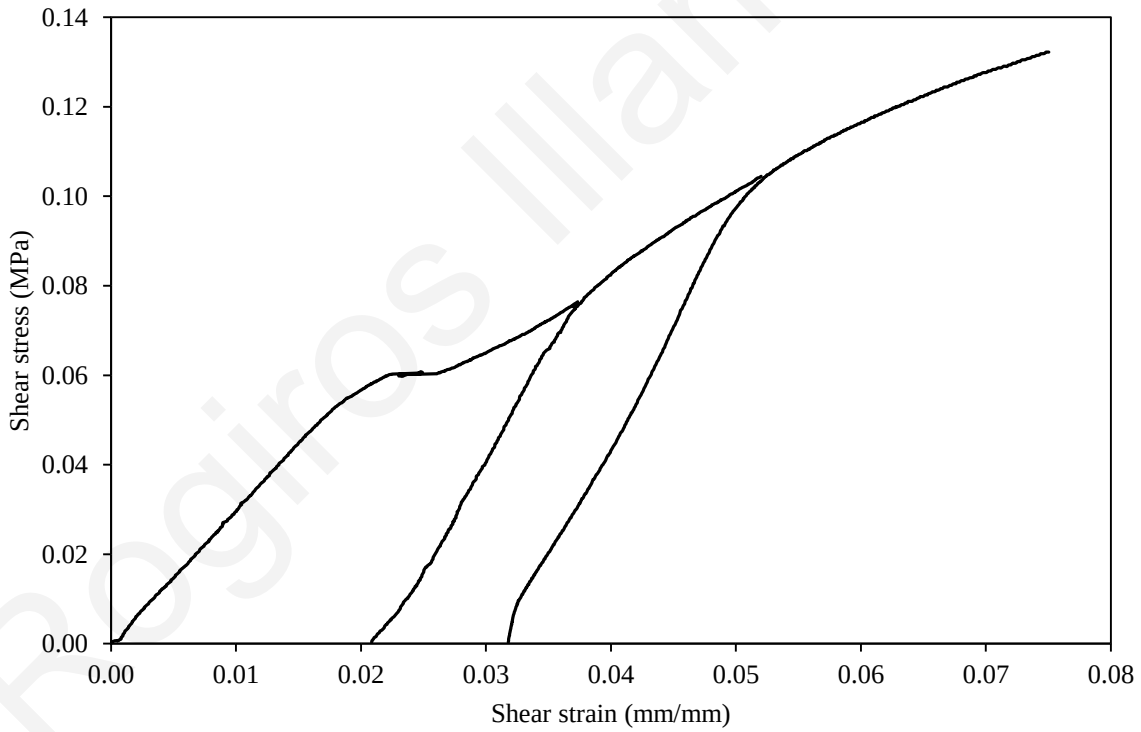

Figure 4.17: Stress-strain diagrams obtained from the implementation of three consecutive diagonal tension test cycles on a running bond adobe wallette. Data reported refer to the loading phase of each test.

The stress-strain curves derived from the three test cycles conducted are given in Figure 4.17. From the results obtained, two stages can be identified in the response of adobe

masonry to shear loading. The initial linearly ascending loading branch is followed by stiffness degradation and permanent distortion as the influence of cracking progressively becomes predominant. Yielding occurs at a shear stress of approximately 0.06 MPa. Despite a significant reduction in the resistance of the specimen to loading, this remains capable of undertaking considerable deformations. This is confirmed by the noticeable horizontal and vertical deflections measured in all test runs, which exceeded 1% of the specimen's diagonal length. Although the shear deformations induced in each test cycle surpassed 3%, no abrupt loss of bearing capacity was recorded. This is mainly because the steel frame accommodating the specimen precluded complete collapse of the masonry and provided the capability to sustain greater displacements.

The behaviour described above is not directly comparable to findings reported elsewhere (e.g. Turanli and Saritas, 2011). This is attributed to the different boundary conditions applied in analogous experimental studies. Specimens examined by other researchers do not incorporate any restrains at their perimeter. Therefore, as soon as cracking develops the masonry falls apart, leading to the conclusion of brittle failure (Turanli and Saritas, 2011). However, in actual buildings, the base of masonry components (i.e. continuous walls and piers formed by openings) is always constrained. Often, the upper and/or side edges of such elements are also interconnected with other structural members (i.e. vertical resisting elements, bracing, etc.). Hence, unlike what is commonly observed in unrestrained diagonal tension tests, shear cracking does not cause immediate collapse. In-plane lateral load tests on full-scale walls verify that unreinforced adobe masonry, despite having rather limited shear resistance, can develop certain ductility (Varum et al., 2008; Vera and Miranda, 2004). Moreover, the implementation of in-situ diagonal tension tests on traditional structures confirms the existence of a post-yield phase. In particular, Liberatore et al. (2006) examined masonry panels whose lower side and one edge were attached to adjacent walls. During these tests, significant stiffness reduction was noted after cracking, while plastic deformations from 1% to 1.5% were measured along the panels' diagonals.

4.4.3.3 Shear strength and shear modulus

Shear strength (f_{tk}) was assimilated to the maximum principal tensile stress ($\sigma_{I,\max}$) generated during the three aforementioned load cycles. The latter was computed from equation 4.11c as 0.06 MPa. This exceeds the 0.025 MPa limit set by the Peruvian adobe code (NTE E0.80) and it is higher than the 0.02 MPa shear strength evaluated by

Liberatore et al. (2006) during a test on an existing adobe structure. Nevertheless, it falls within the range of data reported by Bartolomé et al. (2009), Silveira et al. (2007), Yamin et al. (2004), Gavrilovic et al. (1998) and Tolles and Krawinkler (1990). The laboratory tests carried out by these researchers gave values for the shear capacity of adobe walls, assessed through the application of diagonal compression, between 0.05 and 0.25 MPa. Shear strength values given by Quagliarini et al. (2010) and Dowling (2006) are also in context with the result reported in this thesis, despite being produced by different experimental set-ups (direct shear testing of stack bonded masonry prisms).

The shear modulus *G* was evaluated from the experimentally obtained resistance curves. It was defined as the secant stiffness of the linear elastic branch at 30% of the maximum stress generated and it was calculated as:

$$G = \frac{\sigma_{xy,30\%} - \sigma_{xy,5\%}}{\gamma_{s,30\%} - \gamma_{s,5\%}} \tag{4.14}$$

where $\sigma_{xy,5\%}$ and $\sigma_{xy,30\%}$ are the shear stresses computed at 5% and 30% of the maximum load exerted at each test run and $\gamma_{s,5\%}$ and $\gamma_{s,30\%}$ are the corresponding shear strains.

The results deduced from successive tests on the same masonry specimen are 2.9, 4.9 and 4.5 MPa. These are significantly lower than shear moduli encountered in the literature. Yamin et al. (2004), who carried out diagonal compression tests on 1:5 scaled wall panels, obtained shear moduli in the region of 18 MPa. In-plane loading tests on full scale walls conducted by the same researchers produced values near 30 MPa. On the other hand, Tolles and Krawinkler (1990), who also performed tests on scaled masonry assemblages, found values close to 540 MPa. The much lower shear moduli reported in this thesis are most probably due to the highly deformable nature of local adobes.

Assuming that the theoretical principles of isotropic elasticity apply, the shear modulus should be related with the elastic modulus as:

$$G = \frac{E}{2(1+\nu)} \tag{4.15}$$

Considering the mean secant elastic modulus (E_{mean} = 17.4 MPa) and the Poisson ratio (ν = 0.3) obtained from stack-bonded prisms composed of the same adobes as the shear specimen, results in the region of 6.7 MPa should have been expected. On the other hand, Tomaževič (2009) indicates that, due to the inelastic, non-homogeneous and anisotropic characteristics of masonry, the actual correlation among *G* and *E* is quite different. Based

on experimental data, he suggested that G can only be as high as 6-13% of E. Although the isotropic elastic theory provides estimates closer to the experimental results hereby derived, due to considerable deviations in the computed E_{mean} (coefficient of variation = 24.2%) no safe conclusions can be made regarding any definite correlation between the two parameters.

4.5 Summary

According to observations made during the compressive strength testing of adobe masonry assemblages, the mode of failure sustained under axial loads depends on the construction pattern. Commonly encountered damage mechanisms include spalling of the units' lateral sides or opening of head-joints and tensile cracking of adobes. The behaviour of adobe masonry under compression is characterized by distinct lack of elasticity, progressive compaction, intense deformability and gradual stiffening. Experimental results indicate that, the bearing capacity of the masonry lies between 0.8 and 2.2 MPa. The values derived depend on the nature of the adobes composing the assemblage and can be affected by the specimen's age. Loading-unloading compression tests have shown different deformation rates than monotonic loading tests. An evaluation of various analytical/empirical models revealed that certain equations could be adopted for estimating the compressive strength of adobe masonry; however, better calibration and verification through further experimental research is needed.

The implementation of diagonal tension tests has confirmed that the shear resistance of adobe construction is adversely affected by inadequate bonding among its units. Failure induced by shear loading is characterized by diagonal stepped cracking passing through the masonry joints. Regarding the stress-strain response recorded, this is greatly influenced by the experimental set-up used, the boundary conditions imposed and the hypotheses made for the data analysis. The outcomes deduced in the framework of the present study indicate that, although damage initiation and propagation is rather brittle, adobe masonry can develop some level of ductility if it is restrained at the perimeter. The assessed shear strength of local adobe masonry is 0.06 MPa, whereas its shear modulus was found to be below 5 MPa.

5 NUMERICAL SIMULATION OF ADOBE MASONRY

5.1 Introduction

The current chapter reviews the main modeling strategies employed in the simulation of masonry construction. References are made to commonly used constitutive laws and to the practical applicability of each modeling method. Moreover, examples of numerical studies involving adobe structures are noted.

Using the commercially available code Abaqus/CAE, finite element analyses of adobe masonry assemblages are carried out. The computational work is based on a continuum macro-modeling approach. It focuses on the simulation of the compression and diagonal tension laboratory tests conducted in the framework of this thesis.

The adopted damaged plasticity constitutive model is described in detail. Appropriate material parameters are defined based on the experimental results of this study and relevant data from the literature. The outcomes obtained are presented and their validity is verified through comparison with the experimentally observed modes of failure and load-deformation responses.

5.2 Review of numerical modeling strategies for masonry structures

The structural behaviour of masonry construction is quite complex and its accurate numerical simulation entails significant challenges. Masonry is characterized by its intrinsic composite nature, as it incorporates units and joints that possess different mechanical properties. It also presents distinct anisotropy (i.e. response is sensitive to the orientation of loads), which may be further "enhanced" by irregularity in the construction pattern. Depending on the degree of accuracy and simplicity desired, computational analyses of masonry structures can follow different levels of sophistication. In fact, two major modeling strategies can be identified (Figure 5.1):

- **Macro-modeling** – either discrete load-bearing members (i.e. piers, spandrels) are represented by macro-elements, capable of reproducing certain failure modes (i.e. compression, bending, shear), or masonry is treated as a fictitious homogeneous medium represented by continuum finite elements;

- **Micro-modeling** – unit-mortar interfaces are considered as potential crack/slip planes, while masonry constituents are individually described (detailed micro-modeling) or represented by repeated expanded cellular units interacting at their boundaries (simplified micro-modeling).

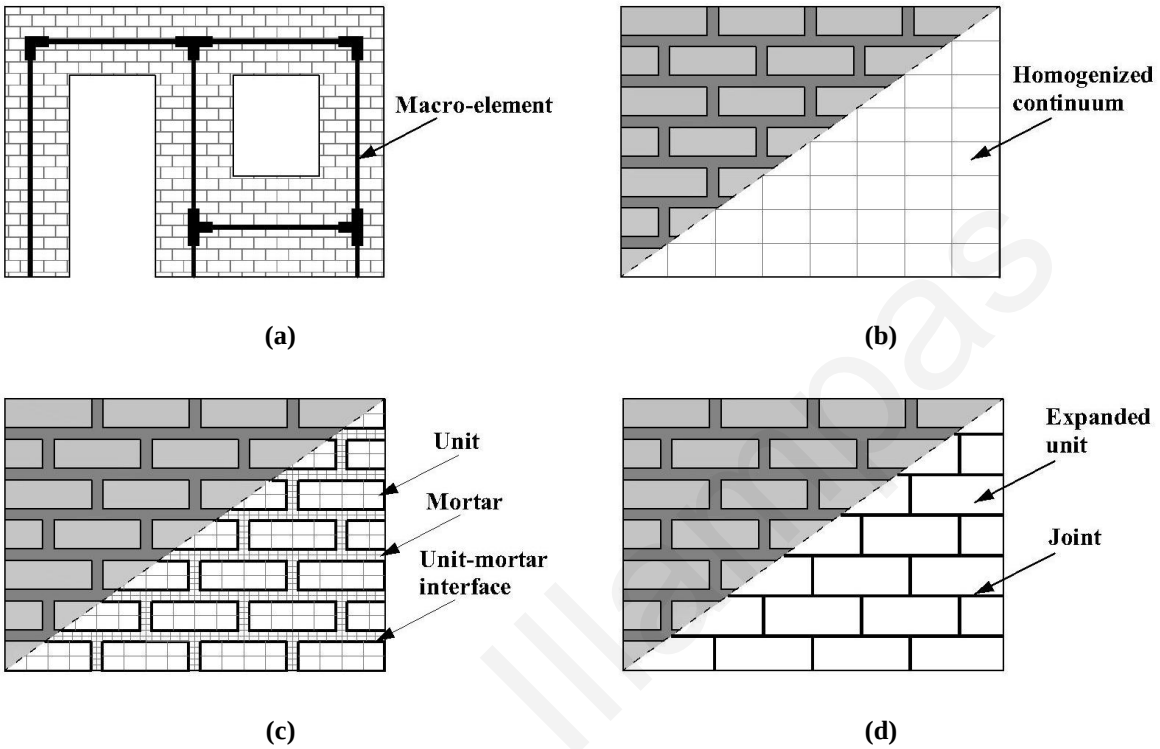

Figure 5.1: Modeling strategies for masonry structures: (a) discretization into macro-elements, (b) continuum finite element modeling, (c) detailed micro-modeling and (d) simplified micro-modeling.

Examining the extensive relevant literature, it is evident that the choice of modeling strategy is determined by the objectives of each study and the information sought. Furthermore, considerable constrains are imposed by the availability of experimental data required for the formulation of numerical models.

A brief revision of all modeling techniques, with references to their application, is given in the following paragraphs. Particular emphasis is given to the use of continuum finite element models, since this approach is adopted in this study for the simulation of adobe masonry.

5.2.1 Macro-modeling strategies

5.2.1.1 Structural component models

The simplest modeling methodology developed involves discretizing a masonry structure into an assemblage of vertical and horizontal elements. Vertical resisting elements (piers) are assumed to sustain both dead loads and seismic forces, while horizontal ones (spandrels) are considered as secondary elements, able to couple the piers in case of lateral thrusts. For modeling the structural response of individual load-bearing members, beam elements, truss elements and/or specially formulated panel macro-elements are used. The behaviour assigned to each element is such that certain in-plane masonry failure modes can be accounted for. Usually, compressive crushing, bending-rocking and shear damage (friction sliding or diagonal cracking) mechanisms are considered. Connection among intercepting members is generally represented by means of rigid offsets.

Recommendations on the application of simplified macro-models have been made by Tomaževič (1978), Brencich et al. (1998), Sabatino and Rizzano (2011) and Belmouden and Lestuzzi (2009). Experimental investigation aiming at the formulation of appropriate constitutive relations describing the response of macro-elements has been conducted by Gattesco et al. (2008). Moreover, Magenes and Calvi (1997) have undertaken laboratory tests in order to assess the reliability of the methodology. 2D equivalent frame models of masonry structures have been developed and examined by Salonikios et al. (2003), Kappos et al. (2002) and Rizzano and Sabatino (2010). Lagomarsino et al. (2002) and Galasco et al. (2004, 2006) used 3D macro-element models to evaluate the seismic capacity of historic masonry buildings. The simulation of adobe structures with purposely calibrated macro-elements has not been detected in the literature. Comparisons between the outcomes yielded by the implementation of elastic and non-linear analyses with macro-element models, continuum finite element models and discrete element models can be found in Kappos et al. (2002), Salonikios et al. (2003) and Calderini et al. (2009).

Despite the low computational cost of macro-element modeling, and the important research developments associated with its application, it is clear that this approach introduces strong simplifications into the analysis procedure. Due to the fact that it enables only the examination of predefined failure mechanisms, its accuracy relies heavily on the consistency between the adopted hypotheses and the actual structural problem (Sabatino and Rizzano, 2011).

5.2.1.2 Continuum finite element models

According to this approach, masonry is idealized as a homogeneous continuum to be discretized with a finite element mesh. The mesh does not copy the exact physical configuration of the simulated structural member. Instead, masonry units, mortar joints and unit-mortar interfaces are smeared out in the continuum. The behaviour of the fictitious homogeneous medium is associated with an average structural response that depends on the composite action of the masonry's constituents. For this purpose, appropriate relationships are established among average masonry strains and average masonry stresses. Sophisticated macro-models account for different tensile and compressive strengths and may accommodate different inelastic properties along each material axis. Continuum parameters can be estimated and validated based on laboratory tests conducted on specimens of adequate size and scale (e.g. Brignola et al., 2008; Lourenço et al., 1998; Lotfi and Shing, 1991). Alternatively, individual masonry components (i.e. brick/mortar and/or simple wallettes) may be experimentally examined and the data obtained utilized for the derivation of continuum parameters through numerical homogenization techniques (e.g. Milani et al., 2006a,b; Cluni and Gusella, 2004; Wei and Hao, 2009).

Non-linear continuum models have generally been based on smeared cracking and damaged plasticity constitutive laws. In both cases masonry damage is treated as a smeared property spreading over the volume of the elements. In smeared cracking models, fracture is initiated when the maximum principal stress in a material point exceeds the assigned yielding stress. Crack propagation is mainly controlled by the shape of the tensile softening diagram. Smeared crack models can either follow a decomposed- (Rots et al., 1985) or a total-strain (Lin and Scordelis, 1975) approach. In the former, total strains are defined as the sum of an elastic material strain plus a crack (inelastic) strain. Crack strains are addressed with the plasticity theory through the definition of suitable yield functions. In total-strain models, material behaviour is described via stress-total strain relations. Smeared crack models can be further classified into single-fixed (Suidan and Schnobrich, 1973), multidirectional-fixed (Cruz et al., 2006) and rotating crack (Gupta and Akbar, 1984) formulations. Single-fixed crack models assume orthogonal crack orientation. Hence, crack direction is fixed at the moment of crack initiation. In multidirectional-fixed models, contributions of a discrete set of cracks at different directions (e.g. 30^o, 60^o, 90^o) are evaluated at a sampling point of each element. On the other hand, in rotating crack formulations the direction of a (single) crack changes constantly, according to the variation of the principal strain's direction.

Damaged plasticity models (Lee and Fenves, 1988; Lubliner et al., 1989) consider two failure mechanisms; tensile cracking and compressive crushing. Cracking and crushing damage states are controlled by hardening variables linked with equivalent plastic strains in tension and compression, respectively. The reduction of the elastic modulus caused by material damage is catered for by means of scalar stiffness degradation parameters.

Constitutive laws used in continuum macro-models are either intended for concrete-like quasi-brittle materials, or have been developed specifically for masonry. Both simple isotropic damage criteria and more complex anisotropic ones have been adopted. The smeared crack concept based upon strain decomposition, which was first applied on concrete structures, was extended to the analysis of masonry by Rots (1991) and Lotfi and Shing (1991). Cervera et al. (2010) proposed a modification of the smeared crack representation by the introduction of a crack-tracking algorithm, capable of reproducing the localized damage patterns commonly encountered in masonry structures. The potential of this approach to accurately simulate masonry has been further enhanced through the development of orthotropic damage criteria by Pelà et al. (2013). Analogous research on masonry-orientated orthotropic damage models has been conducted by Berto et al. (2002). Vratsanou (1992) revised a hypoelastic concrete model (Darwin and Pecknold, 1974) that uses the principle of equivalent uniaxial strains, so that it can be applied in the dynamic analysis of masonry buildings. Lourenço (2000) developed an anisotropic softening model for masonry plates and shells in which the material admissible field is bounded by a Hill-type yield criterion for compression and a Rankine-type yield criterion for tension. Syrmakezis and Asteris (2001) formulated a yield surface for masonry under biaxial stress state that was used for undertaking plane-stress non-linear analyses (Asteris and Tzamtzis, 2003). Papa (1996) proposed a unilateral damage model, based on the introduction of internal damage variables related to simple tension, uniaxial compression and shear stresses. Of similar format is the smeared crack model developed by Karapitta et al. (2011). The latter uses total-strain-based constitutive relations that represent the hysteretic behaviour in each failure mode (compression, tension, shear). Wawrzynek and Cińcio (2005) have suggested the adaptation of a damaged plasticity model incorporating an extension of the Drucker-Prager criterion with isotropic hardening rules. A comparison among the numerical results obtained from the application of various constitutive models can be found in Genna et al. (1998).

The level of refinement implied by the use of continuum macro-models introduces a considerable number of degrees of freedom, thus increasing computational effort.

However, the procedure is not as demanding as detailed micro-modeling, since it does not require the explicit simulation of all masonry components. In addition, the available computational resources nowadays make large finite element meshes practically manageable. This has led continuum macro-modeling become, probably, the most widely adopted approach, with extensive applications in research-related and practice-orientated analyses of masonry (Roca et al., 2010).

The broad variety of structures examined through continuum modeling also includes adobe masonry construction. Che et al. (2010) prepared full 3D models of adobe-wood buildings that were subjected to elastic time domain analysis in order to examine their seismic response. Linear dynamic analyses by response spectra have been conducted by Gomes et al. (2011) using 3D models of unreinforced and reinforced adobe buildings. Tarque et al. (2010a, 2012a, b) performed non-linear static and dynamic analyses on continuum models composed of shell elements. These authors focused on simulating the behaviour of wall configurations and model buildings recorded during laboratory tests. The material input parameters used were calibrated by matching numerical-experimental of results. Both total-strain smeared cracking models with orthotropic yield criteria and damaged plasticity constitutive laws based on isotropic damage hypotheses were considered.

5.2.2 Micro-modeling strategies

Considering the inhomogeneous and anisotropic nature of masonry construction, the explicit numerical simulation of its constituents seems a logical step towards a rigorous analysis tool. In terms of modeling, either a detailed or a simplified approach may be adopted. In detailed micro-modeling, the different components of masonry, namely the units, the mortar and the unit-mortar interface, are distinctly described. The units and mortar are represented using continuum finite elements and may copy the exact layout of the member examined. Unit-mortar interfaces are modeled using discontinuous elements. In the simplified approach, masonry is assumed to be composed by an assembly of expanded cellular units bonded by potential fracture/slip lines at the joints. The expanded cells are used to model both the masonry units and mortar, while the behaviour of the joints and unit-mortar interfaces is lumped to discontinuous elements.

The concept of fracture mechanics, based upon discrete numerical modeling, was introduced in the field of masonry analysis by Page (1978). This was followed by significant efforts to develop constitutive laws for interface elements, capable of capturing

all the failure mechanisms of masonry (i.e. cracking/sliding of joints, cracking of units and compressive crushing). Lourenço and Rots (1997) worked on the theoretical formulation and numerical implementation of a multi-surface interface model that accounts for softening plasticity in tension, shear and compression, as well as interactions among damage modes. The model was also extended and validated to predict non-linear cyclic behaviour (Oliveira and Lourenço, 2004). Lotfi and Shing (1994) developed a dilatant constitutive model capable of simulating the initiation and propagation of interface fracture under combined normal and shear stresses, in both tension-shear and compression-shear regions. Giambanco et al. (2001) proposed interface laws in the framework of elasto-plasticity for non-standard materials, aiming to reproduce the softening response of joints subjected to shear and tension tractions. Tzamtzis and Asteris (2004a,b) formulated and used a special interface element that can simulate relative slip, debonding and cyclic closing-opening of joints. Gambarotta and Lagomarsino (1997) derived a damage model for joints that considers both mortar damage and decohesion at the unit-mortar interface. The model predicts damage evolution through the adoption of damage variables and can simulate the hysteretic response of joints under cyclic shearing strains.

According to Lourenço (2002), micro-modeling strategies are suitable for small structures in which strongly heterogeneous states of stress and strain are generated. Their efficient application demands extensive experimental investigation for the derivation of the material and interface mechanical properties. Furthermore, the higher computational effort required limits the applications of micro-modeling strategies to academic research and to small models for localized analysis. In fact, detailed micro-models that are computationally burdensome have been mainly used for the purpose of numerical homogenization (Zucchini and Lourenço, 2002, 2009) and for the simulation of relatively small-scale laboratory tests (Šejnoha et al., 2008; Shieh-Beygi and Pietruszczak, 2008).

Simplified discontinuum applications have been broader and have been carried out using finite element (Lourenço, 1994), discrete element (Psycharis et al., 2000; Lemos, 2007) and limit analysis (Orduña and Lourenço, 2001) methods. It is interesting to note that simplified micro-modeling has also been used in the analysis of adobe masonry structures. Tarque et al. (2010a) performed static non-linear simulations on a complete 3D model of an adobe wall configuration subjected to lateral loading. In this study, adobe blocks were assumed to be elastic isotropic, while non-linear behaviour was assigned to the joints via a combined crushing-shearing-cracking interface damage model. Based on the theory of the finite element method and the principle of discontinuities, Cao and Watanabe (2004)

developed 3D models of a single-storey adobe building. Cao and Watanabe used non-linear anisotropic constitutive laws for the adobe bricks and modeled joints, with a specially formulated viscoelastic joint element, which can simulate interface opening and sliding. Numerical models were analyzed under dynamic excitation using scaled seismic accelograms. Dynamic analyses of adobe structures have also been conducted by Furukawa et al. (2009) and Furukawa and Ohta (2009). These researchers adopted the discrete element method, modeling masonry as an assemblage of rigid blocks connected by zero-thickness non-linear interfaces that may sustain tensile, shear or compressive damage. Aiming to examine the seismic capacity of single- and two-storey adobe walls, Morales and Delgado (1992) prepared 2D models that were analyzed under the imposition of reversing horizontal accelerations. The models examined were composed of several discrete circular elements. These were connected with springs and dashponts that acted as possible fracture points.

5.3 Finite Element modeling strategies adopted

5.3.1 Constitutive model for the simulation of adobe masonry

For simulating the behaviour of adobe masonry, the Abaqus/CAE (Simulia Corp., 2009) concrete damaged plasticity model was adopted. This model was primarily selected because it has already been used by Tarque et al. (2010a, 2012a, b) for the analysis of adobe construction producing encouraging results. The choice of the model was also based on its capability to simulate materials subjected to arbitrary loading conditions, including cyclic/dynamic loading. Although the physical problems examined in this thesis do not involve the imposition of reversing forces, it is anticipated that the calibration of the specific model using experimentally derived material data will encourage further research that will extend its applicability to the dynamic analysis of adobe structures.

The adopted model is based on the work of Lubliner et al. (1989) and Lee and Fenves (1988). It is primarily intended to macroscopically capture the response of concrete structures and quasi-brittle materials (i.e. rocks, ceramics) subjected to cyclic and/or dynamic loading. The modes of failure assumed are tensile cracking and compressive crushing. These are associated with the irreversible damage mechanisms sustained by concrete-like materials under fairly low confining pressures (less than four or five times the ultimate compressive stress).

Inelastic behaviour is represented using concepts of isotropic damaged elasticity, in combination with isotropic tensile and compressive plasticity. The yield surface is controlled by means of hardening variables that are linked to cracking and crushing strains. Stiffness degradation is considered via uniaxial damage variables. In addition, the model allows for the simulation of stiffness recovery effects during cyclic load reversals, through the definition of appropriate scalar factors.

5.3.1.1 Strain rate decomposition and hardening variables

The constitutive model adopts the incremental theory of plasticity, decomposing the total strain rate ($\dot{\varepsilon}$) into an elastic ($\dot{\varepsilon}^{el}$) and a plastic ($\dot{\varepsilon}^{pl}$) part, as per equation 5.1.

$$\dot{\varepsilon} = \dot{\varepsilon}^{el} + \dot{\varepsilon}^{pl} \tag{5.1}$$

The plastic strain represents all irreversible deformations, including those caused by micro-cracks, creep, thermal loads etc.

Non-linear behaviour is characterized by two hardening variables, $\tilde{\varepsilon}_t^{pl}$ and $\tilde{\varepsilon}_c^{pl}$, that determine material yielding and elastic modulus reduction. The variables refer to equivalent plastic strains in tension and compression and their evolution is given by:

$$\dot{\tilde{\varepsilon}}^{pl} = \boldsymbol{h}(\bar{\boldsymbol{\sigma}}, \tilde{\varepsilon}^{pl}) \cdot \dot{\varepsilon}^{pl} \tag{5.2}$$

$$\tilde{\varepsilon}_t^{pl} = \int_0^t \dot{\tilde{\varepsilon}}_t^{pl} dt \tag{5.3}$$

$$\tilde{\varepsilon}_c^{pl} = \int_0^t \dot{\tilde{\varepsilon}}_c^{pl} dt \tag{5.4}$$

where $\bar{\boldsymbol{\sigma}}$ is the effective stress.

5.3.1.2 Stress-strain response

Under uniaxial tension, the material is presumed to be linearly elastic, until failure stress (σ_{t0}) is reached (Figure 5.2a). Failure stress corresponds to the onset of micro-cracking in the medium. Typically, beyond failure stress, crack formation is represented in a macroscopic sense with a softening stress-strain response, which induces strain localization. Under uniaxial compression, material linearity is assumed up to the initial yield stress (σ_{c0}). Inelastic compressive response is characterized by stress hardening until

the ultimate strength (σ_{cu}) is attained (Figure 5.2b). This is generally followed by stress softening.

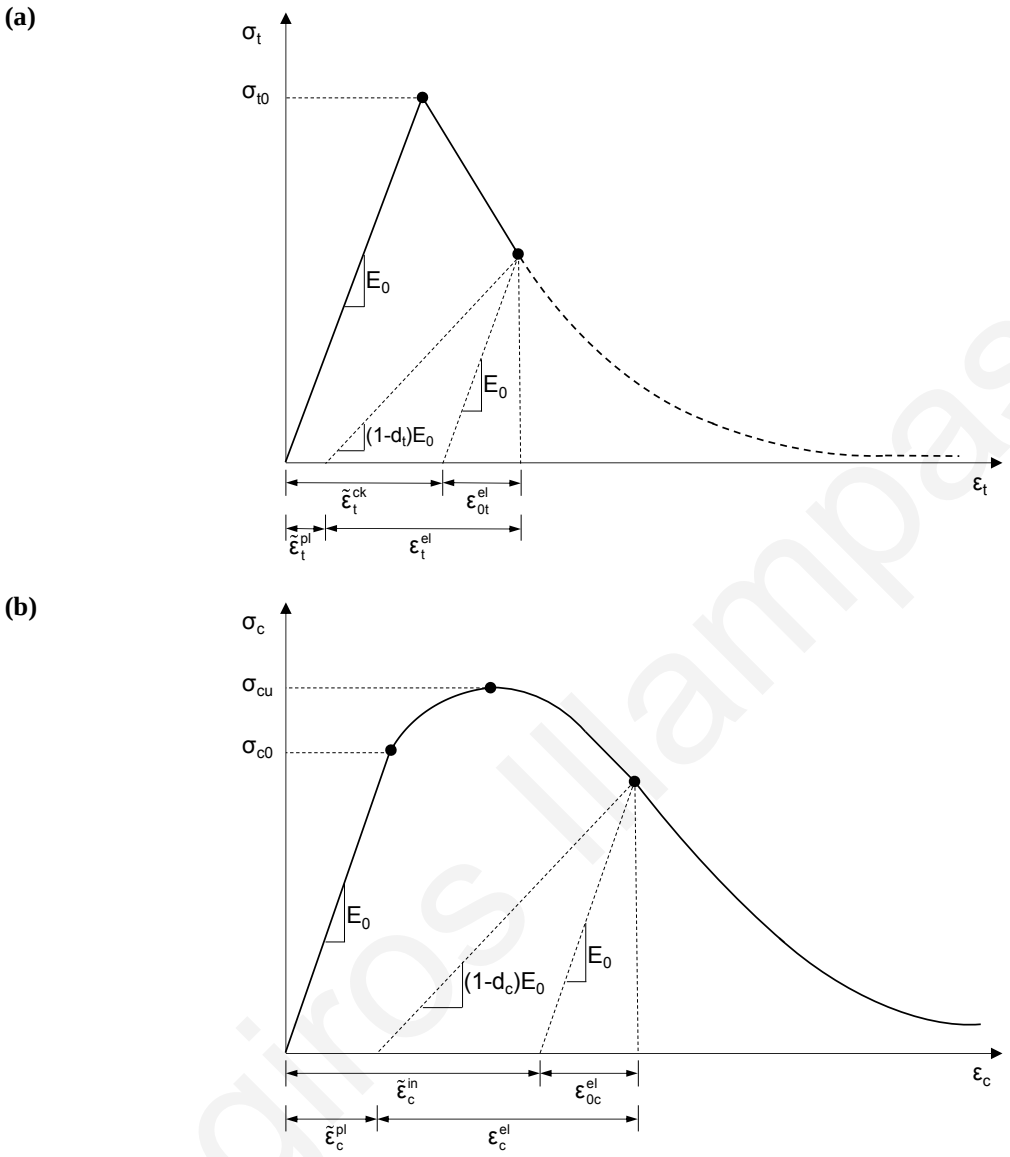

Figure 5.2: Typical stress-strain response in uniaxial tension (a) and compression (b) assigned to materials modeled with the concrete damaged plasticity constitutive law (Source: Simulia Corp., 2009).

When unloading of the material takes place in the softening regime, scalar damage variables (d_t and d_c) that account for elastic stiffness reduction are introduced. Tension (d_t) and compression (d_c) damage variables are independent and can take values from 0 (undamaged material) to 1 (total loss of strength). They are computed as functions of plastic strains (optionally they can also be linked to temperature magnitudes and/or other field variables).

5.3.1.3 Uniaxial and multiaxial behaviour

According to the above, if E_0 is the initial (undamaged) elastic stiffness of the material, the stress-strain relations formulated in uniaxial tension and compression are, respectively:

$$\sigma_t = (1-d_t)E_0(\varepsilon_t - \tilde{\varepsilon}_t^{pl}) \tag{5.5}$$

$$\sigma_c = (1-d_c)E_0(\varepsilon_c - \tilde{\varepsilon}_c^{pl}) \tag{5.6}$$

The equivalent plastic stain rates in uniaxial conditions are given as $\dot{\tilde{\varepsilon}}_t^{pl} = \dot{\varepsilon}_{11}^{pl}$ for tension and $\dot{\tilde{\varepsilon}}_c^{pl} = -\dot{\varepsilon}_{11}^{pl}$ for compression.

For determining the size of the yield (or failure) surface, the "effective" tensile ($\bar{\sigma}_t$) and compressive ($\bar{\sigma}_c$) cohesion stresses are derived by:

$$\bar{\sigma}_t = \frac{\sigma_t}{(1-d_t)} = E_0(\varepsilon_t - \tilde{\varepsilon}_t^{pl}) \tag{5.7}$$

$$\bar{\sigma}_c = \frac{\sigma_c}{(1-d_c)} = E_0(\varepsilon_c - \tilde{\varepsilon}_c^{pl}) \tag{5.8}$$

During the imposition of cyclic loads, the damaged material elastic modulus is given by:

$$E = (1-d)E_0 \tag{5.9}$$

Equation 5.9 holds both in the tensile ($\sigma_{11} > 0$) and the compressive ($\sigma_{11} < 0$) sides of the cycle. The stiffness degradation variable (d) is associated with the stress state, while the two uniaxial damage variables (d_t and d_c) are based on the following assumption:

$$(1-d) = (1-s_t d_c)(1-s_c d_t) \tag{5.10}$$

In equation 5.10, s_t and s_c are functions of the stress state that represents the stiffness recovery for reversing loads. They are defined as:

$$\begin{aligned} s_t &= 1 - w_t r^*(\sigma_{11}) \qquad \text{and } 0 \le w_t \le 1 \\ s_c &= 1 - w_c(1 - r^*(\sigma_{11})) \qquad \text{and } 0 \le w_c \le 1 \end{aligned} \tag{5.11}$$

where w_t and w_c are weight factors that control tension and compression stiffness recovery upon stress reversal. $r^*(\sigma_{11})$ is a function which depends upon the tensile and compressive sides of the load cycle. It is computed as:

$$r^*(\sigma_{11}) = H(\sigma_{11}) = \begin{cases} 1 & \text{if } \sigma_{11} > 0 \\ 0 & \text{if } \sigma_{11} < 0 \end{cases} \tag{5.12}$$

Figure 5.3 shows the effect of the recovery factors in a complete uniaxial load cycle (tension-compression-tension). Compressive stiffness is recovered upon crack closure when the load changes from tension to compression. On the other hand, once crushing damage is generated, tensile stiffness is not recoverable as the load changes from compression to tension. This behaviour corresponds to the limit values $w_t = 0$ and $w_c = 1$. Intermediate values of the aforementioned factors result in partial recovery of the material's stiffness.

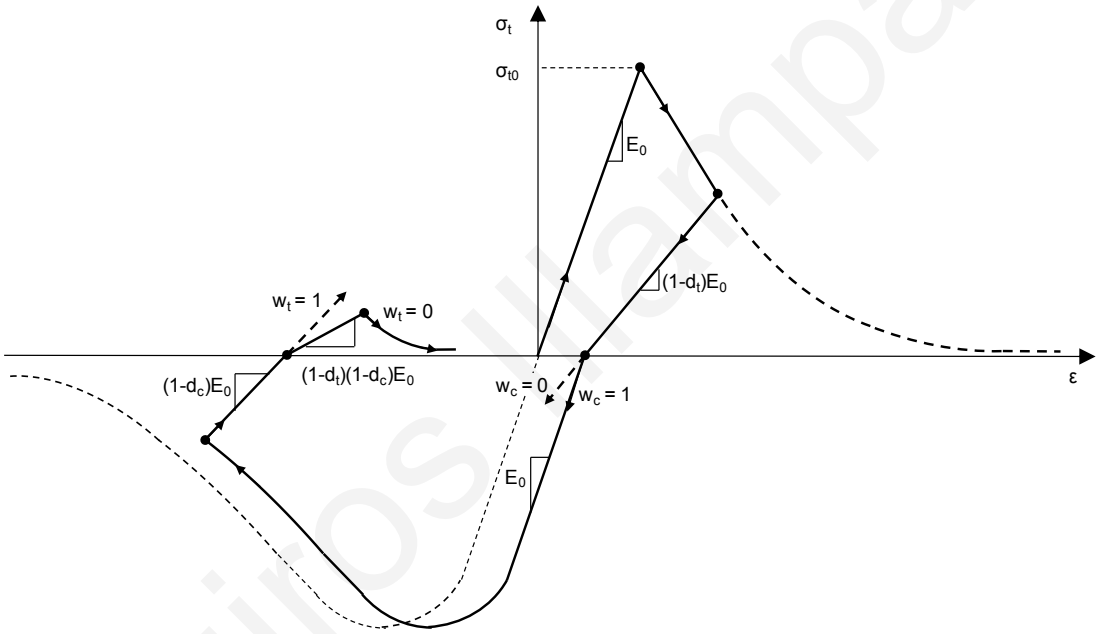

Figure 5.3: Uniaxial load cycle (tension-compression-tension) assuming default values for the stiffness recovery values w_t = 0 and w_c = 1 (Source: Simulia Corp., 2009).

In the general three-dimensional multiaxial condition, the scalar damage elasticity equation is revised to:

$$\boldsymbol{\sigma} = (1-d)\mathbf{D}_0^{el} : (\varepsilon - \varepsilon^{pl}) \tag{5.13}$$

where $\mathbf{D}_0^{el}$ refers to the initial (undamaged) elasticity matrix. The effective stress tensor ($\bar{\boldsymbol{\sigma}}$) used in the definition of the material's admissible field is estimated as:

$$\bar{\boldsymbol{\sigma}} = \mathbf{D}_0^{el} : (\varepsilon - \varepsilon^{pl}) \tag{5.14}$$

For the multiaxial case, the evaluation of the scalar stiffness degradation variable (***d***) is achieved by replacing the unit step function $r^*(\sigma_{11})$ with a stress weight factor $r(\hat{\boldsymbol{\sigma}})$ that accounts for all three principal stress components $\hat{\sigma}_i$ (i = 1, 2, 3) according to the expression:

$$r(\hat{\boldsymbol{\sigma}}) = \frac{\sum_{i=1}^{3} \langle \hat{\sigma}_i \rangle}{\sum_{i=1}^{3} |\hat{\sigma}_i|} \qquad \text{and } 0 \le r(\hat{\boldsymbol{\sigma}}) \le 1 \tag{5.15}$$

In equation 5.15 the Macauley bracket $\langle . \rangle$ is defined by $\langle x \rangle = \frac{1}{2}(|x| + x)$.

5.3.1.4 Plastic flow and yield function

The damaged plasticity constitutive model adopts a flow potential function (G) that is based on the theory of non-associated potential plastic flow. It also incorporates a yield function (F) that accounts for different evolution of strength under tension and compression (Figure 5.4). The latter has been formulated in accordance with the propositions of Lubliner et al. (1989) and the modifications made by Lee and Fenves (1988).

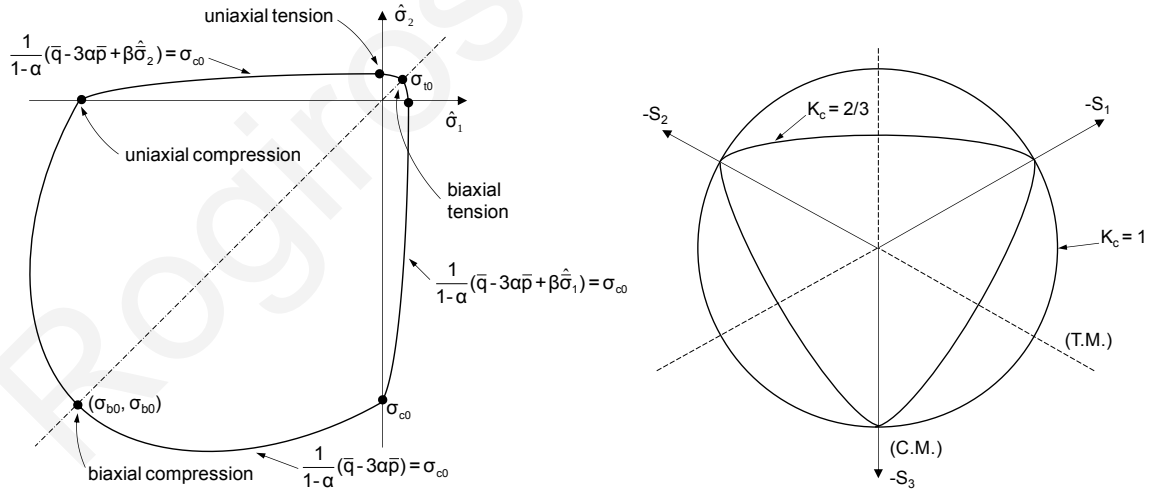

Figure 5.4: (a) Representation of the yield surface in the plane stress condition and (b) yield surfaces in the deviatoric plane, corresponding to different values of parameter K_c (Source: Simulia Corp., 2009).

Both the plastic flow potential function and the yield surface make use of two stress invariants of the effective stress tensor: the hydrostatic pressure stress ($\bar{p}$) and the von Mises equivalent effective stress ($\bar{q}$). These are defined as:

$$\bar{p} = -\frac{1}{3}\text{trace}(\bar{\boldsymbol{\sigma}}) \tag{5.16}$$

$$\bar{q} = \sqrt{\frac{3}{2}(\bar{\mathbf{S}} : \bar{\mathbf{S}})} \tag{5.17}$$

In the above, $\bar{\mathbf{S}}$ represents the deviatoric part of the effective stress tensor ($\bar{\boldsymbol{\sigma}}$) and is computed by:

$$\bar{\mathbf{S}} = \bar{\boldsymbol{\sigma}} + \bar{p}\mathbf{I} \tag{5.18}$$

The flow potential is continuous and smooth, resembling the Drucker-Prager hyperbolic function:

$$G = \sqrt{(e\sigma_{t0}\tan\psi)^2 + \bar{q}^2} - \bar{p}\tan\psi \tag{5.19}$$

Parameter *e* is referred to as eccentricity and defines the rate at which the function approaches the asymptote (i.e. the flow potential tends to a straight line as the eccentricity tends to zero). Stress σ_{t0} is the uniaxial tensile strength and ψ is the dilation angle measured in the *p-q* plane at high confining pressures.

As previously noted, the yield function is associated with the two hardening variables, $\tilde{\varepsilon}_t^{pl}$ and $\tilde{\varepsilon}_c^{pl}$. In terms of effective stresses, its form is the following:

$$F = \frac{1}{1-a}(\bar{q} - 3a\bar{p} + \beta(\tilde{\varepsilon}^{pl})\langle\hat{\bar{\sigma}}_{\max}\rangle - \gamma\langle-\hat{\bar{\sigma}}_{\max}\rangle) - \bar{\sigma}_c(\tilde{\varepsilon}_c^{pl}) = 0 \tag{5.20}$$

Dimensionless material constants *a*, β and γ are given by:

$$a = \frac{(\sigma_{b0}/\sigma_{c0}) - 1}{2(\sigma_{b0}/\sigma_{c0}) - 1}; \quad 0 \le a \le 0.5 \tag{5.21}$$

$$\beta = \frac{\bar{\sigma}_c(\tilde{\varepsilon}_c^{pl})}{\bar{\sigma}_t(\tilde{\varepsilon}_t^{pl})}(1-a) - (1+a) \tag{5.22}$$

$$\gamma = \frac{3(1-K_c)}{2K_c - 1} \tag{5.23}$$

Moreover, $\hat{\bar{\sigma}}_{\max}$ is the algebraically maximum principal effective stress, while $\bar{\sigma}_t$ and $\bar{\sigma}_c$ are the effective tension and compressive cohesion stresses of equations 5.7 and 5.8. σ_{b0} stands for the initial equibiaxial compressive yield stress and σ_{c0} is the initial uniaxial compressive yield stress. K_c takes values between 0.5 and 1 (Figure 5.4b). It represents the ratio of the second stress invariant on the tensile meridian ($q_{(TM)}$) to the equivalent invariant on the compressive meridian ($q_{(CM)}$) at initial yield for any given value of pressure invariant p, such that the maximum principal stress is negative ($\hat{\sigma}_{\max} < 0$).

5.3.1.5 Input parameters

The model presumes that the elastic behaviour of the material is isotropic and linear. It requires the determination of the initial (undamaged) elastic modulus and Poisson ratio. Compressive stress data can be expressed as a tabular function of inelastic (or crushing) strain ($\sigma_c = \sigma_c(\tilde{\varepsilon}_c^{in})$). Inelastic strain refers to the total strain minus the strain at initial yielding. Post-yield behaviour under direct tensile loading is modeled in the context of a tension softening theory. Tension softening can be specified by means of a stress-cracking strain relation ($\sigma_t = \sigma_t(\tilde{\varepsilon}_t^{ck})$), or by applying a fracture energy criterion. The definition of the cracking strain is analogous to that of the crushing stain.

In the case of unreinforced masonry, where cracking failure is not stabilized by evenly distributed elastic elements (i.e. rebar reinforcements), the use of stress-strain relations in tension may introduce mesh sensitivity in the results. This is because finite element predictions do not converge to a unique solution, since refined meshes simply lead to narrower crack bands. As an alternative, it is recommended by Simulia Corp. (2009) to adopt the fracture energy proposal of Hillerborg et al. (1976). According to this approach, the energy required to open a unit area of crack (G_f) is defined as a material parameter using brittle fracture concepts. Stress may then be expressed as a function of crack-opening displacement ($\sigma_t = \sigma_t(u_t^{ck})$), provided that a characteristic crack length is determined. The characteristic crack length is associated with an integration point and depends on the element geometry and formulation.

Information concerning the unloading response can be specified in terms of compressive or tensile damage curves as: $d_c = d_c(\tilde{\varepsilon}_c^{in})$ and $d_t = d_t(\tilde{\varepsilon}_t^{ck})$ or $d_t = d_t(u_t^{ck})$. The model can

compute plastic strains ($\tilde{\varepsilon}_c^{pl}, \tilde{\varepsilon}_t^{pl}$), based on the related damage parameters and the corresponding crushing ($\tilde{\varepsilon}_c^{in}$) and cracking ($\tilde{\varepsilon}_t^{ck}$) strains. In the absence of damage parameters, it is assumed that: $\tilde{\varepsilon}_c^{pl} = \tilde{\varepsilon}_c^{in}$ and $\tilde{\varepsilon}_t^{pl} = \tilde{\varepsilon}_t^{ck}$.

To avoid numerical instability problems, the finite element code assumes that the post-failure residual bearing capacity is at least 1% of the initial yielding stress. It is also recommended to use a value for the eccentricity e = 0.1 (Simulia Corp., 2009), which implies that the simulated medium has almost the same dilation angle over a wide range of confining pressures. Furthermore, default values for parameter K_c = 2/3 and for the ratio of initial equibiaxial compressive yield stress to initial uniaxial compressive yield stress, $\sigma_{b0} / \sigma_{c0}$ = 1.16 are recommended (Simulia Corp., 2009). For materials exhibiting strong softening behaviour and significant stiffness degradation, visco-plastic regularization may be applied, in order to overcome possible convergence difficulties. For this purpose, a non-zero viscosity parameter should be defined.

5.3.2 Mechanical behaviour assigned to the homogenized continuum

5.3.2.1 Elastic properties

The density of adobe masonry was set as 1300 kg/m^3. It was estimated following simple gravimetric measurements on adobe brick samples and earth mortar specimens. The Poisson ratio used in all analyses was 0.3. This was the ratio between the transversal and axial deformations recorded during the implementation of a single uniaxial compression test on a stack-bonded prism (see section 4.3.3.4).

Different Young's moduli (E) were used for the simulation of loading-unloading compression and monotonic loading (i.e. diagonal tension, lateral loading on adobe scaled building) tests. In the former case, the final unload-reload modulus after six test cycles of the particular specimen modeled (i.e. SB13(DC)) was adopted ($E = E_{ur}$ = 90 MPa). It should be noted that, if no damage parameters are defined, the constitutive law assumes that, upon load removal and reapplication, the medium exhibits a stress-strain behaviour based on the initial undamaged modulus. However, progressive densification and stiffness augmentation cannot be accounted for by the damaged plasticity theory.

For the analysis of masonry members under monotonously increasing forces, stress-strain data were generated using the compression model defined in section 3.4.4 for individual

adobe bricks (equation 3.7). Despite the fact that the adopted function does not account for the extended consolidation phase noted in certain specimens, it provides a reasonable approximation to the compressive hardening response observed in the majority of cases (see Annex 2). Furthermore, it enables the definition of post-peak softening.

Compressive strength in monotonic loading simulations was assumed to be equal to the average bearing capacity of all stack-bonded prisms tested (f_w = 1.2 MPa), since these specimens were composed of identical materials as the simulated masonries (see section 4.3). Strain at peak stress was also defined from the average corresponding experimental value recorded for stack-bonded prisms, ε_{cu} = 0.1 mm/mm. The onset of material non-linearity was assumed at 5% of its maximum bearing capacity. This is close to the lowest stress magnitude where inelastic deformation of masonry specimens was noted during loading-unloading compression tests. Young's modulus was estimated from the assigned compressive stress-strain response as a secant modulus (E_{sec}) up to the yielding point. By adopting the compression model of equation 3.7 and for 1.2 MPa compressive strength, 0.1 mm/mm strain at peak stress and yielding strain at 5% of the maximum bearing capacity, the secant modulus derived following the stress-strain diagram of Figure 3.11 is $E = E_{sec}$ = 18 MPa. The computed value is very close to the average 17.4 MPa secant modulus obtained from laboratory tests (see section 4.3.3.4).

5.3.2.2 Plasticity Parameters

For the rate at which the hyperbolic flow potential approaches its asymptote, the recommended value of e = 0.1 was adopted. The default ratio $\sigma_{b0} / \sigma_{c0}$ = 1.16 was used for defining the relation among the initial equibiaxial compressive yield stress to the initial uniaxial compressive yield stress. For parameter K_c, the 0.8 value reported in the Simulia Corp. (2009) manual for modeling soils with a Drucker-Prager yield function was adopted, instead of the 2/3 value normally used for concrete. Visco-plastic regularization of the constitutive equations was not performed in any of the analyses implemented in this study. Therefore, the viscosity parameter was always set equal to zero.

Regarding the dilation angle, a very low value of $\psi = 1^o$ was assumed. This is because, according to Houlsby (1991), clayey soils (such as those composing adobe materials) are characterized by limited dilation, typically $0^o < \psi < 10^o$ (regardless of over-consolidated layers). It is worth noting that a dilation angle of $\psi = 1^o$ has also been used by Tarque et al.

(2012a) for simulating the non-linear response of adobe masonry structures with the damaged plasticity theory.

5.3.2.3 Response to compression

For the simulation of a loading-unloading compression test, the experimental data obtained for the specific specimen studied (SB13(DC)) were used in the definition of the medium's compressive behaviour. Since the average unload-reload modulus adopted in this type of analysis was greater than the primary deformation modulus, a very low compressive yielding stress (≈ 1% of the maximum allowable compressive stress) was assigned to avoid overestimation of initial stresses upon increasing axial straining (Figure 5.5). The maximum allowable compressive stress was set equal to the highest stress magnitude recorded during the simulated laboratory test: f_w = 1.48 MPa. The post-yield deformation response was associated with the behaviour under continuously ascending loads and was defined based on experimentally derived stress-strain data. In this way, the tendency of adobe masonry to follow different deformation rates when the exerted pressure is constantly increasing and when load is removed and reapplied could be adequately represented.

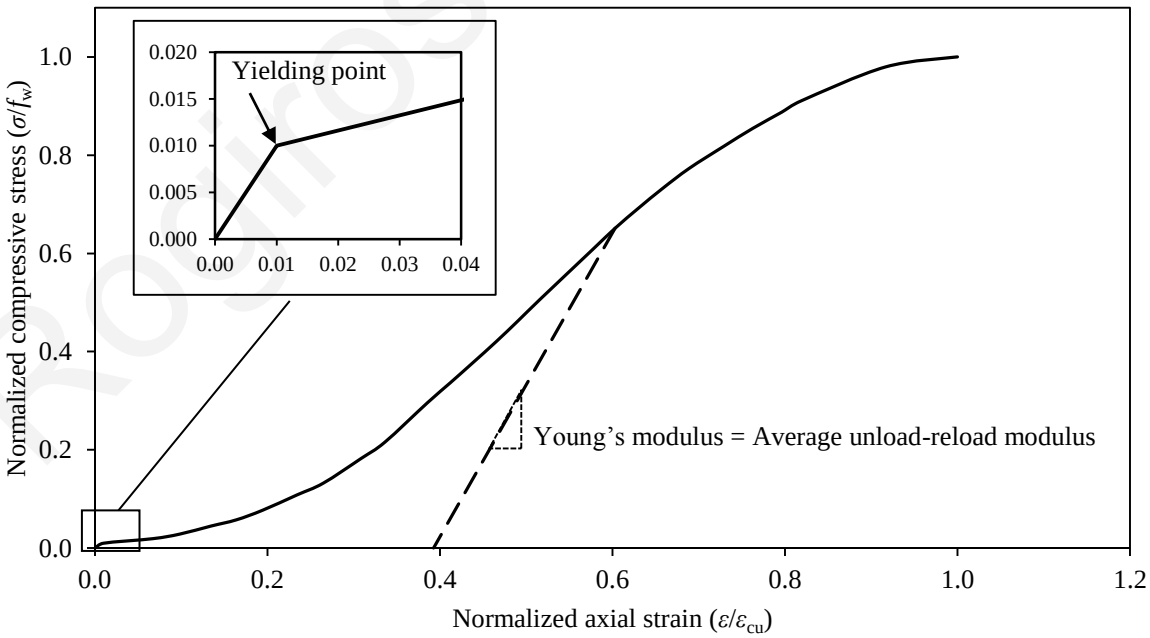

Figure 5.5: Normalized stress-strain diagram showing the compressive response assigned to the homogenized continuum for the simulation of loading-unloading tests. The Young's modulus is assumed to be equal to the average unload-reload modulus, while onset of material non-linearity is set at stress levels not exceeding 1% of the compressive strength.

As already noted in section 5.3.2.1, in monotonic loading analysis scenarios, the response of the medium to compression was approximated using the model proposed in section 3.4.4. Hence, for the wallette subjected to diagonal tension and the scaled building examined in section 6, the same stress-strain data were generated using equation 3.7 and assuming a maximum allowable stress of 1.2 MPa, a 0.1 mm/mm strain at peak stress and a yielding stress corresponding to 5% of the compressive strength.

5.3.2.4 Response to tension

It was assumed that the medium responds elastically to tension, until the maximum allowable stress is reached. From this point onwards, cracking is initiated and the behaviour is governed by softening.

When simulating a stack-bonded prism subjected to compressive loading-unloading, the medium's tensile behaviour was assimilated to that of individual adobe bricks. The imposition of axial compressive loads induces lateral strains which, in turn, generate the development of tensile stresses parallel to the bedding plane. The particular specimen examined did not incorporate head joints that could have failed under this stress state. Instead, tensile stresses led to circumferential cracking and exfoliation of the adobes' lateral sides (see section 4.3.3.1).

Uniaxial tensile strength of individual adobes was assumed to be equal to bending tensile strength. As the simulated masonry prism was composed of adobes originating from producer Ly, the average flexural strength assessed for specimens belonging to batches LyB and LyC was used: f_t = 0.4 MPa. The tensile yielding strain was computed as the ratio between the tensile strength and the Young's modulus (E = 90 MPa): ε_t^{ck} = 0.0044 mm/mm. Stress-strain data were obtained by applying the aforementioned values to equation 3.14.

For simulating the tensile failure of running-bond masonry, the exponential softening function developed by Lourenço (2000) was adopted. Stresses in the softening region were computed using the equation:

$$\sigma_t = f_t \exp\left(-\frac{hf_t}{G_f}\varepsilon_t^{ck}\right) \tag{5.24}$$

In the above, f_t is the tensile strength of masonry, G_f is the tensile fracture energy, ε_t^{ck} is the tensile cracking strain and h is the characteristic crack length.

Since the damaged plasticity constitutive law used in the analyses is based on isotropic failure concepts, uniaxial tensile strength was defined in accordance to the outcomes of the diagonal tension tests conducted in this study (see section 4.4). Tensile strength was set to be equal to the average tensile yielding stress (σ_I) recorded during three consecutive laboratory tests; f_t = 0.04 MPa. The yielding stress for each test was computed from the corresponding stress-strain experimental curve, in accordance with equation 4.11c. The same value of f_t = 0.04 MPa has also been used by Tarque et al. (2010a) when simulating the in-plane response of adobe walls.

It should be pointed out that, although the association established between the medium's uniaxial tensile behaviour and the experimentally observed response to diagonal tension is numerically acceptable, in physical terms it may be deemed as a rather oversimplifying approach. In practice, the tensile behaviour of adobe masonry is more complex and is actually characterized by orthotropic damage mechanisms. Tensile loads acting perpendicular to the bed joints cause debonding between the units, whereas tensile loads acting parallel to the bed joints can either lead to splitting of the units or decohesion and frictional sliding along the joints (Backes, 1985).

The tensile fracture energy of the homogenized masonry (G_f) was evaluated based on the data reported by Almeida (2012). Almeida (2012) performed direct tension tests on prisms composed of two adobe blocks joined with hydraulic lime mortar. On average, the energy required for the failure of the couplets was 4.5 N/m for a mean tensile strength of 0.01 MPa. Assuming a linear analogy between the tensile strength and the fracture energy, f_t = 0.04 MPa yields G_f = 18 N/m.

The characteristic crack length h was defined based on the element geometry and formulation. For the first order elements used in this thesis, h was assumed to be equal to a typical length of a line across the element (Simulia Corp., 2009). According to the recommendations of Dhanasekar (2010), the characteristic crack length of 4-noded 2D plane stress elements was computed as:

$$h = \sqrt{2h_x h_y} \tag{5.25}$$

For 8-noded 3D linear brick elements the above expression was revised to (Saetta et al., 1999; Creazza et al., 2002):

$$h = \sqrt[3]{h_z h_x h_y} \tag{5.26}$$

In equations 5.25 and 5.26 h_x, h_y and h_z are the element's lengths along the x, y and z axes. The element size during meshing was selected to satisfy the energy criterion given in equation 5.27:

$$h \leq \frac{G_f E}{f_t^2} \tag{5.27}$$

Theoretically, through the definition of the characteristic crack length, mesh-dependency of numerical results is treated. However, the use of this parameter implies that, in non-structured meshes, the elements with larger aspect ratios will tend to have rather different behaviour, depending on the direction in which they crack. This effect may have introduced some mesh sensitivity to the results presented in this thesis, despite making efforts to use elements with aspect ratios close to one, especially in areas where tensile damage was expected.

5.3.3 Contact modeling

In all numerical analyses carried out, contact interactions among adjacent surfaces representing different materials were modeled via the definition of contact pairs and the formulation of corresponding master-slave associations. Contact modeling was implemented for simulating the interaction among adobe masonry specimens and steel loading platens. It was also used for modeling the interaction among adobe walls and timber members, when simulating the scaled building (see section 6). In all cases, the master surface was chosen as the surface of the stiffer body, or as the surface with the coarser mesh, if the two contact bodies had comparable stiffnessess.

The normal contact pressure between interacting surfaces (p) was defined as a function of the interpenetration of the surfaces (h_{pen}). For this purpose, a "hard" contact pressure-overclosure relationship that minimizes penetration of the slave nodes into master surface and does not allow the transfer of tensile stress across interfaces was adopted (equation 5.28).

$p = 0$ for $h_{pen} < 0$ (no contact between surfaces)

$h_{pen} = 0$ for $p > 0$ (surfaces in contact) (5.28)

According to the above, when surfaces are in contact, any contact pressure can be transmitted between them. The surfaces separate if the contact pressure reduces to zero. Separated surfaces come into contact when the clearance between them reduces to zero. "Hard" contact constraints were enforced through the default penalty method, which assumes that the contact force is proportional to the penetration distance. Although the assumption implies that some degree of penetration will occur, the method provides adequate accuracy for macroscopic simulations and allows for improved solver efficiency (Simulia Corp., 2009).

Interface properties along the tangential direction were specified using the finite-sliding formulation available in Abaqus/Standard. This formulation is suitable for modeling interactions between deformable bodies, where separation and sliding of finite amplitude and arbitrary rotation of surfaces may arise. Depending on the physical problem examined, interacting surfaces were either assumed to slide freely, or transmit shear stresses at their interface through friction.

In the first case, a frictionless constitutive law that simulates unobstructed tangential slippage was used. Alternatively, a simple Coulomb friction model was adopted. The Coulomb friction model assumes that two contacting surfaces can carry shear stresses up to a certain magnitude across their interface, before they start sliding relative to one another. The shear stress at which sliding initiates (τ_{crit}) is defined as a function of the contact pressure (p) and the coefficient of friction (μ) between the surfaces:

$$\tau_{crit} = \mu p \tag{5.29}$$

For three-dimensional simulations, slip calculations were conducted after combining the two orthogonal components of shear stress (τ_1 and τ_2) along the contact interface as:

$$\bar{\tau} = \sqrt{\tau_1^2 + \tau_2^2} \tag{5.30}$$

In addition, the two slip velocity components ($\dot{\gamma}_1$ and $\dot{\gamma}_2$) were combined into an equivalent slip rate as:

$$\dot{\gamma}_{eq} = \sqrt{\dot{\gamma}_1^2 + \dot{\gamma}_2^2} \tag{5.31}$$

The Coulomb friction model available in Abaqus/CAE cannot account for cohesion among interacting surfaces.

For imposing frictional tangential constraints, an isotropic stiffness (penalty) method was adopted. This method permits some relative motion of the surfaces (an "elastic slip") when they should be sticking instead of sliding. The default 0.005 tolerance was used for specifying the allowable elastic slip as a fraction of the "characteristic contact surface length". The latter parameter was automatically computed by the finite element code by scanning all facets of the slave surfaces.

5.4 Simulation of compression tests on adobe masonry assemblages

The plastic-damage constitutive law and the modeling parameters presented in section 5.3.2 were implemented in Abaqus/CAE for simulating the behaviour of a stack-bonded masonry prism (specimen SB13(DC)) under compressive loading-unloading cycles. For this purpose, a full 3D finite element model of the experimental set-up (see section 4.3) was developed. The finite element model consisted of different representations for the masonry specimen and the upper and lower load-imposition steel platens. Meshing was carried out using 8-noded 3D linear brick elements. Each platen was discretized into 24 elements. A denser mesh consisting of 576 elements with approximate side lengths of 40 mm was used in the case of the masonry specimen. The final model incorporated a total of 624 elements and 959 nodes, involving 2877 degrees of freedom.

The boundary conditions provided were chosen to adequately simulate the test set-up. All nodes at the base of the lower steel platen were considered to be pinned. In addition, movement within the x-y plane was constrained for the nodes of the upper platen. A frictionless contact was assumed at the interfaces between the adobe masonry and the steel platens. A uniformly distributed vertical displacement was assigned to the upper steel plate. The amplitude of the displacement over time was formulated according to the data recorded during the experimental procedure. The finite element model is shown in Figure 5.6.

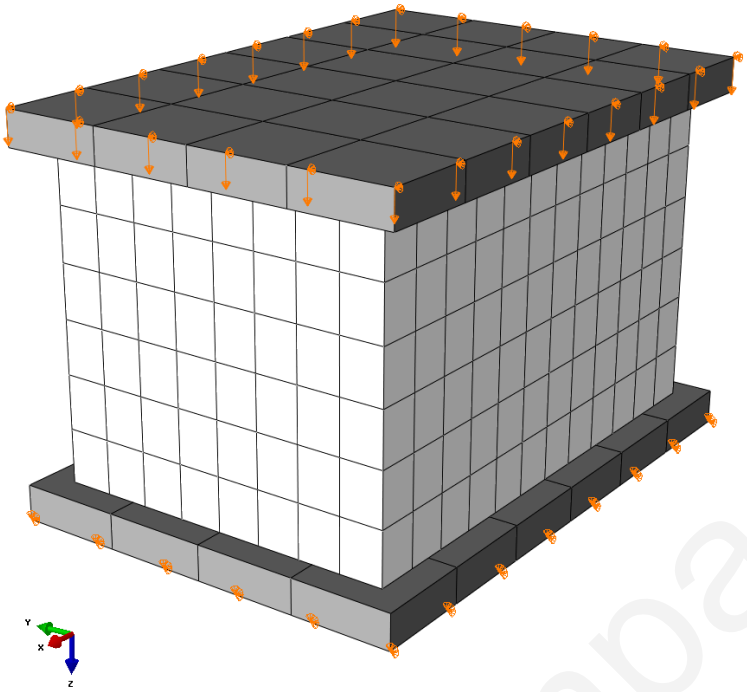

Figure 5.6: Finite element model developed for the simulation of a loading-unloading compression test on a stack-bonded adobe masonry prism.

The selection of appropriate parameters for the simulation of the stack-bonded masonry has been discussed in section 5.3.2. The data used are summarized in Table 5.1. The stress-strain curves used for defining the medium's response to compression and tension are given in Figure 5.7. It is worth noting that, in order to avoid mesh dependency of the results, tensile plastic strain input data were converted to cracking displacements using the element characteristic length (h = 40 mm). The steel platens are extremely stiff when compared to adobe masonry and were thus modeled as linearly elastic and isotropic, with density ρ = 7850 kg/m^3, Young's modulus E = 220x10^3 MPa and Poisson ratio v = 0.3.

Table 5.1: Material properties used for the simulation of a stack-bonded adobe masonry prism subjected to loading-unloading compression cycles.

Elastic properties	
Density	ρ = 1300 kg/m^3
Young's modulus	E = 90 MPa
Poisson's ratio	v = 0.3
Plasticity parameters	
Dilation angle (degrees^o)	$\psi = 1^o$
Flow potential eccentricity	e = 0.1
Ratio of initial equibiaxial compressive yield stress to initial uniaxial compressive yield stress	$\sigma_{b0} / \sigma_{c0}$ = 1.16
Ratio of the second stress invariant on the tensile meridian to that on the compressive meridian at initial yield for any given value of the pressure invariant such that the maximum principal stress is negative	K_c = 0.8
Viscosity parameter	μ_v = 0 s
Compressive behaviour	
Compressive stress-strain response	Experimental data
Compressive strength	f_w = 1.48 MPa
Compressive yielding stress	f_{wy} = 0.01 MPa
Strain at peak compressive stress	ε_{cu} = 0.1 mm/mm
Tensile behaviour	
Tensile stress-strain response	Equation 3.14
Tensile yielding stress	f_t = 0.4 MPa

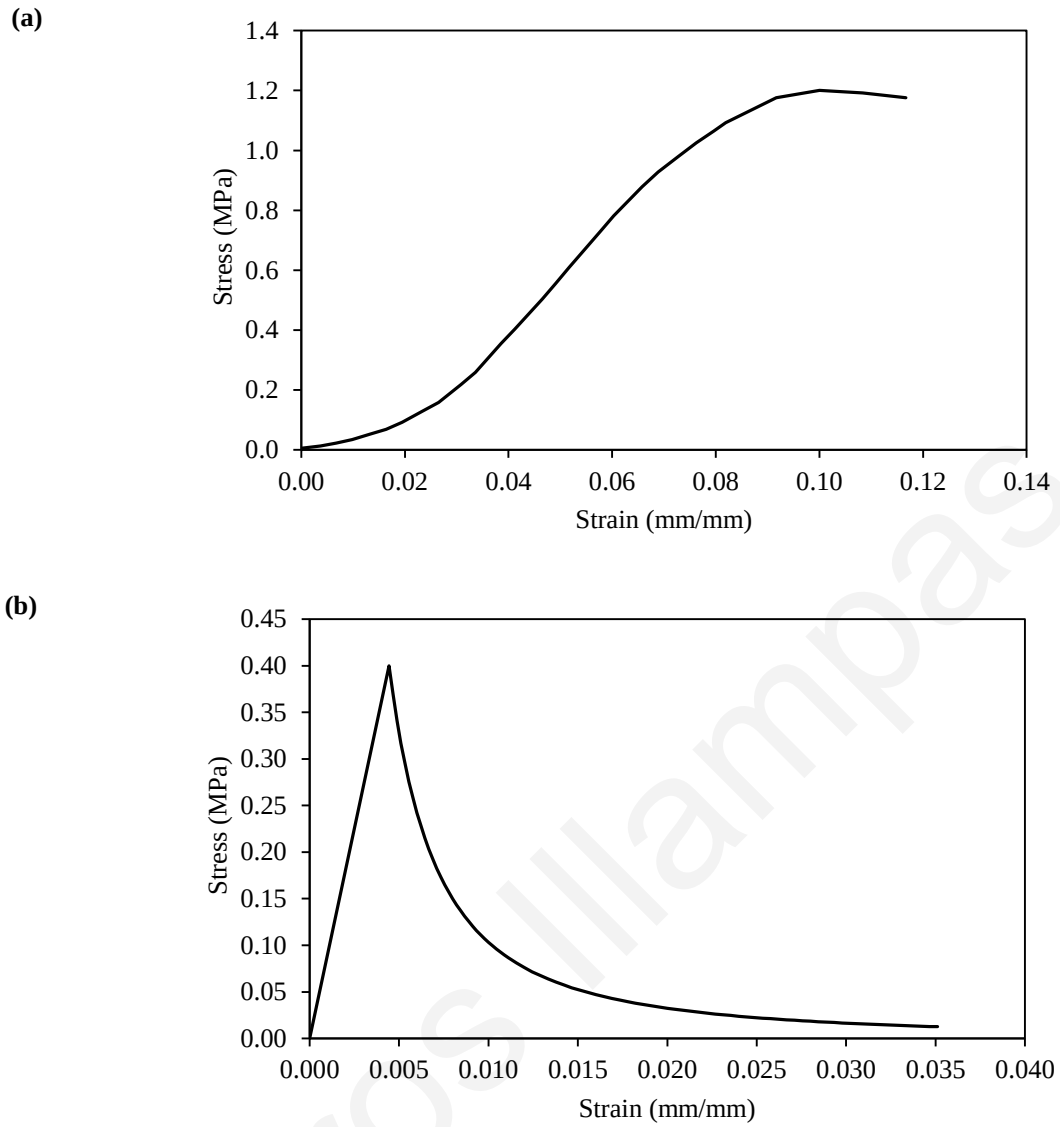

Figure 5.7: Compressive (a) and tensile (b) stress-strain response assigned to the homogenized continuum for the simulation of a loading-unloading compression test on a stack-bonded adobe masonry prism.

The non-linear numerical problem was solved using the full Newton technique, with a direct equation solver. Figure 5.8 presents the distribution of maximum tensile plastic strains computed at the element integration points when the imposed load attained its maximum value. It is noted that the development of plastic strains at certain areas indicates that the stresses generated have exceeded the medium's yielding stress and that damage (i.e. cracking) has occurred. The distribution of tensile plastic strains in the vertical central section of the prism coincides with the conical fracture shape noted during the laboratory test. In addition, the magnitudes of the strains tend to increase towards the lateral sides of the prism (Figure 5b). This is in line with the experimentally observed circumferential

spalling. The above indicate that the mode of failure sustained by the specimen is well captured by the finite element model.

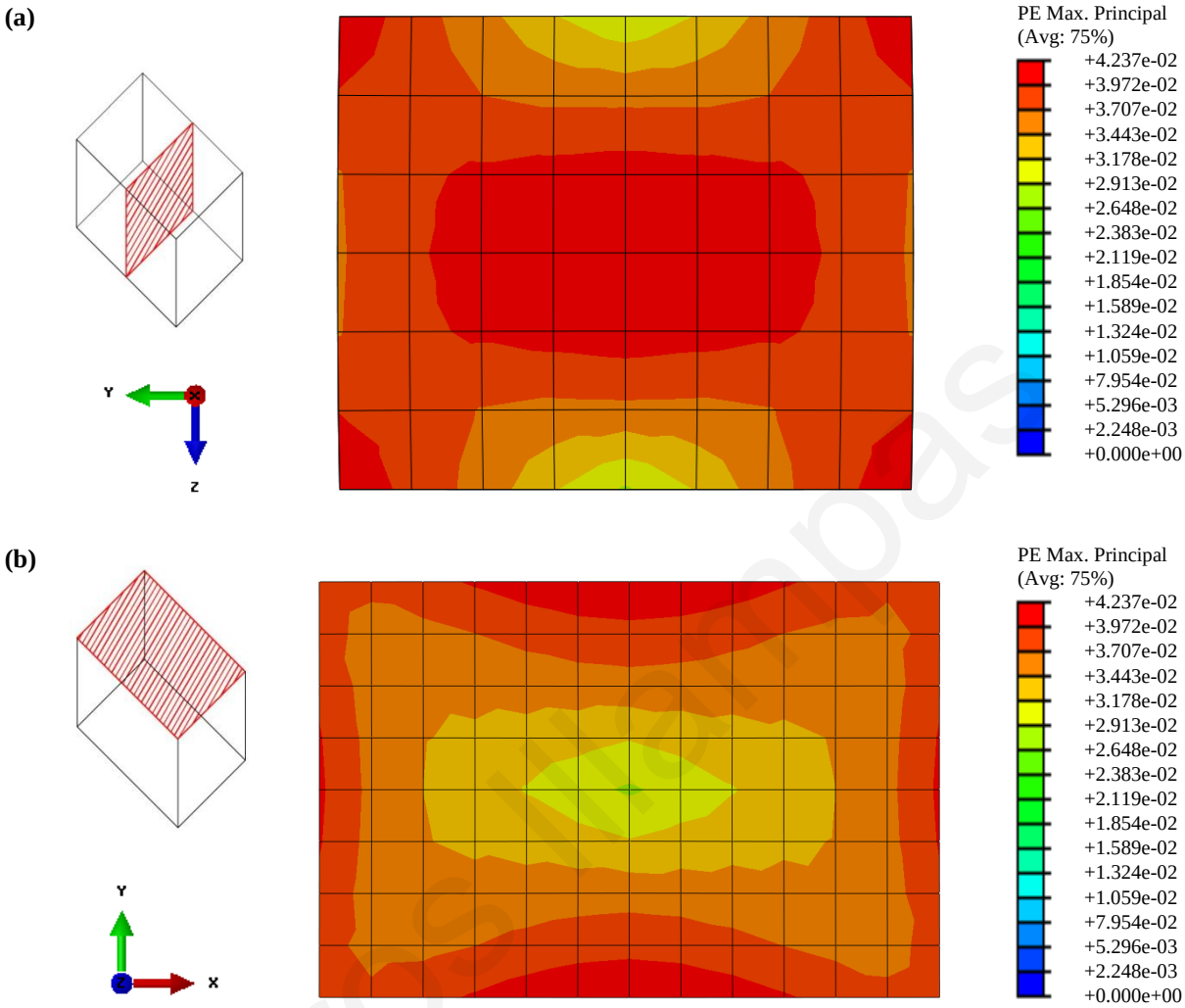

Figure 5.8: Contour diagrams showing the distribution of the maximum tensile plastic strains computed at the element integration points when the imposed load attained its maximum value (deformation scale x1). (a) Vertical central section of the prism and (b) upper view of prism.

Figure 5.9 compares the numerical results with the experimental data, in terms of a force-displacement diagram which presents the variation of the load imposed on the prism in relation to the upper platen's vertical translation. Numerical force values were estimated as the sum of all vertical reaction forces at the nodes of the lower steel platen. Results show that the finite element model, although quite simplistic compared to the actual complex behaviour of adobe masonry, reproduces very well the shape of the experimental diagram's envelope. The difference between the ultimate load recorded during the experiment and that obtained from the analysis is less than 2%. Taking into consideration the variability recorded in the mechanical properties of individual adobe bricks (see section 3), it may be

argued that this difference is actually negligible. Regarding the loading-unloading branches, these cannot be reproduced in detail by the constitutive model chosen, since it is not possible to implement a formulation with progressive material densification and dynamically increasing deformation moduli. However, despite the fact that in the finite element model the loading-unloading branches coincide, they occur at approximately the same value of strain as the experimental ones. Furthermore, the stress computed by the numerical model after the end of each unloading cycle is equal to zero, as in the case of the actual masonry specimen. Therefore, the simulated response can be deemed adequate when the main aim is the macroscopic investigation of structural behaviour.

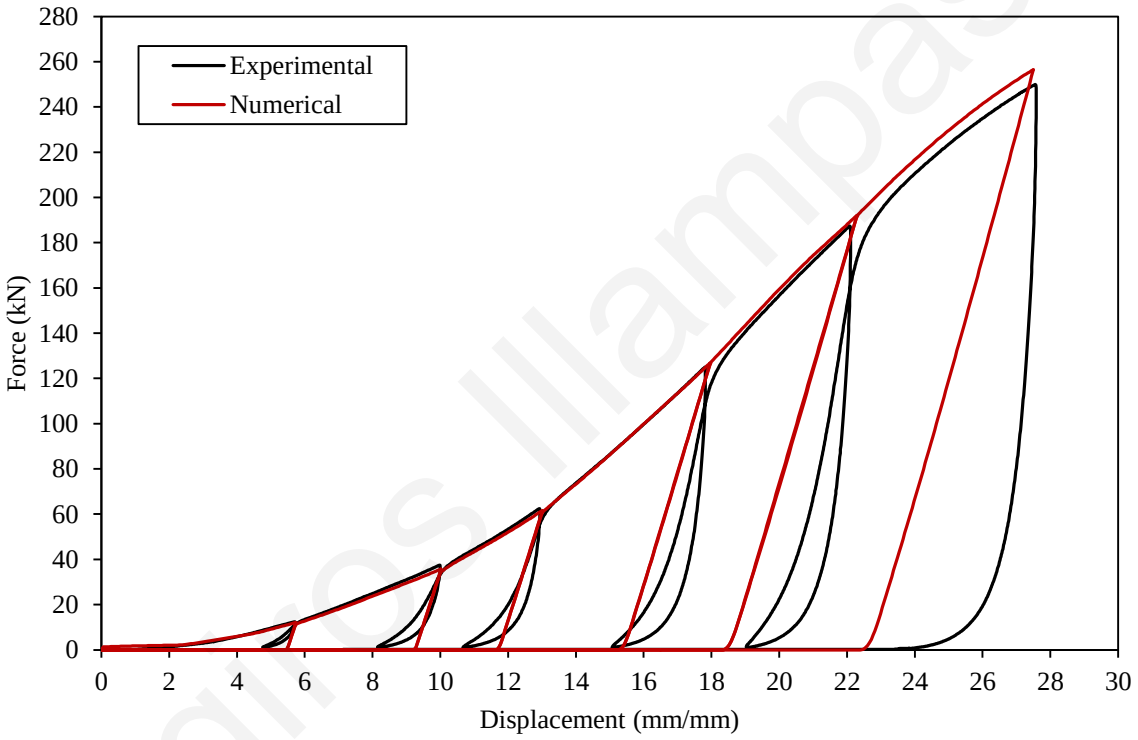

Figure 5.9: Comparison between experimental and numerical force-displacement data referring to the loading-unloading compression test performed on stack-bonded prism SB15(DC).

A more accurate simulation of the response to loading-unloading cycles entails the use of a detailed micro-modeling strategy and/or the introduction of a constitutive law that will account for different deformation moduli, depending on the loading conditions and the stress state. Obviously, this approach involves high computational effort and, considering the randomness and inhomogeneity of adobes, it requires further thorough experimental research. Regardless of academic interest, it is doubtful whether such advanced simulation practices can have extensive applications in practice-orientated engineering design.

5.5 Simulation of diagonal tension tests on adobe masonry wallette

Following the simulation of a loading-unloading compression test, the diagonal tension experiment presented in section 4.4 was also numerically examined. The objective in this case was to verify the capability of the adopted constitutive model to macroscopically capture the observed failure mode (i.e. tensile splitting along the line of loading) and to reproduce the envelope of the force-displacement experimental data.

The diagonal tension test was treated as a plain stress problem. Both the masonry specimen and the enclosing steel frame were simulated. All bodies were discretized using 4-noded bilinear quadrilateral 2D elements with plain stress formulation (CPS4). The mesh representing the masonry wallette was composed of 40 x 40 mm^2 elements, whereas for the steel frame's members 10 x 40 mm^2 elements were used. The complete finite element mesh consisted of a total of 285 elements and 384 nodes, resulting in 768 degrees of freedom. The thickness over which the plane stress condition applied was set as 300 mm, in accordance to the dimensions of the test set-up.

The base of the steel frame was assumed to be pinned. The hinged connections between the frame's steel members were modeled via the imposition of corresponding kinematic constraints at coincident nodes, which enforced equal displacements while enabling free rotation. Contact between the masonry specimen and the steel enclosure was assumed to be frictionless. The finite element model developed is shown in Figure 5.10.

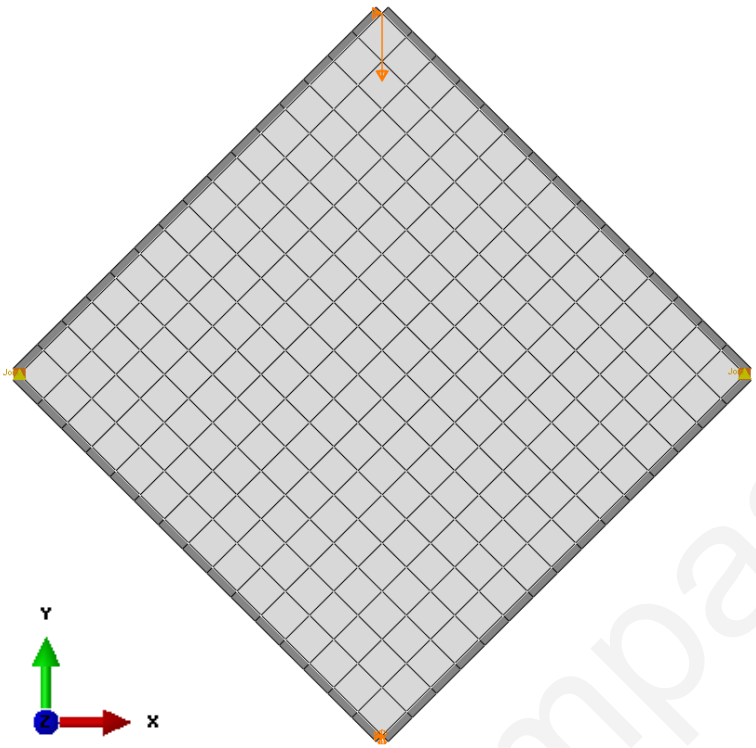

Figure 5.10: Plane stress finite element model developed for the simulation of the diagonal tension tests on the adobe masonry wallette.

The material parameters used for modeling the behaviour of the homogenized masonry are summarized in Table 5.2. The selection of these parameters has been previously analyzed in section 5.3.2. The compressive and tensile responses assigned to the continuum are shown in Figure 5.11. The variation of the tensile stress, in relation to the cracking strain, was computed by applying the characteristic element length, h = 57 mm, of the masonry's mesh to equation 5.24. The members of the enclosing steel frame were modeled as elastic isotropic with density ρ = 7850 kg/m^3, Young's modulus E = 220x10^3 MPa and Poisson ratio v = 0.3.

Table 5.2: Material properties used for the simulation of adobe masonry under monotounously increasing loads.

Elastic properties	
Density	ρ = 1300 kg/m^3
Young's modulus	E = 18 MPa
Poisson's ratio	v = 0.3
Plasticity parameters	
Dilation angle (degrees^o)	$\psi = 1^o$
Flow potential eccentricity	e = 0.1
Ratio of initial equibiaxial compressive yield stress to initial uniaxial compressive yield stress	$\sigma_{b0} / \sigma_{c0}$ = 1.16
Ratio of the second stress invariant on the tensile meridian to that on the compressive meridian at initial yield for any given value of the pressure invariant such that the maximum principal stress is negative	K_c = 0.8
Viscosity parameter	μ_v = 0 s
Compressive behaviour	
Compressive stress-strain response	Equation 3.7
Compressive strength	f_w = 1.2 MPa
Compressive yielding stress	f_{wy} = 0.06 MPa
Strain at peak compressive stress	ε_{cu} = 0.1 mm/mm
Tensile behaviour	
Tensile stress-strain response	Equation 5.24
Tensile yielding stress	f_t = 0.04 MPa
Tensile fracture energy	G_f = 18 N/m

(a)

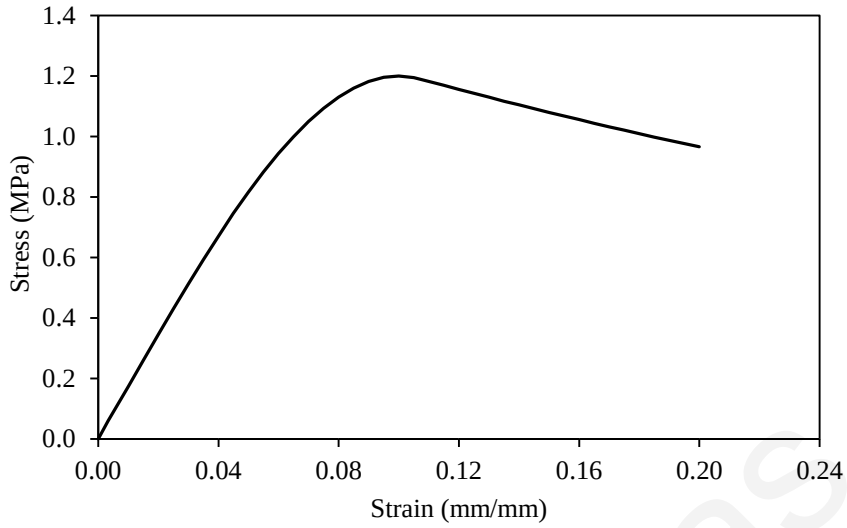

(b)

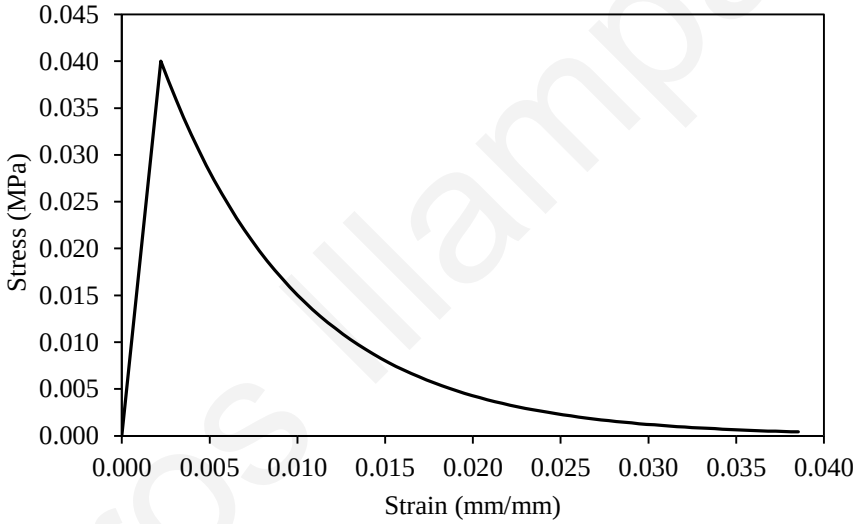

Figure 5.11: Compressive (a) and tensile (b) stress-strain response assigned to the homogenized continuum for the simulation of a diagonal tension test on an adobe masonry wallette.

The analysis was performed under displacement control, with the load applied as a kinematic constraint at the upper node of the enclosing frame. The vertical displacement assigned at this point was 32.5 mm and was equal to the total cumulative displacement recorded after the completion of all three diagonal tension test cycles. Movement of the enclosing frame's head was incrementally enforced at time intervals ranging from $1x10^{-21}$ to $1x10^{-4}$ s over the 1 s analysis period. The full Newton numerical solution was obtained. An automatic stabilization scheme was selected for the criterion of convergence, adopting the default stabilization parameters suggested by Simulia Corp. (2009). During the numerical procedure, geometric non-linearities were accounted for.

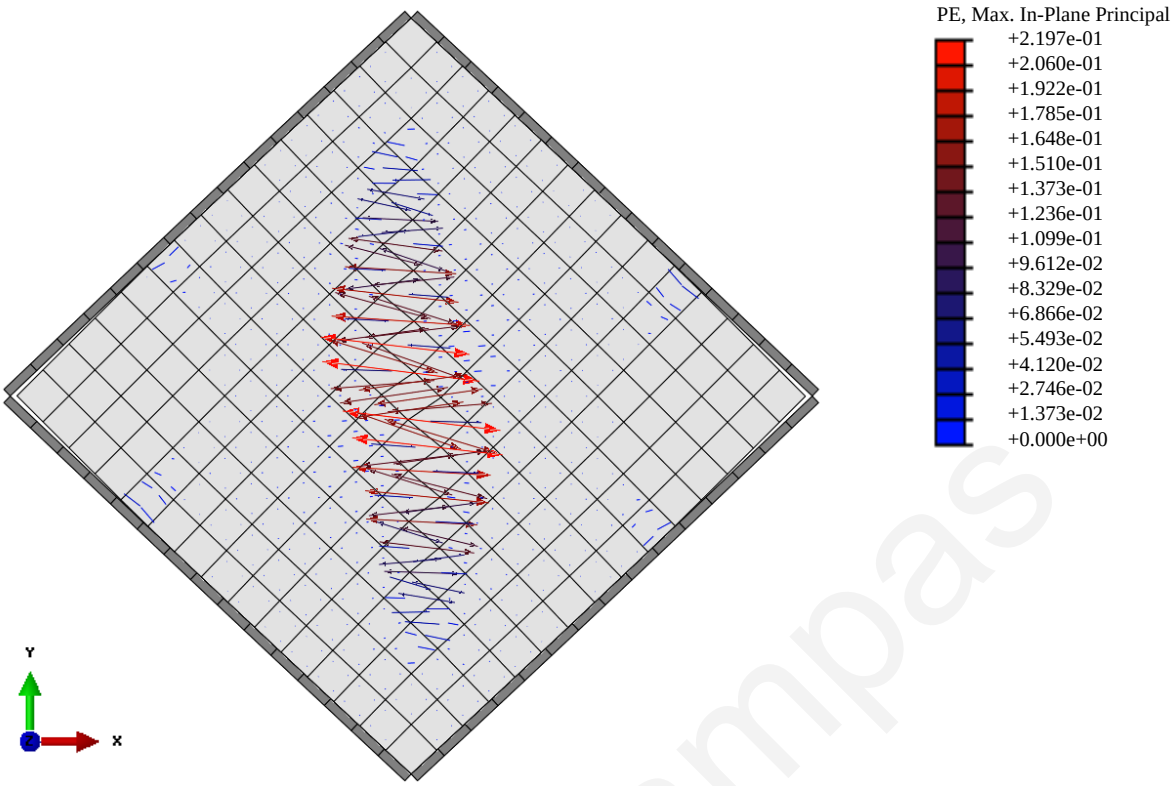

Figure 5.12: Deformed mesh (deformation scale x1) at the final step of the numerical solution process with tensor diagram showing the maximum tensile plastic strains computed at the element integration points.

Figure 5.12 shows the deformed mesh at the final step of the numerical solution process and gives a tensor diagram with the maximum tensile plastic strains computed at the element integration points. In line with the experimentally observed behaviour, principal tensile cracks in the finite element model initiate at the center of the wallette and propagate towards the corners. However, cracking in the finite element model does not extend throughout the entire length of the diagonal. This is possibly due to a confining effect by the steel enclosure. The finite element model also predicts the onset of cracking at the lateral corners of the specimen. This is a product of localized stress development from the stiff steel frame and is in total agreement with the damage recorded during laboratory tests (Figure 4.15). The partial detachment of the wallette's lateral corners from the enclosing frame is also verified by the experimental observations made (Figure 4.15c).

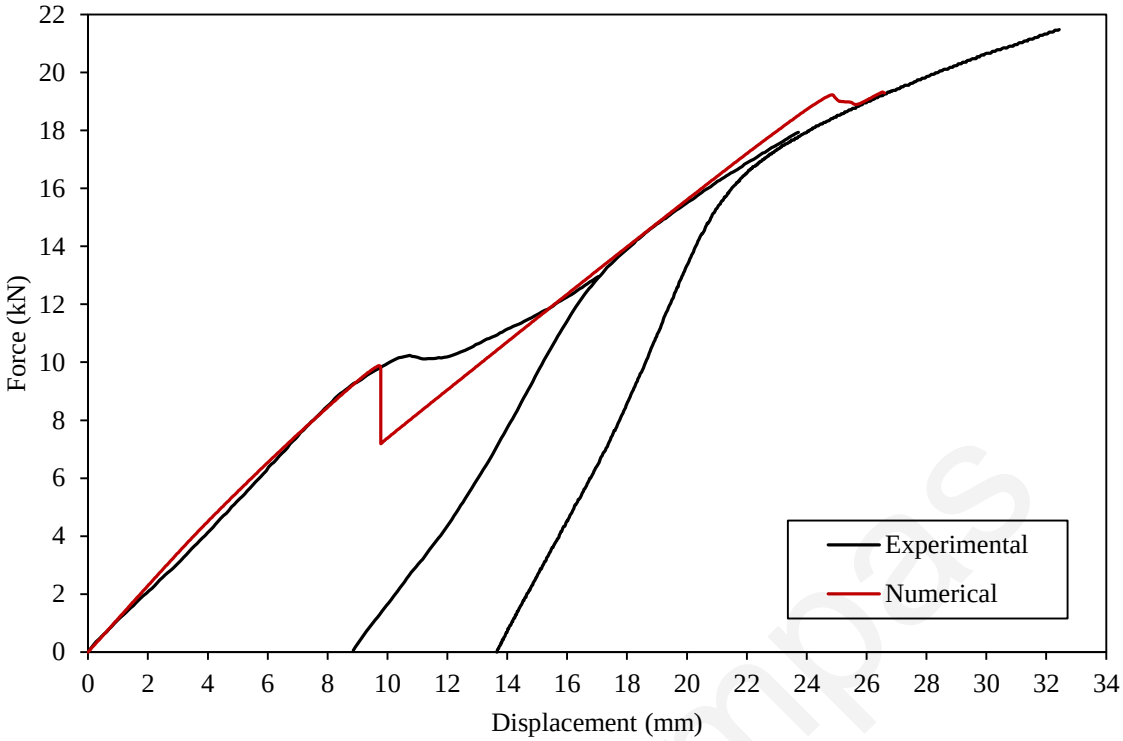

Figure 5.13: Comparison between numerical and experimental force-displacement data referring to the diagonal tension testing of an adobe masonry wallette. Experimental results correspond to three subsequent loading-unloading cycles performed on the same specimen, whereas numerical results were obtained from the implementation of a monotonic loading simulation.

The load-displacement curve yielded by the analysis is shown in Figure 5.13. The load data reported correspond to the reaction force computed at the lower pinned nodes of the steel frame. Displacement data refer to the vertical translation of the steel frame's upper node. Unfortunately, due to lack of convergence, numerical results could not be obtained for the full range of imposed displacements. Nevertheless, the initial linear branch is very well captured, while the load at which stiffness reduction initiates is accurately predicted. Furthermore, the non-linear branch corresponding to the second test cycle is adequately approximated. Despite the fact that the finite element model predicts a more abrupt load-drop upon the initiation of tensile splitting, the load sustained by the masonry continues to increase due to confinement by the enclosure and due to the existence of diagonal compressive strength. The sudden strength reduction, which occurs immediately after cracking, is attributed to a rapid increase in the evolution of plastic strains imposed by the exponential softening tension model. In the actual specimen, some additional resistance along the line of failure probably did exist, due to friction among the adobes.

5.6 Summary

Finite element simulation of adobe masonry was examined in the context of a continuum-based macro-modeling strategy. A damaged plasticity constitutive law, which uses isotropic failure concepts in tension and compression was adopted.

Within this framework, 3D numerical modeling was implemented to study the behaviour of a stack-bonded prism subjected to loading-unloading compression cycles. To account for the different response of adobe masonry under constantly increasing axial loads and loading-unloading cycles, the medium was assigned a fully non-linear compressive response (compressive yielding at < 1% of maximum allowable stress), while the unload-reload modulus was used. In the absence of head-joints that could sustain tension damage, the medium's tensile response was assimilated to that of the individual adobe bricks. The aforementioned approach enabled an adequate approximation of the experimental data envelope. In addition, the numerical results obtained indicate good correspondence between the computed distribution of tensile plastic strains and the specimen's mode of failure.

A diagonal tension test was also simulated through the development of a plane stress finite element model. In this case, a polynomial compression model and an exponential softening tension law were adopted for defining the medium's behaviour. The limit strength and deformation values used were decided in accordance with the average results of the tests carried out in this thesis and with reference to relevant data reported in the literature. Despite convergence difficulties, which precluded derivation of numerical results for the full range of loads, the envelope of the experimental force-displacement diagram is well captured. The point at which stiffness reduction initiates is predicted with sufficient accuracy, while the computed distribution of tension damage coincides with the specimen's cracking mode.

6 EXPERIMENTAL AND NUMERICAL INVESTIGATION OF THE STRUCTURAL RESPONSE OF AN ADOBE SCALED BUILDING

6.1 Introduction

This chapter examines the structural response of complete adobe masonry buildings. Relevant studies carried out by other researchers are reviewed, while the results obtained from monotonic lateral loading laboratory tests on a 1:2 scaled replica of a traditional single-storey structure are presented. Through the experimental investigation conducted, useful conclusions concerning the initiation and propagation of cracking failure are deduced. In addition, damage limit states at different levels of deformation are identified and compared against corresponding data from the literature.

Using simplified kinematic models, analytical predictions regarding the ultimate bearing capacity of the tested structure are made. Furthermore, based on the computational work presented in section 5, the response of the adobe scaled building is simulated using finite element analysis. The validity of the numerical results yielded is verified both qualitatively and quantitatively through comparisons with the experimental damage patterns and force-displacement curves.

6.2 Review of experimental research on full- and reduced-scale adobe modules

Several studies examining the structural behaviour of adobe structures have been conducted. Research is mainly focused on laboratory testing of full- or reduced-scale wall configurations and complete buildings. Depending on the test apparatus available and the information sought, dynamic or static experiments may be implemented. Emphasis is usually given on investigating the response of adobe construction to horizontal loads and/or on evaluating the efficiency of various repair/retrofitting techniques.

Systematic testing of adobe structures has taken place in the framework of various research projects developed by the Pontifical Catholic University of Peru (PCUP). Initially, a number of static tilt tests were carried out on full-scale model buildings (Corazao and

Blondet, 1974). The structures examined were composed of four walls with dimensions (height x length x width) 2.6 x 2.6 x 2.4 m^3 and incorporated various openings and reinforcement elements. During these tests, the forces generated by the inclination of the base platform would simulate horizontal static accelerations, while the tilt angle at collapse was used for quantifying the bearing capacity of each module.

Static experiments were followed by shake table tests on full-scale house modules (Ottazzi et al., 1988). These aimed at evaluating the effect of timber ring beams and cane reinforcement on the seismic behaviour of adobe masonry construction. The models tested had timber roofs and consisted of four walls, approximately 3.2 m long, 2-2.25 m high and 260 mm thick, with door and window openings. Model structures of the same form and size were later used by Zegarra et al. (1997) in dynamic loading experiments, in order to examine the effectiveness of external welded steel wire mesh reinforcement. A similar experimental programme was undertaken by Blondet et al. (2006) who considered the use of polymer meshes (geogrids) for increasing lateral resistance and for preventing brittle collapse. For this particular project, in addition to rectangular house modules, vaulted structures were constructed and tested (Blondet et al., 2005; Torrealva et al., 2006). Furthermore, 'I'-shaped full-scale wall configurations were subjected to displacement-controlled cyclic tests in order to investigate the behaviour of geogrid-reinforced adobe construction under in-plane and out-of-plane loading (Torrealva et al., 2008). Laboratory testing of model structures retrofitted with innovative materials has also been conducted. Garcia et al. (2004) installed vertical and horizontal GFRP bars on small size adobe modules (dimensions: height x length x width = 1.15 x 0.95 x 0.95 m^3) tested under dynamic excitation. In all aforementioned studies, the results obtained from strengthened structures were compared against those derived from unreinforced reference models.

More recently, Bartolomé et al. (2009) performed shake table tests on a full-scale two-storey structure composed of a reinforced concrete frame and adobe masonry infill walls. Charleson (2011) tested single-storey model buildings in order to examine the use of car tire straps as a means for confining the out-of-plane movement of adobe walls during earthquakes. It is worth mentioning that, apart from laboratory testing, efforts have been made in the PCUP to simulate the experimentally observed behaviour of certain model structures using the finite element method (Tarque et al., 2010a, 2012b).

Noticeable research work on the seismic behaviour of adobe buildings has been carried out in the framework of the Getty Seismic Adobe Project, sponsored by the Getty Conservation Institute. In the first phase of this project, several 1:5 scaled replicas of the

same single-storey structure were subjected to impact hammer and shake table tests at Stanford University (Tolles and Krawinkler, 1990). In the latter, loading was applied before and after the application of repair and strengthening interventions. The techniques considered included the removal of roof weight, the anchoring of roof rafters, the addition of timber bond beams and the reconstruction of damaged masonry. The outcomes of impact hammer measurements were used for identifying the natural frequencies of the tested structures and were utilized for the validation of linear finite element models to numerically predict the mode shapes and fundamental frequencies of earthen buildings.

Larger model buildings (scale 1:2) were examined in the second phase of the aforementioned project (Tolles et al., 2000). The study addressed the seismic stabilization of historic adobe buildings. Therefore, along with unreinforced models, structures retrofitted with various combinations of elements (e.g. bond beams, horizontal/vertical straps, local ties, center-core rods, wood roof diaphragms) were tested. Experiments were carried out at the Institute of Earthquake Engineering and Engineering Seismology in FYROM and involved the application of dynamic excitations based on real accelerograms. During the experimental procedure, failure initiation and propagation were recorded in detail and the displacements induced were monitored. In addition, indicative measurements of the stresses generated at reinforcing straps were taken.

Aiming to propose seismic rehabilitation alternatives for the historic earthen buildings of Colombia, Yamin et al. (2004) implemented an extended experimental research project. This involved shake table tests and static horizontal loading tests on 1:5 and 1:1.5 scaled buildings. The model structures represented one- and two-storey buildings and were strengthened using wire meshes and boundary wooden elements. Comparisons among the different types of reinforcement were made following mostly qualitative criteria based on the observed collapse mechanisms.

Shake table tests on 1:2.5 scaled replicas of typical Mexican masonry dwellings were carried out by Meli et al. (1980). In this study, both unreinforced and reinforced models were examined. The latter incorporated concrete ring beams at their top, welded wire meshes nailed on the walls' faces and perimeter steel tie rods. In order to quantify the extent of damage suffered by the different structures, after each level of seismic motion imposed, free vibration tests were performed to measure the period and damping of the walls. Experimental results were used to establish correlations among the vibration intensity, the decrease in the structure's original natural frequency and the damage state. Further research on the seismic vulnerability of earthen houses in Mexico, was undertaken

by Rojas et al. (2008) who conducted vibration tests on small 1:10 scaled model buildings. Experimental work focused on noting the structures' damage modes and dominant oscillation periods.

Tests on models at the 1:10 scale have also been conducted by Ersubasi and Korkmaz (2010). The models used by these researchers were constructed either of unreinforced masonry or of masonry incorporating strengthening additions, such as wire meshes, steel plates and post-tensioned rods. All models were forced to collapse under dynamic excitation; the failure sequence generated and the maximum acceleration sustained were recorded during each test.

On the other hand, Samali et al. (2011) used 1:3 scaled-down square and circular model structures. These were subjected to static-tilt table tests, in order to compare the response of different wall layouts to lateral loading. Structural behaviour was evaluated by recording the failure mechanism, the first cracking angle and the angle at which the models collapsed.

For assessing the seismic performance of adobe structures, Dowling (2006) performed transient dynamic load tests on a series of 1:2 scaled models of complete buildings. These models consisted of 'U'-shaped wall configurations. The experimental results derived enabled the determination of the structures' modal characteristics (i.e. fundamental frequencies and mode shapes). Moreover, the ability of several retrofitting systems to constrain cracking and to prevent collapse was evaluated. This was achieved by testing a number of selected models reinforced with pilasters/buttresses, wire meshes, internal/external bamboo poles and timber ring beams. Analogous laboratory tests for the determination of dynamic properties have taken place at the University of Bristol by Hardwick and Little (2010), who recorded the modes of failure and assessed the natural frequencies of 1:4 scaled 'U'-shaped models by conducting shake table tests.

Furthermore, 'U'-shaped adobe walls constructed at a scale of 1:3 were subjected to shake table tests and static tilt tests by Tipler et al. (2010) at the University of Auckland. The models examined represented earthen structures reinforced with vertical steel bars, bond beams and layers of polysynthetic geogrid embedded in the mortar joints. Pre-cracked dynamic behaviour of the models was gauged by applying sine sweep waves. The collapse sequence developed under dynamic loading was studied by imposing scaled earthquake records until the ultimate limit state was reached. The results from the tilt tests enabled a comparison between the displacement capacities of the different wall systems.

A real-scale 'I'-shaped adobe wall measuring 3 m in height, 3.5 m in length and 290 mm in thickness has recently been tested at Aveiro University (Figueiredo et al., 2013). The experimental program commenced with the implementation of cyclic loading tests aiming to investigate the structural response of unreinforced masonry. After the first series of tests, cracking damage was repaired with lime mortar injections and a seismic retrofit solution, based on the installation of polymeric mesh, was applied. To validate the efficiency of the repair and retrofitting techniques, a new series of cyclic tests was performed.

6.3 Laboratory testing of an adobe scaled building

6.3.1 Construction of model building

The model used for investigating the structural response of complete adobe masonry structures is a 1:2 scaled replica of a traditional Cypriot dwelling. It represents the simplest and oldest typology of vernacular architecture encountered on the island, i.e. the "monochoro" (Figure 6.1). The "monochoro" is a rectangular, single-roomed structure. Its longitudinal interior space is usually 8-15 m long. Its width is limited by the length of the roof's timber rafters and can vary from 2.5 m to 4.5 m.

The construction of the model structure was carried out by an experienced mason and lasted five days. Pictures showing the various construction phases are shown in Annex 3. A schematic representation of the model structure is shown in Figure 6.2.

(a) (b)

Figure 6.1: A traditional "monochoro" adobe building located in Limassol, Cyprus (a) and the model structure examined in the framework of this thesis (b).

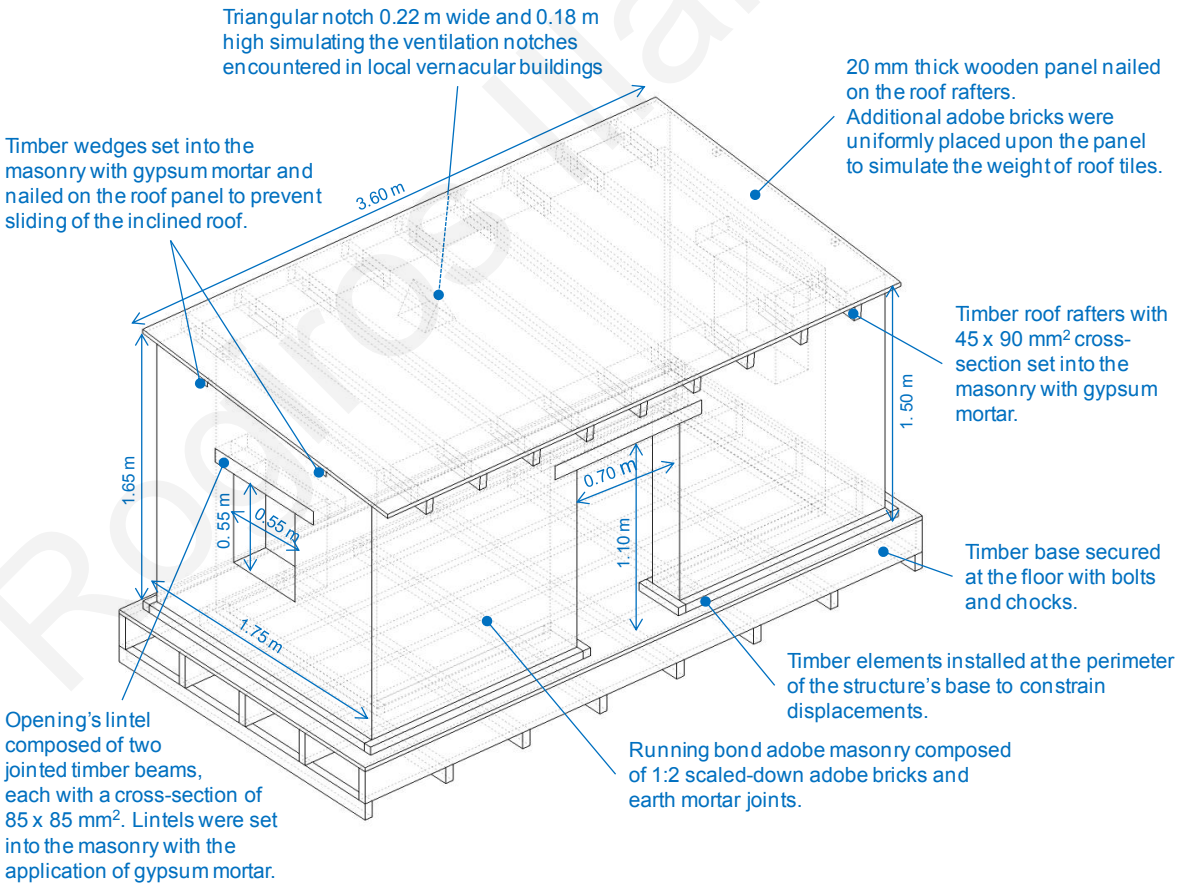

Figure 6.2: Schematic representation of the model structure examined in the framework of this thesis.

For the construction of the masonry walls, scaled-down adobes (dimensions: height x width x length = 30 x 150 x 220 mm^3) were obtained from producer Ly. These were prepared using the same raw materials and following the methodology adopted for the production of full-scale bricks (see section 3.3). The composition of the earth mortar used in the masonry joints was very similar to that of the adobes. It was prepared in the laboratory using soil and straw fibers, also supplied by producer Ly. The solid constituents were identical to those used in the production of the scaled bricks. For the production of the earth mortar, soil was manually mixed with water (1 kg per 2 kg of soil) to plastic consistency; approximately 3% of straw (w/w) was added to the mixture. The mortar was thoroughly kneaded using shovels and was allowed to ferment indoors for two days before being used for construction purposes. During the production of the mortar, a total of 18 specimens were sampled and tested in accordance to EN 1015-11. Their average compressive strength was found to be 1.9 MPa, while their average flexural strength was 0.8 MPa.

The model structure was built inside the laboratory upon a timber base that was secured on the concrete floor with bolts and chocks. The structure's external dimensions were (width x length) 1.75 x 3.60 m^2. The height of the front elevation was 1.50 m, while the height of the opposite rear wall was 1.65 m. A door measuring 1.10 m in height and 0.70 m in width was formed on the façade. Two openings with dimensions 0.55 x 0.55 m^2 were also created on the two side walls. A triangular notch measuring 0.22 m in width and 0.18 m in height was formed on the rear wall to simulate the ventilation notches encountered in local vernacular buildings.

Traditionally, adobe load bearing walls were constructed upon stone masonry foundations. It was presumed that boundary conditions at the base of these structures preclude horizontal translation of the walls at the ground level, but allow bending. Therefore, the first layer of adobe bricks was simply set on the base with the application of earth mortar, while horizontal displacements at this level were constrained by timber elements installed at the perimeter.

The model's walls were constructed following a running bond masonry pattern and their thickness was 220 mm. To simulate the local vernacular building technique, joint thickness was kept below 10 mm. Construction was executed in layers, allowing sufficient time for the mortar to set. This ensured adequate bonding between the bricks. Particular attention was given to the construction of the structure's corners. At these areas, overlapping bricks were placed upon each other, so that adequate connection of the cross-walls could be

achieved. During the construction of the model building, a fine piece of string set on the perimeter of the structure and a spirit level were used to level the walls horizontally. The verticality of the walls was checked by the use of a plump line.

Above all openings, lintels consisting of two jointed timber beams, each with a cross-section of 85 x 85 mm^2, were installed. The roof structure comprised of nine timber rafters (45 x 90 mm^2 in cross-section) placed in parallel, at intervals of approximately 350 mm. The rafters spanned the space between the two opposite longitudinal walls. All timber members were set into the masonry using gypsum mortar. In local adobe buildings, the roof space above the rafters is usually covered with tiles that may be supported on purlins, reed matting, densely tied canes or wood planks. For simulating this flexible roof diaphragm configuration, a 20 mm thick inclined wooden panel was fixed on the model structure's rafters. To account for the weight of the roof tiles, additional adobe bricks were uniformly placed upon the aforementioned panel. In order to avoid sliding, two timber wedges were set with gypsum mortar into the masonry of each side wall (orthogonally to the roof rafters) and were nailed on the roof panel.

Before commencing the implementation of load tests, the model structure remained for nine weeks in the laboratory (25 ± 9 ºC and 50 ± 5% R.H.) in order to allow sufficient time for the curing of the jointing mortar and the settling of the walls.

6.3.2 Testing methodology

The model building was tested under the imposition of monotonically increasing lateral forces. Loading was imposed via a steel hydraulic jack with 60 kN maximum capacity (Figure 6.3). The jack was supported by a rigid steel reaction frame. A timber beam was used for transferring the loads on the structure's rear wall. To achieve a more even distribution of forces on all members of the model, the timber beam was strengthened at the center by installing an additional timber piece, while more flexibility was retained at its two side ends. It should be noted that the use of a rather stiff beam throughout its length would result in transferring all forces at the wall sections parallel to the direction of loading (i.e. to the transversal walls), leaving the rear and façade walls with unrealistically low forces. The hydraulic jack accommodated a swivel head that enabled the loading-beam to stay in contact with the walls when out-of-plane bending was induced. Loading was applied at approximately 2/3 of the model's height; this implies that this is the height of the structure's center of mass, where, in an idealized situation, the forces generated from an

earthquake excitation would act. Thus, with the loading imposition and distribution configuration described above, it is envisaged that forces were properly induced and transferred to all bearing walls of the structure.

Figure 6.3: Test set-up used for the implementation of monotonic lateral loading on a 1:2 scaled adobe masonry building.

LVDTs (range ± 50.8 mm, accuracy ± 0.25%) were placed at 15 different points of the model structure to record displacements (Figure 6.4). Emphasis was given in monitoring the out-of-plane movement of the longitudinal walls and the in-plane bending of the side walls. Therefore, one of the side walls and the two adjacent halves of the longitudinal walls were instrumented throughout the experimental procedure. Visual observations made during the tests confirmed that there was close analogy between the responses of the halve-structure's sections examined and of the parts of the structure symmetric to them. LVDTs were also placed at the timber base to verify that no translation or rotation of the basal support took place during the tests. A purposely made electronic transducer was installed on the hydraulic jack to measure the force exerted on the structure during the loading phase. This apparatus, however, did not enable precise force monitoring at the unloading phase. All measurements were recorded automatically via a data acquisition system. Digital cameras were also used for recording failure evolution and crack opening-closing.

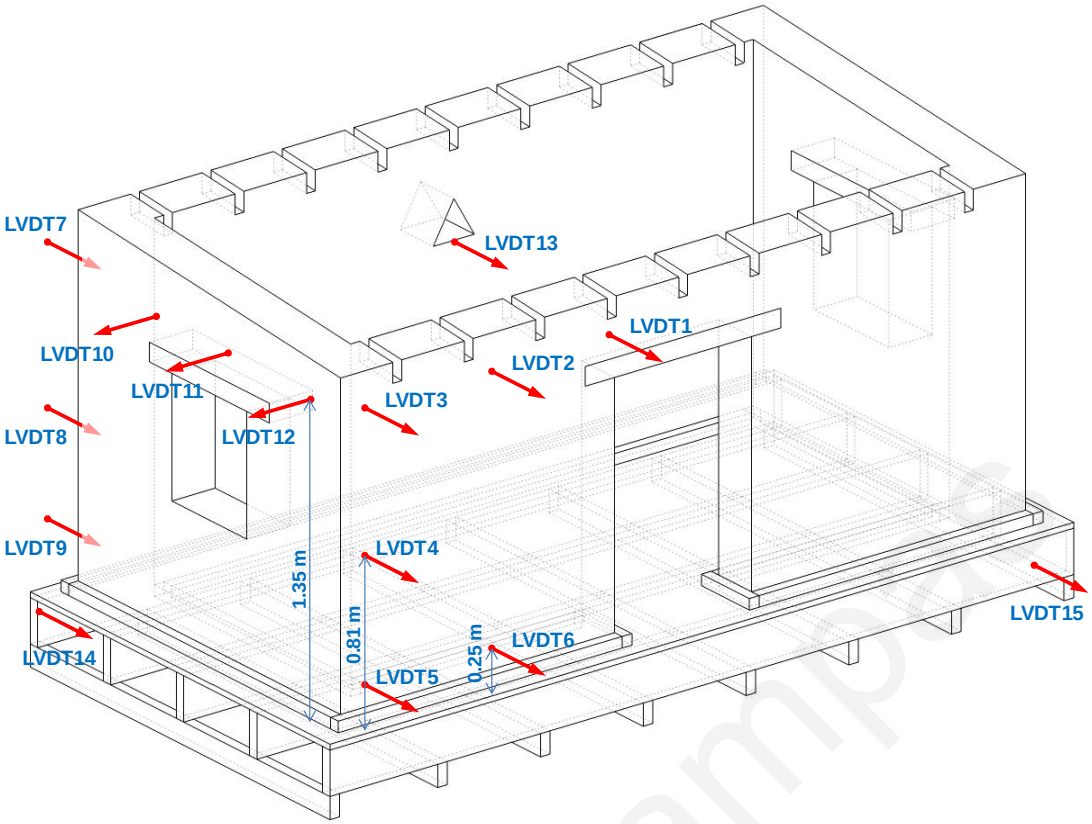

Figure 6.4: Points on the model structure where displacements were monitored through LVDTs during the testing procedure.

The model structure was subjected to a total of 10 test cycles. During each cycle, the exerted load was progressively increased up to the point where noticeable damage (i.e. severe cracking of the masonry walls) developed. Afterwards, the applied force was completely removed, the remaining displacement was recorded and a new test cycle was initiated. Loading-unloading cycles were repeated until a significant reduction of the lateral resistance was detected. However, for the purpose of future research work, the structure was not forced to partial or total collapse.

6.3.3 Results and discussion

6.3.3.1 Mode of failure

The resulting crack pattern after the completion of the 10 test cycles is shown in Figure 6.5. It should be pointed out that, the damage modes recorded during all experiments were almost identical. Most cracks developed during the first four test cycles. Subsequent test cycles simply led to the re-opening of pre-existing fissures and increased the cracks' width.

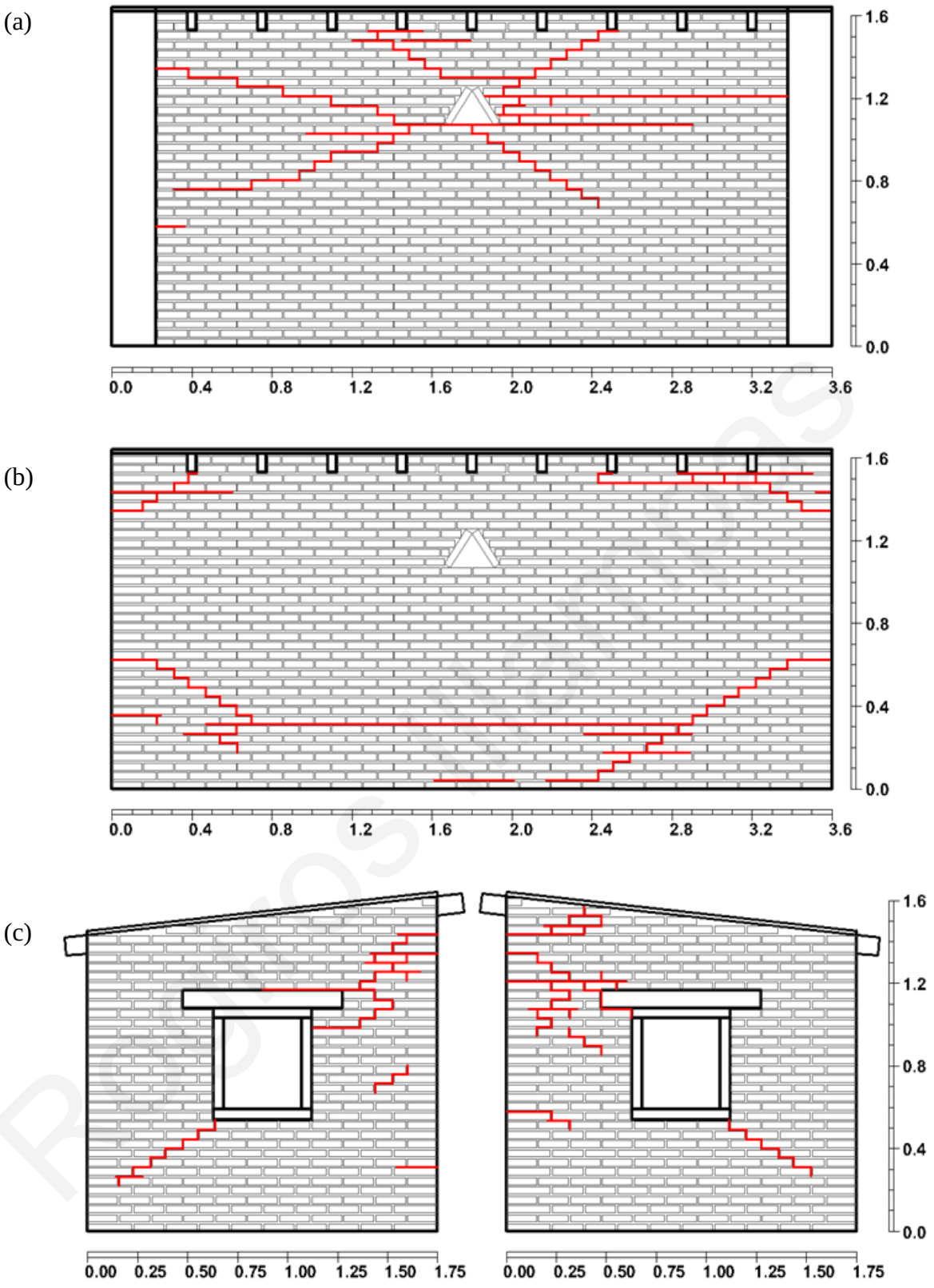

Figure 6.5: Cracking pattern obtained after the implementation of 10 test cycles, in which the model structure was subjected to monotonously increasing horizontal loading: (a) Rear wall interior surface, (b) rear wall exterior surface and (c) side walls.

As expected, the various timber elements did not suffer any damage; failure occurred at the more fragile adobe walls. Masonry cracking was noted at the rear and the two side walls, but not at the façade. Damage localization reveals stress concentration and implies that the load-bearing members of the model failed to react as a homogeneous assemblage of structural elements (i.e. as a fully connected structural system). In addition, it indicates a lack of diaphragmatic function at the roof level.

(a) **(b)**

Figure 6.6: Horizontal and diagonal cracks noted at the central interior section of the model structure's rear wall (a) and characteristic crack opening (b).

Initially, horizontal and diagonal cracks developed at the interior surface of the rear wall (Figure 6.6). These were caused by out-of-plane bulging. The onset of damage occurred at the center of the wall, at the height where loading was applied. A major horizontal crack was formed at this area and spread towards the cross-walls. Due to overstressing at the load imposition point, two diagonal cracks were generated below the aforementioned horizontal fissure. These diagonal cracks extended from the center of the wall towards its two lower sides. In addition, a 'V'-shaped cracked section was formed between the walls' triangular ventilation notch and the four central roof rafters.

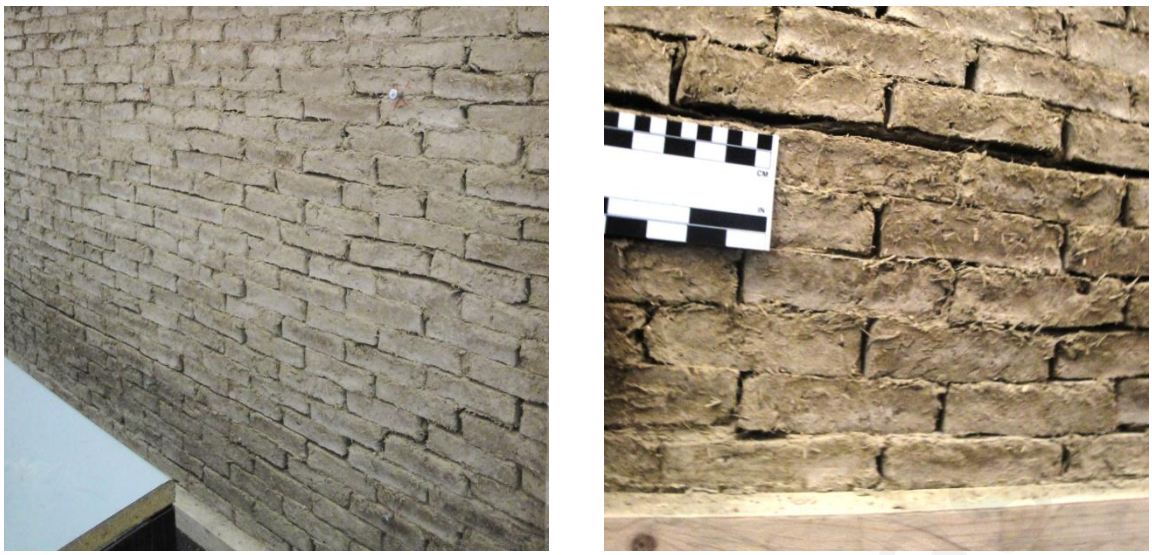

(a) **(b)**

Figure 6.7: Inclined and horizontal cracking on the lower exterior surface of the model structure's rear wall (a) and characteristic crack opening at the center of the same wall (b).

(a) **(b)**

Figure 6.8: (a) Cracks formed at the exterior upper side of the model structure's rear wall, at the vicinity of the roof rafters' supports. (b) Debonding at a roof rafter's support and subsequent sliding. The red lines denote the initial setting of the roof rafter in the masonry and its position after sliding occurred.

Moreover, the out-of-plane bending of the rear wall caused cracking on its exterior surface (Figure 6.7). In this case, the principal crack was formed at the central lower section of the wall. The crack was horizontal and continuous, passing throughout the length of the bed

joint between the 7th and 8th rows of adobes. At the two sides, the crack was inclined, following the head and bed joints and extending to the two side walls. After the first three test cycles, a number of cracks also developed below the initially damaged zone. Furthermore, horizontal and diagonal cracks were reported at the two upper sides of the rear wall, at the vicinity of the roof rafters' supports (Figure 6.8a). As the wall was subjected to significant out-of-plane bulging, considerable stress concentrations developed at the points where the timber rafters were in contact with the masonry. This is because the rafters were much stiffer than adobe masonry and could not follow the deformations induced. Consequently, tensile stresses acting parallel to the bed joints were generated, causing debonding and shear sliding among the adobes. In addition, during the second test cycle, failure of the gypsum mortar joints and subsequent sliding of the timber members was noted at the points where the roof rafters had been set into the masonry (Figure 6.8b).

(a) **(b)**

Figure 6.9: Diagonal shear cracking of the model structure's side wall (a) and characteristic crack opening (b).

The mode of failure sustained by the two side walls was mainly characterized by the formation of diagonally orientated shear cracks (Figure 6.9). Damage initiation was influenced by stress concentration at the corners of the openings and the abutments of the stiff timber lintels. Cracks radiated out of openings' corners and propagated through the joints in a stepped pattern. They extended throughout the whole width of the side walls and were visible both from the exterior and the interior of the structure. Damage at the upper section of the walls spread towards the intersections with the rear wall, eventually joining

with the cracks that formed just below the roof rafters. During the two final test cycles, out-of-plane displacement of the side walls' upper cracked sections was also recorded. No dislocation of the openings' lintels was noted in the tests, although loss of bonding between timber and masonry occurred.

In all cases, failure was characterized by loss of bonding between the masonry units; no damage of the adobe bricks was reported. Crack opening was significant and ranged from 5 to 20 mm (Figures 6.6b, 6.7b, 6.9b). Interestingly enough, when the loading was removed, the fissures formed at the cracked joints closed completely and no sign of damage was visible. However, cohesion between the masonry units at these areas had been lost and when load was exerted again, re-opening of the cracks was mobilized.

Despite the fact that the experimental setup enabled only the imposition of monotonously increasing forces, the recorded modes of damage correspond to those observed in dynamic tests and to those sustained by adobe buildings during earthquakes. The realistic reproduction of cracking patterns and failure mechanisms verifies the accurate simulation of boundary conditions and load distributions, enhancing the reliability of the experimental data obtained (Tomaževič, 2000).

Regarding the cracks recorded at the external surface of the rear wall, most researchers (e.g. Tolles et al., 1996; Houben and Guillard, 1994; Doat et al., 1991; McHenry, 1989; Yucheng and Liu, 1987) agree that adobe walls are quite susceptible to damage resulting from out-of-plane flexural stresses. According to the data reported in the literature, out-of-plane crack damage initiates at the cross-walls and can either extend vertically, or propagate diagonally and run horizontally along the wall's base. When basal horizontal cracks are formed, these act as centers of out-of-plane rotation for damaged walls. Cracking analogous to that hereby described and subsequent overturning of adobe walls, have been observed by Tolles and Krawinkler (1990) and Tolles et al. (2000) during shake table tests on 1:5 and 1:2 scaled model buildings. Similar out-of-plane failure of adobe masonry has also been reported by Illampas et al. (2013), following in situ inspections to earthen buildings. It must be noted however that separation between the model structure's intersecting walls did not occur, although such response to dynamic excitation has been observed in experiments (Ottazzi et al., 1988; Meli et al., 1980) and in field conditions (Blondet et al., 2008b). This is attributed to the unilateral and monotonic load imposition process.

The damage mode observed at the interior face of the rear wall is consistent with the observations made by Torrealva et al. (2008) who conducted loading-unloading out-of-plane bending tests on full-scale adobe walls incorporating horizontal supports at their top and bottom. Torrealva et al. noted that bending failure is characterized by the formation of a static instability zone along the line of lateral loading. When examining the effects of the 1994 Northbridge earthquake, Tolles et al. (1996) recorded the formation of such continuous horizontal cracks near the mid-height of long and slender adobe walls that were restrained at the top and were subjected to out-of-plane seismic forces.

Most experimental studies on full- or reduced-scale adobe buildings involve the implementation of shake table tests. During such tests, dynamic oscillations are imposed to all walls of a structure and, therefore, similar forms of damage are generally observed at all sections perpendicular to the direction of loading. Likewise to rear longitudinal walls, façade walls subjected to out-of-plane bending tend to develop horizontal, diagonal and/or vertical detachment cracks, which may occasionally lead to overturning and partial or total collapse (Tolles and Krawinkler, 1990; Tolles et al., 2000). The static loads imposed to the model building hereby examined could not be effectively transferred from its rear wall to its façade due to the lack of diaphragmatic roof function caused by sliding failure at the rafters' supports. Instead, the movement of the façade was dictated by the in-plane drift of the two side walls and was, thus, rather limited. As a result, at the levels of loading examined, no noticeable damage (i.e. cracking and/or detachment) of the façade occurred.

The two side walls exhibited diagonal shear cracking. The development of diagonal shear cracks on walls subjected to in-plane loading has also been reported by Torrealva et al. (2008) and Figueiredo et al. (2013), who performed cyclic load tests on full-scale adobe wall configurations. The same form of damage has been observed by Ersubasi and Korkmaz (2010) and by Tolles and Krawinkler (1990), who carried out shake table tests on 1:10 and 1:5 scaled-down model buildings. Field studies conducted after the 1994 Northbridge (Tolles et al., 1996) and the 2007 Pisco (Blondet et al., 2008b) earthquakes confirm that diagonal cracks can develop on adobe walls with orientations parallel to the principal component of the seismic action. According to Tolles et al. (1996), in-plane shear damage tends to concentrate at parts of the structure located between openings, or in areas between intersections with perpendicular walls. Tolles et al. (1996), Tolles and Krawinkler (1990) and Houben and Guillard (1994) mention that diagonal cracks generally occur near the corners of doors and windows, where tensile stresses are concentrated, and usually

extend towards the top and bottom of the walls. This is entirely in line with the damage mode reported for the two side walls of the model building tested herein.

The propagation of failure through the earth mortar joints observed in all cracked sections verifies the outcomes of diagonal tension tests (see section 4.4). Moreover, it is in agreement with the statements of Ottazzi et al. (1988), Tolles and Krawinkler (1990), Walker (1999) and Azeredo and Morel (2009). These researchers concluded that the effect posed by the block/mortar interface properties on the behaviour of adobe construction is critical. This is further supported by the comments of Kiyono and Kalantari (2004), who studied the collapse mechanisms of adobe masonry structures during the 2003 Iran Bam earthquake. The aforementioned researchers point out that the damage induced by seismic action is, in the majority of cases, primarily a product of weak adherence among the adobes.

Of particular interest is the complete closing of cracks recorded in the unloading phase. This should be taken into consideration carefully, since it implies that the in situ inspection of adobe buildings after seismic events may not necessarily reveal all damaged parts of the structure. Tolles and Krawinkler (1990) emphasize the cumulative effect that such pre-existing damage poses on the behaviour of adobe masonry construction. They indicate that, traditional earthen buildings tend to respond poorly to earthquakes, as their load-bearing elements often incorporate planes of weakness (i.e. cracked sections) due to previous seismic action or ground settlement.

6.3.3.2 Force-displacement response

Table 6.1 reports the maximum force applied to the model building by the hydraulic jack and the maximum displacements and permanent deformations recorded at the rear (LVDT13), façade (LVDT1) and side (LVDT3) walls for each test cycle. It also presents cumulative displacement and deformation data for the same monitoring points; these were computed by adding to the recordings of each individual test cycle the permanent deformations noted after the completion of all previous cycles. Force-displacement curves obtained from the implementation of the 10 test cycles are presented in Figure 6.10. Figures 6.10a and b show the cumulative out-of-plane displacements for the upper central parts of the rear wall and the façade, in relation to the load imposed. The variation of the cumulative in-plane displacement monitored at the upper section of the side wall, in relation to the load imposed is presented in Figure 6.10c. The envelopes of all force-

displacement curves are also noted in Figure 6.10 and are compared in Figure 6.11. Based on the structural response recorded, and the corresponding state of damage, limit states at different levels of deformation are additionally denoted in Figure 6.11.

Table 6.1: Maximum force applied to the model building by the hydraulic jack and actual maximum displacements and permanent deformations recorded at the rear (LVDT13), façade (LVDT1) and side (LVDT3) walls for each test cycle. Corresponding cumulative displacement and deformation data computed by adding to the recordings of each individual cycle the permanent deformations noted after the completion of all previous tests are also reported.

		Maximum displacement (mm)						Permanent deformation (mm)					
		Actual			Cumulative			Actual			Cumulative		
Test cycle	Force (kN)	Rear Wall	Façade	Side Wall	Rear Wall	Façade	Side Wall	Rear Wall	Façade	Side Wall	Rear Wall	Façade	Side Wall
1	12.0	4.1	3.9	3.8	4.1	3.9	3.8	0.4	0.6	0.2	0.4	0.6	0.2
2	10.6	16.2	9.7	10.3	16.6	10.3	10.4	6.1	0.9	1.5	6.4	1.5	1.7
3	12.7	16.6	7.7	8.5	23.0	9.2	10.2	3.6	0.5	0.7	10.1	2.1	2.4
4	14.2	11.5	4.9	5.3	21.5	7.0	7.7	3.0	0.5	1.4	13.1	2.6	3.8
5	14.2	30.7	12.8	13.7	43.7	15.3	17.5	6.7	3.0	2.4	19.7	5.5	6.2
6	13.5	27.5	12.4	12.9	47.3	17.9	19.1	2.0	0.6	0.7	21.8	6.1	6.9
7	13.2	51.4	15.0	15.7	73.2	21.1	22.6	9.1	0.5	1.8	30.9	6.6	8.7
8	11.2	28.2	8.4	8.8	59.1	15.0	17.5	5.4	2.4	1.6	36.4	9.0	10.3
9	13.1	48.5	14.9	14.9	84.9	23.8	25.2	1.3	0.4	1.0	37.7	9.4	11.3
10	9.1	58.4	17.3	17.7	96.0	26.6	27.1	7.5	2.2	1.3	45.2	11.6	12.6

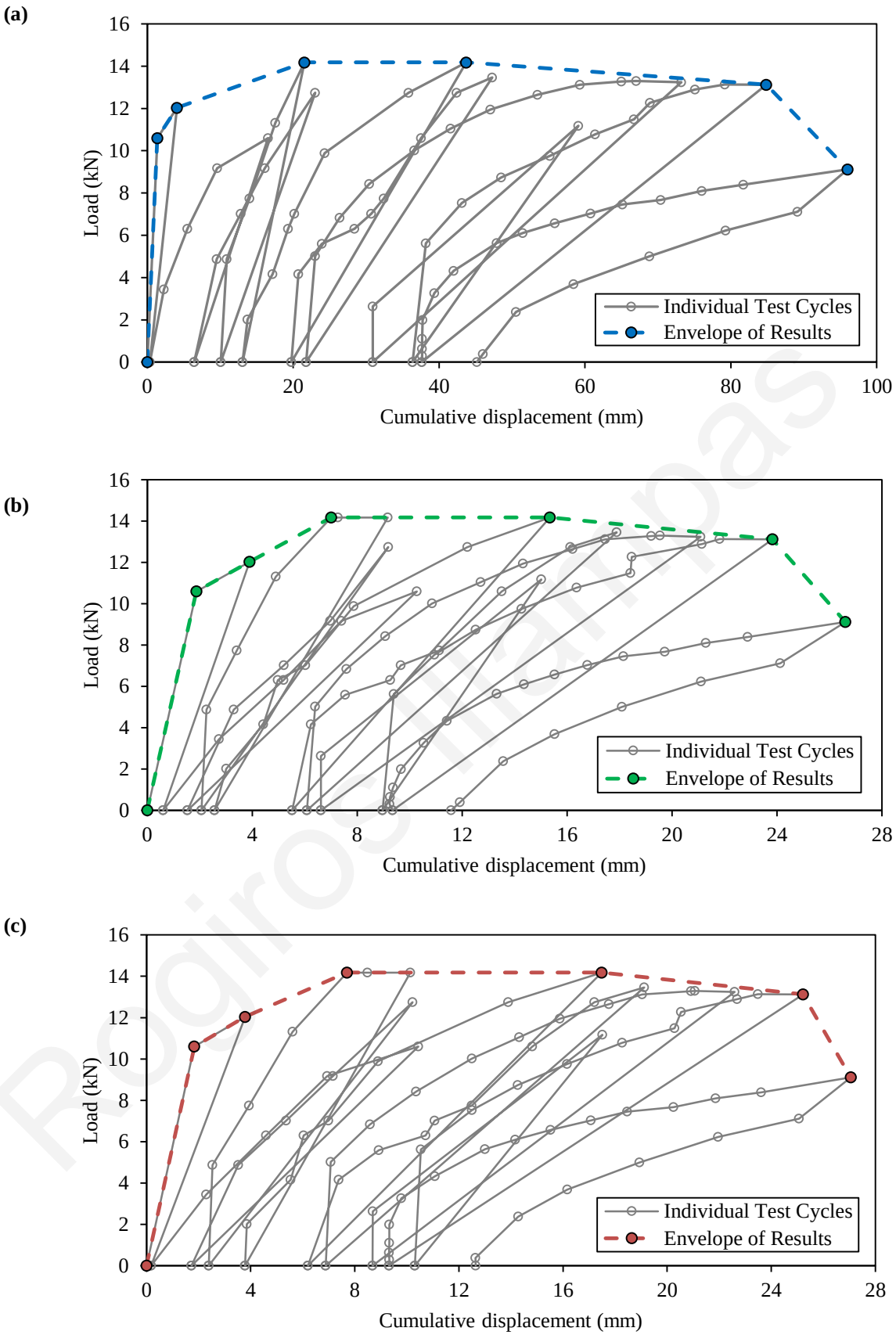

Figure 6.10: Load vs. out-of-plane cumulative displacement for the upper central sections of the rear wall (LVDT13) (a) and the façade (LVDT1) (b); Load vs. in-plane cumulative displacement for the upper section of the side wall (LVDT3) (c).

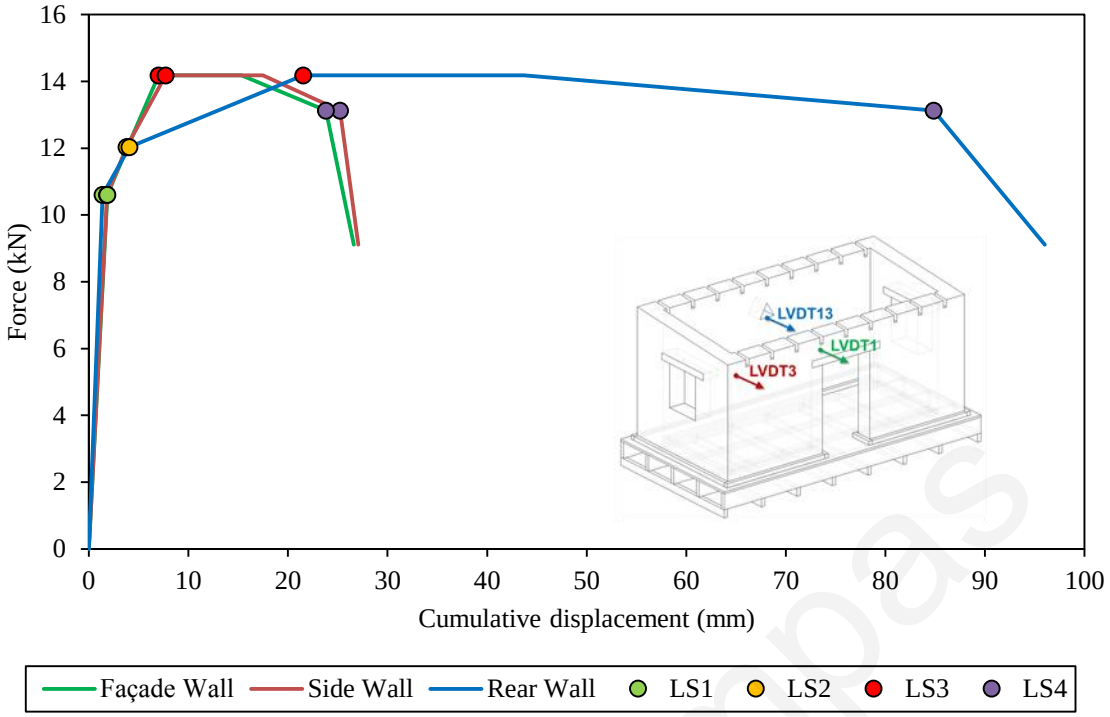

Figure 6.11: Comparison between the force-displacement data envelopes for the upper sections of the façade, the side wall and the rear wall. Four limit states are identified at different levels of deformation. A consistent response to loading, with no or negligible damage occurs prior to LS1. Up to LS2, cracking and stiffness degradation start to develop, but the load-resisting elements maintain a homogeneous response. This is followed by differential movement, considerable stiffness reduction, cracking damage and permanent distortion up to LS3. Depletion of the overall stiffness and severe deformation occur until the lateral resistance falls to a residual value in LS4.

From the results reported above, it is evident that systematically higher displacement values were recorded at the center of the rear wall, at the level where loading was applied. The maximum displacement measured at this point increased, almost linearly, from 4 to 58 mm between test cycles 1 to 10. In the first test cycle, a 12 kN force was applied. This led to a 4 mm lateral translation of the rear wall and caused the onset of cracking damage, which reduced resistance to loading. As a result, in test cycles 2 to 4 the imposition of forces (10.6-14.2 kN) generated higher displacements, which ranged between 11.5-16.6 mm. Further loading increased the crack width and exacerbated strength degradation. Therefore, in test cycles 5 and 6, forces near 14 kN were able to move the rear wall's central section by approximately 30 mm. Subsequent test cycles led to the formation of additional cracks and mobilized the opening of pre-existing fissures. During test cycles 7 and 9, the maximum lateral translations measured were close to 50 mm, while the forces imposed on the structure were in the region of 13 kN. In the last test cycle, the overall

bearing capacity of the structure reduced significantly, since all load resisting elements (i.e. the rear and the two side walls) had already sustained severe cracking. Although the force exerted did not exceed 10 kN, the out-of-plane displacement of the rear wall was as high as 58.4 mm.

According to the data obtained, horizontal loading also led to the development of considerable permanent deformations at the model's rear wall. This occurred in the form of bulging at its central region. Inelastic lateral translations noted after the completion of individual load tests range from 0.4 mm to 9.1 mm. By considering the sum of all deformations, along with the recorded displacements, the cumulative lateral translation of the rear wall was found to be 96 mm, while the total, non-reversible shifting at its center was 45 mm.

The actual displacements recorded at the upper sections of the side wall and the façade during the individual test cycles were approximately equal and varied from 3.8 to 17.7 mm. In the first test cycle, the maximum translation of all walls was almost the same and lied in the region of 4 mm. Masonry cracking and sliding failure of the roof rafters' supports altered the stress distribution among the load resisting elements, thus precluding further homogenous structural response. Consequently, during test cycles 2 to 4 the displacements noted at the rear wall were greater than those generated at the side wall and the façade. The upper sections of the side wall and the façade shifted by 4.9-10.3 mm when 10.6-14.2 kN loads were imposed. Due to the accumulation of cracking damage on the masonry, the lateral displacements of these same monitoring points increased to 8.4-15.7 mm under the 11.2-13.5 kN horizontal forces exerted in cycles 5 to 9. Finally, the 9.1 kN force applied in test cycle 10 caused the same walls to move by approximately 18 mm.

The cumulative out-of-plane and in-plane displacements, obtained respectively for the upper sections of the façade and the side wall, were near 26.6 mm and 27.1 mm. These are below 30% of the corresponding value measured for the rear wall. Experimental data show that, by the end of each load cycle, the monitoring point at the center of façade had shifted horizontally 0.4-3 mm from its original position. The façade's cumulative inelastic out-of-plane deformation reached 11.6 mm at the end of the experimental program.

Likewise, the side wall sustained 0.2-2.4 mm irreversible displacements during individual tests. The cumulative deformation noted at the top of this wall was 12.6 mm, which accounts for 0.84% in-plane drift (estimated as the recorded horizontal displacement divided by the monitoring point's vertical distance from the model building's base).

Although the monitored response of the transversal wall was characterized mainly by in-plane angular distortion, some out-of-plane movement of the upper cracked section was also observed in the last test cycle. According to the readings of LVDT10, the out-of-plane displacement at this point was approximately 7 mm and was non-reversible.

The significant differential movement of the walls verifies the inadequate interaction among the structure's load-bearing members and the lack of homogeneous response to horizontal loading. This behaviour is primarily attributed to the fact that the timber roof was not stiff enough and was poorly connected with the underlying walls. Therefore, it was unable to function as a diaphragm and could not provide the required lateral support. After the first test cycle, where the bonding mortar at the abutments of the rafters failed, the transfer of forces from the roof to the masonry could only be achieved via friction mechanisms. Friction alone however, was not enough to prevent sliding of the rafters and to ensure an effective transfer of loads between the two opposite longitudinal walls. The rear wall functioned as a panel hinged at the base and the two sides, but unconstrained at the top. On the other hand, the response of the façade was governed by the behaviour of the stiffer side walls. The in-plane drift of the side walls was transferred to the façade through the cross-walls. Hence, the out-of-plain displacement of the façade was equivalent to the in-plane lateral translation of the side walls.

Apart from the recorded lateral in- and out-of plane translations of the various walls, significant upwards displacement of rear and side walls' upper sections was observed during the tests. Unfortunately, relevant quantitative information cannot be given since the upwards movement of these sections was not monitored with the available equipment.

Examining the experimental data envelopes, three limit states of damage can be identified (Figure 6.10). Up to approximately 5% of its total displacement capacity and 75% (10.6 kN) of its maximum lateral resistance (LS1), the structure performed with no or negligible damage and the various load-bearing members maintained a consistent response to horizontal loading. The displacements recorded at the model structure's walls during this stage were rather uniformly distributed. Displacement values measured at the upper sections of the rear wall, the side wall and the façade were almost equal and were close to 1.8 mm, corresponding to approximately 0.11% drifts.

After the 10.6 kN threshold was exceeded, stiffness degradation and cracking damage started to develop. A major horizontal crack at the interior of the model structure's rear wall was noted, while the formation of diagonal cracks at the two side walls was initiated.

The structure however, could still function as a homogeneous structural system up to 11% of its total displacement capacity and 85% (12 kN) of its maximum lateral resistance (LS2). A coinstantaneous movement of 4 mm and a lateral drift of 0.26% were recorded at the upper sections of the walls monitored. It must be noted that the first and second limit states were already reached by the end of the initial test cycle.

When the displacement induced exceeded 11% of the total displacement capacity, interaction among the structure's load-bearing members was effectively lost and differential movement of the masonry walls took place (LS3). This was accompanied by further cracking, permanent distortion and considerable reduction of the overall stiffness. Such non-linear response continued until the load exerted became equal to the maximum force the structure could withstand and the displacement induced was 26% of the total deformation capacity. During this stage, debonding at the roof rafters' supports was observed and cracking at the base of the rear wall developed. Furthermore, the cracks previously formed at the interior surface of the rear wall extended and the diagonal shear cracks at the two side walls became clearly visible. The magnitude of the maximum horizontal force was 14.2 kN. Cumulative displacements at the façade and the side wall were 7 and 7.7 mm, respectively. In terms of lateral drift, these values can be interpreted as 0.5%. Cumulative displacement at the center of the rear wall was 21.6 mm and accounts for 1.4% lateral drift. The aforementioned data were obtained after the completion of the first four test cycles.

The last limit state was characterized by depletion of the overall stiffness and by inability of the structure to sustain higher levels of loading (LS4). Crack opening increased considerably and relatively small augments of the imposed load could generate large in- and out-of-plane drifts. Moreover, significant inelastic deformations were generated. During this stage, crack openings at the walls of the model building attained their maximum value (≈ 20 mm). The cumulative horizontal translation of the side wall was 23.8 mm, while that of the façade was 25.2 mm. The lateral drift at these sections was estimated as 1.6%. The total movement of the rear wall was 84.9 mm, while the lateral drift at its central section was 5.7%.

Beyond this stage, an abrupt drop in the structure's lateral resistance occurred. Certain sections of the masonry (e.g. upper section of the side walls) were isolated by cracking damage, thus forming kinematic mechanisms and reducing the effective resisting area. These mechanisms were mobilized under the application of load. Although the overall strength fell to a residual value, total or partial collapse did not occur. Nevertheless, it can

be argued that crack growth and/or formation at this state could have been critical, if the relative displacement induced across the planes of weakness had been larger.

Due to the fact that most experimental studies investigating the behaviour of adobe model buildings involve shake table tests and/or static tilt tests on retrofitted structures, many of the results quoted in the literature are not directly comparable to the force-displacement response hereby described. However, some direct analogies can be found with the data reported by certain researchers (e.g. Figueiredo et al., 2013; Torrealva et al., 2008; Blondet et al., 2005), who performed cyclic static tests on unreinforced adobe masonry wall configurations.

In particular, the deformation levels associated with the various damage states of the full-scale 'I'-shaped wall examined by Figueiredo et al. (2013) are in agreement with those hereby reported. Figueiredo et al. (2013) noted that damage initiation occurs at drift levels 0.02-0.2%. They also observed a considerable strength reduction and an intensification of damage evolution at drift levels exceeding 0.5%.

Using the experimental data of Torrealva et al. (2008) and Blondet et al. (2005), which refer to the in-plane response of full-scale 'I'-shaped walls, Tarque et al. (2010b) also defined damage limit states similar to those reported in this thesis. Tarque et al. (2010b) stated that non-linear response is initiated after 0.052% lateral drift; crack propagation and stiffness degradation occur between 0.1-0.26% drift and the near-collapse state is reached at 0.52% drift.

The experimentally recorded maximum load resistance accounts for approximately 30% of the model building's self-weight. Shake table tests conducted by Ottazzi et al. (1988) on unreinforced adobe masonry buildings produced base shear force-to-weight ratios of 45% and 80%, depending on the quality of the materials used in their construction. Adobe model houses reinforced with tie beams and/or cane rods that were tested by the same researchers sustained loads between 50-100% of their total weight. Base shear force-to-weight ratios computed from the data reported by Blondet et al. (2005) and Tarque (2011) regarding cyclic displacement-controlled tests performed on full-scale 'I'-shaped walls lie between 37% and 50%. A maximum base load accounting for 130% of the total structure's weight was recorded by Bartolomé et al. (2009) during the dynamic testing of a two storey confined adobe building. According to the results given in Samali et al. (2011), 1:3 scaled adobe modules with square and circular wall configurations were able to resist horizontal loads up to 34% and 46% of their self-weight , respectively, when subjected to static tilt-

table tests. It is worth noting that most peak load resistance values reported by researchers examining adobe structures are considerably high, compared to relevant data concerning other types of masonry construction. An extended experimental program carried out by Benedetti et al. (1998) revealed that the capacity of unreinforced masonry buildings to resist lateral seismic forces does not exceed 30% of their self-weight for structures composed of fired clay bricks and 19% of their self-weight for structures composed of ashlar stone.

Although the value of load-bearing capacity hereby assessed is more conservative than most corresponding values encountered in the literature, it cannot be adopted as a safe indicator for the dynamic response of unreinforced adobe masonry construction. This is because the monotonic imposition of forces during the testing procedure did not enable the development of certain failure mechanisms (e.g. detachment of intersecting walls) that would drastically reduce lateral resistance in the event of seismic excitation. Nevertheless, valuable information regarding the general behaviour of adobe structures under horizontal loads can be deduced from the experimental outcomes reported.

6.4 Analytical prediction of the load-bearing capacity of scaled adobe model building

In this section the experimentally recorded lateral resistance of the scaled model building is compared against analytical predictions of load-bearing capacity. The methodology adopted is based on the idealization of the observed damage modes into simplified kinematic mechanisms and on the calculation of the force-displacement response for each of the structure's load-resisting elements, following the suggestions of Magenes and Della Fontana (1998), Anania and Badalà (1998), Doherty et al. (2002), Tomaževič (2008), Sabatino and Rizzano (2011), Marques and Lourenço (2011) and Griffith et al. (2003). A detailed review of the analytical methods hereby used is presented in Magenes (2006), while comparative examples of their application can be found in Marques and Lourenço (2011) and in Shahzada et al. (2012).

The kinematic model used for evaluating the lateral load resistance of the side walls is shown in Figure 6.12. It is considered that the horizontal thrusts imposed on the structure cause the development of plastic hinges at upper and lower sides of the wall and at the corners of the window opening. Failure propagation causes separation between the piers

and the wall's base and top. The two cracked panels that are eventually formed are subjected to parallel in-plane rotation and/or sliding and the overlying structure undertakes rigid translation.

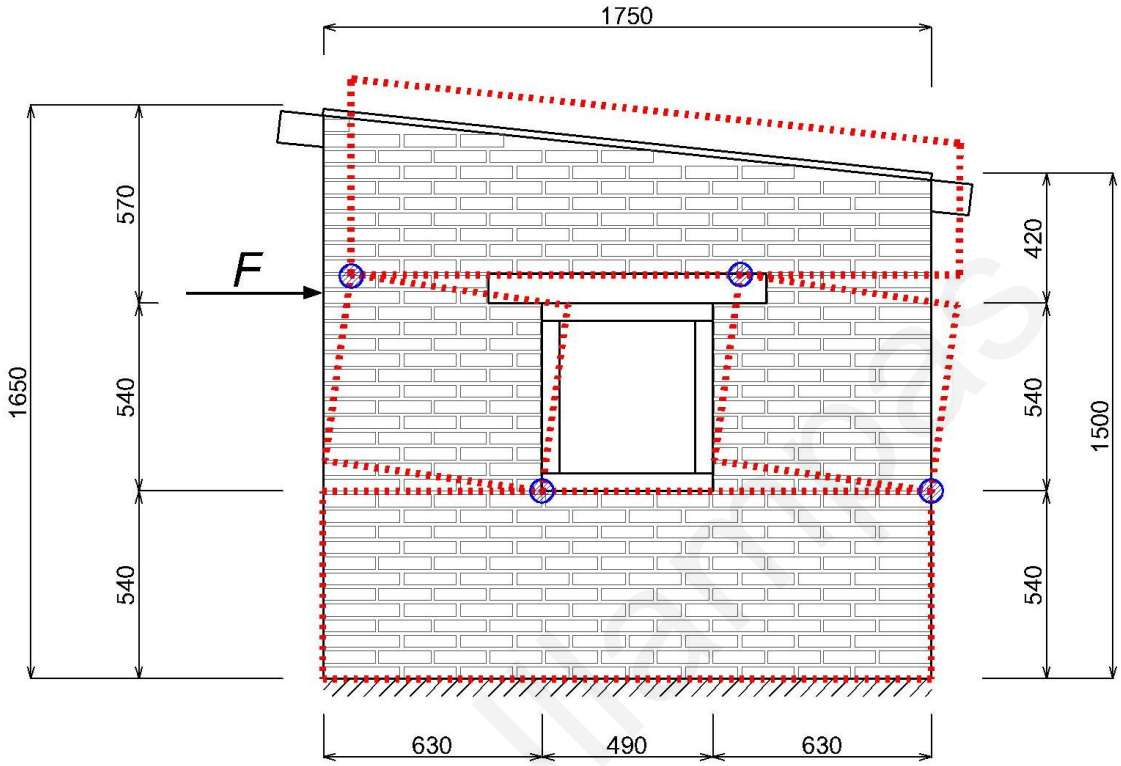

Figure 6.12: Simplified kinematic model used for evaluating the lateral load resistance of the scaled building's side walls.

The load capacity of the piers was evaluated by considering three possible failure mechanisms: combined flexure, sliding shear and diagonal tension. The computation of the resistance domains under these mechanisms was made in accordance to the relations given in Figure 6.13. In-plane lateral resistance V was computed as a function of (a) the panel dimensions: length B_w, height H_w and thickness t_w; (b) the masonry mechanical properties: compressive strength f_w, diagonal tensile strength f_t, friction coefficient μ and cohesion c among the masonry units and (c) the axial forces N_1 and N_2 acting on the upper and lower ends of the panel. The latter were estimated as N_1 = 1.55 kN and N_2 = 0.95 kN after considering the overbearing weights of the masonry and the roof.

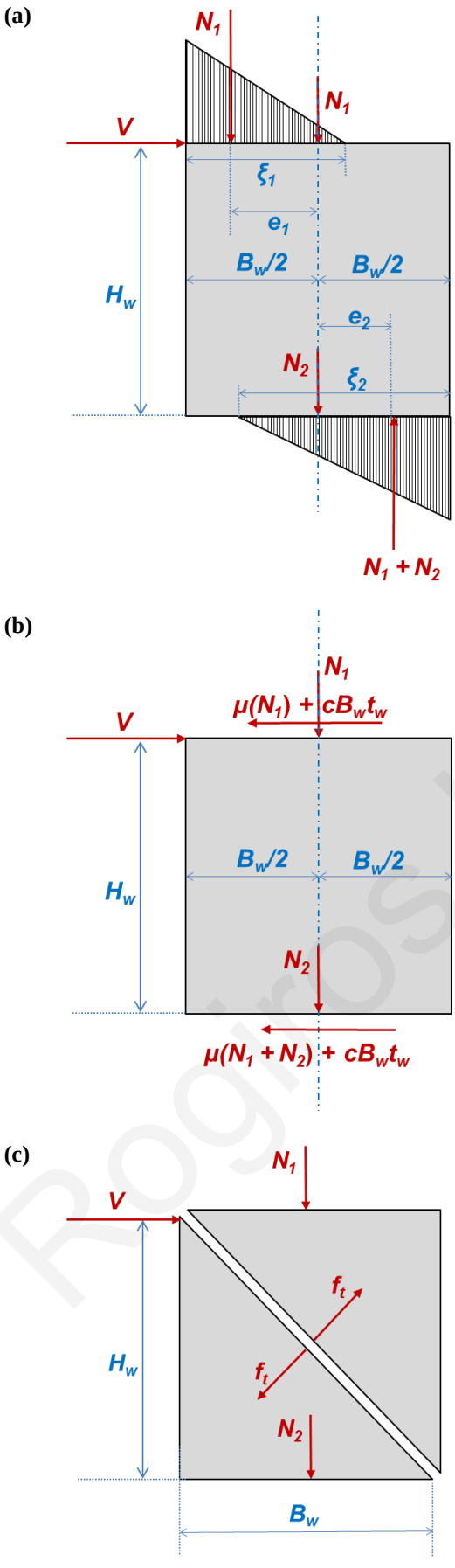

$$V_{bend} = \frac{1}{H_w}\left[(N_1 + N_2)\left(\frac{B_w}{2} - \frac{\xi_2}{3}\right) + N_1\left(\frac{B_w}{2} - \frac{\xi_1}{3}\right)\right]$$

$$V_{slid} = \mu(2N_1 + N_2) + 2cB_w t_w$$

$$V_{diag} = B_w t_w \frac{f_t}{b_s}\sqrt{\frac{\sigma_d}{f_t} + 1}$$

Figure 6.13: Formulation of the resistance domains in the *V–N* plane for the side walls' piers: (a) combined flexure, (b) sliding shear and (c) diagonal tension.

The formulation of the resistance domain under combined flexure was established from the equilibrium of moments produced by the imposed lateral load and the resultant forces of the triangular compressive stress distributions assumed at the upper and lower pier ends (Figure 6.13a). The initial bending resistance (V_{bend}^{0}) was computed by setting the lengths of the compression zones (ξ_1 and ξ_2) equal to the total length of the panel (B_w). It was found to be V_{bend}^{0} = 0.74 kN. The minimum allowable lengths ξ_1 = 7.6 mm and ξ_2 = 12.3 mm used in estimating the ultimate bending resistance (V_{bend}^{ult}) were such that the stresses acting at the two extreme compression fibers of the panel would not exceed the compressive strength of adobe masonry (f_w = 1.8 MPa). This yielded an ultimate bending resistance of V_{bend}^{ult} = 2.18 kN.

The sliding shear (V_{slid}) was formulated using the Mohr-Coulomb criterion, which expresses the maximum shear strength as the sum of frictional resistance and cohesive strength capacity (Figure 6.13b). A friction coefficient μ = 0.5 was used in accordance to the data reported by Kiyono and Kalantari (2004). Since the experimental investigation conducted in this study revealed that weak bonding exists among adobes joint with earth mortar (see sections 4.3.3, 4.4.3 and 6.3.3), a null cohesive strength (c = 0) was assumed in all calculations. The parameteres adopted produsedan estimation for the shear sliding resistance V_{slid} = 2.02 kN.

The formulation for the diagonal tension (V_{diag}) was derived by considering the stress state in the center of the pier for the limit case in which the principal stress attains a critical value (Figure 6.13c). In this case, the relation proposed by Tomaževič (2008), which is based on the assumption of elastic, homogeneous and isotropic masonry, was adopted. For the implementation of the analytical calculations, the compressive stress at the center of the pier was computed (σ_d = 0.0092 MPa). The tensile strength of the masonry (f_t) was assumed equal to the average tensile stress recorded in the diagonal tension tests conducted in this study; f_t = 0.04 MPa. In addition, a shear stress distribution factor of b_s = 1.5 was considered, based on the recommendations of Tomaževič (2008). The diagonal tensile resistance of the pier was evaluated as V_{diag} = 3.99 kN.

The response of the pier at each stage depends on the minimal resistance computed through all three possible mechanisms. According to the calculations made, the elastic limit is

reached as soon as the initial bending resistance (V_{bend}^{0}) is exceeded. However, shear sliding precedes ultimate bending failure and diagonal tensile failure ($V_{\text{slid}} < V_{bend}^{ult} < V_{\text{diag}}$).

The displacement d_{pier} generated at the top of the piers at each of the aforementioned behaviour stages was computed as a function of bending and shear deformations. Since the piers are pinned at both ends, the following equation was adopted (Tomaževič, 2008; Marques and Lourenço 2011):

$$d_{pier} = \frac{V_i h^3}{12 E I_w} + \frac{\kappa V_i h}{G A_w} \tag{6.1}$$

In equation 6.1 V_i is the lateral force at each critical state, I_w is the moment of inertia of the pier's horizontal cross-section and κ is the shear coefficient, considered as $\kappa = 1.2$ for the rectangular section examined (Tomaževič, 2008). The elastic (E = 17.4 MPa) and shear (G = 4.1 MPa) moduli used for computing the displacement at the elastic limit (d_{pier}^{el}) were set equal to the average experimental results obtained from the implementation of compression tests on stack-bonded prisms and of diagonal tension tests on an adobe wallette (see section 4). The above parameters yielded $d_{pier}^{el} = 1$ mm. Displacement at the plastic limit stage was estimated as $d_{pier}^{pl} = 5.6$ mm by assuming that the elastic and shear moduli of the cracked section are reduced to 30% of their original magnitude. Bearing in mind that the damage recorded on the piers during the laboratory tests had a generally stepped pattern, frictional resistance was considered to diminish when contact among the adobes ceased to exist. Hence, the ultimate displacement capacity (d_{pier}^{ult}) under shear sliding was assumed to be equal to the overlapping length among the bricks; $d_{pier}^{ult} = 75$ mm. The above calculations enabled the formulation of the tri-linear force-displacement diagram shown in Figure 6.14.

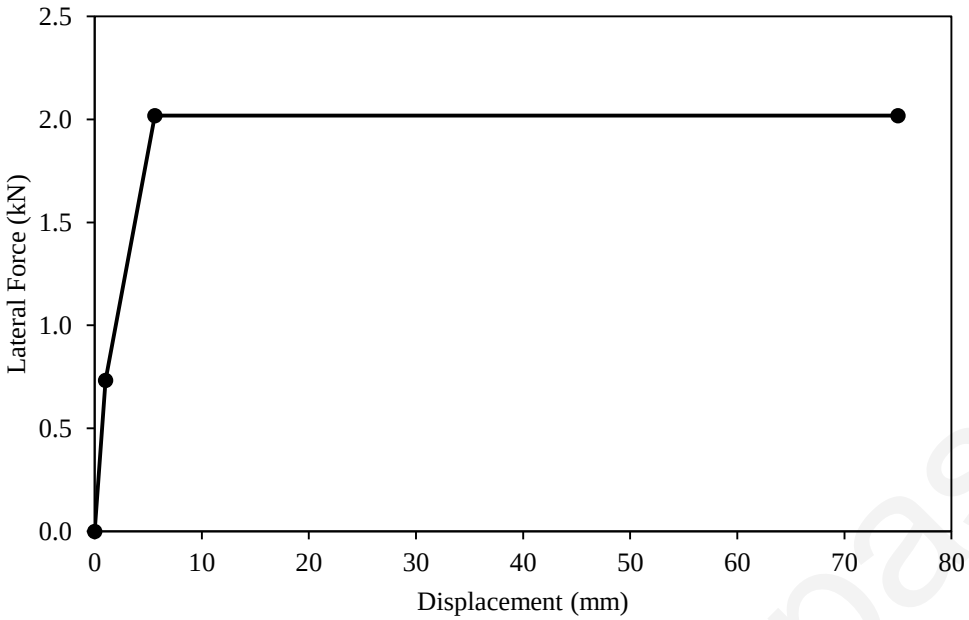

Figure 6.14: Tri-linear force-displacement approximation of the response of the side walls' piers to lateral loading.

The kinematic model used for studying the response of the rear wall is given in Figure 6.15a. The position of the plastic hinges was defined in accordance to the experimental observations made (Figure 6.5a, b). In this case, the failure mechanism was solely attributed to bending. The formulation of the bending resistance domain was again established from the equilibrium of moments as shown in Figure 6.15b. The elastic limit by flexure was computed as V_{bend}^{0} = 2 kN, while ultimate bending resistance was estimated as V_{bend}^{ult} = 3.5 kN. The corresponding lateral displacements were computed as δ^{el} = 0.05 mm and δ^{pl} = 0.17 mm by ignoring the shear deformation part of equation 6.1 and by using the same assumption for the elastic modulus reduction as previously noted.

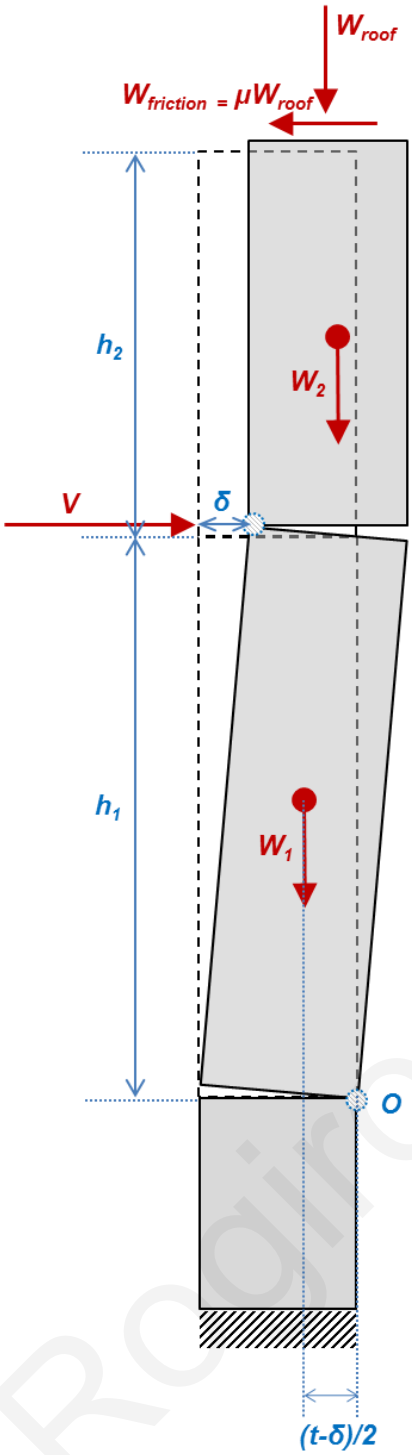

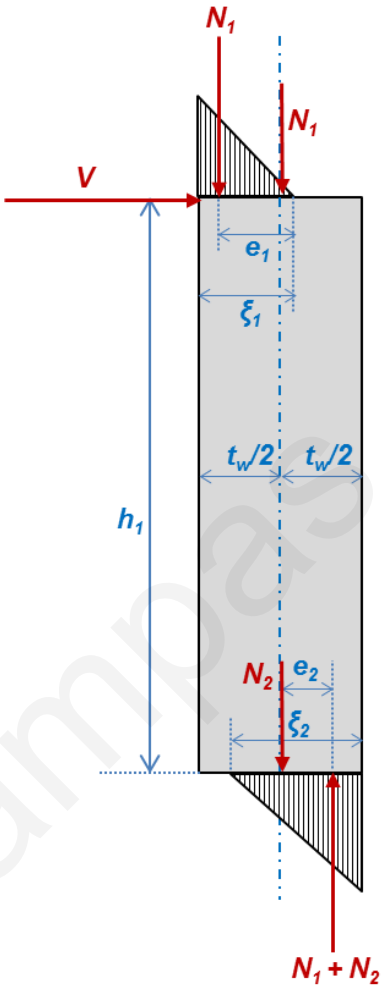

$$V = \frac{1}{h_1}\left[W_1(\frac{t_w}{2} - \frac{\delta}{2}) + (W_2 + W_{roof})(\frac{t_w}{2} - \delta) + W_{friction}(h_1 + h_2) \right]$$

$$V_{bend} = \frac{1}{h_1}\left[(N_1 + N_2)(\frac{t_w}{2} - \frac{\xi_2}{3}) + N_1(\frac{t_w}{2} - \frac{\xi_1}{3}) \right]$$

(a) **(b)**

Figure 6.15: (a) Kinematic model used for studying the response of the scaled structure's rear wall and moment equilibrium about the pivotal point *O* established for deriving the kinematic solution of rigid body motion. (b) Free body diagram and moment equilibrium equation defined used for determining the bending resistance domain of the rear wall's central cracked section.

According to the calculations made, the minimum lengths of the compression zones ξ_1 and ξ_2 are below 5.5 mm. This is particularly small and indicates that, when the section is fully cracked, crashing of the wall's extreme compression fibers is not likely to occur. Instead, rigid body rotation between the central and upper cracked sections can develop. Therefore, the moment equilibrium about the pivotal point *O* was established (Figure 6.15a) and the kinematic solution was obtained. The force-displacement response of the rear wall was approximated as the intersection between the flexural strength domain and the kinematic solution. This yielded the multi-linear diagram presented in Figure 6.16.

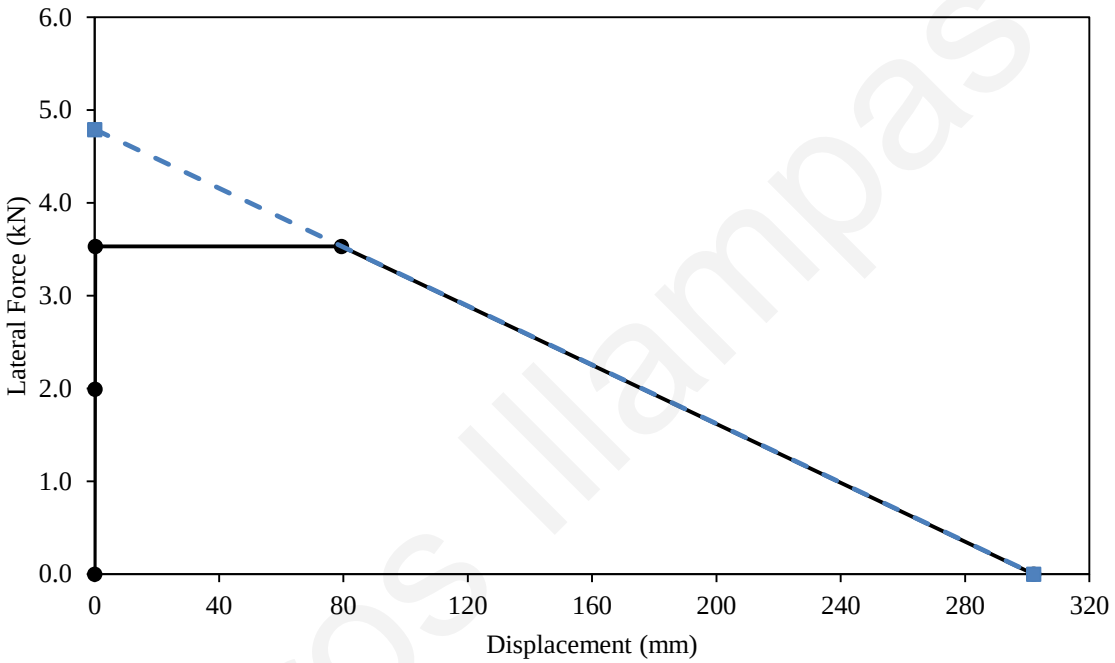

Figure 6.16: Multi-linear approximation of the force-displacement response of the rear wall derived from the intersection between the flexural strength domain and the kinematic solution.

After computing the response for each individual load-resisting element, the global capacity curve of the structure was derived by integrating the characteristic force-displacement curves. Since the data obtained from the laboratory tests show that the building's walls were subjected to differential movement, the contribution of each member to the global resistance was defined in accordance to the cumulative displacements recorded at every load cycle. Thus, the corresponding lateral strengths of the piers and the rear wall could be defined from the force-displacement diagrams hereby computed. In the calculation of the global resistance, an additional contribution from the façade wall was also accounted for. The façade wall was considered to perform in the elastic range due to the fact that it sustained no damage during the experimental procedure. Hence, its lateral

resistance at each load step was estimated by multiplying its total stiffness with the displacement recorded at its upper central section.

The resulting capacity curve is compared against the experimental data envelope for the scaled building's rear wall in Figure 6.17. Despite being overly simplistic, the result obtained from the implementation of the analytical method described herein underestimates the experimentally recorded maximum load only by 12.4%. This difference can be attributed to the crude hypothesis made regarding the absence of cohesive strength among the masonry units. In addition, some degree of frame action certainly develops among the various members of the actual building, as the structural system deforms under lateral loading. Nevertheless, the analytical model adequately captures the general form of the experimental force-displacement response, predicting the occurrence of an extended post-yield plateau. The abrupt drop in load-resistance could not be accurately predicted, possibly due to overestimation of the resisting elements' deformation capacity. In any case, considering the natural randomness and inhomogeneity of adobe materials, the analytical results obtained may be deemed as sufficiently accurate.

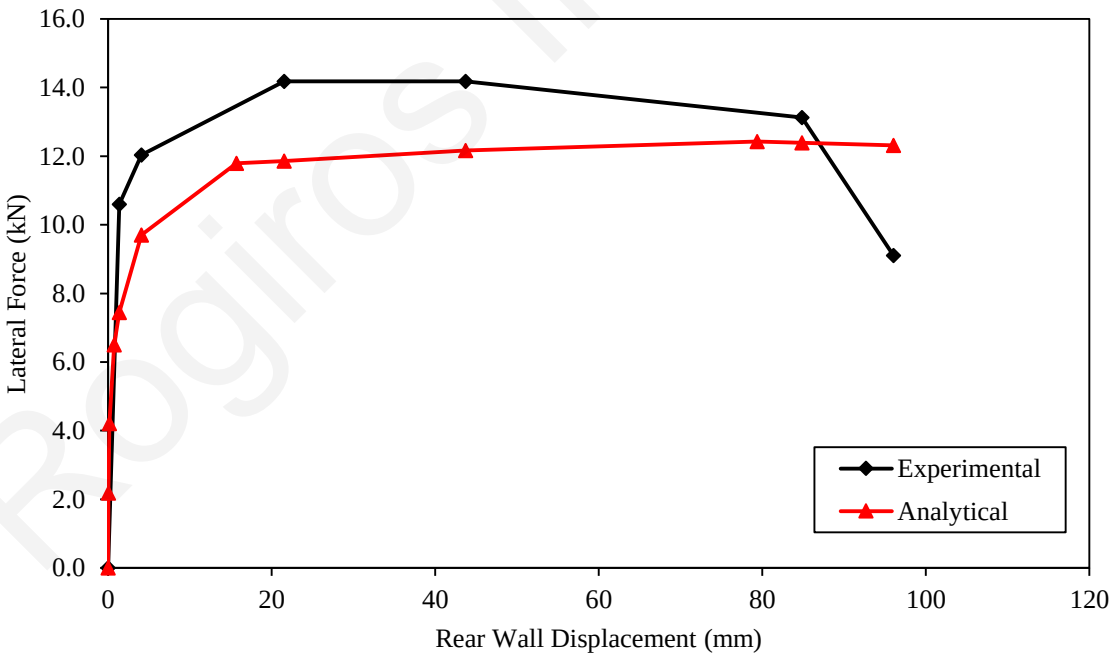

Figure 6.17: Comparison between experimental and analytical force-displacement curves for the scaled building's rear wall.

6.5 Numerical simulation of the response of adobe scaled model building

6.5.1 Finite element model

The response of the tested scaled building was simulated using a static non-linear analysis procedure provided in the Abaqus/CAE software. Computational work focused on reproducing the observed modes of damage and on approximating the load-displacement envelopes recorded for the rear wall, the façade and the side wall. For this purpose, a full 3D finite element model was developed. The various parts composing the experimental setup were modeled as individual bodies interacting with each other. Hence, the finite element model included different representations for the adobe masonry walls, the openings' lintels, the roof's rafters and panel and the timber loading-beam. Since all components of the test configuration are symmetric, only half the structure was numerically examined by imposing proper boundary conditions to the nodes lying on the symmetry plane.

All bodies were discretized using 8-noded 3D linear brick elements (C3D8). In order to examine the effect of mesh discretization in the results obtained, two models composed of elements with sides 100 and 40 mm in length were developed and analyzed (Figure 6.18). Acceptable deviation of the elements' size was set as ±10%. In the first case, the final model consisted of 4888 elements, 4998 nodes and involved 14994 degrees of freedom. The use of a denser mesh resulted in a total of 47808 elements, 68139 nodes and 169515 degrees of freedom.

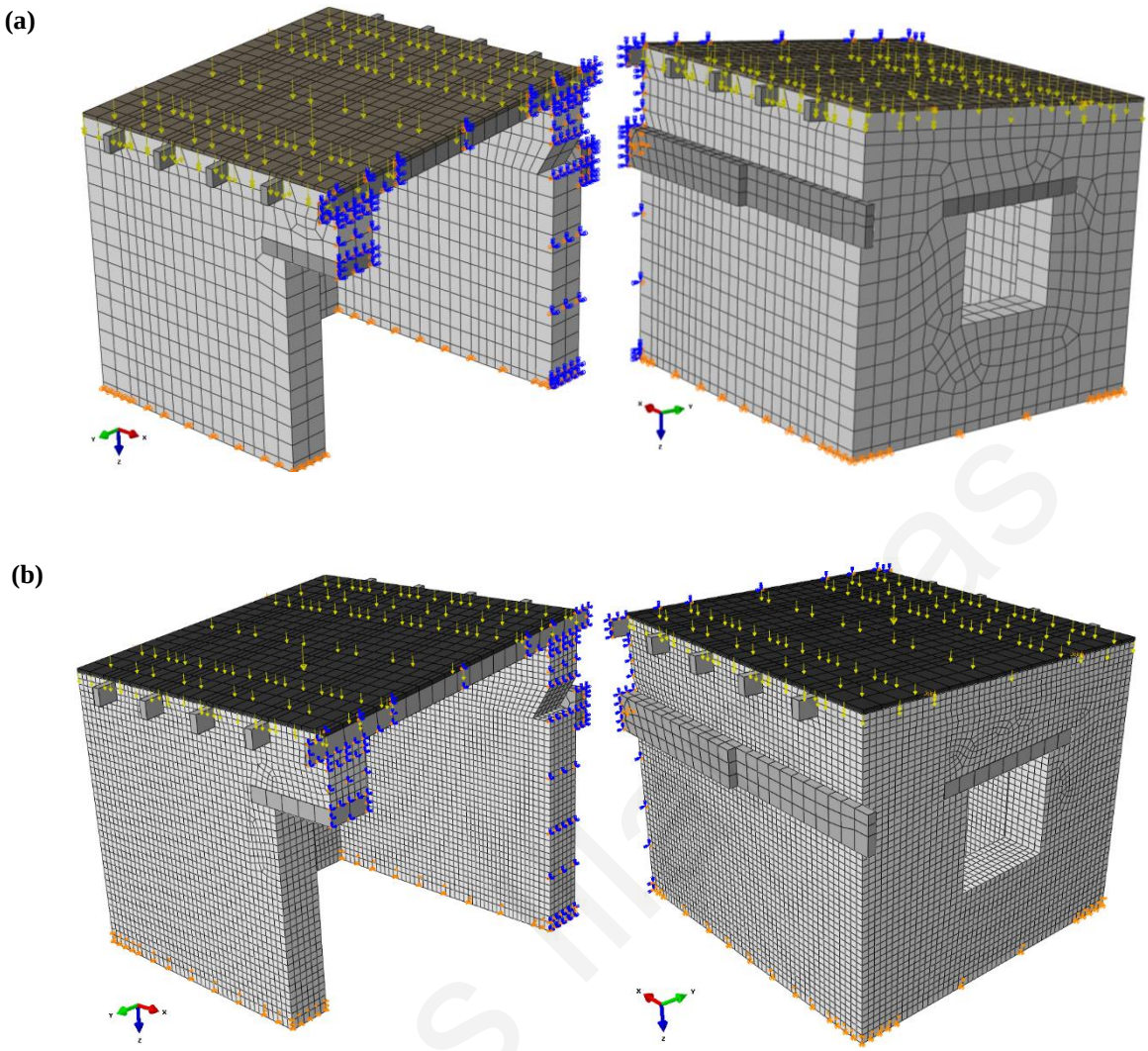

Figure 6.18: 3D finite element model developed for the simulation of lateral load tests on an adobe scaled building. Discretization into brick elements with sides (a) 100 and (b) 40 mm long.

Adobe masonry was numerically handled in the context of a macro-modeling strategy. It was thus treated as a fictitious homogeneous continuum and no distinction between masonry units and mortar joints was made. For simulating its behaviour, the concrete damaged plasticity constitutive model described in section 5.3 was adopted. As previously noted, this is a continuum, plasticity-based, isotropic damage model that assumes two main failure mechanisms: tensile cracking and compressive crushing. All material parameters used for modeling adobe masonry were the same as those adopted in the simulation of the diagonal tension test (see Table 5.2). However, due to the different characteristic element lengths of the masonry meshes (h = 100 mm and h = 40 mm as opposed to h = 57 mm for the diagonal tension test), the stress-strain diagrams describing the medium's tensile

response were recomputed in accordance with equation 5.24. The revised diagrams are given in Figure 6.19.

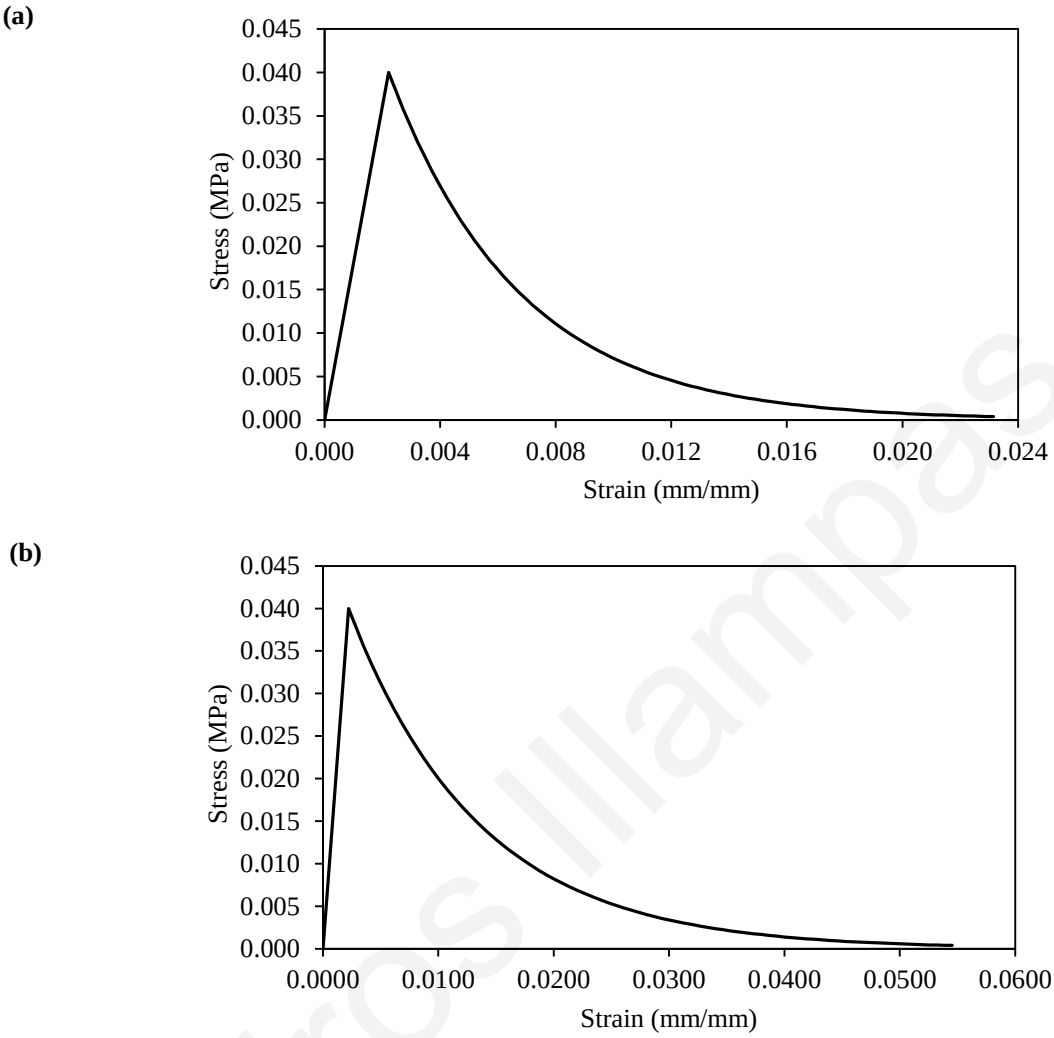

Figure 6.19: Stress-strain diagrams showing the tensile response assigned to the homogenized masonry for simulating a lateral load test on an adobe model building. Diagrams refer to meshes discretized into brick elements with sides (a) 100 and (b) 40 mm long.

Considering that, during the experimental procedure no damage or considerable deformation was observed in any of the timber members (lintels, rafters, loading-beam, roof panel), these were all presumed to perform in the elastic range at the levels of loading examined. Therefore, they were modeled using linear elasticity constitutive laws. In addition, the simplifying assumption that timber's mechanical properties are isotropic was made. The material parameters used were drawn from the literature (Green et al., 1999; Katsaragakis, 2000) and are as follows: (a) hardwood panel - density ρ = 380 kg/m^3; Young's modulus E = 8000 MPa; Poisson's ratio v = 0.2 and (b) timber lintels, rafters and

loading-beam - density ρ = 670 kg/m^3; Young's modulus E = 7000 MPa; Poisson's ratio ν = 0.3.

At the areas where the masonry was in contact with the loading-beam, the openings' lintels, the roof rafters and the roof panel, contact pairs were formed and surface to surface interactions were formulated. In all cases, timber elements were chosen as the master surface, as these belonged to structures stiffer than the masonry walls.

A friction coefficient of μ = 0.5 was adopted for modeling mechanical contact at the interfaces between the masonry and the openings' lintels and the masonry and the roof rafters. Experimental data regarding the frictional properties of timber elements embedded in adobe masonry members were not detected in the literature. Information however, was found for adobe bricks alone, jointed with different types of mortar. Kiyono and Kalantari (2004), who conducted in situ shear-sliding tests on adobes jointed with earth mortar, measured friction coefficients between 0.5 and 0.65, whereas Almeida (2012), who performed direct shear tests on adobe couplets with lime mortar joints, derived a friction coefficient of 1.35. Several numerical analyses were implemented using different friction coefficients within the above range of values ($0.5 < \mu < 1.35$). It was noted that better matching between experimental-numerical results could be achieved for μ = 0.5, while for $\mu > 0.6$ the shear sliding observed at the roof rafters supports during the laboratory tests could not be simulated.

The forces resisting the relative tangential motion between the masonry and the loading-beam were considered to be practically negligible. Therefore, frictionless tangential contact interaction was assigned in this case. Frictionless sliding was also assumed to take place between the sleek face of the roof panel and the masonry. Common nodes were assigned at the positions where the roof rafters were connected with the superjacent panel. Furthermore, joint connectors were used for modeling the timber wedges that had been set into the masonry of the side walls and nailed onto the roof panel of the actual structure. Hence, the nodes of the roof panel and the masonry walls at the two points of interconnection were constrained to have equal displacements.

The weight of the adobes placed upon the roof was evenly distributed to the panel in the form of an additional body force (approximately 53 kN/m^3). All nodes at the base of the walls were considered to be pinned. At the basal perimeter, where timber elements were installed in the actual structure to retain lateral movement, corresponding kinematic constrains were imposed. At the area where the hydraulic jack was in contact with the

timber loading-beam, the mesh of the simulated body was refined and constraints precluding movement along the x and z axes were imposed. Along the plane of symmetry, appropriate boundary conditions were assigned, so that movement in the x direction and rotations around the y and z axes were not allowed during the analysis. Horizontal loads were applied in the form of lateral displacements at the nodes of the timber loading-beam in contact with the jack. As the aim of the analysis was to approximate the experimental data envelope, the magnitude of the exerted displacements was assumed to be constantly increasing. Their amplitude was formulated according to the cumulative displacement data obtained from the laboratory tests.

The numerical solution process was completed in two successive steps. At the initial step, the dead loads were imposed. At the second step, the lateral load was applied. The total time period for each of these analysis steps was set at 1 s, while the minimum and maximum incremental sizes for imposing the loads were defined as $1x10^{-19}$ s and $1x10^{-4}$ s respectively. In both cases, a general non-linear static procedure was implemented, adopting the full Newton solution scheme with a direct sparse equation solver. Due to the highly non-linear nature of the analysis, automatic stabilization was applied using default values of the respective Abaqus/CAE parameters. The effect of geometric non-linearities was accounted for in all numerical steps.

6.5.2 Comparison between experimental-numerical results

6.5.2.1 Mode of failure

Figure 6.20 shows plots of the deformed mesh with contour representations of the lateral displacements (displacements in the y direction). The plots of Figure 6.20 refer to the model composed of 40 mm brick elements. Outcomes yielded by the analysis of a more sparse mesh are practically the same. The results show that the finite element model captures well the deformed shape of the structure. As expected, the maximum lateral displacement occurs at the rear wall, at the level where loading was applied. The displacement pattern computed for the façade displays a linear increase towards the wall's top. In line with the experimental observations, the out-of-plane movement of the façade is dictated by the in-plane drift of the side-wall.

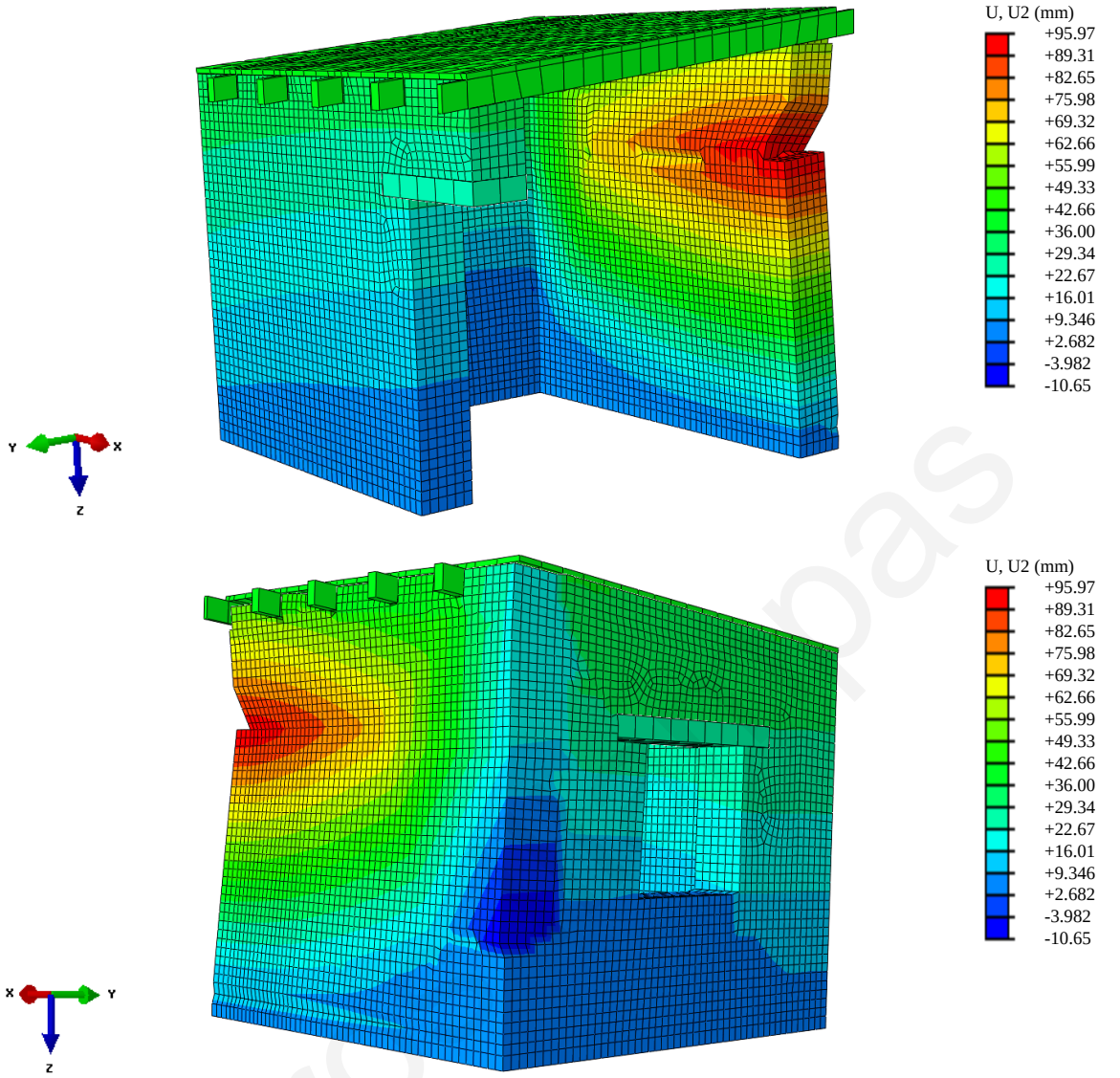

Figure 6.20: Plots of deformed mesh (deformation scale x 1) with contour representations of the lateral displacement distribution.

By examining the plots of Figure 6.20, it can be observed that a section between the side wall's base and rear central part moves backwards, in relation to its original position along the y direction. This is due to out-of-plane bending of the side wall and the subsequent torsion of its rear region. According to the readings of LVDT8, that was placed about 30 mm above the aforementioned region, a 2.5 mm backwards shift occurred.

The out-of-plane movement computed for the side wall is shown in Figure 6.21. From a qualitative point of view, the predicted translation of the rear cracked section is verified by the experimental results (see section 6.3.3.2). However, comparing the 7 mm displacement measured by LVDT10 during the last test cycle, with the 13 mm displacement computed at the corresponding nodal point, it may be argued that the finite element model tends to

overestimate the torsion induced to the side wall. Again, close correspondence was noted among the results yielded by different mesh densities.

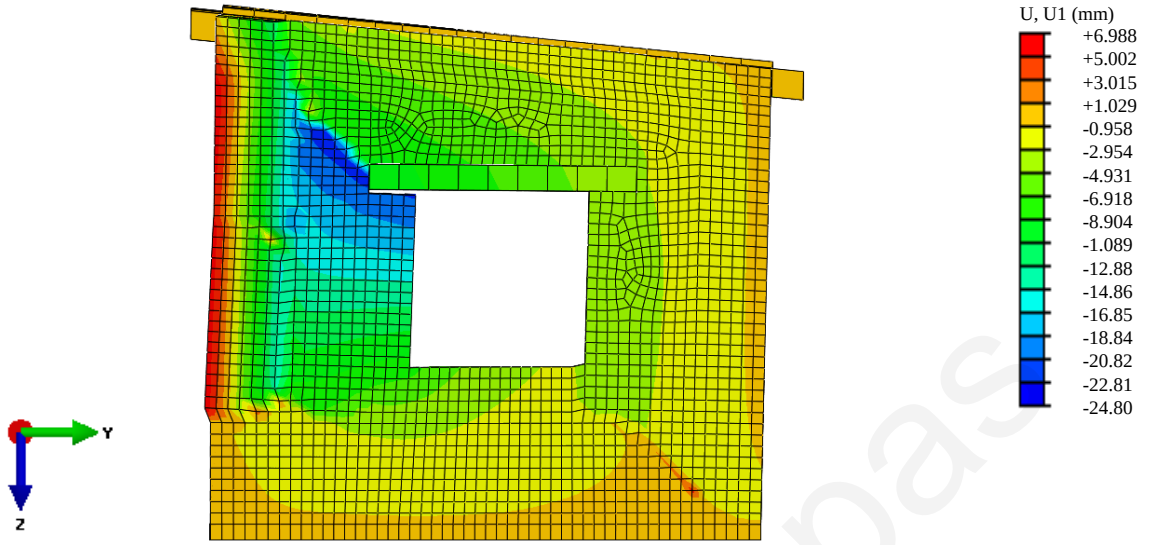

Figure 6.21: Contour diagram with the distribution of out-of-plane displacements (along the x axis) for the model's side wall (deformation scale x 1) (positive displacement values towards the interior of the structure).

In order to obtain a graphical visualization of the damage pattern sustained by the structure, the concept of effective crack directions developed by Lubliner et al. (1989) was adopted. According to this theory, cracking can be assumed to initiate at points where the tensile equivalent plastic strain is greater than zero ($\tilde{\varepsilon}_t^{pl} > 0$) and the maximum principal plastic strain is positive. The direction of the vector normal to the crack plane is assumed to be parallel to the direction of the maximum principal plastic strain (Simulia Corp., 2009). The predicted crack directions can be viewed in the contour diagrams of Figures 6.22 and 6.23, which present the maximum principal plastic strains computed at the final step of the analysis. As expected, the use of a denser mesh led to the prediction of narrower crack bands, producing more localized and distinctive damage patterns. The size of elements used did not affect the general mode of failure and the distribution of cracks.

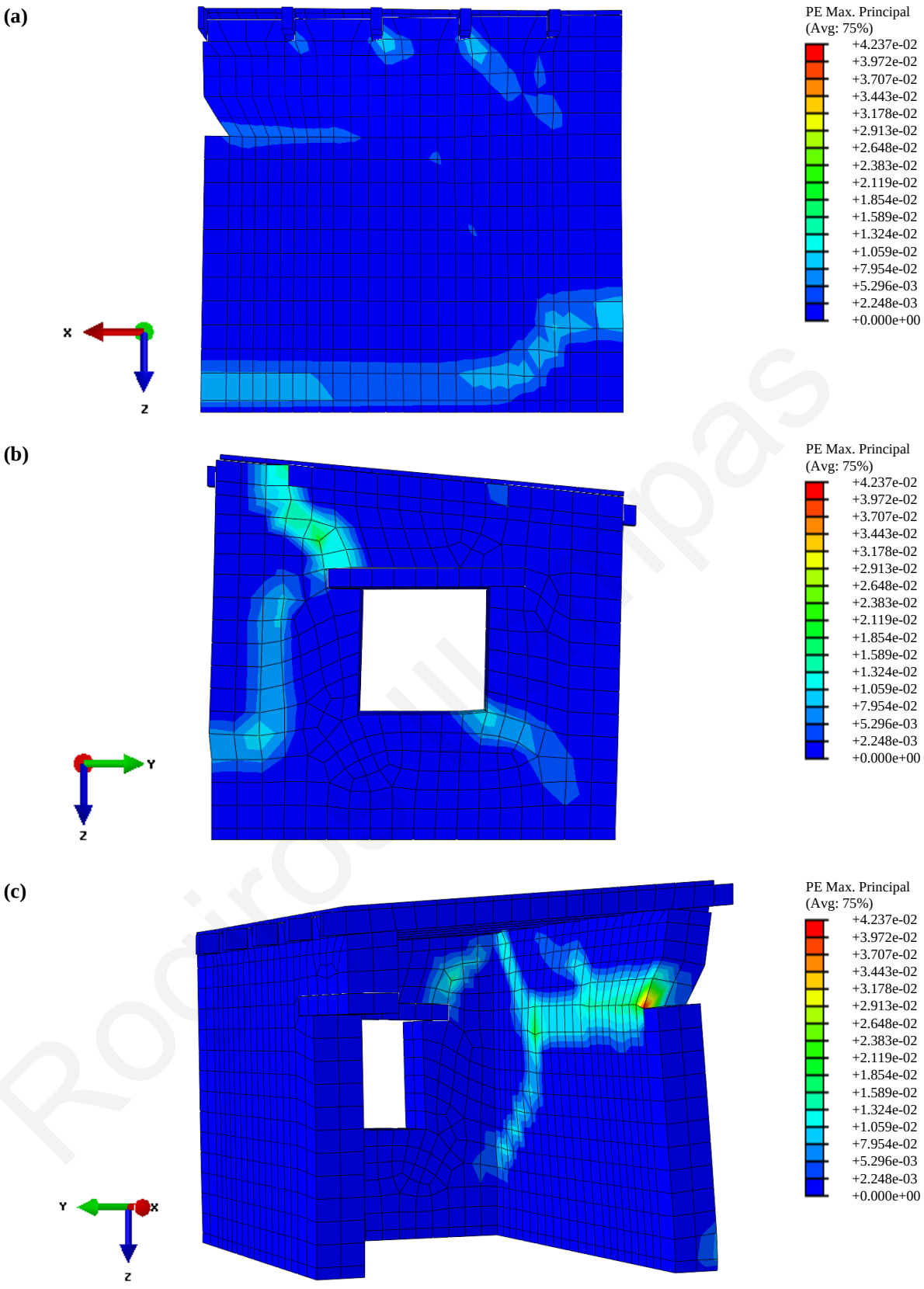

Figure 6.22: Contour diagrams with the maximum principal plastic strains computed using a mesh composed of elements with 100 mm sides. Predicted damage is shown for the external side of the rear wall (a), the external side of the side wall (b) and the interior of the structure (c) (deformation scale x 1).

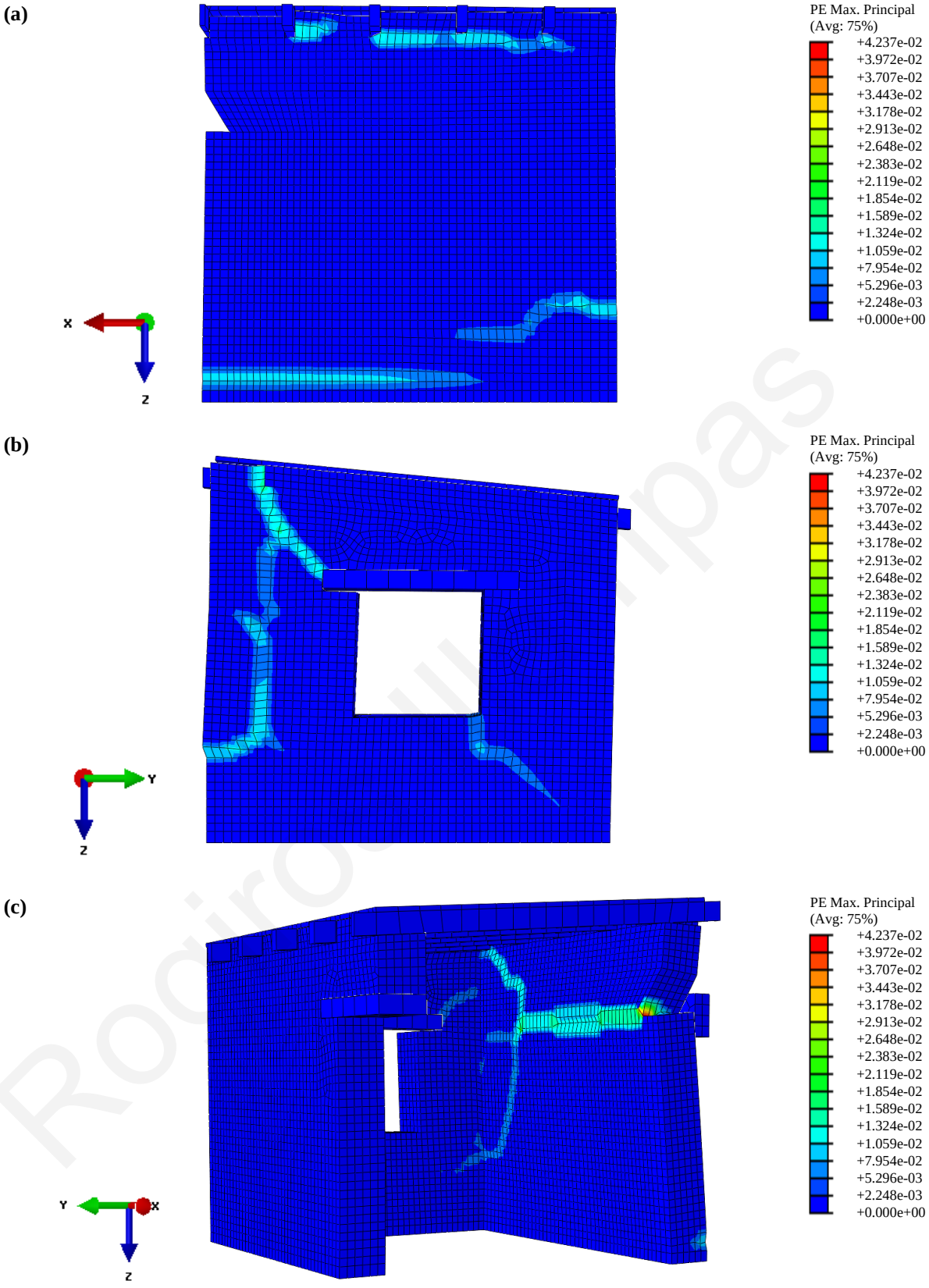

Figure 6.23: Contour diagrams with the maximum principal plastic strains computed using a mesh composed of elements with 40 mm sides. Predicted damage is shown for the external side of the rear wall (a), the external side of the side wall (b) and the interior of the structure (c) (deformation scale x 1).

Comparing Figures 6.22, 6.23 and 6.5, it is evident that the cracking pattern is well approximated. Damage was adequately captured in terms of crack initiation and propagation as well. Tensile failure during the simulation initially occurred at the upper central section of the rear wall's interior side. The plastic strain magnitude at this point attained the highest computed value (Figures 6.22c, 6.23c), coinciding with the location where the maximum crack opening was recorded during the laboratory tests. Crack propagation was rapid, with tensile plastic strains spreading across a horizontal band parallel to the line of loading. As higher forces were progressively imposed, plastic strains following inclined paths were also generated at the side end of the wall. These extended from the principal line of failure towards the upper and lower sections of the wall (Figures 6.22c, 6.23c). Analogous 'V'-shaped crack patterns were noted during experiments (see Figure 6.5a). Furthermore, the horizontal crack appearing at the lower external section of the rear wall was reproduced (Figures 6.22a, 6.23a). As in the case of the actual building, damage near the cross-wall had a diagonal form and extended to the side wall.

Almost coinstantaneously with the horizontal cracking of the rear wall's interior, tension failure was initiated at the two opposite corners of the side wall's window opening (Figures 6.22b, 6.23b). The concentration of significantly high tensile stresses at this area produced a diagonal distribution of plastic strains, similar to the crack pattern observed in the tested building. Tensile failure was also predicted for the elements close to the abutments of the roof rafters (Figure 6.22a, 6.23a). Although the horizontal spreading of these cracks was adequately approximated using a denser mesh (Figure 6.23a), failure did not propagate to the side wall and did not intersect with the crack appearing above the window's lintel, as observed in the experiments. Instead, the finite element model predicted the development of a near-vertical crack at the upper rear section of the side wall (Figure 6.22b, 6.23b). This was caused by torsional movement of the aforementioned section. Some cracks were indeed noted at this area during tests, however, damage was mainly characterized by small inclined cracks produced by the in-plane shear loading of the wall. This inconsistency is attributed to the overestimation of the side wall's out-of-plane displacement by the finite element model.

6.5.2.2 Force-displacement response

Figure 6.24 compares the outcomes of the finite element analyses with the experimentally derived force-displacement data envelopes for the upper sections of the façade, the side

wall and the rear wall. Numerical load data were estimated as the sum of all lateral contact forces generated at the nodes of the timber loading-beam. Both results yielded by meshes composed of brick elements with 100 and 40 mm sides are presented.

Reasonable agreement is found between the experimental and numerical diagrams, as in both cases the same trends are generally observed. The finite element model successfully predicts the occurrence of a post-yield plateau, succeeded by a gradual reduction of the load-bearing capacity. The computed reduction in lateral resistance increases with mesh densification, thus leading to better predictions concerning the bearing capacity of the structure after the maximum displacement has been imposed. However, the abrupt drop in load resistance, observed in the experimental data envelopes during the final test cycle, was not captured. This is likely due to the fact that the kinematic mechanisms forming at large deformation levels could not be accurately simulated though the use of a homogenized continuum, which does not allow discrete modeling of units and joints.

Striking correspondence is found between the maximum lateral load obtained by the mesh composed of brick elements with 40 mm sides and the maximum force measured on the actual structure. The use of a mesh composed by elements with 100 mm sides led to slight underestimation of the overall lateral resistance by 4.5%. The ultimate displacement computed at the rear wall's control nodal point is the same for both meshes examined and practically coincides with the one recorded by LVDT13. Regarding the out-of-plane movement of the façade, this is adequately approximated by the mesh composed of brick elements with 100 mm sides, but is underestimated by 7.1% (24.7 mm computed instead of the test's 26.6 mm) when a denser mesh is adopted. A 3.3% and a 9.2% overestimation (28 and 29.6 mm computed instead of the test's 27.1 mm) of the side wall's ultimate in-plane translation is respectively observed in the results yielded by meshes composed of brick elements with 40 and 100 mm sides. This is probably due to the isotropic elastic model used for the simulation of the timber loading-beam. Wood is an orthotropic material and stiffness along its grain is higher than in the other two axes (Green et al., 1999). As a result, out-of-plane (i.e. perpendicular to the grain direction) bending of the timber beam was greater in the experiments and the actual forces exerted on the side wall were hence lower, thus leading to lower wall displacements.

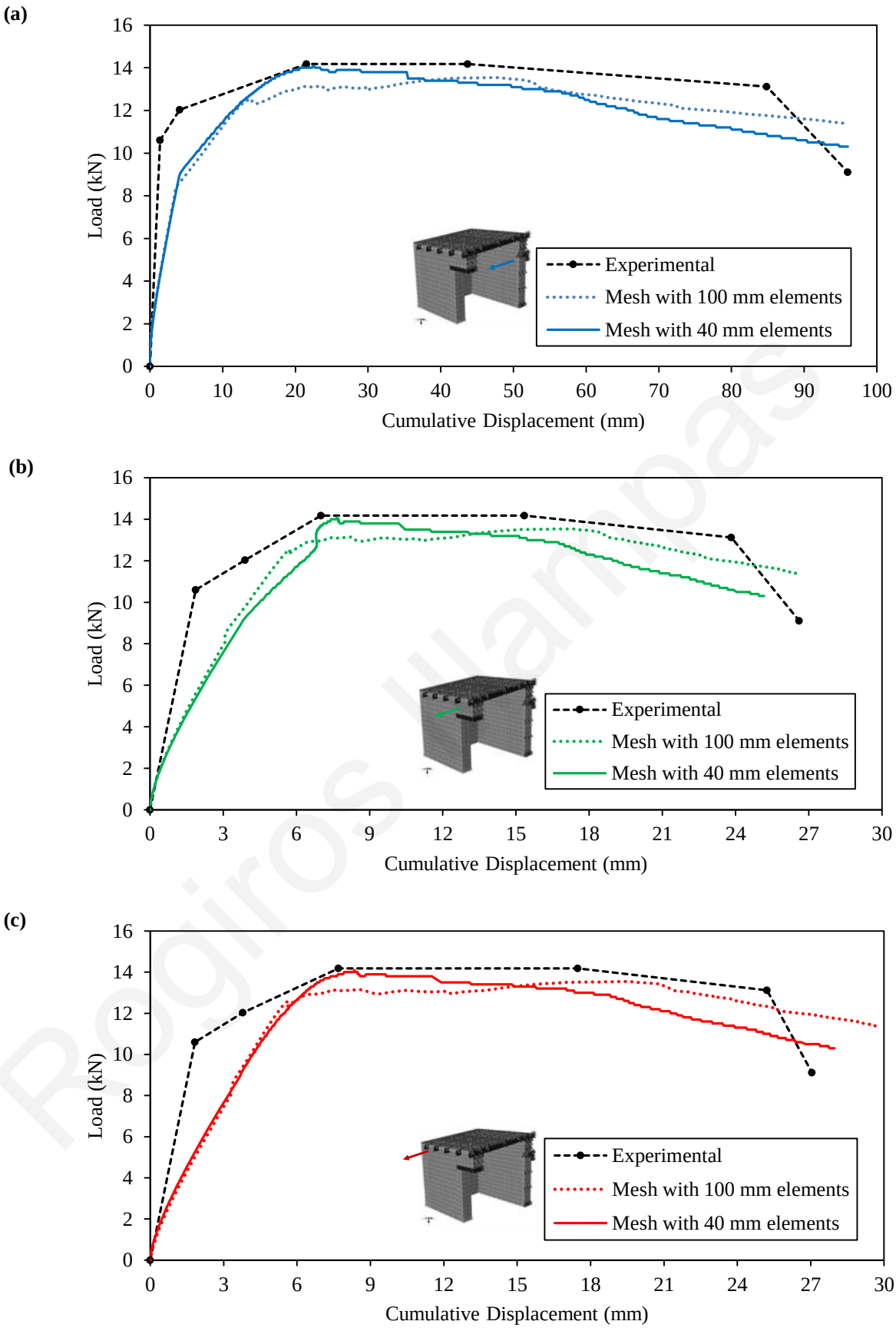

Figure 6.24: Comparison between experimental force-displacement data envelopes and numerical results obtained from finite element meshes composed of brick elements with 100 and 40 mm sides for the upper sections of the rear wall (a), the façade (b) and the side wall (c).

The underestimation of forces at the first section of the diagrams is attributed to the isotropic fracture criterion adopted. As it has been already pointed out in section 5.3.2.4, tensile failure of masonry can occur as debonding between the units, splitting of the units or joint decohesion and frictional sliding, depending on the stress state and the material properties (Backes, 1985). Direct tension and shear tests undertaken by Almeida (2012) on adobe bricks and on couplets with lime mortar joints, revealed that the tensile strength of the material itself and the frictional resistance along the joints can be at least an order of magnitude higher than the bonding strength. This indicates that, the actual stiffness and bearing capacity of the masonry in the direction parallel to the bed joints has been underestimated. Presumably, this has also led to overprediction of the side wall's torsional movement. Another factor which may have influenced the structural response predicted prior to the development of the maximum load is that no bonding strength (cohesion) was assigned to the roof rafter-brick interface. Consequently, the effective transfer of forces among opposite longitudinal walls at low levels of deformation was precluded and global response was inaccurately simulated.

6.5.2.3 General discussion of results

Overall, the numerical results obtained can be deemed as sufficiently accurate. Of particular importance is the correspondence between the predicted distribution of plastic strains and the failure mechanisms observed in the experiments. This is possibly the most critical aspect for evaluating the adequacy of the numerical model to simulate structural response. Considering the inhomogeneous and random nature of earthen materials, the correlation between the numerical and experimental load-displacement data is satisfactory. The need for further attempts to closely reproduce the experimental diagrams is questionable, as perfect agreement between the results of simulations and the outcomes of laboratory tests must be regarded as a coincidence and not as an objective of numerical modeling (Lourenço et al., 1998). This is because of the inherent variability and scatter in the data produced by experiments. In addition, despite applying an energy-based regularization of the medium's tensile response, a slight mesh dependency of numerical results possibly remained (see section 5.2.3.4), affecting to a limited degree the simulation results.

A number of simulations conducted in the process of model calibration, using different material properties (i.e Young's modulus, Poisson's ratio, plasticity parameters, tensile and

compressive strengths, friction coefficient at the timber-masonry interface), revealed which modeling parameters are more critical. The Young's modulus assigned to adobe masonry determines the stiffness of the walls and defines the tensile cracking strain (the higher the Young's modulus the lower the tensile cracking strain), thus affecting damage initiation. On the other hand, the masonry's Poisson's ratio and plasticity characteristics (i.e. dilation angle, flow potential eccentricity, ratio of initial equibiaxial compressive yield stress to initial uniaxial compressive yield stress, ratio of the second stress invariant on the tensile meridian to that on the compressive meridian at initial yield for any given value of the pressure invariant such that the maximum principal stress is negative) have very limited influence on the outcomes yielded. No significant alteration of the results was observed when different compressive strength values in the range $1 < f_w < 2.2$ MPa were assumed. However, it was noted that the assumption of a significantly low compressive yielding stress ($f_{wy} < 0.05$ MPa) introduces strong non-linearities in the procedure, which may preclude numerical convergence. Analyses revealed that, tensile response is the most crucial aspect of the simulation, since it dictates the lateral resistance and the displacement capacity predicted. It should be pointed out that, Tarque et al. (2010a), who simulated laboratory tests on 'I'-shaped adobe wall configurations using the same damaged plasticity constitutive law, also concluded that numerical results are much more sensitive to variations in tensile strength than to variations in compressive strength. The friction coefficient assigned to the timber-masonry interface controls the transfer of forces between the two opposite longitudinal walls and determines whether shear sliding of the roof rafters will occur. Consequently, it has some effect on the displacements computed at the façade, particularly when considerably high values are selected ($\mu > 0.6$).

The above highlight the importance of having experimentally derived material data, adequate for simulating all significant features of adobe masonry's structural behaviour. Considering the effect that the various modeling parameters pose on numerical outcomes with respect to the availability of relevant information in the literature, it may be argued that, further experimental investigation is required in certain fields. Future work should mainly focus on assessing adobe construction's stiffness characteristics and on examining its response to tensile loads. In addition, the frictional and bonding properties at interfaces between adobes and timber elements embedded in earth masonry should be evaluated.

The damaged plasticity constitutive model used in this study has proven to be adequate for the analysis of complete adobe structures, despite the fact that it involves some crude assumptions, such as isotropic damage. Provided that appropriate material data have been

used and that proper calibration has been undertaken, the model can capture cracking patterns and can predict with sufficient accuracy both the load-bearing and displacement capacities. Moreover, it has the potential to be applied in non-linear dynamic simulations, given that the respective damage parameters required are derived through experimental research.

6.6 Summary

Laboratory testing of a 1:2 scaled module produced outcomes which are in line with the data reported in the literature, regarding the behaviour of adobe masonry construction. Although the experimental setup used enabled only the imposition of monotonously increasing forces, the recorded modes of failure correspond to forms of seismic damage encountered in the field. The observations made verified that, under the imposition of lateral loading, cracking is characterized by loss of bonding between the adobes. Loading-unloading test cycles revealed that, upon load removal, complete closing of cracks takes place.

The accumulated force-displacement data indicate that, despite suffering from brittle tensile failure, adobe masonry structures do possess considerable deformation capacity. However, results show that homogeneous structural response is lost as soon as stiffness degradation occurs and differential movement of the walls takes place. This highlights the negative effect posed on the global behaviour of adobe structures by the insufficient interaction between the various load-bearing members and by the absence of a stiff diaphragm configuration at the roof level.

The force-displacement response of the model structure was adequately captured by an analytical approach. Using the finite element method and adopting a continuum-based damaged plasticity theory, the experimentally assessed response of the scaled building was quite satisfactorily simulated. In a qualitative sense, the numerical model succeeded in predicting damage initiation and propagation. Furthermore, the distribution of tensile cracking among the masonry walls was well captured. Quantitative comparisons reveal that the forces and displacements computed are in good agreement with the experimental data envelopes. Some deviations that occur between the experimental and the numerical results are attributed to the generic limitations of continuum modeling and to the use of a constitutive law based on isotropic damage concepts.

7 CONCLUSIONS AND RECOMMENDATIONS FOR FUTURE RESEARCH

Extensive use of adobes throughout the centuries has led to strong local traditions of building with earth and has established mud-brick masonry as an important feature of the international architectural and cultural heritage. Nowadays, adobes are mainly used in the conservation of historic buildings. At the same time, considerable efforts are being made to introduce the material in contemporary sustainable construction. A review of the international literature revealed that, although research related to adobe materials and structures is quite common today, the application of detailed engineering appraisal/design methods is still hindered by the absence of internationally accepted standardized testing procedures and by the lack of appropriate computational tools. In many countries, including Cyprus, additional problems arise due to the lack of information regarding the local material characteristics.

In the framework of this thesis, both experimental and computational investigation was undertaken in order to assess the properties of mud-bricks and earth masonry, to examine the structural response of unreinforced adobe buildings and to evaluate the application of numerical analysis methods to adobe masonry. The originality and significance of the contribution of this research work to the international scientific community is underlined by the following:

- The present thesis is, to the author's knowledge, the first that examines adobe construction at all scales/levels (starting from the material itself, passing to masonry members and finally progressing to complete adobe buildings), combining both experimental and numerical investigation.
- It includes a thorough and detailed record of the current state-of-the-art.
- The research on the mechanical properties of adobe bricks has led, for the first time, to the development of an analytical model describing the materials' stress-strain response under bending.
- The stress-strain relation proposed for describing the response of adobe bricks to compression has increased validity, compared to the few relevant models quoted in the international literature, as it is based on a much wider range of experimental data.

- For the first time rigorous laboratory testing has been implemented to characterize local earthen materials. This has led to the creation of an extensive database of information, which can be utilized by practitioners and can facilitate future research.
- The experimental and numerical investigation of the structural response of adobe masonry members and buildings extends existing knowledge and vigorously contributes to the development of appropriate assessment procedures and computational analysis methods.

The major findings of the thesis are listed in the following paragraphs.

7.1 Mechanical behaviour of adobe bricks

Extensive laboratory testing was undertaken in order to assess the mechanical properties of local adobes. More than 50 bricks were sampled from various production batches of active local producers. A total of 338 cylindrical, cubic and prismatic specimens were cut from the sample bricks and subjected to uniaxial compressive strength tests. In addition, three-point bending tests were performed on 55 half brick specimens. The results confirm that:

- The mechanical properties of non-industrialized local adobes show considerable deviations. Differences occur among the properties of: (a) adobes produced by different manufactures; (b) adobes made by the same manufacturer but originating from different production batches and (c) specimens originating from the same brick. This uncertain mechanical behaviour is attributed to the inherent inhomogeneity and natural randomness of local adobes, which is aggravated by the adoption of empirical production methods, the absence of standardization and the lack of effective quality control.
- The response of adobe to compression is characterized by an initial consolidation phase, followed by progressive hardening up to the maximum allowable stress. Softening is observed after the peak stress is attained.
- The shape of local adobes approaches that of a flat slab, making compressive strength testing quite challenging. Hence, selection of the appropriate tests specimen is of crucial importance. Experimental investigation confirms that the mode of failure under compression depends on the form and size of the test unit. Prismatic specimens, the length of which is at least two times their height, suffer axial shortening and circumferential spalling, while retaining consistency of their central

core. On the other hand, cylindrical and cubic specimens, with height-to-width ratios near 1, develop cracks parallel to the direction of loading.

- The maximum stress recorded in compressive strength tests also depends on the height-to-width ratio of the specimen examined. Prisms with height-to-width ratios < 1 confront severe platen restrain effects and hence lead to results which overestimate the material's load-bearing capacity.
- The compressive strengths of local adobes lie between 0.7-2.3 MPa and are generally below, or at best marginally above, the lowest permissible limits of foreign national codes (e.g. NZ4298; NTE E0.80; 14.7.4NMAC).
- Due to their granular soil matrix, adobes tend to develop considerable deformations under compressive loads. For the specimens examined in this thesis, typical values of axial strain at peak stress lie in the region of 10%, while strains as high as 30% were also encountered. The intense deformability of the material indicates that stress-based assessment criteria should be revised. Combined failure criteria accounting both for permissible deformation and load limits appear to be more suitable.
- When subjected to bending loads, adobes respond almost linearly before cracking. In the post-cracking regime, exponential loss of the bearing capacity occurs.
- The flexural strength is affected by the presence of discontinuities (e.g. shrinkage cracks, large sized particles etc.) within the material mass. These provoke crack initiation and propagation. A valid correlation between flexural and compressive strengths was not observed.
- The full stress-strain response of adobes under compression and bending can be described by analytical models. Two such models are proposed in this thesis. The validity of these models is enhanced by their satisfactory overall coefficients of determination ($R^2 > 0.7$) and by the considerable range of experimental data used in developing them. The equations proposed have a dimensionless format and can be potentially applied on adobe materials with different strength and deformation characteristics. They can also be exploited for performing non-linear structural analyses.

7.2 Mechanical behaviour of adobe masonry

Monotonic and loading-unloading compression tests were conducted to examine the response of adobe masonry to axial loads. Laboratory tests were performed on 13 stack-

bonded prisms and 2 running bond wallettes. The behaviour of adobe masonry under shear was also studied through the implementation of diagonal tension tests on a running bond wall panel. The results vividly show that:

- When subjected to compression, adobe masonry initially suffers consolidation. This is succeeded by a progressive hardening response until the maximum stress is reached. The hardening phase includes a stress range over which deformations tend to increase linearly.
- The mode of failure sustained by adobe assemblages under compression depends on the construction pattern. Stack-bonded prisms develop a conical fracture shape, while spalling of their lateral sides also takes place. In running bond wallets, damage is characterized by vertical cracking, initially at the head-joints and gradually propagating to the bricks.
- The compressive strength of adobe masonry lies between 0.8 and 2.2 MPa, depending on the properties of the masonry units, the construction pattern and the specimen's drying/curing period.
- Compressive loads can induce significant axial deformations to adobe masonry. This is particularly true when the soil particles within the materials are poorly compacted. The large strains recorded in this thesis are in line with the outcomes of compression tests on individual bricks and further highlight the need for introducing appropriate deformation-based criteria in assessment and design methods.
- Plastic/permanent deformation of adobe masonry occurs at low levels of compressive loading because of non-reversible sliding and displacement mechanisms between the soil grains.
- When adobe masonry is subjected to continuously ascending compressive loads and to loading-unloading cycles, different deformation moduli can be computed from the slopes of the stress-strain curves' corresponding sections. Unload-reload moduli are systematically higher than primary deformation moduli. In addition, their magnitude tends to increase with the pressure applied, due to gradual stiffening of the specimens, caused by progressive compaction and densification.
- Although certain existing analytical/empirical models (e.g. Eurocode 6; Tassios, 1987) for estimating the compressive strength of adobe masonry provide conservative estimates within the range of experimental results, their broad applicability is questionable and requires further research, since they refer to

conventional types of masonry, the physical and mechanical properties of which differ greatly from those of adobe construction.

- The tensile strength of mud-brick masonry strongly affects the overall structural response of adobe load-bearing members. Unreinforced adobe masonry has low resistance to diagonal tensile loading. The maximum principal tensile stress measured during experiments was 0.06 MPa, while the corresponding maximum shear stress was 0.13 MPa. The shear stiffness of adobe masonry is rather limited. Shear moduli assessed by diagonal tension tests were below 5 MPa.

7.3 Structural response of adobe buildings

The structural response of complete adobe buildings was investigated through monotonic lateral loading laboratory tests on a 1:2 scaled replica of a single-storey traditional dwelling. The findings of the experimental work are summarized below:

- Under the imposition of horizontal forces, the damage sustained by unreinforced adobe structures is primarily concentrated at the masonry walls, whereas stiffer load-bearing members (i.e. timber elements) practically develop no damage.
- The prevalent damage mechanism observed in adobe masonry walls is cracking; this is attributed to inadequate bonding between the bricks and the mortar. Walls subjected to in-plane loading develop diagonal cracks. The onset of failure in such walls is influenced by stress augmentation at the corners of openings and the abutments of lintels. Out-of-plane flexural loads cause the formation of horizontal cracks at the base of walls. Towards the cross-walls, these cracks may propagate in an inclined pattern or may extend vertically, leading to detachment between the intersecting members. Horizontal and diagonal cracks can also occur at areas where concentrated loads are applied.
- When horizontal loading is removed, cracks in adobe masonry walls close completely, leaving limited indications of damage. However, cracked sections act as planes of weakness and crack re-opening is almost instantly mobilized when loading is applied again. This highlights the cumulative effect that pre-existing damage poses on the structural behaviour of adobe buildings. It also indicates that particular attention should be paid during the in situ inspection of earthen structures after seismic events.

- Four damage limit states (LS1-4) could be identified, based on the force-displacement response of the model building examined. Initially, the load-bearing members of the building maintain a consistent response to horizontal forces, while limited or no damage develops (LS1). After a certain threshold, cracking and stiffness reduction start to develop, but the load-resisting elements maintain a homogeneous response (LS2). When higher deformations are generated, differential movement, considerable stiffness reduction, cracking damage and permanent distortion occur (LS3). After the building's lateral resistance is exceeded, depletion of the overall stiffness and severe deformation take place, until eventually the bearing capacity falls to a residual value (LS4).
- The structural response of adobe masonry buildings is adversely affected by the insufficient interaction among the various load-bearing members and by the absence of a stiff diaphragm configuration at the roof level.

7.4 Numerical simulation of adobe masonry structures

By adopting a continuum macro-modeling strategy and a damaged plasticity material constitutive law, the compression and diagonal tension tests on adobe masonry and the lateral load testing of the adobe model building were simulated through finite element analyses. All material parameters used in the simulations were based on the experimental data derived in this study and on relevant information reported in the literature. The numerical investigation conducted revealed the following:

- The damaged plasticity constitutive law can be adopted for modeling adobe masonry as an idealized homogenized continuum. Provided that appropriate material data have been used, the model can macroscopically capture the response of masonry members and complete buildings approximating with adequate accuracy their force-displacement response and failure mode. However, some inconsistencies may arise by the assumption of isotropic damage which is imposed by the model's formulation.
- The Young's modulus used in simulations depends on the loading scenario examined. When monotonic load scenarios are examined, the primary deformation modulus can be adopted. In order to account for the different response of adobe masonry under constantly increasing compressive loads and under loading-unloading cycles, it is proposed to set the Young's modulus equal to the unload-reload modulus

and assign the simulated medium a fully non-linear compressive response (compressive yielding < 1% of maximum allowable stress).

- The compressive and tensile response of adobe masonry can be defined using appropriate stress-strain relations. In the absence of experimental curves, the compression model proposed in this study and the tension softening model developed by Lourenço (2000) can be adopted.
- Certain plasticity parameters (e.g. dilation angle, flow potential eccentricity) of the damaged plasticity material model pose limited influence on numerical results and their values can be assumed without rigorous testing/investigation.
- The numerical results yielded by the analysis of complete adobe buildings subjected to lateral loading are highly sensitive to the variation of the stiffness (i.e. Young's modulus) and tension softening (i.e. tensile strength, fracture energy) parameters assigned to the masonry medium. The interaction among the timber roof elements and adobe masonry can also affect the results obtained.
- The kinematic mechanisms formed at masonry sections isolated due to extensive cracking cannot be accurately reproduced by continuum models. Therefore, the abrupt drops that occur in the lateral resistance of structures that have sustained such damage cannot be easily captured with the modeling method described in this thesis.

7.5 Recommendations for future research

Apart from enriching existing knowledge concerning the structural behaviour of adobe materials and structures, the results of this thesis have helped define specific areas for potential future research:

- The existing database of experimental results regarding the mechanical properties of local adobe materials and masonry components should be extended. Future experimental work should exhaustively examine the full stress-strain response under different forms of loading. Since the tests undertaken in this thesis revealed that there is significant uncertainty in the post-peak compressive behaviour of adobe specimens, the implementation of relevant displacement-controlled experiments is strongly recommended.
- Appropriate failure criteria for assessing the compressive strength of adobe materials and masonry components should be developed. These should account for the intense deformability caused by the fragile granular soil microstructure.

- Compression testing after different specimen curing ages along with close monitoring of moisture content should be undertaken in order to examine strength evolution in adobe masonry and define an optimum testing age.
- Existing analytical/empirical equations should be properly calibrated and verified against experimental results, so that these relations can accurately predict the compressive strength of adobe masonry.
- Experimental and theoretical investigation should be undertaken in order to introduce adobe masonry into the clauses of Eurocode 6, which is currently the basis of structural design for masonry buildings in Europe. The principles and requirements prescribed for safety, serviceability and durability, as well as the respective assessment procedures (both experimental and analytical/empirical) should be extended and/or revised to account for the particular characteristics of earthen construction.
- Emphasis should be given to the tensile behaviour of adobe masonry, as this appears to strongly influence the structural response of earthen construction. For this purpose, laboratory tests investigating the response of adobe masonry to tensile loads acting parallel and perpendicular to the bed joints should be conducted; the frictional and bonding properties at the brick-mortar interface should also be assessed. The effects that the mortar composition, joint thickness and block size pose on adhesion should be included in such an assessment.
- Considering the natural randomness and inhomogeneity of earthen materials, probabilistic description and analysis of the mechanical properties of adobe materials and masonry components should be carried out. Moreover, the effect that uncertain mechanical behaviour poses on the predicted structural response of adobe buildings should be numerically investigated.
- The influence of roof-wall connections in the structural response of adobe constructions should be studied. Since the roof rafters of traditional adobe buildings are usually set into the masonry with the application of mortar, the sliding resistance and bonding strength among the interacting materials should also be evaluated. This will provide valuable information regarding the capability of timber roof configurations to function as diaphragms during earthquakes. It will also enhance computational accuracy, as it will facilitate the correct simulation of the roof-wall interaction mechanism.

- The dynamic behaviour of adobe structures should be investigated through systematic laboratory testing following an integrated approach that addresses all construction scales/levels (i.e. brick, masonry, structure). The dynamic characteristics of earthen materials and masonry components should be assessed, while shake table tests should be implemented to examine the structural response of complete buildings.
- The use of damage plasticity constitutive laws for the simulation of adobe masonry can be extended to dynamic loading scenarios through the definition of respective damage parameters. In order to achieve this, a detailed investigation of stiffness degradation under the application of reversing loads is required.
- The use of non-linear orthotropic constitutive models (e.g. Lourenço, 2000; Berto et al., 2002; Pelà et al., 2013) for the simulation of adobe masonry may also be considered. Since the tension failure mechanisms which develop in adobe masonry structures depend on the orientation of imposing loads, such models may offer increased accuracy and a more detailed representation of damage modes. Their proper application however, requires extensive experimental research for the definition of material properties along both axes of orthotropy.
- Repair and strengthening solutions for adobe masonry structures should be developed and examined through laboratory testing and numerical analysis. Both existing and innovative techniques that can be applied in newly erected buildings and non-invasive measures that can be adopted in heritage structures should be considered.

In general, academic research should focus on setting the necessary formal guidelines that will enable adobe masonry to become an appropriate and acceptable building technique, with applications in contemporary architecture. For this purpose, practice-orientated, user-friendly but academically rigorous technical guides must be compiled. Such documents should include recommendations on production processes, quality control procedures, construction practices, repair/strengthening techniques and structural analysis methods.

REFERENCES

14.7.4NMAC (2006) *New Mexico Earthen Building Materials Code*, New Mexico State: Construction Industries Division of the Regulation and Licensing Department.

Adorni, E., Coïsson, E. and Ferretti, D. (2013) 'In situ characterization of archaeological adobe bricks', *Construction and Building Materials*, vol. 40, Special Section on Recycling Wastes for Use as Construction Materials, pp. 1-9.

Almeida, J.A.P.P. (2012) *Mechanical characterization of traditional adobe masonry elements*, MSc Thesis, Department of Civil Engineering: University of Minho.

Anania, L. and Badalà, A. (1998) 'A limit analysis by means of linear programming of masonry panels discretized in macroelements' in Idelsohn, S.R., Oñate, E. and Dvorkin E. (eds.) *Computational mechanics: New trends and applications*, Barcelona: CIMNE.

Asteris, P.G. and Tzamtzis, A.D. (2003) 'On the use of a regular yield surface for the analysis of unreinforced masonry walls', *Electronic Journal of Structural Engineering*, vol. 3, no. -, pp. 23-42.

ASTM C1006 - 07 (2007) *Standard test method for splitting tensile strength of masonry units*, West Conshohocken, PA: ASTM International, DOI: 10.1520/C1006-07, www.astm.org.

ASTM C1314 - 12 (2012) *Standard test method for compressive strength of masonry prisms*, West Conshohocken, PA: ASTM International, DOI: 10.1520/C1314-12, www.astm.org.

ASTM C67 - 12 (2012) *Standard test methods for sampling and testing brick and structural clay tile*, West Conshohocken, PA: ASTM International, DOI: 10.1520/C0067-12, www.astm.org.

ASTM D2166 - 06 (2006) *Standard test method for unconfined compressive strength of cohesive soil*, West Conshohocken, PA: ASTM International, DOI: 10.1520/D2166-06, www.astm.org.

ASTM E519 / E519M - 10 (2010) *Standard test method for diagonal tension (shear) in masonry assemblages*, West Conshohocken, PA: ASTM International, DOI: 10.1520/E0519_E0519M-10, www.astm.org.

Atzeni, C. and Sanna, A. (2008) *Architettura in terra cruda dei Campidani, del Cixerri e del Sarrabus [In Italian]*, Rome: DEI Tipografia del Genio Civile.

Augenti, N. and Parisi, F. (2010) 'Constitutive models for tuff masonry under uniaxial compression', *Journal of Materials in Civil Engineering*, vol. 22, no. 11, pp. 1102-1111.

Aymerich, F., Fenu, L. and Meloni, P. (2012) 'Effect of reinforcing wool fibres on fracture and energy absorption properties of an earthen material', *Construction and Building Materials*, vol. 27, no. 1, pp. 66-72.

Azeredo, G. and Morel, J.C. (2009) 'Tensile strength of earth mortars and its influence on earth masonry behaviour', Proceedings of the 11th International Conference on Non-conventional Materials and Technologies NOCMAT2009, Bath, UK, 6-9 September.

Azeredo, G., Morel, J.C. and Barbosa, N.P. (2007) 'Compressive strength testing of earth mortars', *Journal of Urban and Environmental Engineering*, vol. 1, no. 1, pp. 26-35.

Backes, H.P. (1985) *On the behaviour of masonry under tension in the direction of the bed joints [In German]*, PhD Thesis: Aachen University of Technology.

Bartolomé, A.S., Delgado, E. and Quiun, D. (2009) 'Seismic behaviour of two storey model of confined adobe masonry', Proceedings of the 11th Canadian Masonry Symposium, Toronto, Ontario, Canada, 31 May - 3 June.

Beatty, H.B., Graham, S.S., Moxley, R.E., Akers, S.A. and Reed, P.A. (2012) *Laboratory characterization of adobe*, Report ERDC/GSL TR-12-26: Geotechnical and Structures Laboratory, Washington: U.S. Army Corps of Engineers.

Belmouden, Y. and Lestuzzi, P. (2009) 'An equivalent frame model for seismic analysis of masonry and reinforced concrete buildings', *Construction and Building Materials*, vol. 23, no. 1, pp. 40-53.

Benedetti, D., Carydis, P. and Pezzoli, P. (1998) 'Shaking table tests on 24 simple masonry buildings', *Earthquake Engineering and Structural Dynamics*, vol. 27, no. 1, pp. 67-90.

Bera, A.K., Chandra, S.N., Ghosh, A. and Ghosh, A. (2009) 'Unconfined compressive strength of fly ash reinforced with jute geotextiles', *Geotextiles and Geomembranes*, vol. 27, no. 5, p. 391–398.

Berto, L., Saetta, A., Scotta, R. and Vitaliani, R. (2002) 'An orthotropic damage model for masonry structures', *International Journal for Numerical Methods in Engineering*, vol. 55, no. 2, pp. 127-157.

Binda, L., Schueremans, L., Verstrynge, E., Ignoul, S., Oliveira, D.V., Lourenço, P.B. and Modena, C. (2008) 'Long term compressive testing of masonry – test procedure and practical experience', Proceedings of the 6th International Conference on Structural analysis of Historical Constructions, Bath, UK, 2-4 July.

Binici, H., Aksogan, O. and Shah., T. (2005) 'Investigation of fibre reinforced mud brick as a building material', *Construction and Building Materials*, vol. 19, no. 4, pp. 313-318.

Binici, H., Aksogan, O., Bodur, M.N., Akca, E. and Kapur, S. (2007) 'Thermal isolation and mechanical properties of fibre reinforced mud bricks as wall materials', *Construction and Building Materials*, vol. 21, no. 4, pp. 901-906.

Blondet, M. and Vargas, J. (1978) *Investigación sobre vivienda rural [In Spanish]*, Report of the Division of Civil Engineering, Pontificia Universidad Católica del Perú, Lima, Peru: Ministerio de Comunicaciones, Infraestructura y Vivienda.

Blondet, M., Madueño, I., Torrealva, D., Villa-García, G. and Ginocchio, F. (2005) 'Using industrial materials for the construction of safe adobe houses in seismic areas', Proceedings of the Earth Build 2005 Conference, Sydney, Australia, 19-21 January.

Blondet, M., Vargas, J. and Tarque, N. (2008a) 'Available low-cost technologies to improve the seismic performance of earthen houses in deloping countries', Proceedings of the 14th World Conference on Earthquake Engineering, Beijing, China, 12-17 October.

Blondet, M., Vargas, J. and Tarque, N. (2008b) 'Observed behaviour of earthen structures during the Pisco earthquake (Peru)', Proceedings of the 14th World Conference on Earthquake Engineering, Beijing, China, 12-17 October.

Blondet, M., Vargas, J., Velasquez, J. and Tarque, N. (2006) 'Experimental study of synthetic mesh reinforcement of historical adobe buildings', Proceedings of the 5th

Conference on the Structural Analysis of Historical Constructions, New Delhi, India, 6-8 November.

Brencich, A., Gambarotta, L. and Lagomarsino, S. (1998) 'A macroelement approach to the three-dimensional seismic analysis of masonry buildings', Proceedings of the 11th European Conference on Earthquake Engineering, CNIT, Paris la Défense, France, 6-11 September.

Briaud, J.L. (2001) 'Introduction to soil moduli', *Geotechnical News*, vol. 19, no. 2, pp. 54-58.

Briaud, J., Li, Y. and Rhee, K. (2006) 'BCD: A soil modulus device for compaction control', *Journal of Geotechnical and Geoenvironmental Engineering*, vol. 132, no. 1, pp. 108-115.

Brignola, A., Frumento, S., Lagomarsino, S. and Podestà, S. (2008) 'Identification of shear parameters of masonry panels through the in-situ diagonal compression test', *International Journal of Architectural Heritage*, vol. 3, no. 1, pp. 52-73.

Brown, P.W. and Clifton, J.R. (1978) 'Adobe I: The properties of adobe', *Studies in Conservation*, vol. 23, no. 4, pp. 139-146.

Bui, Q.B., Morel, J.C., Hans, S. and Meunier, N. (2009a) 'Compression behaviour of non-industrial materials in civil engineering by three scale experiments: The case of rammed earth', *Materials and Structures*, vol. 42, no. 8, pp. 1101-1116.

Bui, Q.B., Morel, J.C., Reddy, B.V.V. and Ghayad, W. (2009b) 'Durability of rammed earth walls exposed for 20 years to natural weathering', *Building and Environment*, vol. 44, no. 5, pp. 912-919.

Burroughs, S. (2008) 'Soil property criteria for rammed earth stabilization', *Journal of Materials in Civil Engineering*, vol. 20, no. 3, pp. 264-273.

Calabria, J.A., Vasconcelos, W.L. and Boccaccini, A.R. (2009) 'Microstructure and chemical degradation of adobe and clay bricks', *Ceramics International*, vol. 35, no. 2, pp. 665-671.

Calderini, C., Cattari, S. and Lagomarsino, S. (2009) 'In plane seismic response of unreinforced masonry walls: Comparison between detailed and equivalent frame models', Proceedings of the 2nd International Conference on Computational Methods in Structural Dynamics and Earthquake Engineering COMPDYN 2009, Rhodes, Greece, 22-24 June.

Calderini, C., Cattari, S. and Lagomarsino, S. (2010) 'The use of the diagonal compression test to identify the shear mechanical parameters of masonry', *Construction and Building Materials*, vol. 24, no. 5, pp. 677-685.

Cao, Z. and Watanabe, H. (2004) 'Earthquake response prediction and retrofitting techniques of adobe structures ', Proceedings of the 13th World Conference on Earthquake Engineering, Vancouver, B.C., Canada, 1-6 August.

Carmona, S. and Aguado, A. (2012) 'New model for the indirect determination of the tensile stress–strain curve of concrete by means of the Brazilian test', *Materials and Structures*, vol. 45, no. 10, pp. 1473-1485.

Cervera, M., Pelà, L., Clemente, R. and Roca, P. (2010) 'A crack-tracking technique for localized damage in quasi-brittle materials', *Engineering Fracture Mechanics*, vol. 77, no. 13, pp. 2431-2450.

Charleson, A. (2011) *Seismic strengthening of earthen houses using straps cut from used car tires: Construction guide*, Oakland: Earthquake Engineering Research Institute.

Che, A.L., Wu, Z.J., Sun, J.J. and Qi, J.H. (2010) 'Seismic damage characteristics of rural adobe-wood building in Gansu province induced by the Wenchuan Great Earthquake', Proceedings of the International Symposium on Geoenvironmental Engineering, Hangzhou, China, 8-10 September.

Clementi, F., Lenci, S. and Sadowski, T. (2008) 'Fracture characteristics of unfired earth', *International Journal of Fracture*, vol. 149, no. 2, pp. 193-198.

Cluni, F. and Gusella, V. (2004) 'Homogenization of non-periodic masonry structures', *International Journal of Solids and Structures*, vol. 41, no. 7, pp. 1911-1923.

Corazao, M. and Blondet, M. (1974) *Estudio experimental del comportamiento estructural de las construcciones de adobe frente a solicitaciones sísmicas [In Spanish]*, Lima: Banco Peruano de los Constructores.

Correia, M., Dipasquale, L. and Mecca, S. (ed.) (2011) *Terra Europae: Earthen architecture in the European Union*, Pisa: Edizioni ETS.

Creazza, G., Matteazzi, R., Saetta, A. and Vitaliani, R. (2002) 'Analyses of masonry vaults: A macro approach based on three-dimensional damage model', *Journal of Structural Engineering*, vol. 128, no. 5, pp. 646-654.

Cruz, J.S., Barros, J. and Azevedo, A. (2006) *Elasto-plastic multi-fixed smeared crack model for concrete*, Report 04-DEC/E-05, Escola de Engenharia, Departamento de Engenharia Civil: Universidade do Minho.

Darwin, D. and Pecknold, D.A.W. (1974) *Inelastic model for cyclic biaxial loading of reinforced concrete*, Technical Report on Civil Engineering Studies SRS-409, University of Illinois Engineering Experiment Station, College of Engineering: University of Illinois at Urbana-Champaign.

Degirmenci, N. (2008) 'The using of waste phosphogypsum and natural gypsum in adobe stabilization', *Construction and Building Materials*, vol. 22, no. 6, pp. 1220-1224.

Delgado, C.J. and Guerrero, I.C. (2006) 'Earth building in Spain', *Construction and Building Materials*, vol. 20, no. 9, pp. 679-690.

Delgado, M.C.J. and Guerrero, I.C. (2007) 'The selection of soils for unstabilised earth building: A normative review', *Construction and Building Materials*, vol. 21, no. 2, pp. 237-251.

Demetriou, T., Pattichis, A., Constantinides, A. and Papadouris, G. (2006) *Restoration and maintenance of traditional settlements*, Nicosia: Cyprus Civil Engineers and Architects Association.

Dhanasekar, M. (2010) 'Review of modelling of masonry shear', *International Journal of Advances in Engineering Sciences and Applied Mathematics*, vol. 2, no. 3, pp. 106-118.

Doat, P., Hays, A., Houben, H., Matuk, S. and Vitoux, F. (1991) *Building with earth*, New Delhi: The Mud Village Society.

Doherty, K., Griffith, M.C., Lam, N. and Wilson, J. (2002) 'Displacement-based seismic analysis for out-of-plane bending of unreinforced masonry walls', Earthquake Engineering and Structural Dynamics, vol. 31, no. 4, pp. 833-850.

Dowling, D. (2004) 'Improved adobe mudbrick in application: Child-care centre construction in El Salvador', Proceedings of the 13th World Conference on Earthquake Engineering, Vancouver, B.C., Canada, 1-6 August.

Dowling, D. (2006) *Seismic strengthening of adobe-mudbrick houses*, PhD Thesis, Faculty of Engineering: University of Technology Sydney.

Dowling, D.M., Diaz, J. and Samali, B. (2004) 'Horizontal shear testing of mudbrick masonry mortar joints', Proceedings of 7th Australasian Masonry Conference, Newcastle, Australia, 13-16 July.

Dowling, D., Samali, B. and Li, J. (2005) 'Seismic improvement of adobe-mudbrick walls: Comparison between internal and external reinforcement', Proceedings of the 2005 Australian Earthquake Engineering Conference, Albury, Australia, 25-27 November.

Dymiotis, C. and Gutlederer, B.M. (2002) 'Allowing for uncertainties in the modelling of masonry compressive strength', *Construction and Building Materials*, vol. 16, no. 8, pp. 443-452.

Eftychiou, M. (2013) *Laboratory production and optimization of traditional adobe bricks [In Greek]*, MSc Thesis, Department of Civil and Environmental Engineering: University of Cyprus.

EN 1015-11 (1999) *Methods of test for mortar for masonry - Part 11: Determination of flexural and compressive strentgth of hardened mortar*, Brussels: CEN.

EN 1052-1 (1999) *Methods of test for masonry - Part 1: Determination of compressive strength*, Brussels: CEN.

EN 1052-3 (2002) *Methods of test for masonry - Part 3: Determination of initial shear strength*, Brussels: CEN.

EN 12372 (2006) *Natural stone test methods - Determination of flexural strength under concentrated load*, Brussels: CEN.

EN 772-1 (2000) *Methods of test for masonry units - Part 1: Determination of compressive strength*, Brussels: CEN.

EN 772-6 (2001) *Methods of test for masonry units - Part 6: Determination of bending tensile strength of aggregate concrete masonry units*, Brussels: CEN.

Ersubasi, F. and Korkmaz, H.H. (2010) 'Shaking table tests on strengthening of masonry structures against earthquake hazard', *Natural Hazards and Earth System Sciences*, vol. 10, no. 6, pp. 1209-1220.

Eurocode 6 (2005) *EN 1996-1-1: Design of masonry structures - Part 1-1: General rules for reinforced and unreinforced masonry*, Brussels: CEN.

Figueiredo, A., Varum, H., Costa, A., Silveira, D. and Oliveira, C. (2013) 'Seismic retrofitting solution of an adobe masonry wall', *Materials and Structures*, vol. 46, no. 1-2, pp. 203-219.

Fratini, F., Pecchioni, E., Rovero, L. and Tonietti, U. (2011) 'The earth in the architecture of the historical centre of Lamezia Terme (Italy): Characterization for restoration', *Applied Clay Science*, vol. 53, no. 3, pp. 509-516.

Frocht, M.M. (1931) 'Recent advances in photoelasticity: And an investigation of the stress distribution in square blocks subjected to diagonal compression', *Transactions of the American Society of Mechanical Engineers, Applied mechanics*, vol. 53, no. 15, pp. 135-153.

Fujii, Y., Fodde, E., Watanabe, K. and Murakami, K. (2009) 'Digital photogrammetry for the documentation of structural damage in earthen archaeological sites: The case of Ajina Tepa, Tajikistan', *Engineering Geology*, vol. 105, no. 1-2, pp. 124-133.

Furukawa, A. and Ohta, Y. (2009) 'Failure process of masonry buildings during earthquake and associated casualty risk evaluation', *Natural Hazards*, vol. 49, no. 1, pp. 25-51.

Furukawa, A., Spence, R., Ohta, Y. and So, E. (2009) 'Analytical study on vulnerability functions for casualty estimation in the collapse of adobe buildings induced by earthquake', *Bulletin of Earthquake Engineering*, vol. 8, no. 2, pp. 451-479.

Galán-Marín, C., Rivera-Gómez, C. and Petric, J. (2010) 'Clay-based composite stabilized with natural polymer and fibre', *Construction and Building Materials*, vol. 24, no. 8, pp. 1462-1468.

Galasco, A., Lagomarsino, S. and Penna, A. (2006) 'On the use of pushover analysis for existing masonry buildings', Proceedings of the First European Conference on Earthquake Engineering and Seismology, Geneva, Switzerland, 3-8 September.

Galasco, A., Lagomarsino, S., Penna, A. and Resemini, S. (2004) 'Non-linear seismic analysis of masonry structures', Proceedings of the 13th World Conference on Earthquake Engineering , Vancouver, B.C., Canada, 1-6 August.

Gambarotta, L. and Lagomarsino, S. (1997) 'Damage models for the seismic response of brick masonry shear walls. Part I: The mortar joint model and its applications', *Earthquake Engineering and Structural Dynamics*, vol. 26, no. 4, pp. 423-439.

Garcia, G., Ginocchio, F., Tumialan, G. and Nanni, A. (2004) 'Reinforcing of adobe structures with FRP bars', Proceedings of the 1st International Conference on Innovative Materials and Technologies for Construction and Restoration, Naples, Italy, 6-9 June.

Gattesco, N., Clemente, I., Macorini, L. and Noè, S. (2008) 'Experimental investigation of the behaviour of spandrels', Proceedings of the 14th World Conference on Earthquake Engineering, Beijing, China,12-17 October.

Gavrilovic, P., Sendova, V., Ginell, W.S. and Tolles, L. (1998) 'Behaviour of adobe structures during shaking table tests and earthquakes', Proceedings of the 11th European Conference on Earthquake Engineering, CNIT, Paris la Défense, France, 6-11 September.

Genna, F., Pasqua, M.D. and Veroli, M. (1998) 'Numerical analysis of old masonry buildings: A comparison among constitutive models', *Engineering Structures*, vol. 20, no. 1, pp. 37-53.

Ghavami, K., Filho, R.D.T. and Barbosa, N.P. (1999) 'Behaviour of composite soil reinforced with natural fibres', *Cement and Concrete Composites* , vol. 21 , no. 1, pp. 39-48.

Giambanco, G., Rizzo, S. and Spallino, R. (2001) 'Numerical analysis of masonry structures via interface models', *Computer Methods in Applied Mechanics and Engineering*, vol. 190, no. 49-50, pp. 6493-6511.

Ginell, W. and Tolles, E. (2000) 'Seismic stabilization of historic adobe structures', *Journal of the American Institute of Conservation*, vol. 39, no. 1, pp. 147-163.

Gomes, M.I., Lopes, M. and Brito, J.D. (2011) 'Seismic resistance of earth construction in Portugal', *Engineering Structures*, vol. 33, no. 3, pp. 932-941.

González, A.J.R. (1999) 'Uniaxial deformation-stress behaviour of the rammed-earth of the Alcazaba Cadima', *Materials and Structures*, vol. 32, no. 215, pp. 70-74.

Grau, P., Neumann, J. and Beas, M. (2006) 'Seismic retrofitting guidelines for the conservation of doctrinal chapels on the Oyon Highlands in Peru', Proccedings of the Getty Seismic Adobe Project 2006 Colloquium, Los Angeles, U.S.A., 11-13 April.

Green, M. and Watson, A. (1988) 'Seismic rehabilitation of the Parra adobe', *APT Bulletin*, vol. 20, no. 2, pp. 18-20.

Green, D.W., Winandy, J.E. and Kretschman, D.E. (1999) 'Mechanical properties of wood', in *Wood handbook: Wood as an engineering materia*, General Technical Report FPL-GTR-113, Madison WI: U.S. Department of Agriculture, Forest Service, Forest Products Laboratory.

Griffith, M.C., Magenes, G., Melis, G. and Picchi L. (2003) 'Evaluation of out-of-plane stability of unreinforced masonry walls subjected to seismic excitation', *Journal of Earthquake Engineering*, vol. 7, no. S1, pp. 141-169.

Guettala, A., Abibsi, A. and Houari, H. (2006) 'Durability study of stabilized earth concrete under both laboratory and climatic conditions exposure', *Construction and Building Materials*, vol. 20, no. 3, pp. 119-127.

Gullu, H. and Hazirbaba, K. (2010) 'Unconfined compressive strength and post-freeze–thaw behaviour of fine-grained soils treated with geofiber and synthetic fluid', *Cold Regions Science and Technology*, vol. 62, no. 2-3, pp. 142-150.

Gupta, A. and Akbar, H. (1984) 'Cracking in reinforced concrete analysis', *Journal of Structural Engineering*, vol. 110, no. 8, pp. 1735-1746.

Hall, M. and Djerbib, Y. (2004) 'Moisture ingress in rammed earth: Part 1- The effect of soil particle-size distribution on the rate of capillary suction', *Construction and Building Materials*, vol. 18, no. 4, pp. 269-280.

Hall, M. and Djerbib, Y. (2006a) "Moisture ingress in rammed earth: Part 2 – The effect of soil particle-size distribution on the absorption of static pressure-driven water', *Construction and Building Materials*, vol. 20, no. 6, pp. 374-383.

Hall, M. and Djerbib, Y. (2006b) 'Moisture ingress in rammed earth: Part 3 – Sorptivity, surface receptiveness and surface inflow velocity', *Construction and Building Materials*, vol. 20, no. 6, pp. 384-395.

Hammond, A.A. (1973) 'Prolonging the life of earth buildings in the tropics', *Building Research and Information*, vol. 1, no. 3, pp. 154-163.

Hardwick, J. and Little, J. (2010) 'Seismic performance of mud brick structures', Proceedings of the EWB-UK National Research Conference, London, UK, 19 February.

Heath, A., Lawrence, M., Walker, P. and Fourie, C. (2009) 'The compressive strength of modern earth masonry', Proceedings of the 11th International Conference on Non-conventional Materials and Technologies NOCMAT 2009, Bath, UK, 6-9 September.

Hejazi, S.M., Sheikhzadeh, M., Abtahi, S.M. and Zadhoush, A. (2012) 'A simple review of soil reinforcement by using natural and synthetic fibers', *Construction and Building Materials*, vol. 30, no. 1, pp. 100-116.

Hillerborg, A., Modéer, M. and Petersson, P.E. (1976) 'Analysis of crack formation and crack growth in concrete by means of fracture mechanics and finite elements', *Cement and Concrete Research*, vol. 6, no. 6, pp. 773-781.

Houben, H. and Guillard, H.. (1994) *Earth construction: A comprehensive guide*, London: ITDG Publishing.

Houlsby, G.T. (1991) *How the dilatancy of soils affects their behaviour*, Report Number OUEL 1888/91, Soil Mechanics Report 121/91, Department of Engineering Science: University of Oxford.

Hurd, J. (2006) 'Observing and applying ancient repair techniques to pise and adobe in seismic regions of Central Asia and Trans-Himalaya', Proccedings of the Getty Seismic Adobe Project 2006 Colloquium, Los Angeles, U.S.A., 11-13 April.

Illampas, R., Charmpis, D.C. and Ioannou, I. (2010c) 'An assessment of the compressive strength of adobe brick assemblages', Proceedings of the 9th HSTAM International Congress on Mechanics, Limassol, Cyprus, 11-14 July.

Illampas, R., Charmpis, D.C. and Ioannou, I. (2011c) 'Dynamic finite element analysis of earth masonry structures based on experimental matrerial data', Proceedings of the III ECCOMAS Thematic Conference on Computational Methods in Structural Dynamics and Earthquake Engineering, Corfu, Greece, 26-28 May.

Illampas, R., Charmpis, D.C. and Ioannou, I. (2011d) 'Finite element analysis of adobe masonry using experimentally derived material data', Proceedings of the 13th International Conference on Civil, Structural and Environmental Engineering Computing, Chania, Greece, 6-9 September.

Illampas, R., Ioannou, I. and Castrillo, M.C. (2011a) 'Earthen architecture in Cyprus', in Mecca, S. and Dipasquale, L. (ed.) *Terra Europae - Earthen architecture in European Union*, Pisa: Edizioni ETS.

Illampas, R., Ioannou, I. and Charmpis, D.C. (2010a) 'A study of the deterioration and rehabilitation of adobe structures', Proceedings of the 8th International Symposium on the Conservation of Monuments in the Mediterranean Basin, Patras, Greece, 31 May - 2 June.

Illampas, I., Ioannou, I. and Charmpis, D.C. (2010b) 'Destructive and non-destructive testing of hand-made adobe bricks', Proceedings of the 13th International Congress and Exhibition on Structural Faults and Repairs, Edinburgh, UK, 15-17 June.

Illampas, R., Ioannou, I. and Charmpis, D.C. (2011b) 'A study of the mechanical behaviour of adobe masonry', Proceedings of the 12th International Conference on Structural Repairs and Maintenance of Heritage Architecture, Chianciano Terme, Italy, 5-7 September.

Illampas, R., Ioannou, I. and Charmpis, D.C. (2013) 'Overview of the pathology, repair and strengthening of adobe structures', *International Journal of Architectural Heritage*, vol. 7, no. 2, pp. 165-188.

Islam, M.S. and Iwashita, K. (2010) 'Earthquake resistance of adobe reinforced by low cost traditional materials', *Journal of Natural Disaster Science*, vol. 32, no. 1, pp. 1-21.

Islam, M.S. and Watanabe, H. (2004) 'FEM simulation of seismic behaviour of adobe structures', Proceedings of the 13th World Conference on Earthquake Engineering, Vancouver, B.C., Canada, 1-6 August.

Jager, W. and Fuchs, C. (2010) 'Restoring adobe masonry in a world cultural heritage site: The Sistani house in Bam, Iran', Proceedings of the 8th International Masonry Conference, Dresden, Germany, 31 May - 2 June.

Jerome, P., Chiari, G. and Borelli, B. (1999) 'The architecture of mud: Construction and repair technology in the Hadhramaut region of Yemen', *APT Bulletin*, vol. 30, no. 2/3, pp. 39-48.

Kappos, A., Penelis, G. and Drakopoulos, C. (2002) 'Evaluation of simplified models for lateral load analysis of unreinforced masonry buildings', *Journal of Structural Engineering*, vol. 128, no. 7, pp. 890-897.

Karapitta, P., Mouzakis, H. and Carydis, H. (2011) 'Explicit finite-element analysis for the in-plane cyclic behaviour of unreinforced masonry structures', *Earthquake Engineering and Structural Dynamics*, vol. 40, no. 2, pp. 175-193.

Karaveziroglou, M. and Papayianni, I. (1993) 'Compressive strength of masonry with thick mortar joints', Proceedings of the UNESCO/RILEM International Conference on the Conservation of Stone and Other Materials, Paris, France, 29 June - 1 Jule.

Katsaragakis, E.S. (2000) *Timber construction [In Greek]*, Athens: NTUA Academic Publications.

Keefe, L. (2005) *Earth buildings - methods, materials, repair and conservation*, London and New York: Taylor & Francis.

Kiyono, J. and Kalantari, A. (2004) 'Collapse mechanism of adobe and masonry structures during the 2003 Iran Bam Earthquake ', *Bulletin of the Earthquake Research Institute, University of Tokyo*, vol. 79, no. 3/4, pp. 157-161.

Kouakou, C.H. and Morel, J.C. (2009) 'Strength and elasto-plastic properties of non-industrial building materials manufactured with clay as a natural binder', *Applied Clay Science*, vol. 44, no. 1-2, pp. 27-34.

Lagomarsino, S., Galasco, A. and Penna, A. (2002) 'Pushover and dynamic analysis of 3D masonry buildings by means of a non-linear macro-element model', Proceedings of the International Conference on Earthquake Loss Estimation and Risk Reduction, Bucharest, Romania, 24-26 October.

Lee, J. and Fenves, G. (1988) 'Plastic-damage model for cyclic loading of concrete structures', *Journal of Engineering Mechanics*, vol. 124, no. 8, pp. 892-900.

Lehmbau Regeln (1999) *Lehmbau Regeln: Begriffe – Baustoffe – Bauteile*, Braunschweig/Wiesbaden: Dachverband Lehm e.V.

Lemos, J.V. (2007) 'Discrete element modeling of masonry structures', *International Journal of Architectural Heritage*, vol. 1, no. 2, pp. 190-213.

Lenci, S., Clementi, F. and Sadowski, T. (2012) 'Experimental determination of the fracture properties of unfired dry earth', *Engineering Fracture Mechanics*, vol. 87, no. 1, pp. 62-72.

Lenci, S., Piattoni, Q., Clementi, F. and Sadowski, T. (2009) 'A mechanical characterization of unfired dry earth: Ultimate strength, damage and fracture parameters', Proceedings of the XIX Congresso Dell' Associazione Italiana di Meccanica Teorica e Applicata, Ancona, Italy, 14-17 September.

Lenci, S., Piattoni, Q., Clementi, F. and Sadowski, T. (2011) 'An experimental study on damage evolution of unfired dry earth under compression', *Letters in Fracture and Micromechanics*, vol. 172, no. 2, pp. 193-200.

Liberatore, D., Spera, G., Mucciarelli, M., Gallipoli, M.R., Masini, N., Racina, V., Tancredi, C., Capriuoli, A., Cividini, A., Tedeschi, C. and Santarsiero, D. (2006) 'Typological and experimental investigation on the adobe buildings of Aliano (Basilicata, Italy)', Proceedings of the 5th International Conference on the Structural Analysis of Historical Constructions, New Delhi, India, 6-8 November.

Lin, C.S. and Scordelis, A.C. (1975) 'Nonlinear analysis of RC shells of general form', *Journal of the Structural Division*, vol. 101, no. 3, pp. 523-538.

Little, B. and Morton, T. (2001) *Building with earth in Scotland: Innovative design and sustainability*, Edinburgh: Scottish Executive Central Research Unit.

Lotfi, H.R. and Shing, P.B. (1991) 'An appraisal of smeared crack models for masonry shear wall analysis', *Computers and Structures*, vol. 41, no. 3, pp. 413-425.

Lotfi, H.R. and Shing, P.B. (1994) 'Interface model applied to fracture of masonry structures', *Journal of Structural Engineering*, vol. 120, no. 1, pp. 63-80.

Lourenço, P.B. (1994) *Analysis of masonry structures with interface elements: Theory and applications*, TNO Building and Construction Research on Computational Mechanics, TU-DELFT Report no.03-21-22-0-01/TNO-BOUW Report no.94-NM-R0762: Delft University of Technology, Faculty of Civil Engineering.

Lourenço, P.B. (2000) 'Anisotropic softening model for masonry plates and shells', *Journal of Structural Engineering*, vol. 126, no. 9, pp. 1008-1016.

Lourenço, P.B. (2002) 'Computations on historic masonry structures', *Progress in Structural Engineering and Materials*, vol. 4, no. 3, pp. 301-319.

Lourenço, P.B. and Rots, J.G. (1997) 'Multisurface interface model for analysis of masonry structures', *Journal of Engineering Mechanics*, vol. 123, no. 7, pp. 660-668.

Lourenço, P.B., Rots, J. and Blaauwendraad, J. (1998) 'Continuum model for masonry: Parameter estimation and validation', *Journal of Structural Engineering*, vol. 124, no. 6, pp. 642-652.

Lubliner, J., Oliver, J., Oller, S. and Oñate, E. (1989) 'A plastic-damage model for concrete', *International Journal of Solids and Structures*, vol. 25, no. 3, pp. 299-326.

Magenes G., (2006) ‘Masonry building design in seismic areas: recent experiences and prospects from a European standpoint”, Proceedings of the 1st European Conference on Earthquake Engineering and Engineering Seismology, Geneva, Switzerland, 3-8 September.

Magenes, G. and Calvi, G.M. (1997) 'In-plane seismic response of brick masonry walls', *Earthquake Engineering and Structural Dynamics*, vol. 26, no. 11, pp. 1091-1112.

Magenes, G., Della Fontana, A., (1998) ‘Simplified non-linear seismic analysis of masonry buildings’, *Proceedings of the British Masonry Society*, No. 8 – October 1998, pp. 190-195.

Maheri, M.R., Naeim, F. and Mehrain, M. (2005) 'Performance of adobe residential buildings in the 2003 Bam, Iran, Earthquake', *Earthquake Spectra*, vol. 21, no. S1, pp. 337-344.

Mahini, S.S., Eslami, A. and Ronagh, H.R. (2012) 'Lateral performance and load carrying capacity of an unreinforced, CFRP-retrofitted historical masonry vault – A case study', *Construction and Building Materials*, vol. 28, no. 1, pp. 146-156.

Mahini, S.S., Ronagh, H.R. and Eslami, A. (2007) 'Seismic rehabilitation of historical masonry vaults using FRPS - A case study', Proceedings of the Asia-Pacific Conference on FRP in Structures APFIS 2007, Hong Kong, China, 12-14 December.

Mann, W. (1982) 'Statistical evaluation of tests on masonry by potential functions', Proceedings of the 6th International Brick Masonry Conference, Rome, Italy, 16-19 May.

Marques, R. and Lourenço P.B. (2011) 'Possibilities and comparison of structural component models for the seismic assessment of modern unreinforced masonry buildings', *Computers and Structures*, vol. 89, no. 21–22, pp. 2079-2091.

Martins, T. and Varum, H. (2006) 'Adobe's mechanical characterization in ancient constructions: The case of Aveiro's region', *Materials Science Forum Trans Tech Publications*, vol. 514-516, no. 1, pp. 1571-1575.

McHenry, P.G. (1989) *Adobe and rammed earth buildings: Design and construction*, Arizona: University of Arizona Press.

Meli, R., Hernández, O. and Padilla, M. (1980) 'Strengthening of adobe houses for seismic actions', Proceedings of the 7th World Conference on Earthquake Engineering, Istanbul, Turkey, 9-13 September 8-13.

Meyer, C.S. (2013) 'Numerical simulations of the mechanical behaviour of adobe', in Chalivendra, V., Song, B. and Casem, D. (ed.) *Dynamic Behaviour of Materials, Volume 1: Proceedings of the 2012 Annual Conference on Experimental and Applied Mechanics*, New York: Springer.

Milani, G., Lourenço, P.B. and Tralli, A. (2006a) 'Homogenised limit analysis of masonry walls, Part I: Failure surfaces', *Computers and Structures*, vol. 84, no. 3-4, pp. 166-180.

Milani, G., Lourenço, P.B. and Tralli, A. (2006b) 'Homogenised limit analysis of masonry walls, Part II: Structural examples', *Computers and Structures*, vol. 84, no. 3-4, pp. 181-195.

Millogo, Y., Hajjaji, M. and Ouedraogo, R. (2008) 'Microstructure and physical properties of lime-clayey adobe bricks', *Construction and Building Materials*, vol. 22, no. 12, pp. 2386-2392.

Minke, G. (2009) *Building with earth: Design and technology of a sustainable architecture*, Berlin: Birkhäuser.

Monk, C. (1962) 'Testing high-bond clay masonry assemblages', Proceedings of the Symposium on Masonry Testsing of the 65th ASTM Annual Meeting, New York, USA, 28-29 June.

Morales, R. and Delgado, A. (1992) 'Feasibility of construction of two-storey adobe buildings in Peru', Proceedings of the 10th World Conference on Earthquake Engineering, Madrid, Spain, 19-24 July.

Morel, J.C. and Pkla, A. (2002) 'A model to measure compressive strength of compressed earth blocks with the '3 points bending test'', *Construction and Building Materials*, vol. 16, no. 5, pp. 303-310.

Morel, J.C., Pkla, A. and Walker, P. (2007) 'Compressive strength testing of compressed earth blocks', *Construction and Building Materials*, vol. 21, no. 5, pp. 303-309.

Morton, T. (2008) *Earth masonry: Design and construction guidelines*, Watford: IHS BRE Press.

Muntohar, A.S. (2011) 'Engineering characteristics of the compressed-stabilized earth brick', *Construction and Building Materials*, vol. 25, no. 11, pp. 4215-4220.

Ngowi, A.B. (1997) 'Improving the traditional earth construction: A case study in Botswana', *Construction and Building Materials*, vol. 11, no. 1, pp. 1-7.

Norton, J. (1997) *Building with earth: A handbook*, London: Intermediate Technology.

NTE E0.80 (2000) *Adobe: Norma Técnica de Edificación*, Lima: Ministerio de Transportes, Comunicaciones, Vivienda y Construcción.

NZ4297 (1998) *Engineering design of earth buildings*, New Zealand: Standards New Zealand.

NZ4298 (1998) *Materials and workmanship for earth buildings*, Wellington: Standards New Zealand.

NZ4299 (1998) *Earth buildings not requiring specific design*, New Zealand : Standards New Zealand.

Okunade, E.A. (2009) 'Engineering properties of lateritic adobe bricks for local building construction and recommendations for practice', *Journal of Engineering and Applied Sciences*, vol. 2, no. 9, pp. 1455-1459.

Oliveira, D.V. and Lourenço, P.B. (2004) 'Implementation and validation of a constitutive model for the cyclic behaviour of interface elements', *Computers and Structures*, vol. 82, no. 17-19, pp. 1451-1461.

Orduña, A. and Lourenço, P.B. (2001) 'Limit analysis as a tool for the simplified assessment of ancient masonry structures', in Lourenço, P.B. and Roca, P. (ed.) *Historical Constructions*, Guimarães: University of Minho.

Oti, J.E., Kinuthia, J.M. and Bai, J. (2009) 'Compressive strength and microstructural analysis of unfired clay masonry bricks', *Engineering Geology*, vol. 109, no. 3-4, pp. 230-240.

Ottazzi, J., Yep, J., Blondet, M., Villa-Garcia, G. and Ginocchio, J.F. (1988) 'Shaking table tests of improved adobe masonry houses', Proceedings of the 9th World Conference on Earthquake Engineering, Tokyo-Kyoto, Japan, 2-9 August.

Packard, R.Q. (1967) 'Moisture stress in unfired ceramic clay bodies', *Journal of The American Ceramic Society*, vol. 50, no. 5, pp. 223-229.

Page, A.W. (1978) 'Finite element model for masonry', *Journal of the Structural Division*, vol. 104, no. 8, pp. 1267-1285.

Pagliolico, S.L., Ronchetti, S., Turcato, E.A., Bottino, G., Gallo, L.M. and DePaoli, R. (2010) 'Physicochemical and mineralogical characterization of earth for building in North West Italy', *Applied Clay Science*, vol. 50, no. 4, pp. 439-454.

Papa, E. (1996) 'A unilateral damage model for masonry based on a homogenisation procedure', *Mechanics of Cohesive-frictional Materials*, vol. 1, no. 4, pp. 349-366.

Papacharalambous, G.C. (1968) *The Cypriot dwelling [In Greek]*, Nicosia : Scientific Research Center.

Pelà, L., Cervera, M. and Roca, P. (2013) 'An orthotropic damage model for the analysis of masonry structures', *Construction and Building Materials*, vol. 41, no. 1, pp. 957-967.

Philokyprou, M. (1998) *Building materials and structures of Cyprus architecture: From the Neolithic Period to the Late Chalcolithic Period*, PhD Thesis, Department of History and Archeology: University of Cyprus.

Piattoni, Q., Quagliarini, E. and Lenci, S. (2011) 'Experimental analysis and modelling of the mechanical behaviour of earthen bricks', *Construction and Building Materials*, vol. 25, no. 4, pp. 2067-2075.

Pineda-Piñón, J., Vega-Durán, J.T., Manzano-Ramírez, A., Pérez-Robles, J.F., Balmori-Ramírez, H. and Hernández-Landaverde, M.A. (2007) 'Enhancement of mechanical and hydrophobic properties of adobes for building industry by the addition of polymeric agents', *Building and Environment*, vol. 42, no. 2, pp. 877-883.

Pineda-Piñón, J., Vega-Durán, J.T., Manzano-Ramírez, A., Prokhorov, E., Morales-Sánchez, E. and González-Hernández, J. (2008) 'Mechanical properties and humidity absorption measured through impedance spectroscopy in clays used for adobe production', *Applied Clay Science*, vol. 40, no. 1-4, pp. 1-5.

Popovic, S. (1973) 'A numerical approach to the complete stress-strain curve of concrete', *Cement and Concrete Research*, vol. 3, no. 5, pp. 583-599.

Psycharis, I.N., Papastamatiou, D.Y. and Alexandris, A.P. (2000) 'Parametric investigation of the stability of classical columns under harmonic and earthquake excitations', *Earthquake Engineering and Structural Dynamics*, vol. 29, no. 8, pp. 1093-1109.

Psycharis, I.N., Papastamatiou, D., Carydis, P., Papantonopoulos, K., Alexandris, A., Mouzakis, H., Zambas, K. and Lemos, J.V. (2001) 'Numerical and experimental investigation of the seismic response of Classical monuments [In Greek]', Proceedings of the 2nd Hellenic Conference on Earthquake Engineering and Engineering Seismology, Thessaloniki, Greece, 28-30 November.

Quagliarini, E. (2006) 'Earth constructions in the Marche Region (Italy): Building techniques and materials', Proceedings of the Second International Congress on Construction History - Volume 3, Cambridge, UK, 29 March - 2 April,.

Quagliarini, E. and Lenci, S. (2010) 'The influence of natural stabilizers and natural fibres on the mechanical properties of ancient Roman adobe bricks', *Journal of Cultural Heritage*, vol. 11, no. 3, pp. 309-314.

Quagliarini, E., Lenci, S. and Iorio, M. (2010) 'Mechanical properties of adobe walls in a Roman Republican domus at Suasa ', *Journal of Cultural Heritage*, vol. 11, no. 2, pp. 130-137.

Qu, J.J., Cheng, G.D., Zhang, K.C., Wang, J.C., Zu, R.P. and Fang, H.Y. (2006) 'An experimental study of the mechanisms of freeze/thaw and wind erosion of ancient adobe buildings in northwest China', *Bulletin of Engineering Geology and the Environment*, vol. 66, no. 2, pp. 153-159.

Razani, Z. (1978) 'Seismic protection of unreinforced masonry and adobe low-cost housing in less developed countries: Policy issues and design criteria', *Disasters*, vol. 2, no. 2-3, pp. 137-147.

Reddy, B.V.V. and Kumar, P.P. (2010) 'Cement stabilised rammed earth - Part A: Compaction characteristics and physical properties of compacted cement stabilised soils', *Materials and Structures*, vol. 44, no. 3, pp. 681-693.

Reddy, B.V.V., Lal, R. and Rao, K.S.N. (2009) 'Influence of joint thickness and mortar-block elastic properties on the strength and stresses developed in soil-cement block masonry', *Journal of Materials in Civil Engineering*, vol. 21, no. 10, pp. 535-542.

Ren, K.B. and Kagi, D.A. (1995) 'Upgrading the durability of mud bricks by impregnation', *Building and Envrronment*, vol. 30, no. 3, pp. 433-440.

Rizzano, G. and Sabatino, R. (2010) 'An equivalent frame model for seismic analysis of masonry structures', Proceedings of the 8th National Conference on Seismology and Earthquake Engineering, Aveiro, Portugal, 20-23 October.

Roca, P., Cervera, M., Gariup, G. and Pela', L. (2010) 'Structural analysis of masonry historical constructions: Classical and advanced approaches', *Archives of Computational Methods in Engineering*, vol. 17, no. 3, pp. 299-325.

Rojas, J., Ferrer, H. and Cuenca, J.S. (2008) 'Dynamic behaviour of adobe houses in Central Mexico', Proceedings of the 14th World Conference on Earthquake Engineering, Beijing, China, 12-17 October.

Roselund, N. (1990) 'Repair of cracked adobe walls by injection of modified mud', Proceedings of the 6th International Conference on the Conservation of Earthen Architecture, New Mexico, U.S.A., 14-19 October.

Rots, J.G. (1991) 'Numerical simulation of cracking in structural masonry', *HERON*, vol. 36, no. 2, pp. 49-63.

Rots, J.G., Nauta, P., Kusters, G.M.A. and Blaauwendraad, J. (1985) 'Smeared crack approach and fracture localization in concrete', *HERON*, vol. 30, no. 1, pp. 23-48.

Sabatino, R. and Rizzano, G. (2011) 'A simplified approach for the seismic analysis of masonry structures', *The Open Construction and Building Technology Journal*, vol. 5, no. 1-M7, pp. 97-104.

Saetta, A., Scotta, R. and Vitaliani, R. (1999) 'Coupled environmental-mechanical damage model of RC structures', *Journal of Engineering Mechanics*, vol. 125, no. 8, pp. 930-940.

Salonikios, T., Karakostas, C., Lekidis, V. and Anthoine, A. (2003) 'Comparative inelastic pushover analysis of masonry frames', *Engineering Structures*, vol. 25, no. 12, pp. 1515-1523.

Samali, B., Dowling, D.M. and Li, J. (2004) 'Dynamic testing of unreinforced u-shaped adobe mudbrick wall unit', Proceedings of the 18th Australasian Conference on the Mechanics of Structures and Materials, Perth, Australia, 1-3 December.

Samali, B., Jinwuth, W., Heathcote, K. and Wang, C. (2011) 'Seismic capacity comparison between square and circular plan adobe construction', *Procedia Engineering*, vol. 14, no. 1, pp. 2103-2108.

Sayin, E., Yön, B., Calayir, Y. and Karaton, M. (2012) 'Failures of masonry and adobe buildings during the June 23, 2011 Maden-(Elazığ) earthquake in Turkey', *Engineering Failure Analysis*, In Press, http://dx.doi.org/10.1016/j.engfailanal.2012.10.016.

Šejnoha, J., Šejnoha, M., Zeman, J., Sýkora, J. and Vorel, J. (2008) 'Mesoscopic study on historic masonry', *Structural Engineering and Mechanics*, vol. 30, no. 1, pp. 99-117.

Shahzada, K, Khan, A.N, Elnashai, A.S., Ashraf, M., Javed, M., Naseer, A. and Alam, B. (2012) 'Experimental seismic performance evaluation of unreinforced brick masonry buildings', *Earthquake Spectra*, vol. 28, no. 3, pp. 1269-1290.

Shieh-Beygi, B. and Pietruszczak, S. (2008) 'Numerical analysis of structural masonry: Mesoscale approach', *Computers and Structures*, vol. 86, no. 21-22, pp. 1958-1973.

Silva, R., Schueremans, L. and Oliveira, D. (2009) 'Grouting as a repair/strengthening solution for earth constructions', Proceedings of the 1st WTA International PhD Symposium on Building Materials and Building Technology to Preserve the Built Heritage, Leuven, Belgium, 8-9 October.

Silva, R., Schueremans, L. and Oliveira, D. (2010) 'Repair of earth masonry by means of grouting: Importance of clay in the rheology of a mud grout', Proceedings of the 8th International Masonry Conference, Dreden, Germany, 4-7 July.

Silveira, D., Varum, H. and Costa, A. (2007) "Rehabilitation of an important cultural and architectural heritage: The traditional adobe constructions in Aveiro district', Proceedings of the III Conference on Sustainable Development and Planning, Algarve, Portugal, 25-27 April.

Silveira, D., Varum, H. and Costa, A. (2013) 'Influence of the testing procedures in the mechanical characterization of adobe bricks', *Construction and Building Materials*, vol. 40, Special Section on Recycling Wastes for Use as Construction Materials, pp. 719-728.

Silveira, D., Varum, H., Costa, A., Martins, T., Pereira, H. and Almeida, J. (2012) 'Mechanical properties of adobe bricks in ancient constructions', *Construction and Building Materials*, vol. 28, no. 1, pp. 36-44.

Simulia Corp. (2009) *Abaqus 6.10 theory manual*, Rising Sun Mills: Dassault Systèmes.

Sinos, S. (1976) *A review of the traditional architecture of Cyprus [in Greek]* , Athens: Makris A.E.

Suidan, M. and Schnobrich, W.C. (1973) 'Finite element analysis of reinforced concrete', *Journal of the Structural Division*, vol. 99, no. 10, pp. 2109-2122.

Syrmakezis, C.A. and Asteris, P.G. (2001) 'Masonry failure criterion under biaxial stress state', *Journal of Materials in Civil Engineering*, vol. 13, no. 1, pp. 58-64.

Tarque, N. (2011) *Numerical modelling of the seismic behaviour of adobe buildings*, PhD Thesis, Università degli Studi di Pavia: Istituto Universitario di Studi Superiori.

Tarque, N., Camata, G., Spacone, E., Varum, H. and Blondet, M. (2010a) 'Numerical modelling of the in-plane behaviour of adobe walls', Proceedings of the 8th National Conference on Seismology and Earthquake Engineering, Aveiro, Portugal, 20-23 October.

Tarque, N., Camata, G., Spacone, E., Varum, H. and Blondet, M. (2012a) 'Elastic and inelastic parameters for representing the seismic in-plane behaviour of adobe wall', Proceedings of the XIth International Conference on the Study and Conservation of Earthen Architectural Heritage Terra 2012, Lima, Peru, 22-27 April.

Tarque, N., Camata, G., Spacone, E., Varum, H. and Blondet, M. (2012b) 'Non-linear dynamic analysis of an adobe module', Proceedings of the XIth International Conference on the Study and Conservation of Earthen Architectural Heritage Terra 2012, Lima, Peru, 22-27 April.

Tarque, N., Crowley, H., Prinho, R. and Varum, H. (2010b) 'Seismic capacity of adobe dwellings', Proceedings of the 14th European Conference On Earthquake Engineering, Ohrid, FYROM, 30 August - 3 September.

Tarque, N., Crowley, H., Prinho, R. and Varum, H. (2012c) 'Displacement-based fragility curves for seismic assessment of adobe builidngs in Cusco, Peru', *Earthquake Spectra*, vol. 28, no. 2, pp. 759-794.

Tassios, T.P. (1987) *Masonry mechanics [In Greek]*, Athens: Symmetria.

Tastani, S.P., Papadopoulos, M. and Pantazopoulou, S.J. (2009) 'Seismic response of traditional masonry buildings: Parametric study and evaluation', Proceedings of the International Conference on the Protection of Historical Buildings PROHITECH 09, Rome, Italy, 21-24 June.

Tavares, A., Costa, A. and Varum, H. (2012) 'Common pathologies in composite adobe and reinforced concrete constructions', *Journal of Performance of Constructed Facilities*, vol. 26, no. 4, pp. 389-401.

Tipler, J., Worth, M., Morris, H. and Ma, Q. (2010) 'Shake table testing of scaled geogrid-reinforced adobe wall models', Proceedings of the 2010 New Zealand Society for Earthquake Engineering Conference, Wellington, New Zealand, 26-28 March.

Tolles, E.L., Kimbro, E.E. and Ginnel, S.W. (2003) *Planning and engineering guidelines for the seismic retrofitting of historic adobe structures*, Los Angeles: Getty Conservation Institute.

Tolles, E.L., Kimbro, E.E., Webster, A.F. and Ginnel, S.W. (2000) *Seismic stabilization of historic adobe structures: Final report of the Getty seismic adobe project*, Los Angeles: Getty Conservation Institute.

Tolles, E.L. and Krawinkler, H. (1990) *Seismic studies on small-scale models of adobe houses*, Technical Report No. 91: Department of Civil and Environmental Engineering Stanford University, Stanford: John A. Blume Earthquake Engineering Center.

Tolles, E.L., Webster, F.A., Crosby, A. and Kimbro, E.E. (1996) *Survey of damage to historic adobe buildings after the January 1994 Northridge earthquake*, Los Angeles: The Getty Conservation Institute.

Tomaževič, M. (1978) *The computer program POR*, Report ZMRK, Ljubljiana, Slovenia,: Institute for Testing and Research in Materials and Structures.

Tomaževič, M. (2000) 'Some aspects of experimental testing of seismic behaviour of masonry walls and models of masonry buildings', *ISET Journal of Earthquake Technology*, vol. 37, no. 4, pp. 101-117.

Tomaževič, M. (2009) 'Shear resistance of masonry walls and Eurocode 6: Shear versus tensile strength of masonry', *Materials and Structures*, vol. 42, no. 7, pp. 889-907.

Torrealva, D., Cerrón, C. and Espinoza, Y. (2008) 'Shear and out of plane bending strength of adobe walls externally reinforced with polypropylane grids', Proceedings of the 14th World Conference on Earthquake Engineering, Beijing, China, 12-17 October.

Torrealva, D., Neumann, J. and Blondet, M. (2006) 'Earthquake resistant design criteria and testing of adobe buildings at Pontificia Universidad Catolica del Peru', Proccedings of the Getty Seismic Adobe Project 2006 Colloquium, Los Angeles, U.S.A., 11-13 April.

Toumbakari, E.E. (2010) 'Mechanical properties and durability of cement-stabilized earth mortars for application in prehistoric monuments', Proceedings of the 8th International Symposium on the Conservation of Monuments in the Mediterranean Basin, Patras, Greece, 31 May - 2 June.

Turanli, L. and Saritas, A. (2011) 'Strengthening the structural behaviour of adobe walls through the use of plaster reinforcement mesh ', *Construction and Building Materials*, vol. 25, no. 4, pp. 1747-1752.

Turnšek, V. and Čačovič, F. (1970) 'Some experimental results on the strength of brick masonry walls', Proceedings of the 2nd International Brick Masonry Conference, Stoke on Trent, UK, 12-15 April.

Tzamtzis, A.D. and Asteris, P.G. (2004a) 'FE analysis of complex discontinuous and jointed structural systems (Part 1: Presentation of the method – A state-of-the-art review)', *Electronic Journal of Structural Engineering*, vol. 1, no. -, pp. 75-92.

Tzamtzis, A.D. and Asteris, P.G. (2004b) 'FE analysis of complex discontinuous and jointed structural systems (Part 2: Application of the method – Development of a 3D model for the analysis of unreinforced masonry walls)', *Electronic Journal of Structural Engineering*, vol. 1, no. -, pp. 93-107.

Vamvatsikos, D. and Pantazopoulou, S.J. (2010) 'Development of simplified mechanical model to estimate the seismic vulnerability of cultural heritage masonry buildings', Proceedings of the 9th HSTAM International Congress on Mechanics, Limassol, Cyprus, 12-14 July.

Van Mier, J.G.M. (2012) *Concrete fracture: A multiscale approach*, New York: CRC Press.

Vargas, J., Bariola, J., Blondet, M. and Mehta, P.K. (1986) 'Seismic strength of adobe masonry', *Materials and Structures*, vol. 19, no. 4, pp. 253-258.

Vargas, J. and Ottazzi, G. (1981) *Investigaciones en adobe [in Spanish]*, Report of the Division of Civil Engineering, Pontificia Universidad Católica del Perú, Lima, Peru: Ministerio de Comunicaciones, Infraestructura y Vivienda.

Varum, H., Costa, A., Pereira, H. and Almeida, J. (2006) 'Comportamento estrutural de elementos resistentes em alvenaria de adobe [In Portugese]', Proceedings of the TerraBrasil 2006 I Seminário Arquitetura e Construção com Terra no Brasil / IV Seminário Arquitectura de Terra em Portugal, Ouro Preto, Minas Gerais, Brazil, 4-8 November.

Varum, H., Costa, A., Pereira, H., Almeida, J. and Rodrigues, H. (2008) 'Caracterização do comportamento estrutural de paredes de alvenaria de adobe [In Portugese]', *Revista Mecânica Experimental, APAET - Associação Portuguesa de Análise Experimental de Tensões*, vol. 15, no. 1646-7078, pp. 23-32.

Varum, H., Figueiredo, A., Silveira, D., Martins, T. and Costa, A. (2011) 'Investigaciones realizadas en la Universidad de Aveiro sobre caracterización mecánica de las construcciones existentes en adobe en Portugal y propuestas de rehabilitación y refuerzo - Resultados alcanzados [In Spanish]', *Informes de la Construcción*, vol. 63, no. 523, pp. 127-142.

Vega, P., Juan, A., Guerra, M.I., Morán, J.M., Aguado, P.J. and Llamas, B. (2011) 'Mechanical characterisation of traditional adobes from the north of Spain', *Construction and Building Materials*, vol. 25, no. 7, pp. 3020-3023.

Velosa, A., Varum, H. and Sáez, M. (2010) 'Characterization of adobe blocks from Burgos', Proceedings of the 9º SIACOT, Seminário Ibero-Americano de Construção e Arquitectura com Terra / 6º ATP, Seminário de Arquitectura de Terra em Portugal, Coimbra, Portugal, 20-23 February.

Vera, R. and Miranda, S. (2004) 'Experimental study of retrofitting techniques for adobe walls', Proceedings of the 13th World Conference on Earthquake Engineering, Vancouver, B.C., Canada, 1-6 August.

Vratsanou, V. (1992) *Das nichtlineare Verhalten unbewehrter Mauerwerksscheiben unter Erdbebenbeanspruchung: Hilfsmittel zur Bestimmung der q-Faktoren [In German]*, PhD Thesis, Institut für Massivbau und Baustofftechnologie: Universität Karlsruhe.

Walker, P. (1999) 'Bond characteristics of earth block masonry', *Journal of Materials in Civil Engineering*, vol. 11, no. 3, pp. 249-256.

Walker, P. (2002) *Standards Australia - HB195: The australian earth building handbook*, Sydney: Standards Australia International.

Walker, P.J. (2004) 'Strength and erosion characteristics of earth blocks and earth block masonry', *Journal of Materials in Civil Engineering*, vol. 16, no. 5, pp. 497-506.

Walker, R. and Morris, H. (1997) 'Development of new performance based standards for earth building', Proceedings of the Australian Structural Engineering Conference , Auckland, Australia, 30 September - 2 October.

Wawrzynek, A. and Cińcio, A. (2005) 'Adaptation of a plastic-damage concrete model for masonry material subjected to cyclic load', Proceedings of the VIII International Conference on Computational Plasticity, Barcelona, Spain, 5-8 September.

Wei, X. and Hao, H. (2009) 'Numerical derivation of homogenized dynamic masonry material properties with strain rate effects', *International Journal of Impact Engineering*, vol. 36, no. 3, pp. 522-536.

Wu, F., Li, G., Li, H.N. and Jia, J.Q. (2012) 'Strength and stress–strain characteristics of traditional adobe block and masonry', *Materials and Structures*, In Press, DOI 10.1617/s11527-012-9987-y.

Yamin, L.E., Phillips, C.A., Reyes, J.C. and Ruiz, D.M. (2004) 'Seismic behaviour and rehabilitation alternatives for adobe and rammed earth buildings', Proceedings of the 13th World Conference on Earthquake Engineering, Vancouver, B.C., Canada, 1-6 August.

Yetgin, S., Cavdar, O. and Cavdar, A. (2008) 'The effects of the fiber contents on the mechanic properties of the adobes', *Construction and Building Materials*, vol. 22, no. 3, pp. 222-227.

Yokel, F.Y. (1976) 'Failure hypothesis for masonry shear walls', *Journal of the Structural Division*, vol. 102, no. 3, pp. 515-532.

Yucheng, Y. and Liu, Y. (1987) 'Earthquake damage to and aseismic measures for earth-sheltered buildings in China', *Tunnelling and Underground Space Technology*, vol. 2, no. 2, pp. 209-216.

Zegarra, L., Quiun, D., San Bartolomé, A. and Giesecke, A. (1997) 'Reforzamiento de viviendas de adobe existentes, 2da parte: Ensayo sísmico de módulos [In Spanish]', Proceedings of XI National Congress of Civil Engineering , Trujillo, Peru, 4-8 November.

Zucchini, A. and Lourenço, P.B. (2002) 'A micro-mechanical model for the homogenisation of masonry', *International Journal of Solids and Structures*, vol. 39, no. 12, pp. 3233-3255.

Zucchini, A. and Lourenço, P.B. (2009) 'A micro-mechanical homogenisation model for masonry: Application to shear walls', *International Journal of Solids and Structures*, vol. 46, no. 3-4, pp. 871-886.

Zurakowska, M., Hughes, J.J. and Jez, J. (2009) 'History, materials and social aspects of building from unfired earth in Poland', Proceedings of the 11th International

Conference on Non-conventional Materials and Technologies NOCMAT 2009, Bath, UK, 6-9 September.

ANNEXES

Annex 1: Results of compression tests on adobe brick specimens

Size-independent mean compressive strength values and corresponding coefficients of variation for cylindrical (height = diameter = 50 mm), prismatic (height x width x length = 50 x 100 x 100 mm^3) and cubic (edges = 50 mm) adobe specimens originating from 51 sample bricks. Samples are referenced as "X a b", where "X" refers to the manufacturer (Ly, Ath or Ge), "a" denotes the production batch and "b" indicates the sample (adobe brick) number. Size-independent values were derived by applying the shape factors suggested in EN 772-1.

Sample brick (cylinders + prisms + cubes)	Size-independent mean compressive strength [MPa] (coefficient of variation)		
	Cylinders	Prisms	Cubes
Ly A 1 (0 + 5 + 5)	- -	2.27 (21.2%)	2.26 (11.8%)
Ly A 2 (0 + 6 + 5)	- -	2.02 (27.4%)	2.05 (11.6%)
Ly A 3 (0 + 4 + 0)	- -	2.63 (32.6%)	- -
Ly A 4 (0 + 4 + 0)	- -	3.05 (51.1%)	- -
Ly A 5 (0 + 4 + 0)	- -	2.84 (4.0%)	- -
Ly B 1 (0 + 8 + 3)	- -	5.66 (17.4%)	1.90 (22.1%)
Ly B 2 (0 + 8 + 4)	- -	5.23 (12.5%)	1.80 (11.3%)
Ly B 3 (0 + 4 + 0)	- -	3.85 (26.1%)	- -
Ly B 4 (0 + 5 + 0)	- -	4.36 (15.7%)	- -
Ly B 5 (0 + 2 + 0)	- -	5.09 (8.1%)	- -
Ly B 6 (0 + 4 + 0)	- -	5.28 (5.5%)	- -
Ly C 1 (0 + 4 + 0)	- -	3.02 (50.3%)	- -
Ly C 2 (0 + 5 + 0)	- -	3.00 (40.8%)	- -
Ly C 3 (0 + 4 + 0)	- -	3.25 (4.7%)	- -
Ly C 4 (0 + 4 + 0)	- -	3.38 (18.4%)	- -
Ly C 5 (0 + 4 + 0)	- -	3.55 (18.2%)	- -
Ly C 6 (0 + 4 + 0)	- -	2.91 (28.1%)	- -
Ly C 7 (7 + 2 + 0)	1.80 (24.3%)	5.12 (17.2%)	- -
Ly C 8 (8 + 2 + 0)	1.97 (27.5%)	5.99 (21.3%)	- -
Ly C 9 (7 + 1 + 0)	1.65 (19.7%)	6.85 (-)	- -
Ly C 10 (8 + 3 + 0)	2.06 (20.9%)	2.68 (42.5%)	- -

Sample brick (cylinders + prisms + cubes)	Size-independent mean compressive strength [MPa] (coefficient of variation)		
	Cylinders	Prisms	Cubes
Ath A 1 (0 + 5 + 4)	- -	1.24 (4.3%)	0.87 (31.6%)
Ath A 2 (0 + 6 + 6)	- -	2.69 (15.3%)	1.16 (15.7%)
Ath A 3 (0 + 0 + 8)	- -	- -	1.25 (11.5%)
Ath A 4 (0 + 2 + 0)	- -	2.01 (-)	- -
Ath B 1 (0 + 6 + 0)	- -	1.32 (17.4%)	- -
Ath B 2 (0 + 5 + 0)	- -	1.28 (11.4%)	- -
Ath B 3 (0 + 8 + 4)	- -	5.67 (17.4%)	1.90 (22.1%)
Ath B 4 (0 + 8 + 4)	- -	5.12 (11.4%)	1.80 (11.3%)
Ath B 5 (0 + 4 + 0)	- -	1.70 (12.1%)	- -
Ath C 1 (0 + 5 + 3)	- -	2.02 (18.5%)	1.00 (24.9%)
Ath C 2 (0 + 7 + 3)	- -	2.13 (15.9%)	0.82 (27.3%)
Ath C 3 (0 + 8 + 4)	- -	1.44 (23.7%)	0.78 (76.8%)
Ath C 4 (0 + 4 + 0)	- -	2.01 (23.9%)	- -
Ath C 5 (0 + 4 + 0)	- -	2.79 (32.6%)	- -
Ath C 6 (0 + 4 + 0)	- -	1.77 (24.7%)	- -
Ath C 7 (0 + 4 + 0)	- -	2.18 (31.3%)	- -
Ath C 8 (0 + 4 + 0)	- -	1.87 (16.6%)	- -
Ath E 1 (4 + 1 + 0)	1.11 (17.7%)	1.85 (-)	- -
Ath E 2 (6 + 1 + 0)	1.24 (2.6%)	2.79 (-)	- -
Ath E 3 (6 + 1 + 0)	1.20 (15.4%)	4.96 (-)	- -
Ath E 4 (6 + 1 + 0)	1.24 (10.3%)	4.28 (-)	- -
Ath E 5 (6 + 1 + 0)	1.13 (10.8%)	3.38 (-)	- -
Ath F 1 (6 + 1 + 0)	1.56 (11.9%)	9.19 (-)	- -
Ath F 2 (6 + 1 + 0)	1.20 (11.4%)	6.65 (-)	- -
Ath F 3 (6 + 1 + 0)	1.37 (12.7%)	4.76 (-)	- -
Ath F 4 (5 + 1 + 0)	1.33 (14.1%)	6.38 (-)	- -
Ath F 5 (5 + 1 + 0)	1.50 (16.0%)	6.31 (-)	- -

Sample brick (cylinders + prisms + cubes)	Size-independent mean compressive strength [MPa] (coefficient of variation)		
	Cylinders	Prisms	Cubes
Ge A 1 (0 + 8 + 3)	- -	2.12 (14.7%)	0.94 (32.9%)
Ge A 2 (0 + 4 + 0)	- -	2.10 (51.6%)	- -
Ge A 3 (0 + 4 + 0)	- -	1.82 (19.2%)	- -

Annex 2: Stress-strain diagrams obtained from monotonic compression tests on adobe masonry specimens

Results for 12 adobe masonry specimens. Specimens are hereby reported as *Xa*(*Y*), where *X* = specimen form (SB for stack bond prisms), *a* = specimen number and *Y* = load imposition procedure (LC for load-controlled and DC for displacement-controlled compressive loading).

Specimen SB1(LC)

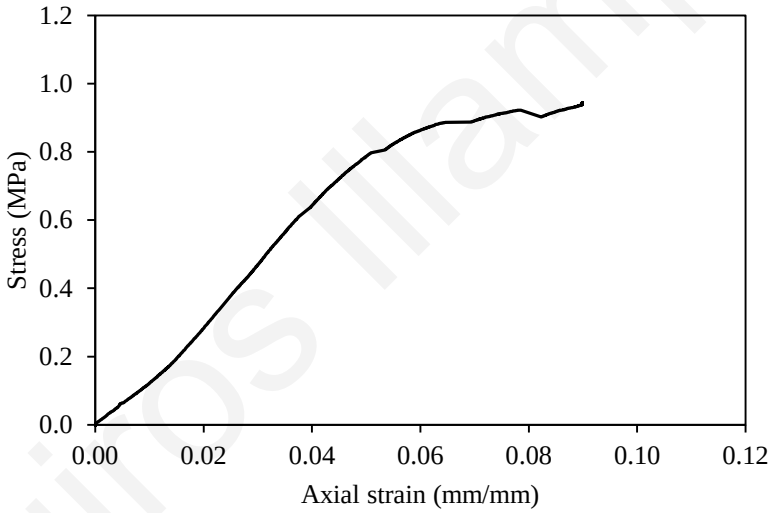

Specimen SB2(LC)

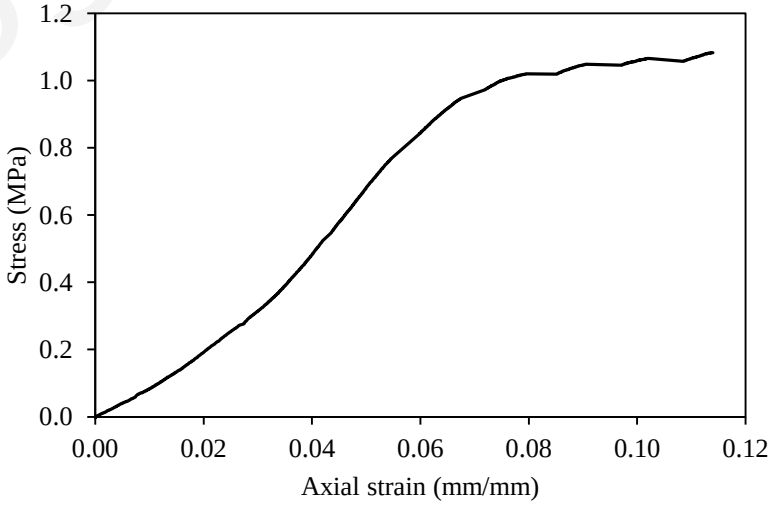

Specimen SB3(LC)

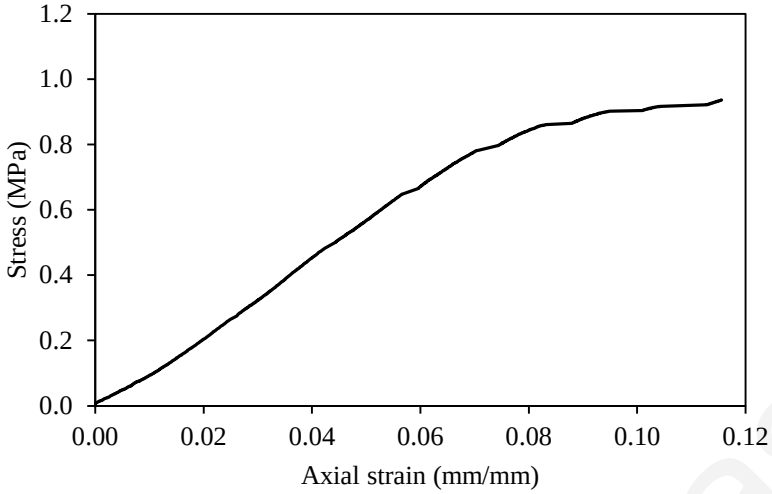

Specimen SB4(LC)

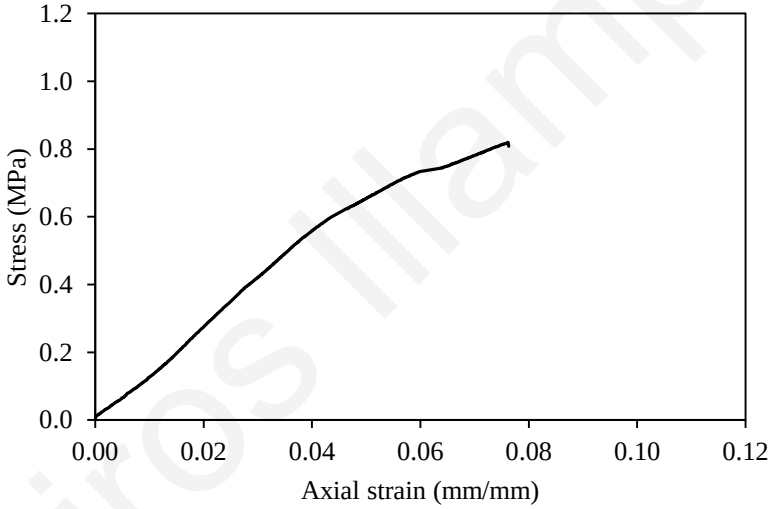

Specimen SB5(LC)

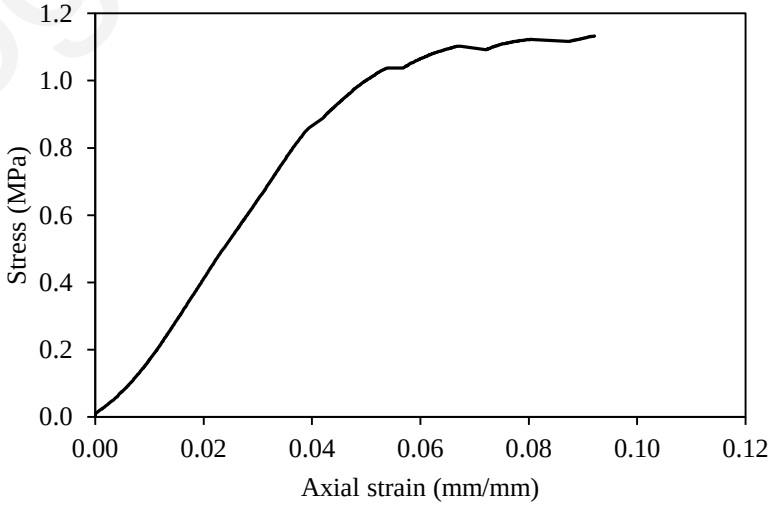

Specimen SB6(LC)

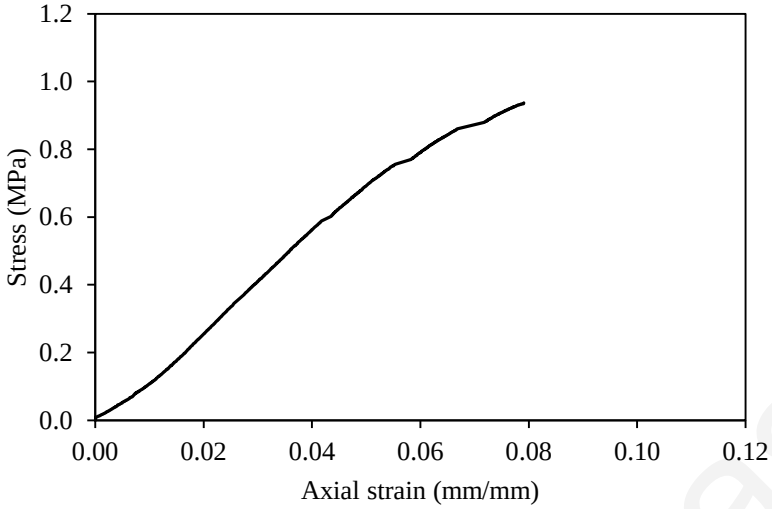

Specimen SB7(LC)

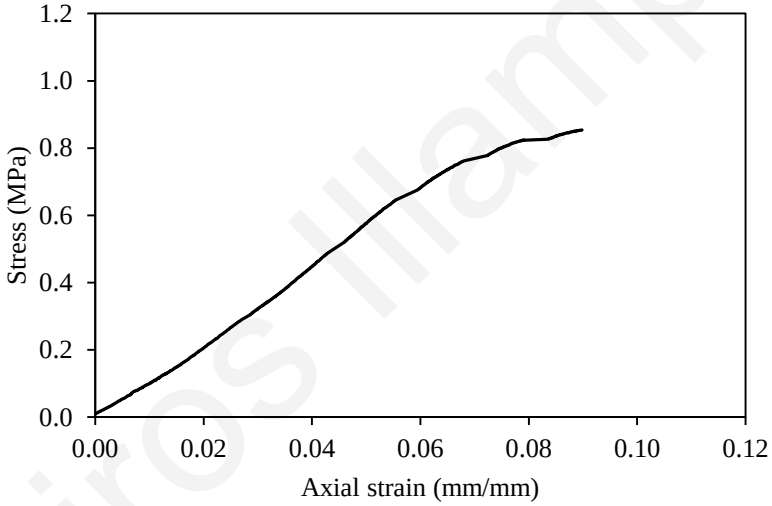

Specimen SB8(LC)

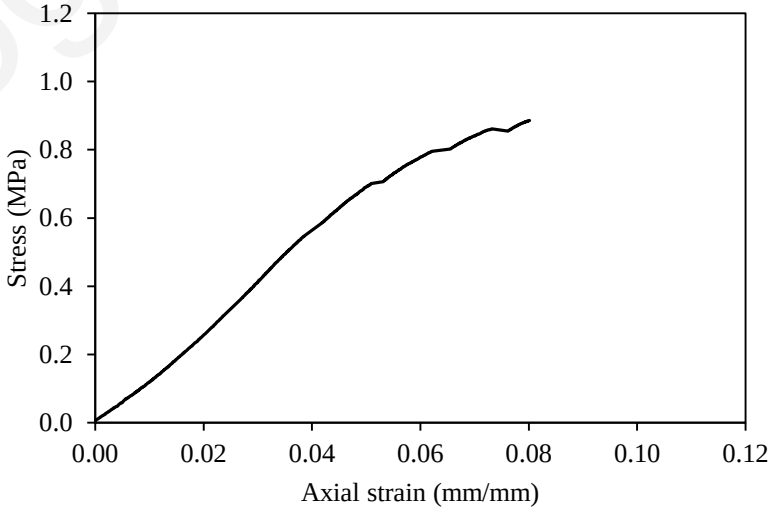

Specimen SB9(LC)

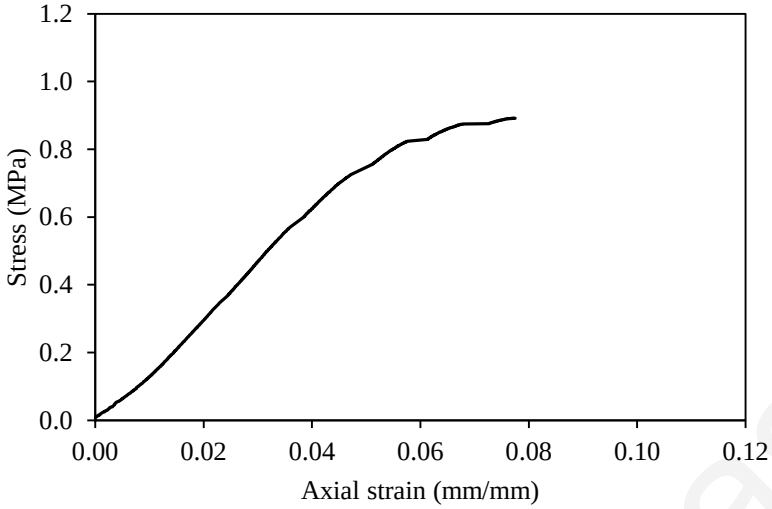

Specimen SB10(DC)

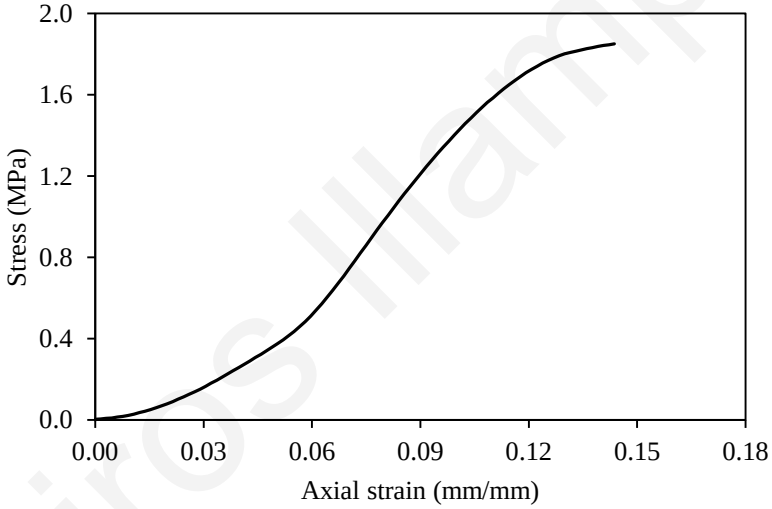

Specimen SB11(DC)

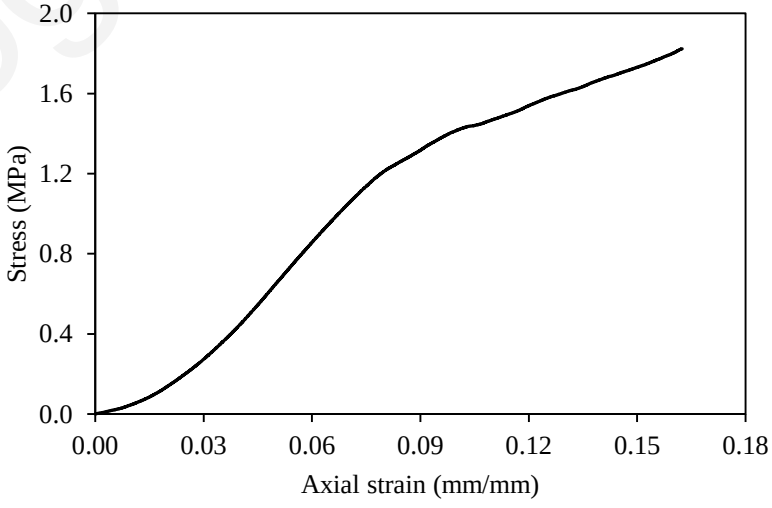

Specimen SB12(DC)

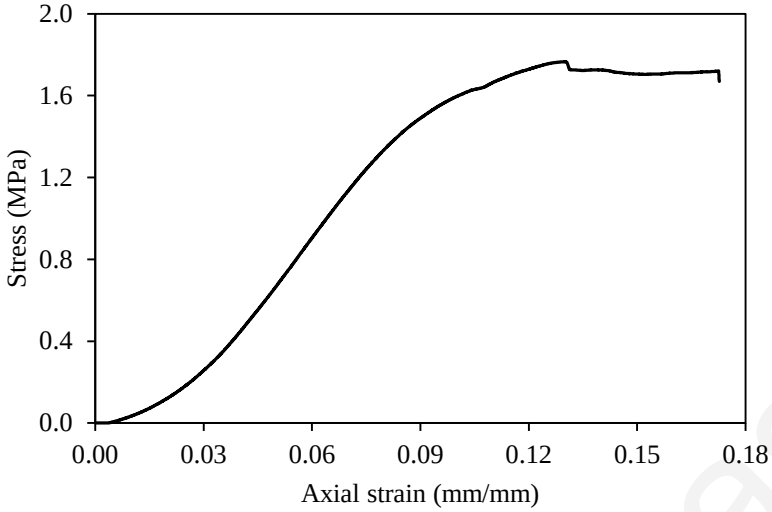

Annex 3: Pictures showing the various phases during the construction of the scaled model building

A3.1: Construction of the timber base. The cross-sections of the beams used were 50 x 100 and 50 x 200 mm^2. The beams were orthogonally connected. Above them, wooden panels with thickness of 20 mm were fixed.

A3.2: Application of the first layer of adobes. Timber elements were installed at the perimeter of the first masonry course to constrain lateral movement at the base of the structure.

A3.3: Construction of wall corners. Connection at the cross-bricks was achieved by placing overlapping adobes.

A3.4: Construction of walls. 5-6 masonry courses were first built at the corners of the structure. These acted as guides for laying the rest of adobe bricks.

A3.5: Formation of openings. A door opening 1.10 m high and 0.70 m wide was formed on the façade and two openings 0.55 x 0.55 m^2 resembling windows were formed on the two side walls.

A3.6: Formation of triangular notch. A triangular notch 0.22 m wide and 0.18 m high was formed on the rear wall to simulate the ventilation notches encountered in local vernacular buildings.

A3.7: Lintels at opening. All opening lintels were composed of two jointed timber beams, each with a cross-section of 85 x 85 mm^2. The gap between the two beams was filled with gypsum mortar.

A3.8: Installation of lintels. The lintels were set into the masonry with the application of gypsum mortar. Their abutments extended approximately 150 mm into the masonry.

A3.9: Installation of roof rafters. Timber beams with 45 x 90 mm^2 cross-sections were used to span the space between the two opposite longitudinal walls. These were set into the masonry with gypsum mortar.

A3.10: Installation of timber wedges to prevent sliding of the inclined roof. On each side wall two timber wedges were set with gypsum mortar into the masonry. These were later nailed on the roof panel.

A3.11: After completing the construction of the walls, a 20 mm thick wooden panel was fixed on the roof rafters. Additional adobes were placed upon the panel to simulate the weight of roof tiles.